
Theses and Dissertations

2007

Application of solid-state kinetics to desolvation reactions

Ammar Khawam
University of Iowa

Copyright 2007 Ammar Khawam

This dissertation is available at Iowa Research Online: <http://ir.uiowa.edu/etd/170>

Recommended Citation

Khawam, Ammar. "Application of solid-state kinetics to desolvation reactions." PhD (Doctor of Philosophy) thesis, University of Iowa, 2007.
<http://ir.uiowa.edu/etd/170>.

Follow this and additional works at: <http://ir.uiowa.edu/etd>



Part of the [Pharmacy and Pharmaceutical Sciences Commons](#)

APPLICATION OF SOLID-STATE KINETICS TO DESOLVATION REACTIONS

by

Ammar Khawam

An Abstract

Of a thesis submitted in partial fulfillment
of the requirements for the Doctor of
Philosophy degree in Pharmacy
in the Graduate College of
The University of Iowa

May 2007

Thesis Supervisor: Professor Douglas R. Flanagan

ABSTRACT

Mathematical methods have been developed to evaluate solid-state kinetics. They generally fall into two categories: model-fitting or model-free (isoconversional). Model-fitting methods determine the kinetic triplet (model, frequency factor and activation energy) whereas isoconversional (model-free) methods generate the activation energy as a function of reaction progress without modelistic assumptions.

This work investigated the relationship between calculation methods and artificial variation in activation energy. Variable activation energy, often reported by isoconversional methods, could be an artifact due to experimental errors. This can lead to erroneous mechanistic conclusions about a reaction being complex.

In this work, a new approach is proposed for obtaining the kinetic triplet that combines the advantages of isoconversional and model-fitting methods. An isoconversional method was used to select the reaction model by comparing calculated activation energies to that predicted by modelistic approaches. The selected model was the one that had an activation energy closest to the isoconversional value and the frequency factor was then obtained from the selected model. This complementary approach was used to evaluate simulated and real experimental data.

The desolvation kinetics of several structurally related solvates of sulfamerazine (5-methoxysulfadiazine) were evaluated both isothermally and nonisothermally. Calculated desolvation kinetic parameters were compared and related to the crystal structure of the solvates. A relationship was observed between calculated activation energy and solvent size. The larger the solvent molecule, the higher its solvate's desolvation activation energy. The solid-state reaction models selected were rationalized on the basis of crystal structures of the solvates where the solvent molecules were in cavities in the crystal.

Finally, it was found that kinetic parameters obtained isothermally and nonisothermally were not in agreement. It was concluded that kinetic results from isothermal experiments may not be extended to nonisothermal or vice versa without confirmation of their equivalence.

Abstract Approved: _____
Thesis Supervisor

Title and Department

Date

APPLICATION OF SOLID-STATE KINETICS TO DESOLVATION REACTIONS

by

Ammar Khawam

A thesis submitted in partial fulfillment
of the requirements for the Doctor of
Philosophy degree in Pharmacy
in the Graduate College of
The University of Iowa

May 2007

Thesis Supervisor: Professor Douglas R. Flanagan

Copyright by
AMMAR KHAWAM
2007
All Rights Reserved

Graduate College
The University of Iowa
Iowa City, Iowa

CERTIFICATE OF APPROVAL

PH.D. THESIS

This is to certify that the Ph.D. thesis of

Ammar Khawam

has been approved by the Examining Committee
for the thesis requirement for the Doctor of Philosophy
degree in Pharmacy at the May 2007 graduation.

Thesis Committee: _____
Douglas R. Flanagan, Thesis Supervisor

Dale E. Wurster

Lloyd E. Matheson

S. Alta Botha

Leonard R. MacGillivray

To my beloved family

وما بكم من نعمة فمن الله

“Whatever of blessings you have, it is from God”

Holy Quran (16:52)

ACKNOWLEDGMENTS

Human beings are eccentric, they always hate what they have, look forward to the future and want their “present” to turn into a “past”, however, when the future comes, they will never let go of the past. Here are some of the people that have shaped my life in the present, and, I will always remember them in my future, I truly thank them for being there for me:

My adviser – Dr. Douglas Flanagan, for his scientific, financial and emotional support.

My committee members – Drs. Flanagan, Wurster, Matheson, Botha and MacGillivray.

My faculty members – Drs. Kumar, Salem, Donovan and Guillory.

My colleagues – Praveen, Manpreet, Yi and Mow Yee.

My wife – Sumaya, all the pages in this thesis, are not enough to describe her support.

My mother – Although she passed away in my final year of study, I will always remember her. No matter what good I did in the past or will do in the future, it can never compare to her suffering to bring me to life and raise me. I know I’ll meet her one day, when the past, present and future collide.

My father – Dr. Mouhammad Nizar, who has also been my mentor and best friend.

My brother – Bashar, who has always been my inspiration and comfort.

My friends – Husam, Shadi, Aktham, Omar, Akram, Atta, Nidal, Mohammad, Aiman, Galib, Fadi, Loai, Rania, Amal and Kholoud. Thanks for making life enjoyable.

ABSTRACT

Most solid-state kinetic principles were derived from those for homogenous phases in the past century. Rate laws describing solid-state degradation are more complex than those in homogenous phases. Solid-state kinetic reactions can be mechanistically classified as nucleation, geometrical contraction, diffusion and reaction order models. Experimentally, solid-state kinetics are studied either isothermally or nonisothermally. Many mathematical methods have been developed to interpret experimental data for both heating protocols. These methods generally fall into one of two categories: model-fitting and model-free.

Historically, model-fitting methods were widely used because of their ability to directly determine the kinetic triplet (i.e., frequency factor $[A]$, activation energy $[E_a]$ and model). However, these methods suffer from several problems among which is their inability to uniquely determine the reaction model. This has led to the decline of these methods in favor of isoconversional (model-free) methods that evaluate kinetics without modelistic assumptions. However, isoconversional methods do not compute a frequency factor nor determine a reaction model which are needed for a complete and accurate kinetic analysis. A new approach was proposed that combines the power of isoconversional methods with model-fitting methods. It is based on using isoconversional methods instead of traditional statistical model-fitting methods to select the reaction model. Once a reaction model has been selected, the activation energy and frequency factor can be determined for that model. This approach was investigated for simulated and real experimental data for desolvation reactions of sulfameter solvates.

Controversies have arisen with regard to interpreting solid-state kinetic results which include variable activation energy, calculation methods and kinetic compensation effects. The concept of variable activation energy in solid-state reaction kinetics has

caused considerable debate because this behavior has been viewed by some as a violation of basic chemical kinetic principles. Activation energy variation has been detected by isoconversional or “model-free” calculation methods which generate activation energy as a function of reaction progress. The relationship between calculation methods and artifactual variation in activation energy was investigated by employing model-fitting and isoconversional methods to analyze both simulated and experimental data. The experimental data was for the sulfameter-dioxolane solvate desolvation by TGA. It was shown that variable activation energy in simple reactions could be an artifact resulting from the use of isoconversional methods; this artifactual behavior can be seen in both isothermal and nonisothermal kinetic experiments. Therefore, care should be taken when interpreting kinetic results from isoconversional methods. If the variation in activation energy is artifactual, this variation can lead to a false mechanistic conclusion about a reaction being complex while, in fact, it is not. Artifactual variation can be reduced by careful experimental design and control of experimental variables in addition to experimental replication, so that averaged kinetic parameters and their confidence intervals can be estimated.

The solid-state stability of several structurally related solvates of sulfameter (5-methoxysulfadiazine) was investigated by studying the kinetics of their desolvation reaction both isothermally and nonisothermally. Calculated kinetic parameters were compared and related to the crystal structure of these solvates. A relationship was established between desolvation kinetic parameters (e.g., activation energy) and the solvent size; the larger the solvent molecule, the higher its activation energy. The solid-state reaction models selected also corresponded to the single crystal structure of the sulfameter-solvate system in which the solvent molecules were in cavities. Finally, it was found that kinetic parameters obtained isothermally and nonisothermally were not in agreement. Therefore, kinetic results from one may not be extended to the other.

TABLE OF CONTENTS

LIST OF TABLES	xi
LIST OF FIGURES	xiv
CHAPTER 1 BASICS AND APPLICATIONS OF SOLID-STATE KINETICS.....	1
Solid-state kinetics: from homogenous to heterogeneous processes.....	2
Rate laws.....	3
Models and mechanisms in solid-state kinetics.....	8
Methods for studying solid-state kinetics	8
Experimental methods	9
Isothermal method.....	9
Nonisothermal method	9
Temperature integral	10
Calculation methods	13
Model-fitting methods.....	13
Isothermal model-fitting methods (Conventional method).....	13
Nonisothermal model-fitting methods	14
Model-free/isoconversional methods	17
Isothermal isoconversional methods.....	18
Nonisothermal isoconversional methods	19
Complementary model-free/modelistic approach	26
Controversies in solid-state kinetics	27
Varying activation energy in solid-state kinetics	27
True variation in activation energy	27
Elementary reactions.....	28
Complex reactions.....	28
Artifactual variation in activation energy.....	31
Temperature dependence of the rate constant	32
Kinetic Compensation Effect	33
ICTAC kinetic project	34
Summary.....	36
CHAPTER 2 MODELS IN SOLID-STATE KINETICS: BASICS AND MATHEMATICAL FUNDAMENTALS.....	49
Introduction.....	49
Model classification.....	49
Model derivation.....	50
Nucleation and nuclei growth models	50
Nucleation	51
Nuclei growth.....	53
Power law (P) models	55
The Avrami-Erofeyev (A) models	56
Autocatalytic models.....	57
Geometrical contraction (R) models	60
The contracting cylinder (contracting area) model – R2.....	61
The contracting sphere/cube (contracting volume) model–R3	62

Diffusion (D) models.....	63
Order-based (F) models.....	69
Summary.....	71
CHAPTER 3 EXPERIMENTAL METHODS	82
Solvates: description and identification.....	82
Drug solvate screening	82
The sulfameter solvate system.....	83
Solvate preparation	84
Drug and solvate characterization	85
Characterization methods	85
Light microscopy.....	85
Thermogravimetric analysis (TGA).....	85
Differential Scanning Calorimetry (DSC).....	85
Powder X-ray diffraction (PXRD)	86
Sulfameter characterization	86
Sulfameter tetrahydrofuran solvate characterization.....	86
Sulfameter dioxolane solvate characterization.....	87
Sulfameter oxane solvate characterization	87
Sulfameter dioxane solvate characterization	87
Sulfameter oxepane solvate characterization	87
Sulfameter chloroform solvate characterization.....	87
Sulfameter bromoform solvate characterization	87
Particle size effect on desolvation TGA analysis	88
Kinetic analysis of the desolvation reaction	88
Data collection.....	88
Data pretreatment	89
Data size reduction	89
Calculating the actual nonisothermal heating rates.....	90
Calculating the actual isothermal temperature	91
Data analysis of pretreated data.....	91
Data simulation.....	91
Isothermal simulation.....	92
Nonisothermal simulation	92
Validation of activation energy calculations	92
CHAPTER 4 ROLE OF ISOCONVERSIONAL METHODS IN VARYING ACTIVATION ENERGIES OF SOLID-STATE KINETICS	147
Introduction.....	147
Varying activation energy.....	147
Experimental.....	149
Data simulation.....	150
Sulfameter solvate desolvation.....	151
Results and Discussion	152
Kinetic analysis of simulated data	152
Isothermal data	152
Isoconversional methods.....	152
Model-fitting results.....	154
Nonisothermal data	154
Isoconversional methods.....	154
Model-fitting methods.....	157
Kinetic analysis of sulfameter desolvation.....	157

Isothermal data	157
Nonisothermal data	158
Confidence intervals for activation energies	160
Conclusions.....	160
CHAPTER 5 COMPLEMENTARY USE OF MODEL-FREE AND MODELISTIC METHODS IN THE ANALYSIS OF SOLID- STATE KINETICS	197
Introduction.....	197
Modelistic and model-free methods	198
Experimental.....	199
Data simulation.....	199
Sulfameter solvate desolvation.....	200
Kinetic analysis	200
Curve reconstruction and stability prediction.....	201
Results and Discussion	201
Simulated data	201
Sulfameter desolvation	202
Conclusions.....	203
CHAPTER 6 AVERAGING KINETIC PARAMETERS IN SOLID-STATE STUDIES	231
Introduction.....	231
Solvates (particle size of 355–710 μm)	232
Dioxolane solvates (particle size of 850–1700 μm)	233
Conclusions.....	233
CHAPTER 7 DESOLVATION AND POLYMORPHIC TRANSFORMATIONS OF SULFAMETER SOLVATES	244
Experimental.....	244
Sulfameter solvate desolvation.....	245
Kinetic analysis of desolvation.....	245
Polymorphic transformation of sulfameter solvates.....	246
Results and Discussion	246
Isothermal desolvation results	246
Nonisothermal desolvation results	247
Polymorphic transformations of sulfameter solvates	247
CHAPTER 8 SUMMARY AND CONCLUSIONS	298
Isothermal and nonisothermal experiments.....	298
Sulfameter system.....	300
Solid-state kinetics future	303
REFERENCES	310
APPENDIX DERIVATION OF THE SENUM-YANG APPROXIMATION TERMS.....	320
1-term.....	320
2-terms	320

3-terms	320
4-terms	321

LIST OF TABLES

Table 1.	Solid-state rate expressions for different reaction models, classifications and mathematical derivations are given in Chapter 2.....	40
Table 2.	Senum-Yang approximations of the temperature integral ^a	43
Table 3.	Summary of temperature dependencies of rate constants [19].....	47
Table 4.	Mathematical expressions for nucleation rates.....	76
Table 5.	Drugs screened for solvate formation.....	94
Table 6.	Sources for chemicals and their batch/lot numbers.....	95
Table 7.	Solvent screening for sulfameter solvate formation.....	102
Table 8.	Drug:solvent stoichiometries (1:1) by TGA for selected sulfameter solvates.....	105
Table 9.	Solvent screening for solvate formation for various structurally related sulfonamides.....	106
Table 10.	X-ray diffraction data ($I/I_0 \geq 20$) for sulfameter (Sigma Chemical, lot no. 107F0910).....	109
Table 11.	X-ray diffraction data ($I/I_0 \geq 10$) for sulfameter tetrahydrofuran solvate.....	114
Table 12.	X-ray diffraction data ($I/I_0 \geq 10$) for sulfameter dioxolane solvate.....	117
Table 13.	X-ray diffraction data ($I/I_0 \geq 10$) for sulfameter oxane solvate.....	120
Table 14.	X-ray diffraction data ($I/I_0 \geq 20$) for sulfameter dioxane solvate.....	123
Table 15.	X-ray diffraction data ($I/I_0 \geq 20$) for sulfameter oxepane solvate.....	126
Table 16.	X-ray diffraction data ($I/I_0 \geq 25$) for sulfameter chloroform solvate.....	129
Table 17.	X-ray diffraction data ($I/I_0 \geq 30$) for sulfameter bromoform solvate.....	132
Table 18.	Data reduction example using the truncation method by rounding down data. (11 data points reduced to 3).....	138
Table 19.	Programmed and calculated heating rates for several nonisothermal TGA thermograms.....	140
Table 20.	Heats of vaporization (literature) compared to vaporization activation energies (E_a) for five substances; activation energies calculated by the Vyazovkin isoconversional method for conversion values (α) of 0.1–0.90.....	146

Table 21.	Variations in isothermal simulations generated from simulation A1 (error-free), produced using a first-order reaction model (F1) with $A=1 \times 10^{15} \text{ min}^{-1}$ and $E_a=100 \text{ kJ/mole}$.	164
Table 22.	Nonisothermal simulations generated from simulation B1 (error-free), produced using a first-order reaction model with (F1) with $A=1 \times 10^{15} \text{ min}^{-1}$ and $E_a=100 \text{ kJ/mole}$. Simulations B2–B13 are perturbations of B1. ...	166
Table 23.	Nonisothermal simulations generated from simulation C1 (error-free), produced using a first-order reaction model with (F1) with $A=1 \times 10^{15} \text{ min}^{-1}$ and $E_a=100 \text{ kJ/mole}$. Simulations C2–C10 are perturbations of C1. ...	168
Table 24.	Fitted kinetic parameters for simulated isothermal data (Table 21) using model-fitting methods.*	177
Table 25.	Fitted kinetic parameters for simulated nonisothermal data (B and C), using the Coats-Redfern method.* [†]	186
Table 26.	Fitted kinetic parameters for sulfameter-dioxolane isothermal desolvation kinetics by model-fitting methods.	189
Table 27.	Fitted kinetic parameters for nonisothermal sulfameter-dioxolane desolvation data sets (Figure 55), using the Coats-Redfern method.*	194
Table 28.	Fitted kinetic parameters for simulated isothermal data (S1) using the conventional model-fitting method.	211
Table 29.	Fitted kinetic parameters for simulated nonisothermal data (S2) using the Coats-Redfern method.*	212
Table 30.	Fitted kinetic parameters for the nonisothermal desolvation of sulfameter-tetrahydrofuran solvate using the Coats-Redfern method*	215
Table 31.	Fitted kinetic parameters for the nonisothermal desolvation of sulfameter-dioxolane solvate using the Coats-Redfern method.*	216
Table 32.	Fitted kinetic parameters for the nonisothermal desolvation of sulfameter-dioxane solvate using the Coats-Redfern method.*	217
Table 33.	Fitted kinetic parameters (A3 model) for the nonisothermal desolvation of sulfameter-tetrahydrofuran solvate (Figure 79) using the Coats-Redfern method.	235
Table 34.	Fitted kinetic parameters (A2 model) for the nonisothermal desolvation of sulfameter-dioxolane solvate (Figure 80) using the Coats-Redfern method.	236
Table 35.	Fitted kinetic parameters (A3 model) for the nonisothermal desolvation of sulfameter-dioxane solvate (Figure 81) using the Coats-Redfern method.	237
Table 36.	Possible combinations of means of A and E_a .	238

Table 37.	Sum of squared differences between actual and reconstructed curves for possible A and E_a mean combinations for each solvate.....	239
Table 38.	Fitted kinetic parameters (A2 model) for the nonisothermal desolvation of sulfameter-dioxolane solvate (Figure 98) with a particle size of 850–1700 μm using the Coats-Redfern method.	242
Table 39.	Sum of squared differences between actual and reconstructed curves for possible A and E_a mean combinations for sulfameter-dioxolane solvate with a particle size of 850–1700 μm	243
Table 40.	Sulfameter polymorphic forms.	250
Table 41.	Fitted kinetic parameters for sulfameter-tetrahydrofuran isothermal desolvation kinetics by the conventional model-fitting method.	256
Table 42.	Fitted kinetic parameters for sulfameter-dioxolane isothermal desolvation kinetics by the conventional model-fitting method.	257
Table 43.	Fitted kinetic parameters for sulfameter-oxane isothermal desolvation kinetics by the conventional model-fitting method.	258
Table 44.	Fitted kinetic parameters (averaged from two experiments) ^a for sulfameter-dioxane isothermal desolvation kinetics by the conventional model-fitting method.	259
Table 45.	Fitted kinetic parameters for sulfameter-oxepane isothermal desolvation kinetics by the conventional model-fitting method.	260
Table 46.	Average fitted kinetic parameters for the nonisothermal desolvation of sulfameter-oxane solvate using the Coats-Redfern method.*.....	275
Table 47.	Average fitted kinetic parameters for the nonisothermal desolvation of sulfameter-oxepane solvate using the Coats-Redfern method.*.....	276
Table 48.	Average fitted kinetic parameters for the nonisothermal desolvation of sulfameter-chloroform solvate using the Coats-Redfern method.*.....	277
Table 49.	Average fitted kinetic parameters for the nonisothermal desolvation of sulfameter-bromoform solvate using the Coats-Redfern method.*.....	278
Table 50.	Kinetic results for the isothermal desolvation reaction of several sulfameter solvates evaluated by the conventional model-fitting approach. ^a	305
Table 51.	Averaged kinetic results for the nonisothermal desolvation reaction of several sulfameter solvates evaluated by the complementary approach. ^a	305
Table 52.	Temperature ranges covered in isothermal and nonisothermal desolvation experiments for several sulfameter solvates.....	307

LIST OF FIGURES

Figure 1.	Schematic representation of reactivity: a. homogenous system; b. heterogeneous system. Black dots represent reaction sites.....	38
Figure 2.	Transformations of TGA and DSC curves to conversion fraction curves: Desolvation thermogram of a solid solvate by TGA (a) and DSC (b); c. α -T plot for the desolvation process for both DSC and TGA results.	39
Figure 3.	Methods for studying solid-state kinetics.	41
Figure 4.	TGA data for a simulated dehydration reaction: a, isothermal; b, nonisothermal.....	42
Figure 5.	Isothermal model fitting method (conventional method): a, simulated α -time curves with 0.25% random error in time at: \blacktriangle , 340 K; \blacklozenge , 345 K; \blacklozenge , 350 K; \square , 355 K and \blacksquare , 360 K. Inset shows simulation parameters: b, tabulated values obtained from the curve in addition to $g(\alpha)$ values for each model; c, first data fit ($g(\alpha)$ vs. t) for each model and temperature (only two temperature values are shown) and d, second data fit (Arrhenius plot) from which A and E_a can be calculated for each model.....	44
Figure 6.	Isoconversional methods for evaluating solid-state kinetics: a, Standard method for a set of isothermal curves at: \blacksquare , 340 K; \square , 345 K; \bullet , 350 K; \circ , 355 K and \blacklozenge , 360 K; b, Ozawa-Flynn-Wall (OFW) method for a set of nonisothermal curves at: \blacksquare , 1 K/min; \square , 2 K/min; \bullet , 4 K/min; \circ , 8 K/min and \blacklozenge , 16 K/min.	45
Figure 7.	Examples of experimental variables that could affect thermograms obtained by TGA/DSC: a, particle shape; b, purge gas flow rate; c, sample mass and d. sample packing.	46
Figure 8.	a, Kinetic compensation effect (KCE); b, isokinetic relationship (IKR). Each point in "a" results from an Arrhenius plot shown in "b".....	48
Figure 9.	Isothermal $d\alpha/dt$ -time and α -time plots for solid-state reaction models (Table 1); data simulated with a rate constant of 0.049 min^{-1} : a, acceleratory; b-d, deceleratory; e, constant; f, sigmoidal.....	72
Figure 10.	Nonisothermal $d\alpha/dT$ and α -temperature plots for solid-state reaction models (Table 1); data simulated with a heating rate of 10 K/min, frequency factor of $1 \times 10^{15} \text{ min}^{-1}$ and activation energy of 80 kJ/mole.	74
Figure 11.	Two types of nuclei growth restrictions: black dots are nucleation sites and shaded areas are nuclei growth regions.....	77
Figure 12.	Isothermal α -time plots for the Prout-Tompkins reaction model (Table 1); data simulated with a rate constant of 0.152 min^{-1} : \blacksquare , data simulated	

according to Eq. (110); □, data simulated according to Eq. (109) where $c = t_{\max}$ (30.21 min.).	78
Figure 13. Geometrical crystal shapes: a, cylinder; b, sphere and c, cube.	79
Figure 14. One-dimensional diffusion through a flat plane [133]. A and B are reactants, AB is the product interface, l is the thickness of the interface AB and x is the distance measured from interface Q into AB.	80
Figure 15. Schematic representation of a spherical particle reaction.	81
Figure 16. Schematic representation of a cylindrical particle reaction.	81
Figure 17. Desolvation TGA thermograms of doxycycline HCl hydrate at a heating rate of 5 K/min.	96
Figure 18. TGA thermograms of triamterene crystallized from different solvents: a, original material (10 K/min); b, butanol (10 K/min); c, dimethylformamide (10 K/min) and d, ethanol (20 K/min).	97
Figure 19. Dehydration TGA thermogram of ouabain octahydrate at 1K/min.	98
Figure 20. Dehydration TGA thermograms for two nitrofurantoin hydrates at 10 K/min, prepared according to ref. [148] to obtain: a. Form I; b. Form II.	98
Figure 21. Dehydration TGA thermogram of carbamazepine hydrate at 16 K/min.	99
Figure 22. TGA thermograms of cortisone acetate crystallized from different solvents: a, original material (10 K/min); b, acetonitrile (10 K/min); c, dimethylformamide (5 K/min); d, n-propanol (16 K/min); e, acetic acid (16 K/min) and f, dioxane (16 K/min).	100
Figure 23. TGA thermograms of spironolactone crystallized from: a, methanol (10 K/min); b, ethanol (16 K/min); c, benzene (10 K/min) and d, ethyl acetate (16 K/min).	101
Figure 24. Thermal analysis of sulfameter from Sigma Chemical (lot no. 107F0910) by: a, TGA at a heating rate of 20 K/min and b, DSC at a heating rate of 10 K/min.	107
Figure 25. Powder X-ray diffraction pattern for sulfameter as supplied (Sigma Chemical, lot no. 107F0910).	108
Figure 26. Light microscopy of sulfameter and different sulfameter solvates at 5X magnification: a, sulfameter; b, tetrahydrofuran; c, dioxolane; d, oxane; e, dioxane; f, oxepane; g, chloroform and h, bromoform.	110
Figure 27. Thermal analysis of sulfameter tetrahydrofuran solvate at a heating rate of 16 K/min by: a, TGA and b, DSC.	112
Figure 28. Powder X-ray diffraction pattern for sulfameter tetrahydrofuran solvate.	113
Figure 29. Thermal analysis of sulfameter dioxolane solvate at a heating rate of 16 K/min by: a, TGA and b, DSC.	115

Figure 30. Powder X-ray diffraction pattern for sulfameter dioxolane solvate.....	116
Figure 31. Thermal analysis of sulfameter oxane solvate at a heating rate of 16 K/min by: a, TGA and b, DSC.....	118
Figure 32. Powder X-ray diffraction pattern for sulfameter oxane solvate.....	119
Figure 33. Thermal analysis of sulfameter dioxane solvate at a heating rate of 16 K/min by: a, TGA and b, DSC.....	121
Figure 34. Powder X-ray diffraction pattern for sulfameter dioxane solvate.....	122
Figure 35. Thermal analysis of sulfameter oxepane solvate at a heating rate of 16 K/min by: a, TGA and b, DSC.....	124
Figure 36. Powder X-ray diffraction pattern for sulfameter oxepane solvate.....	125
Figure 37. Thermal analysis of sulfameter chloroform solvate at a heating rate of 16 K/min by: a, TGA and b, DSC.....	127
Figure 38. Powder X-ray diffraction pattern for sulfameter chloroform solvate.....	128
Figure 39. Thermal analysis of sulfameter bromoform solvate at a heating rate of 16 K/min by: a, TGA (black); DTG (gray) and b, DSC.....	130
Figure 40. Powder X-ray diffraction pattern for sulfameter bromoform solvate.....	131
Figure 41. Isothermal desolvation thermograms at 70°C for sulfameter dioxane solvate having an uncontrolled particle size (i.e., unsieved sample).....	133
Figure 42. Isothermal desolvation thermograms at 75°C for sulfameter dioxane solvate having a particle size range of 90 – 300 µm.....	134
Figure 43. Nonisothermal desolvation thermograms at 16 K/min for sulfameter dioxane solvate having an uncontrolled particle size (i.e., unsieved sample).....	135
Figure 44. Nonisothermal desolvation thermograms at 16 K/min for sulfameter dioxane solvate having a particle size range of 90 – 300 µm.....	136
Figure 45. Nonisothermal desolvation thermograms at 16 K/min for sulfameter oxane solvate having a particle size range of 90 – 300 µm.....	137
Figure 46. Calcium oxalate monohydrate dehydration thermograms at: 2, 4 and 8 K/min evaluated by two data reduction methods: ■, MLR and □, Truncation.....	139
Figure 47. Linear heating rate profile of an empty TG pan for a nonisothermal run at a programmed heating rate of 10 K/min.....	141
Figure 48. Determination of actual experimental temperature of an isothermal desolvation reaction (sulfameter-tetrahydrofuran solvate at T=55°C). Region A represents the heat up period, while region B is the portion where the desolvation reaction occurs at a rapid rate.....	142

Figure 49. Microsoft Excel's Solver [®] parameters used for iterative solving of kinetic equations: a, graphical interface and b, Visual Basic [®] code used in Excel's Macros.	143
Figure 50. Nonisothermal thermograms for the evaporation of five substances and their isoconversional plots: a, water; b, deuterium oxide; c, propanol; d, hexane and e, naphthalene.	144
Figure 51. Error-free simulation (A1) of α versus time for several isothermal kinetic runs at: \blacktriangle , 323 K; \diamond , 328 K; \blacklozenge , 333 K; \square , 338 K; and \blacksquare , 343 K. The inset gives the simulation model, pre-exponential factor (A) and activation energy (E_a).....	163
Figure 52. Error-free simulations (B1) of α versus temperature for nonisothermal kinetic runs at: \blacktriangle , 2 K/min; \diamond , 4 K/min; \blacklozenge , 8 K/min; \square , 16 K/min and \blacksquare , 32 K/min. The inset gives the model, pre-exponential factor (A) and activation energy (E_a) for these simulations.	165
Figure 53. Error-free simulations (C1) of α versus temperature for nonisothermal kinetic runs at: \blacktriangle , 0.5 K/min; \diamond , 1 K/min; \blacklozenge , 1.5 K/min; \square , 2 K/min and \blacksquare , 2.5 K/min. The inset gives the model, pre-exponential factor (A) and activation energy (E_a) for these simulations.	167
Figure 54. α versus time plots for the isothermal desolvation of sulfameter-dioxolane solvate samples: a, sample 1; b, sample 2; c, sample 3 and d, sample 4.	169
Figure 55. α versus temperature plots for the nonisothermal desolvation of sulfameter-dioxolane solvate sets: a, set 1; b, set 2; c, set 3; d, set 4 and e, set 5.	170
Figure 56. E_a versus α plots of simulated isothermal runs (A1), evaluated by three isoconversional methods: \blacktriangle , standard; \diamond , Friedman and \blacklozenge , AIC.	171
Figure 57. E_a versus α plots of simulated isothermal runs (A2–6), evaluated by three isoconversional methods: \blacktriangle , standard; \diamond , Friedman and \blacklozenge , AIC.	172
Figure 58. E_a versus α plots of simulated isothermal runs (A7–10), evaluated by three isoconversional methods: \blacktriangle , standard; \diamond , Friedman and \blacklozenge , AIC.	173
Figure 59. E_a versus α plots of simulated isothermal runs (A11–12), evaluated by three isoconversional methods: \blacktriangle , standard; \diamond , Friedman and \blacklozenge , AIC.	174
Figure 60. E_a versus α plots of simulated isothermal runs (A13–14), evaluated by three isoconversional methods: \blacktriangle , standard; \diamond , Friedman and \blacklozenge , AIC.	175
Figure 61. E_a versus α plots of simulated isothermal runs (A15), evaluated by three isoconversional methods: \blacktriangle , standard; \diamond , Friedman and \blacklozenge , AIC.	176
Figure 62. E_a versus α plots of simulated nonisothermal runs (Simulation B1), evaluated by three isoconversional methods: \square , VYZ; \blacksquare , OFW and \blacklozenge , AIC.....	178

Figure 63. E_a versus α plots of simulated nonisothermal runs (Simulations B2–7), evaluated by two isoconversional methods: \square , VYZ and \blacklozenge , AIC.	179
Figure 64. E_a versus α plots of simulated nonisothermal runs (Simulations B8–13), evaluated by two isoconversional methods: \square , VYZ and \blacklozenge , AIC.	180
Figure 65. E_a versus α plots of simulated nonisothermal runs (Simulation B14), evaluated by three isoconversional methods: \square , VYZ; \blacksquare , OFW and \blacklozenge , AIC.	181
Figure 66. E_a versus α plots of simulated nonisothermal runs (Simulation C1), evaluated by three isoconversional methods: \square , VYZ; \blacksquare , OFW and \blacklozenge , AIC.	182
Figure 67. E_a versus α plots of simulated nonisothermal runs (Simulations C2–9), evaluated by two isoconversional methods: \square , VYZ and \blacklozenge , AIC.	183
Figure 68. E_a versus α plots of simulated nonisothermal runs (Simulation C10), evaluated by three isoconversional methods: \square , VYZ; \blacksquare , OFW and \blacklozenge , AIC.	184
Figure 69. α versus temperature curves for simulations C4, C5 and C9 (a-c) at nominal heating rates of: \blacktriangle , 0.5 K/min; \diamond , 1 K/min; \blacklozenge , 1.5 K/min; \square , 2 K/min; \blacksquare , 2.5 K/min and simulation B13; (d) at: \blacktriangle , 2 K/min; \diamond , 4 K/min; \blacklozenge , 8 K/min; \square , 16 K/min and \blacksquare , 32 K/min.	185
Figure 70. E_a versus α plots for isothermal sulfameter-dioxolane solvate desolvation runs (samples 1–4), evaluated by three isoconversional methods: \blacksquare , standard; \square , Friedman and \blacklozenge , AIC.	187
Figure 71. E_a versus α plots for isothermal sulfameter-dioxolane solvate desolvation runs of four samples. Plots a, c and e are for samples 1–2. Plots b, d and f are for samples 3–4.	188
Figure 72. E_a versus α plots for nonisothermal sulfameter-dioxolane solvate desolvation runs (sets 1–5), evaluated by three isoconversional methods: \blacksquare , OFW; \square , VYZ and \blacklozenge , AIC.	191
Figure 73. E_a versus α plots for nonisothermal sulfameter-dioxolane solvate desolvation evaluated by the Vyazovkin (VYZ) method.	192
Figure 74. α versus temperature plots for the nonisothermal desolvation of sulfameter-dioxolane solvate for five experimental sets: a. sets 1–2 with nominal heating rates of 1, 1.5, 2, 2.5 and 3K/min; b. sets 3–5 with nominal heating rates of 1, 2, 4, 8 and 16 K/min.	193
Figure 75. Model-fitting correlation coefficients (r) for nonisothermal sulfameter-dioxolane solvate desolvation evaluated by the Coats-Redfern method: \blacksquare , set 1; \square , set 2; \bullet , set 3; \circ , set 4 and \blacktriangle , set 5. Values from each set are averages from five curves.	195
Figure 76. E_a versus α plots for isothermal sulfameter-dioxolane solvate desolvation using the average of samples 1–4 with 95% confidence intervals, evaluated by the: a, standard method and b, AIC method.	196

Figure 77. Simulations of α versus time for isothermal kinetic runs with 0.25% random error in time at: \blacktriangle , 340 K; \diamond , 345 K; \blacklozenge , 350 K; \square , 355 K and \blacksquare , 360 K (simulation S1). The inset gives the simulation model, pre-exponential factor (A) and activation energy (E_a).	206
Figure 78. Simulated α -temperature plots with 0.25% random error in temperature ($^{\circ}\text{C}$) for nonisothermal kinetic runs at: \blacktriangle , 1 K/min; \diamond , 2 K/min; \blacklozenge , 4 K/min; \square , 8 K/min and \blacksquare , 16 K/min (simulation S2). The inset gives the simulation model, pre-exponential factor (A) and activation energy (E_a).	207
Figure 79. α versus temperature plots for the nonisothermal desolvation of sulfameter-tetrahydrofuran solvate at: \blacktriangle , 0.95; \diamond , 1.93 \blacklozenge , 3.86 K and \square , 7.61 K/min.....	208
Figure 80. α versus temperature plots for the nonisothermal desolvation of sulfameter-dioxolane solvate at: \blacktriangle , 0.96; \diamond , 1.92 \blacklozenge , 3.80 K and \square , 7.62 K/min.	209
Figure 81. α versus temperature plots for the nonisothermal desolvation of sulfameter-dioxane solvate at: \blacktriangle , 0.98; \diamond , 1.99 \blacklozenge , 3.94 K and \square , 7.71 K/min.	210
Figure 82. Isoconversional-model plot of activation energies for simulation S1 calculated by: \blacksquare , conventional model-fitting method and \square , standard isoconversional method.	213
Figure 83. Isoconversional-model plot of activation energies for simulation S2 calculated by: \bullet , Coats-Redfern's modelistic method and \square , Vyazovkin's isoconversional method.....	214
Figure 84. Isoconversional-model plot of activation energies for the nonisothermal desolvation of sulfameter-tetrahydrofuran solvate calculated by: \bullet , Coats-Redfern's modelistic method and \square , Vyazovkin's isoconversional method.	218
Figure 85. Isoconversional-model plot of activation energies for the nonisothermal desolvation of sulfameter-dioxolane solvate calculated by: \bullet , Coats-Redfern's modelistic method and \square , Vyazovkin's isoconversional method.....	219
Figure 86. Isoconversional-model plot of activation energies for the nonisothermal desolvation of sulfameter-dioxane solvate calculated by: \bullet , Coats-Redfern's modelistic method and \square , Vyazovkin's isoconversional method.....	220
Figure 87 Sum of squared differences between actual and reconstructed nonisothermal desolvation curves ($(T_{\text{actual}} - T_{\text{reconstructed}})^2$) of sulfameter tetrahydrofuran solvate.	221
Figure 88. Sum of squared differences between actual and reconstructed nonisothermal desolvation curves ($(T_{\text{actual}} - T_{\text{reconstructed}})^2$) of sulfameter dioxolane solvate.	222

Figure 89. Sum of squared differences between actual and reconstructed nonisothermal desolvation curves ($(T_{\text{actual}} - T_{\text{reconstructed}})^2$) of sulfameter dioxane solvate.....	223
Figure 90. Reconstructed α -T plots for nonisothermal desolvation of sulfameter-tetrahydrofuran solvate for four heating rates (0.95, 1.93, 3.86, 7.61 K/min): ■, experimental curves and □, reconstructed curves (A3).....	224
Figure 91. Reconstructed α -T plots for nonisothermal desolvation of sulfameter-dioxolane solvate for four heating rates (0.96, 1.92, 3.80, 7.62 K/min): ■, experimental curves and □, reconstructed curves (A2).....	225
Figure 92. Reconstructed α -T plots for nonisothermal desolvation of sulfameter-dioxane solvate for four different heating rates (0.98, 1.99, 3.94, 7.71 K/min): ■, experimental curves and □, reconstructed curves (a. A3; b. P2).....	226
Figure 93. Reconstructed α -T plots for nonisothermal desolvation of sulfameter-dioxane solvate for four heating rates (0.98, 1.99, 3.94, 7.71 K/min): ■, experimental curves and □, reconstructed curves (F1).	227
Figure 94. Predicted α -T plots for nonisothermal desolvation of sulfameter-tetrahydrofuran solvate at three heating rates (2.97, 4.96, 9.66 K/min): ■, experimental and □, predicted (A3).	228
Figure 95. Predicted α -T plots for the nonisothermal desolvation of sulfameter-dioxolane solvate at three heating rates (4.84, 9.42, 28.42 K/min): ■, experimental and □, predicted (A2).	229
Figure 96. Predicted α -T plots for the nonisothermal desolvation of sulfameter-dioxane solvate at three heating rates (1.52, 4.93, 8.80 K/min): ■, experimental and □, predicted (A3).	230
Figure 97. Actual (■) and reconstructed (□) curves for the desolvation of sulfameter dioxolane solvate at 1.92 K/min. Curves reconstructed according to possible combinations of means of A and E_a given in Table 36: a, 1; b, 2; c, 3; d, 4; e, 5; f, 6; g, 7; h, 8 and i, 9	240
Figure 98. α versus temperature plots for the nonisothermal desolvation of sulfameter-dioxolane for 23 samples having a particle size of 850–1700 μm at various heating rates.	241
Figure 99. α versus time plots for the isothermal desolvation of sulfameter-tetrahydrofuran solvate at: ■, 341.19 K; □, 336.00 K; ◆, 330.71 K; ◇, 325.41 K and ▲, 320.34 K.....	251
Figure 100. α versus time plots for the isothermal desolvation of sulfameter-dioxolane solvate at: ■, 341.33 K; □, 336.02 K; ◆, 330.83 K; ◇, 325.70 K and ▲, 320.48 K.....	252
Figure 101. α versus time plots for the isothermal desolvation of sulfameter-oxane solvate at: ■, 341.64 K; □, 336.26 K; ◆, 330.38 K; ◇, 325.68 K and ▲, 320.21 K.....	253

Figure 102. α versus time plots for the isothermal desolvation of sulfameter-dioxane solvate at: a. ■, 341.38 K; □, 336.04 K; ◆, 330.87 K; ◇, 325.53 K and ▲, 320.33 K; b. ■, 346.33 K; □, 341.07 K; ◆, 335.90 K; ◇, 330.64 K and ▲, 325.45 K.	254
Figure 103. α versus time plots for the isothermal desolvation of sulfameter-oxepane solvate at: ■, 341.64 K; □, 336.26 K; ◆, 330.38 K; ◇, 325.68 K and ▲, 320.21 K.	255
Figure 104. α versus reduced time plots ($t/t_{0.9}$) for the isothermal desolvation of sulfameter-tetrahydrofuran solvate and various reaction models: ■, desolvation data (Figure 99); ■, A2; ◆, A3; ▲, A4; ■, D1; ◆, D2; ▲, D3; ●, D4; ■, F1; ◆, F2; ▲, F3; □, P2; ◇, P3; △, P4; ■, R1; ◆, R2 and ▲, R3.	261
Figure 105. α versus reduced time plots ($t/t_{0.9}$) for the isothermal desolvation of sulfameter-dioxolane solvate and various reaction models: ■, desolvation data (Figure 100); ■, A2; ◆, A3; ▲, A4; ■, D1; ◆, D2; ▲, D3; ●, D4; ■, F1; ◆, F2; ▲, F3; □, P2; ◇, P3; △, P4; ■, R1; ◆, R2 and ▲, R3.	262
Figure 106. α versus reduced time plots ($t/t_{0.9}$) for the isothermal desolvation of sulfameter-oxane solvate and various reaction models: ■, desolvation data (Figure 101); ■, A2; ◆, A3; ▲, A4; ■, D1; ◆, D2; ▲, D3; ●, D4; ■, F1; ◆, F2; ▲, F3; □, P2; ◇, P3; △, P4; ■, R1; ◆, R2 and ▲, R3.	263
Figure 107. α versus reduced time plots ($t/t_{0.9}$) for the isothermal desolvation of sulfameter-dioxane solvate and various reaction models: ■, desolvation data (Figure 102 a and b); ■, A2; ◆, A3; ▲, A4; ■, D1; ◆, D2; ▲, D3; ●, D4; ■, F1; ◆, F2; ▲, F3; □, P2; ◇, P3; △, P4; ■, R1; ◆, R2 and ▲, R3.	264
Figure 108. α versus reduced time plots ($t/t_{0.9}$) for the isothermal desolvation of sulfameter-oxepane solvate and various reaction models: ■, desolvation data (Figure 103); ■, A2; ◆, A3; ▲, A4; ■, D1; ◆, D2; ▲, D3; ●, D4; ■, F1; ◆, F2; ▲, F3; □, P2; ◇, P3; △, P4; ■, R1; ◆, R2 and ▲, R3.	265
Figure 109. E_a versus α plots for isothermal sulfameter-tetrahydrofuran solvate desolvation evaluated by the AIC method.	266
Figure 110. E_a versus α plots for isothermal sulfameter-dioxolane solvate desolvation evaluated by the AIC method.	267
Figure 111. E_a versus α plots for isothermal sulfameter-oxane solvate desolvation evaluated by the AIC method.	268
Figure 112. E_a versus α plots for isothermal sulfameter-dioxane solvate desolvation evaluated by the AIC method using two data sets.	269
Figure 113. E_a versus α plots for isothermal sulfameter-oxepane solvate desolvation evaluated by the AIC method.	270

Figure 114. α versus temperature plots for the nonisothermal desolvation of sulfameter-oxane solvate at: \blacktriangle , 1; \diamond , 2; \blacktriangle , 4; \square , 8 and \blacksquare , 16 K/min.	271
Figure 115. α versus temperature plots for the nonisothermal desolvation of sulfameter-oxepane solvate at: \blacktriangle , 1; \diamond , 2; \blacklozenge , 4; \square , 8 and \blacksquare , 16 K/min.	272
Figure 116. α versus temperature plots for the nonisothermal desolvation of sulfameter-chloroform solvate at: \blacktriangle , 1; \diamond , 2; \blacklozenge , 4; \square , 8 and \blacksquare , 16 K/min.	273
Figure 117. α versus temperature plots for the nonisothermal desolvation of sulfameter-bromoform solvate at: \blacktriangle , 1; \diamond , 2; \blacklozenge , 4; \square , 8 and \blacksquare , 16 K/min.	274
Figure 118. Sum of squared differences between actual and reconstructed nonisothermal desolvation curves ($(T_{\text{actual}} - T_{\text{reconstructed}})^2$) for the sulfameter oxane solvate.	279
Figure 119. Sum of squared differences between actual and reconstructed nonisothermal desolvation curves ($(T_{\text{actual}} - T_{\text{reconstructed}})^2$) for the sulfameter oxepane solvate.	280
Figure 120. Sum of squared differences between actual and reconstructed nonisothermal desolvation curves ($(T_{\text{actual}} - T_{\text{reconstructed}})^2$) for the sulfameter chloroform solvate.	281
Figure 121. Reconstructed α -T plots for nonisothermal desolvation of sulfameter-oxane solvate for five heating rates (1, 2, 4, 8 and 16 K/min): \blacksquare , experimental curves and \square , reconstructed curves (A2).	282
Figure 122. Reconstructed α -T plots for nonisothermal desolvation of sulfameter-oxepane solvate for five heating rates (1, 2, 4, 8 and 16 K/min): \blacksquare , experimental curves and \square , reconstructed curves (A3).	283
Figure 123. Reconstructed α -T plots for nonisothermal desolvation of sulfameter-chloroform solvate for five heating rates (1, 2, 4, 8 and 16 K/min): \blacksquare , experimental curves and \square , reconstructed curves (A2).	284
Figure 124. E_a - α plot for nonisothermal sulfameter-bromoform solvate desolvation evaluated by the Vyazovkin (VYZ) isoconversional method.	285
Figure 125. Sum of squared differences between actual and reconstructed nonisothermal desolvation curves ($(T_{\text{actual}} - T_{\text{reconstructed}})^2$) for the sulfameter bromoform solvate.	286
Figure 126. Reconstructed α -T plots for nonisothermal desolvation of sulfameter-bromoform solvate for five heating rates (1, 2, 4, 8 and 16 K/min): \blacksquare , experimental curves and \square , reconstructed curves (R3).	287
Figure 127. DSC analysis of sulfameter at a heating rate of 16 K/min: (—); first heating cycle, (—) and second heating cycle (after cooling sample at room temperature).	288

Figure 128. Amorphous forms of sulfameter prepared by melting any crystalline form and slowly cooling: a, amorphous form produced from original bulk drug; dioxolane; oxane and dioxane solvates; b, amorphous form produced from tetrahydrofuran; oxepane; chloroform and bromoform solvates.....	289
Figure 129. Polymorphic transformations of sulfameter and its solvates upon heating; bolded forms are the major component.....	290
Figure 130. DSC analysis of sulfameter–dioxolane solvate at a heating rate of 16 K/min: (—) first heating cycle and (—) second heating cycle (after cooling sample to room temperature).	291
Figure 131. DSC analysis of sulfameter–dioxane solvate at a heating rate of 16 K/min: (—) first heating cycle and (—) second heating cycle (after cooling sample to room temperature).	292
Figure 132. DSC analysis of sulfameter–oxane solvate at a heating rate of 16 K/min: (—) first heating cycle and (—) second heating cycle (after cooling sample to room temperature).	293
Figure 133. DSC analysis of sulfameter–tetrahydrofuran solvate at a heating rate of 16 K/min: (—) first heating cycle and (—) second heating cycle (after cooling sample to room temperature).	294
Figure 134. DSC analysis of sulfameter – oxepane solvate at a heating rate of 16 K/min: (—) first heating cycle and (—) second heating cycle (after cooling sample to room temperature).	295
Figure 135. DSC analysis of sulfameter–chloroform solvate at a heating rate of 16 K/min: (—) first heating cycle and (—) second heating cycle (after cooling sample to room temperature).	296
Figure 136. DSC analysis of sulfameter–bromoform solvate at a heating rate of 16 K/min: (—) first heating cycle and (—) second heating cycle (after cooling sample to room temperature).	297
Figure 137. Reconstructed α -time plots for isothermal desolvation of sulfameter solvates (■, experimental and □, reconstructed) at five temperatures (323, 328, 333, 338 and 343 K): a, tetrahydrofuran; b, dioxolane; c, oxane; d, dioxane and e. oxepane. Plots reconstructed from parameters calculated nonisothermally (Table 51).....	306
Figure 138. Desolvation activation energy versus solvent molar volume for different sulfameter solvates (□, tetrahydrofuran; ●, dioxolane; ○, oxane; ●, dioxane and ■, oxepane): a. isothermal and b. nonisothermal.	308
Figure 139. Kinetic compensation effect for different sulfameter solvates (□, tetrahydrofuran; ●, dioxolane; ○, oxane; ●, dioxane and ■, oxepane): a. isothermal and b. nonisothermal.	309

CHAPTER 1

BASICS AND APPLICATIONS OF SOLID-STATE KINETICS

Many transformations may occur when a solid sample is heated – melting, sublimation, polymorphic transformation, desolvation or degradation [1]. These solid-state reactions are common, especially polymorphic transformations and degradation. Solid-state chemistry has recently gained much interest in pharmaceutical sciences, which renders the topic of solid-state kinetics important. Solid-state reactions have many forms, however, those that involve weight or enthalpic change are more studied as their kinetics can be followed by thermal analytical methods. For pharmaceutical solids, many solid-state kinetic studies are either desolvation reactions or polymorphic transformations. Interest in these reactions is increasing as many formulated drugs, including compendial drugs, are solvates, mainly hydrates. The stability of solvates is a concern to pharmaceutical scientists since they may convert to an amorphous form upon desolvation while others may become chemically labile. For example, cephadrine dihydrate dehydrates and produces an amorphous form that is more easily oxidized. Other hydrates may change their hydration state producing forms with different solubility characteristics [2]. Due to the impact of solvates on the development process and drug performance, it is important to know the stability of these solvates. In addition, with many possible crystal forms of a drug, stability of the marketed crystal form should be well understood to ensure drug product quality.

One recent example of polymorphic instability is ritonavir, which is Abbott's protease inhibitor for human immunodeficiency virus (HIV). It was temporarily withdrawn from the market because the marketed crystal form (Form I) transformed to a more thermodynamically stable and less soluble form (Form II) [3, 4]. Another classic example is chloramphenicol palmitate which was reported to exist in more than one

crystalline form and one form was found to be as much as seven times therapeutically more potent than other forms [5]. Therefore, the solid-state stability of polymorphic and solvated drug solids and the kinetics of such transformations needs to be evaluated in the development of such drugs and their dosage forms.

Solid-state kinetics bear similarities to those in homogenous phases like solutions or gases. The basic mathematical principles are shared among all three phases. However, solid-state reaction mechanisms differ substantially from those in homogenous phases. These differences include experimental procedures employed for their study and computation methods for analyzing data.

A review of solid-state kinetics has not appeared in the pharmaceutical literature while many such studies have appeared. As several theories and models for solid-state kinetics have been proposed and applied in the last century, a review of them can assist in their proper application. Additionally, kinetic software is available from thermal analysis equipment manufacturers or other sources to analyze solid-state kinetic data. There needs to be an understanding of the underlying assumptions and limitations of such software before one can accurately interpret the results generated. This chapter reviews solid-state reaction kinetic concepts and applications for solids.

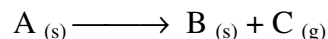
Solid-state kinetics: from homogenous to heterogeneous processes

Chemical kinetic concepts were originally based on generalizations from empirical studies of homogenous reactions first in the gas phase. These concepts were later applied to solution phase processes and eventually to solid-state reactions. Solid-state kinetic concepts did not develop separately. However, applying these concepts was justified in the solid-state because of similarities to some homogenous reactions. For example, the Arrhenius equation was historically developed empirically, after which theoretical justification for its use was later introduced in gases through the collision

theory and in solutions through the transition-state theory. A similar justification was claimed for the use of this equation in solid-state kinetics [6]. Therefore, many solid-state kinetics principles evolved from homogenous kinetic principles. However, application of these kinetic principles are different because of the differences between solids, solutions and gases. For example, particle size, interface advance and geometric shape are variables unique to heterogeneous solid reactions and have no equivalent in homogenous reactions. Differences between homogenous and heterogeneous kinetics will be highlighted throughout this chapter.

Rate laws

There are many types of solid-state reactions but this focus will be on reactions that involve a single solid reactant. A simple reaction is one which follows the reaction scheme below:



Solid-state desolvation is a reaction that obeys the above scheme because it involves the removal of solvent as vapor from a crystalline solvate below its melting point (with dehydration being the loss of water) [7, 8].

In desolvation, A is the solvate or hydrate, B is the parent drug and C is the solvent or water vapor. The rate [9] of the above reaction is often proportional to the concentration (amount or fraction) of the reactant or products raised to an integer or fractional power according to:

$$Rate \propto [A]^n \text{ or } \propto ([A]_0 - [B])^n \text{ or } \propto ([A]_0 - [C])^n \quad (1)$$

Where, A_0 is the initial concentration of A, and n, is the reaction order. The rate of a reaction is usually studied by following the decrease in reactant concentration or increase in product concentration. Therefore, the reaction rate law becomes:

$$\text{Rate} = \frac{d[A]}{dt} = -\frac{d[B]}{dt} = -\frac{d[C]}{dt} = -k[A]^n = k([A]_0 - [B])^n = k([A]_0 - [C])^n \quad (2)$$

Where, k is the reaction rate constant. If the evolved gas (C) is efficiently flushed such that $[C] \approx 0$, the above equation reduces to:

$$\text{Rate} = \frac{d[A]}{dt} = -\frac{d[B]}{dt} = -k[A]^n = k([A]_0 - [B])^n \quad (3)$$

If the reaction is an elementary unimolecular ($n=1$) reaction, the rate law would be (following only the reactant concentration):

$$\text{Rate} = \frac{d[A]}{dt} = -k[A] \quad (4)$$

Which upon integration becomes:

$$-\ln \frac{[A]}{[A]_0} = kt \quad (5)$$

The above expressions use concentration ($[A]$) which is usually measured in solution kinetics. However, in solid-state kinetics, concentration has little meaning because the sample is not homogenous, hence reactivity is not the same throughout the sample (non-isotropic) and “concentration” does not reflect reactivity. Figure 1 depicts the difference between homogeneously (dark spots, Figure 1a) and heterogeneously (dark spots, Figure 1b) distributed reaction sites. In solids, reactions often occur or are initiated at defects in the crystal lattice or at crystal surfaces, edges or corners [5].

Ideally, a perfect crystal contains no imperfections (defects) thus having minimal reactivity. However, in reality, perfect crystals are rare and most crystal lattices contain imperfections. Lattice imperfections can be point defects and/or dislocations. Point defects are defects where units are missing from the lattice leaving “vacancies” in the lattice. These missing units may be atoms, molecules or ions. Point defects are also

generated when foreign atoms or ions (e.g., impurities) occupy normal lattice positions. Dislocations in the lattice structure result during crystal growth due to surface or internal stresses. A dislocation is a discontinuity in the regularity of the lattice that exists in the bulk of a crystal [10]. For example, a group of parallel planes in the lattice could be shifted by a certain lattice spacing which could be due to rapid crystal growth in which molecules (or ions or atoms) do not have time to reach their lowest energy states. Imperfection sites are energized sites (i.e., have a higher free energy) in which the activation energy for reaction is reduced, thus explaining why these sites are highly reactive.

Solid-state kinetics can be studied with thermal analytical methods [1, 11] by measuring a sample property as it is heated or held at a constant temperature. If a reaction involves weight loss, then weight is followed and the kinetics are usually studied by thermogravimetry (TGA). Heat (evolved or consumed) is another measurable property that is used for kinetic evaluation using differential scanning calorimetry (DSC) or differential thermal analysis (DTA). Weight loss or heat flow data are converted to a normalized form called conversion fraction (α). The conversion fraction ranges from 0 and 1 and is a measure of reaction progress as a function of time or temperature. For isothermal thermogravimetric analysis, the conversion fraction (α) at any time is:

$$\alpha = \frac{m_0 - m_t}{m_0 - m_\infty} \quad (6)$$

Where, m_0 is the initial sample weight, m_t is the sample weight at time, t , and m_∞ is the final sample weight. Nonisothermally, the conversion fraction (α) at any temperature is:

$$\alpha = \frac{m_0 - m_T}{m_0 - m_\infty} \quad (7)$$

Where, m_T is the sample weight at temperature, T.

For an isothermal DSC/DTA analysis, the conversion fraction [12] at any time is:

$$\alpha = \frac{AUC_0^t}{AUC_0^\infty} \quad (8)$$

Where, AUC_0^t is the sample peak area from zero to t and AUC_0^∞ is the total sample peak area. Nonisothermally, the conversion fraction at any temperature can be calculated from:

$$\alpha = \frac{AUC_0^T}{AUC_0^\infty} \quad (9)$$

Where, AUC_0^T is the sample peak area from zero to T.

Reaction kinetics in the solid-state can also be studied by other analytical methods such as, powder X-ray diffraction (PXRD) [13] and nuclear magnetic resonance (NMR) [14, 15]. For any analytical method, the measured parameter is transformed into a conversion fraction (α) that can be used in the kinetic equations. Examples of transformations with TGA and DSC data are shown in Figure 2.

Using conversion fraction, rate expressions defined in Eqs. (4) and (5) can be written as:

$$Rate = \frac{d\alpha}{dt} = k(1-\alpha) \quad (10)$$

$$-\ln(1-\alpha) = kt \quad (11)$$

Unlike rate laws in homogenous kinetics which usually depend on reaction order (i.e. first, second, etc.), a rate law for an elementary solid-state reaction could depend on

factors such as rate of nuclei formation, interface advance, diffusion, and/or geometrical shape of solid particles. These factors lead to several decomposition models [16-18] that do not exist in homogenous kinetics and are summarized in Table 1. Equations (10) and (11) can be generally expressed as:

$$\frac{d\alpha}{dt} = k f(\alpha) \quad (12)$$

$$g(\alpha) = k t \quad (13)$$

Where, $f(\alpha)$ is the differential reaction model and $g(\alpha)$ is the integral reaction model. In some references, $f(\alpha)$ and $g(\alpha)$ definitions may be reversed.

The temperature dependence of the rate constant (k) is usually given by the Arrhenius equation [19]:

$$k = A e^{-\frac{E_a}{RT}} \quad (14)$$

Where, A is the pre-exponential (frequency) factor, E_a is activation energy, T is absolute temperature and R is the gas constant. Substitution of Eq. (14) into Eqs. (12) and (13) gives:

$$\frac{d\alpha}{dt} = A e^{-\frac{E_a}{RT}} f(\alpha) \quad (15)$$

and

$$g(\alpha) = A e^{-\frac{E_a}{RT}} t \quad (16)$$

Models and mechanisms in solid-state kinetics

A model is a theoretical, mathematical description of what occurs experimentally. In solid-state reactions, a model can describe a particular reaction type and translate that mathematically into a rate equation. Many models have been proposed in solid-state kinetics and these models have been developed based on certain mechanistic assumptions. Other models are more empirically based and their mathematics facilitates data analysis with less mechanistic meaning. Therefore, different rate expressions are produced from these models.

In homogenous kinetics (e.g., gas or solution phases), kinetic studies are usually directed toward obtaining rate constants that can be used to describe the progress of a reaction. Additionally, the reaction mechanism is typically investigated and rate constant changes with temperature, pressure or reactant/product concentrations are often helpful in uncovering mechanisms. These mechanisms involve to varying degrees the detailed chemical steps by which reactant(s) is (are) converted to product(s). However, in solid-state kinetics, mechanistic interpretations usually involve identifying a reasonable reaction model [20] because information about individual reaction steps is often difficult to obtain. However, the choice of a reaction model should ideally be supported by other complementary techniques such as microscopy, spectroscopy, X-ray diffraction, etc.[21]

Table 1 lists the most common models [16-18]. Classifications and mathematical derivation of reaction models are detailed later (Chapter 2).

Methods for studying solid-state kinetics

There are many methods used to study solid-state kinetics. These methods can be generally grouped into two categories – experimental and computational; the methods are summarized in Figure 3.

Experimental methods

There are two approaches utilized to obtain solid-state kinetic data – isothermal and nonisothermal methods. For isothermal methods, reactions are followed at several constant temperatures while nonisothermal (dynamic) methods involve heating samples at one or more constant heating rates (usually linear) and following the course of the reaction. Isothermal methods are similar to those used in homogenous kinetics to produce α -time data (Figure 4a) compared to concentration-time data in homogenous kinetics. On the other hand, nonisothermal analysis produces α -temperature data (Figure 4b).

Isothermal method

This method is based on maintaining samples at several constant temperatures (i.e., isothermal) and as a result, a set of α -time points is produced at each temperature. These methods are based on the isothermal rate equations (Eqs. (13) and (16)).

Nonisothermal method

This method employs a heating rate (β), usually linear, to raise the temperature. A linear heating program follows:

$$T = T_0 + \beta t \quad (17)$$

Where, T_0 is the starting temperature, β is the linear heating rate (K/min.), and T is the temperature at time, “t”. Nonisothermal experiments are usually common in solid-state kinetics, however, they have been applied to the study of homogenous kinetics [22, 23].

The following relationship can be defined for nonisothermal experiments,

$$\frac{d\alpha}{dT} = \frac{d\alpha}{dt} \cdot \frac{dt}{dT} \quad (18)$$

Where, $d\alpha/dT$ is the nonisothermal reaction rate; $d\alpha/dt$ is the isothermal reaction rate and dT/dt is the heating rate (β). Substituting Eq. (15) into Eq. (18) gives,

$$\frac{d\alpha}{dT} = \frac{A}{\beta} e^{-\frac{E_a}{RT}} f(\alpha) \quad (19)$$

Equation (19) represents the differential form of the nonisothermal rate law.

Temperature integral

Integrating the differential nonisothermal rate law (Eq. (19)) produces the integral form of the nonisothermal rate law:

$$g(\alpha) = \frac{A}{\beta} \int_0^T e^{-\frac{E_a}{RT}} dT \quad (20)$$

This integral is called the “temperature integral” and has no analytic solution [11, 24]. It has been reported that using nonlinear heating programs such as hyperbolic or parabolic [25] or non-Arrhenius temperature functions of the rate constant [26] leads to exact analytical solutions of the temperature integral. However, this approach has not been widely implemented. To transform the above integral to a more general form found in mathematical handbooks, the integration variable can be redefined as,

$$\left(x = \frac{E_a}{RT} \right)$$

and the temperature integral then becomes,

$$g(\alpha) = \frac{AE_a}{\beta R} \int_x^\infty \frac{e^{-x}}{x^2} dx \quad (21)$$

If $p(x) = \int_x^\infty \frac{e^{-x}}{x^2} dx$, then Eq. (21) can be written as,

$$g(\alpha) = \frac{AE_a}{\beta R} p(x) \quad (22)$$

Where, $p(x)$ is the exponential integral which can be found in mathematical tables [27]. The main approaches used for evaluating the temperature/exponential integral are [11]:

1. Calculating values of $p(x)$ numerically.
2. Converting $p(x)$ to an approximate form that can be integrated.
3. Approximating $p(x)$ by a series expansion.

The two series most used for approximating the temperature integral are [1]:

I. An asymptotic series expansion:

$$p(x) = \frac{e^{-x}}{x^2} \left[1 - \left(\frac{2!}{x} \right) + \left(\frac{3!}{x^2} \right) - \left(\frac{4!}{x^3} \right) + \dots + (-1)^n \left(\frac{(n+1)!}{x^n} \right) + \dots \right]$$

II. The Schlömilch series expansion:

$$p(x) = \frac{e^{-x}}{x(x+1)} \left[1 - \left(\frac{1}{(x+2)} \right) + \left(\frac{2}{(x+2)(x+3)} \right) - \left(\frac{4}{(x+2)(x+3)(x+4)} \right) + \dots \right]$$

Many approximations have been reported for the temperature integral [1, 26], two of which will be covered – the Doyle [28-30] and Senum-Yang [31] approximations. They are among the most frequently used temperature/exponential integral approximations as each is the basis of a particular kinetic calculation method.

The Doyle approximation

The Doyle [28-30] approximation is based on the observation that $\log p(x)$ is linear with respect to x over a short range of x values according to:

$$\log p(x) \approx -A - Bx \quad (23)$$

Where, A and B are fitted linear constants. Doyle [28-30] approximated values of $p(x)$ using the first three terms of the Schlömilch series expansion and utilized the relationship in Eq. (23) for x values between 28–50. By interpolation [30], Doyle calculated parameters in Eq. (23) as, 2.315 and 0.4567 for A and B , respectively. Therefore, Eq. (23) becomes,

$$\log p(x) \approx -2.315 - 0.4567x \quad (24)$$

Senum-Yang approximation

Senum and Yang [31] developed an accurate nonlinear approximation of the temperature integral. If variables in Eq. (21) are transformed so that $x = zy$, the integral becomes,

$$g(\alpha) = \frac{AE_a}{\beta Rz} \int_1^\infty \frac{e^{-zy}}{y^2} dy \quad (25)$$

Which can be written as,

$$g(\alpha) = \frac{AE_a}{\beta Rz} E_2(z) \quad (26)$$

$E_2(z)$ or generally, $E_v(z)$ (where v is an integer) is a well known integral [27, 32] for $z > 0$ given by the following continued fraction [33]:

$$\frac{E_v(z)}{z} = \frac{e^{-z}}{z} \left(\frac{1}{z + \frac{1}{1 + \frac{1}{z + \frac{2}{1 + \frac{3}{z + \frac{4}{1 + \frac{v+3}{z + \dots}}}}}}}} \right) \quad (27)$$

Truncating the number of terms in the above continued fraction gives the first (one term), second (two terms), third (three terms) and fourth (four terms) degree rational approximation known as the Senum-Yang approximation as given in Table 2 [26, 31, 34, 35]. Detailed derivation of these terms is given in the appendix section.

Calculation methods

There are two groups of methods used to analyze either isothermal or nonisothermal solid-state kinetic data – modelistic and model-free methods (Figure 3).

Model-fitting methods

For these methods, different models are fit to the data and the model giving the best statistical fit is chosen as the model of choice from which the activation energy (E_a) and frequency factor (A) are calculated.

Isothermal model-fitting methods (Conventional method)

This method is identical to that in homogenous phase kinetics. It involves two fits: the first, determines the rate constant (k) of the model that best fits the data according to Eq. (13), while the second determines specific kinetic parameters such as the activation energy (E_a) and frequency factor (A) using the Arrhenius equation (Eq. (14)). Figure 5 illustrates the application of the conventional method for isothermal model-fitting.

Kinetic data were simulated (see Chapter 3) with $E_a = 100$ kJ/mole and $A = 10^{13} \text{ min}^{-1}$ and

assuming an R3 model with a 0.25% random error in time (Figure 5a). The upper table in Figure 5b tabulates data from Figure 5a while the lower table calculates $g(\alpha)$ for each reaction model in Table 1. Figure 5c shows the first fit which determines the model that best fits the data according to Eq. (13). The slope from this fit gives the reaction rate constant and this fitting is repeated for each model at each temperature (only two temperatures are shown in Figure 5c). For each model, rate constants from all temperatures (five in our simulation) are used for the second fit according to the Arrhenius equation (Eq. (14)) as shown in Figure 5d. The frequency factor and activation energy are obtained from the intercept and slope, respectively, of this plot. It is interesting to note that E_a values calculated isothermally by the conventional model-fitting method appear to be equal regardless of the model (i.e., model independent). This behavior doesn't occur in homogenous kinetic studies where, for example, activation energies obtained from a zero-order fit are substantially different from those obtained by a first, second or third-order fit. This unusual behavior has been previously addressed [21] [36-38] but without a complete explanation.

Nonisothermal model-fitting methods

There are many model fitting methods that extract the three kinetic parameters known as the kinetic triplet (A , E_a and model) from nonisothermal data. These methods were used extensively earlier in solid-state kinetic analysis and they continue to appear. These methods have been critically evaluated [39-43] and it's been shown that the sole use of these methods is not recommended because:

1. They assume a constant kinetic triplet (A , E_a and model).
2. They involve fitting three parameters (A , E_a and model) which are determined from a single run (i.e., one heating rate).
3. They involve a single heating rate which is not always sufficient to determine reaction kinetics.

There are a many of nonisothermal model fitting methods. However, only a few have been extensively used, which will be discussed.

Direct differential method

This method [44, 45] uses the differential form of the nonisothermal rate law (Eq. (19)) by numerically calculating the differential $\left(\frac{d\alpha}{dT} \approx \frac{\Delta\alpha}{\Delta T}\right)$. Taking the logarithm of the nonisothermal rate law, Eq. (19) gives:

$$\ln \frac{d\alpha/dT}{f(\alpha)} = \ln \frac{A}{\beta} - \frac{E_a}{RT} \quad (28)$$

Plotting the left-hand side (including the model $f(\alpha)$) versus $1/T$ gives the activation energy (E_a) and frequency factor (A) from the slope and intercept, respectively. The model that gives the best linear fit is usually chosen as the model.

Freeman–Carroll (difference-differential) method

The Freeman and Carroll method [46, 47] is a differential method that was originally developed assuming a reaction-order model ($f(\alpha) = (1-\alpha)^n$). Taking the natural logarithm of the differential form of the nonisothermal rate law (Eq. (19)) gives,

$$\ln \frac{d\alpha}{dT} = \ln \frac{A}{\beta} - \frac{E_a}{RT} + \ln f(\alpha) \quad (29)$$

If incremental differences in the variables of Eq. (29) are taken, we obtain:

$$\Delta \ln \frac{d\alpha}{dT} = \Delta \ln f(\alpha) - \frac{E_a}{R} \Delta \frac{1}{T} \quad (30)$$

Equation (30) can be rearranged to,

$$\frac{\Delta \ln \frac{d\alpha}{dT}}{\Delta 1/T} = \frac{\Delta \ln f(\alpha)}{\Delta 1/T} - \frac{E_a}{R} \quad (31)$$

or

$$\frac{\Delta \ln \frac{d\alpha}{dT}}{\Delta \ln f(\alpha)} = -\frac{E_a}{R} \frac{\Delta 1/T}{\Delta \ln f(\alpha)} \quad (32)$$

The activation energy can be obtained by plotting the left-hand side of Eqs. (31) and (32) versus $\frac{\Delta \ln f(\alpha)}{\Delta 1/T}$ and evaluating the intercept for Eq. (31) or versus

$\frac{\Delta 1/T}{\Delta \ln f(\alpha)}$ and evaluating the slope for Eq. (32).

Coats-Redfern method.

This method [48, 49] uses the integral form of the nonisothermal rate law (Eq. (22)). Coats and Redfern utilized the asymptotic series expansion for approximating the temperature integral ($p(x)$), producing:

$$\ln \frac{g(\alpha)}{T^2} = \ln \left(\frac{AR}{\beta E_a} \left[1 - \left(\frac{2RT_{\text{exp}}}{E_a} \right) \right] \right) - \frac{E_a}{RT} \quad (33)$$

Where, T_{exp} is the mean experimental temperature.

Plotting the left-hand side (including the model, $g(\alpha)$) of Eq. (33) versus $1/T$ gives the activation energy (E_a) and frequency factor (A) from the slope and intercept, respectively. The model that gives us the best linear fit is chosen as the model. The Coats-Redfern equation was originally derived assuming a first-order model ($g(\alpha) = -\ln(1-\alpha)$) but has been generalized to other reaction models.

Kissinger method.

Kissinger [50, 51] proposed a kinetic analysis method for reaction-order models ($f(\alpha)=(1-\alpha)^n$) based on taking the derivative of Eq. (19) generating $d^2\alpha/dT^2$. According to Kissinger, the maximum reaction rate occurs when the second derivative is zero from which the following equation can be obtained:

$$\frac{E_a \beta}{RT_m^2} = A \left(n(1 - \alpha)_m^{n-1} \right) e^{-\frac{E_a}{RT_m}} \quad (34)$$

Where, (T_m) is the temperature of the maximum rate and α_m is the conversion value at that maximum rate. The maximum reaction rate represents the peak (i.e., inflection point) of a DSC or DTG curve. Taking the natural logarithm of Eq. (34) and rearranging gives,

$$\ln \frac{\beta}{T_m^2} = \ln \left(\frac{AR \left(n(1 - \alpha)_m^{n-1} \right)}{E_a} \right) - \frac{E_a}{RT_m} \quad (35)$$

The activation energy (E_a) is obtained by plotting the left-hand side of Eq. (35) versus $1/T_m$ for a series of runs at different heating rates. Equation (35) has been generalized to any reaction model ($f(\alpha)$) [52].

It is worth noting that the Kissinger method is a model-free method as it does not require any modelistic assumptions to calculate E_a . However, it is not an isoconversional method (discussed below) because it does not calculate E_a values at progressive α values but rather assumes a constant E_a , like other methods. Thus this method can not detect reaction complexities over the course of the reaction [53].

Model-free/isoconversional methods

Model-free methods calculate the reaction activation energy (E_a) without modelistic assumptions which is usually done by grouping terms such as the frequency

factor (A) and model into the intercept of a linear equation and using the slope of that equation to calculate the activation energy (E_a). The frequency factor (A) can be calculated from the intercept of the linear equation but requires modelistic assumptions for such a determination. Therefore, model-free methods usually report only activation energies.

Isoconversional methods are model-free methods that evaluate kinetic parameters, namely the activation energy (E_a) at progressive conversion values (α) [54]. These methods require several kinetic curves to perform the analysis and have therefore been called, “multi-curve” methods [55, 56] as shown in Figure 6. Calculations from several curves at different heating rates are performed on the same value of conversion (α), thus, the name isoconversional. As a result, these methods calculate the activation energy for each conversion point (E_a, α), resulting in an isoconversional plot (E_a vs. α) as seen in Figure 6.

The terms, “model-free” and “isoconversional” are sometimes used interchangeably, however, not all model-free methods are isoconversional. For example, the Kissinger method (discussed above) is a model-free method but is not isoconversional [37]. Isoconversional approaches can be used to analyze both isothermal and nonisothermal data, as described below.

Isothermal isoconversional methods

These methods utilize the isothermal rate law (Eq. (16)) and include the standard and Friedman’s isoconversional methods.

Standard isoconversional method

This method [41, 57] can be derived by taking the logarithm of the isothermal rate law (Eq. (16)) to give:

$$\ln g(\alpha) = \ln A - \frac{E_a}{RT} + \ln t \quad (36)$$

Which can be rearranged to give,

$$-\ln t = \ln\left(\frac{A}{g(\alpha)}\right) - \frac{E_a}{RT} \quad (37)$$

A plot of $-\ln t$ versus $1/T$ for each α gives E_a from the slope for that α regardless of the model according to:

$$-\ln t_\alpha = \ln\left(\frac{A}{g(\alpha)}\right)_\alpha - \frac{E_{a\alpha}}{RT_\alpha} \quad (38)$$

Friedman's isoconversional method

This method [58] is a differential method and was one of the first isoconversional methods. The logarithm of the isothermal rate law (Eq. (15)) gives,

$$\ln\left(\frac{d\alpha}{dt}\right) = (\ln Af(\alpha)) - \frac{E_a}{RT} \quad (39)$$

A plot of $\ln(d\alpha/dt)$ (or $\ln \Delta\alpha/\Delta t$) versus $1/T$ at each α gives E_a from the slope for that α regardless of the model according to:

$$\ln\left(\frac{d\alpha}{dt}\right)_\alpha = (\ln Af(\alpha))_\alpha - \frac{E_{a\alpha}}{RT_\alpha} \quad (40)$$

Nonisothermal isoconversional methods

Unlike isothermal data, nonisothermal data involve the use of the temperature integral (Eq. (22)). Therefore, two common approximations of the temperature integral have been widely used:

1. A linear approximation (less accurate) utilizing the Doyle approximation has been used in the Ozawa and Flynn-Wall methods.
2. A non-linear approximation (more accurate) utilizing the Senum-Yang approximation has been used in the Vyazovkin method.

Ozawa, Flynn and Wall (OFW) method

Ozawa [59] and Flynn-Wall [60] independently developed an isoconversional calculation method for nonisothermal data which is commonly referred to as the OFW method. Taking the common logarithm of the nonisothermal rate law (Eq. (22)) gives the following,

$$\log g(\alpha) = \log \frac{AE_a}{\beta R} + \log p(x) \quad (41)$$

Substituting Doyle's approximation (Eq. (24)) in Eq. (41) gives,

$$\log g(\alpha) = \log \frac{AE_a}{\beta R} - 2.315 - 0.457x \quad (42)$$

Substituting E_a/RT for x and rearranging gives,

$$\log \beta = \log \frac{AE_a}{g(\alpha)R} - 2.315 - 0.457 \frac{E_a}{RT} \quad (43)$$

A plot of $\ln \beta$ versus $1/T$ at each α yields E_a from the slope for that α regardless of the model according to:

$$\log \beta = \log \frac{A_\alpha E_{a\alpha}}{g(\alpha)R} - 2.315 - 0.457 \frac{E_{a\alpha}}{RT_\alpha} \quad (44)$$

Modified Coats-Redfern method

Burnham and Braun [61] have transformed the model-fitting Coats-Redfern method to an isoconversional method by rearranging Eq. (33) to give,

$$\ln \frac{\beta}{T^2} = \ln \left(\frac{AR}{E_a g(\alpha)} \left[1 - \left(\frac{2RT_{\text{exp}}}{E_a} \right) \right] \right) - \frac{E_a}{RT} \quad (45)$$

A plot of $\ln \beta/T^2$ versus $1/T$ at each α yields E_a from the slope for each α regardless of the model according to:

$$\ln \left(\frac{\beta}{T^2} \right)_{\alpha} = \ln \left(\frac{A_{\alpha}R}{E_{a\alpha} g(\alpha)} \left[1 - \left(\frac{2RT_{\text{exp}}}{E_{a\alpha}} \right) \right] \right) - \frac{E_{a\alpha}}{RT_{\alpha}} \quad (46)$$

An Isoconversional example

Figure 6 depicts the application of two isoconversional methods to simulated kinetic data – isothermal (Figure 6a–standard method) and nonisothermal (Figure 6b–Ozawa-Flynn-Wall). The kinetic data were simulated with $E_a = 100$ kJ/mole and $A = 10^{15}$ min^{-1} and assuming an R3 model in Figure 6a and an F1 model in Figure 6b. Figure 6a shows α -time (α -t) plots while Figure 6b shows α -temperature (α -T) plots. Calculations for each plot (α -t or α -T) were performed for a single conversion value (i.e., isoconversional). This is shown as an isoconversional line for $\alpha=0.8$ in Figure 6a and $\alpha=0.4$ for Figure 6b. Values of time (Figure 6a) or temperature (Figure 6b) from each isoconversional line are tabulated below each α -t or α -T plot. Plotting the last two rows ($-\ln t$ vs $10^3/T$ or $\log \beta$ vs $10^3/T$) of these tables according to Eqs. (38) or (44), respectively, as shown in Figure 6 gives Arrhenius-like plots for both isoconversional methods. The activation energy (E_a) is obtained from the slopes of these plots according to Eqs. (38) or (44). The calculated E_a represents a single point ($\alpha=0.8$ or 0.4) in an

isoconversional ($E_a - \alpha$) plot (circled E_a values in Figure 6). Repeating this analysis for different α values gives completed isoconversional plots in Figure 6.

The Vyazovkin (VYZ) method

The temperature integral ($p(x)$) in the nonisothermal rate law (Eq. (22)) is a function of E_a and temperature. Therefore Eq. (22) can be written as,

$$g(\alpha) = \frac{A E_a}{\beta R} I(E_a, T) \quad (47)$$

Where, $I(E_a, T) = p(x)$. The general assumption used in Vyazovkin's [62] method (or any other isoconversional method) is that the reaction model is independent of the heating rate (i.e., $g(\alpha)$ will be the same for any heating rate). Therefore, for a conversion value (α), the relationship below could be defined if two heating rates are applied:

$$g(\alpha) = \frac{A_\alpha E_{a\alpha}}{\beta_1 R} I(E_{a\alpha}, T_{\alpha 1}) = \frac{A_\alpha E_{a\alpha}}{\beta_2 R} I(E_{a\alpha}, T_{\alpha 2}) \quad (48)$$

Where, β_1 is the first heating rate, β_2 is the second heating rate, $T_{\alpha 1}$ is the temperature for a particular α using the first heating rate, $T_{\alpha 2}$ is the temperature at the same α using the second heating rate, $E_{a\alpha}$ is the activation energy at that α and A_α is the frequency factor at that α . For an experiment having "n" heating rates, the relationship would be,

$$\frac{A_\alpha E_{a\alpha}}{\beta_1 R} I(E_{a\alpha}, T_{\alpha 1}) = \frac{A_\alpha E_{a\alpha}}{\beta_2 R} I(E_{a\alpha}, T_{\alpha 2}) = \dots = \frac{A_\alpha E_{a\alpha}}{\beta_n R} I(E_{a\alpha}, T_{\alpha n}) \quad (49)$$

which reduces to:

$$\frac{I(E_{a\alpha}, T_{\alpha 1})}{\beta_1} = \frac{I(E_{a\alpha}, T_{\alpha 2})}{\beta_2} = \dots = \frac{I(E_{a\alpha}, T_{\alpha n})}{\beta_n} = \sigma \quad (50)$$

where, σ is a constant.

For a two heating rate study, using two terms in Eq. (50) gives,

$$\frac{I(E_{a\alpha}, T_{\alpha 1})}{\beta_1} = \frac{I(E_{a\alpha}, T_{\alpha 2})}{\beta_2} = \sigma \quad (51)$$

If both sides are divided by either the right-hand term or left-hand term, we get either:

$$\frac{\beta_2}{\beta_1} \frac{I(E_{a\alpha}, T_{\alpha 1})}{I(E_{a\alpha}, T_{\alpha 2})} = \frac{\sigma}{\sigma} = 1 \quad (52)$$

or

$$\frac{\beta_1}{\beta_2} \frac{I(E_{a\alpha}, T_{\alpha 2})}{I(E_{a\alpha}, T_{\alpha 1})} = \frac{\sigma}{\sigma} = 1 \quad (53)$$

Adding Eq. (52) and Eq. (53) gives,

$$\frac{\beta_2}{\beta_1} \frac{I(E_{a\alpha}, T_{\alpha 1})}{I(E_{a\alpha}, T_{\alpha 2})} + \frac{\beta_1}{\beta_2} \frac{I(E_{a\alpha}, T_{\alpha 2})}{I(E_{a\alpha}, T_{\alpha 1})} = 2 \quad (54)$$

For three heating rates a similar equation can be obtained which is,

$$\frac{\beta_2}{\beta_1} \frac{I(E_{a\alpha}, T_{\alpha 1})}{I(E_{a\alpha}, T_{\alpha 2})} + \frac{\beta_3}{\beta_1} \frac{I(E_{a\alpha}, T_{\alpha 1})}{I(E_{a\alpha}, T_{\alpha 3})} + \frac{\beta_1}{\beta_2} \frac{I(E_{a\alpha}, T_{\alpha 2})}{I(E_{a\alpha}, T_{\alpha 1})} + \frac{\beta_3}{\beta_2} \frac{I(E_{a\alpha}, T_{\alpha 2})}{I(E_{a\alpha}, T_{\alpha 3})} + \frac{\beta_1}{\beta_3} \frac{I(E_{a\alpha}, T_{\alpha 3})}{I(E_{a\alpha}, T_{\alpha 1})} + \frac{\beta_2}{\beta_3} \frac{I(E_{a\alpha}, T_{\alpha 3})}{I(E_{a\alpha}, T_{\alpha 2})} = 6 \quad (55)$$

For “n” heating rates, Eqs. (54) and (55) can be generalized as,

$$\sum_{i=1}^n \sum_{j \neq i}^n \frac{\beta_j I(E_{a\alpha}, T_{\alpha i})}{\beta_i I(E_{a\alpha}, T_{\alpha j})} = n(n-1) \quad (56)$$

or

$$\left(n(n-1) - \sum_{i=1}^n \sum_{j \neq i}^n \frac{\beta_j I(E_{a\alpha}, T_{\alpha i})}{\beta_i I(E_{a\alpha}, T_{\alpha j})} \right) = 0 \quad (57)$$

For experimental data, Eq. (57) might not converge to 0, but an $E_{a\alpha}$ which minimizes the left-hand side can be found if the following form is used:

$$\left| n(n-1) - \sum_{i=1}^n \sum_{j \neq i}^n \frac{\beta_j I(E_{a\alpha}, T_{\alpha i})}{\beta_i I(E_{a\alpha}, T_{\alpha j})} \right| = \Omega \quad (58)$$

Where Ω is a non-zero constant. Minimizing Eq. (58) is equivalent to minimizing the following function,

$$\Omega = \left| \sum_{i=1}^n \sum_{j \neq i}^n \frac{\beta_j I(E_{a\alpha}, T_{\alpha i})}{\beta_i I(E_{a\alpha}, T_{\alpha j})} \right| \quad (59)$$

Minimization of Eq. (59) is equivalent to minimizing Eq. (58) because the summations contain pairs of inverse ratios. These inverse ratios can be easily seen in Eqs. (54) and (55) which forces each ratio to a value of “1” during minimization. Vyazovkin used the 3rd or 4th degree Senum-Yang approximation of the temperature integral. According to this method, the activation energy ($E_{a\alpha}$) at each α is the value that minimizes Ω (i.e., gets closest to 0).

Vyazovkin's modified isoconversional method

Vyazovkin [25] modified his isoconversional method to account for random temperature variation. This modified method is not limited to linear heating programs and can be used to analyze kinetics from a nonlinear heating program and also isothermal experiments. A modification was introduced to the nonisothermal rate law (Eq. (20)) where the heating rate (β) has been included in the integral to represent a heating function rather than a single temperature ($T(t)$ versus T). Since the heating function is a time

dependent function, the integral was changed from a temperature integral (Eq. (20)) to a time integral as shown below:

$$g(\alpha) = A \int_0^t \exp\left(-\frac{E_a}{RT(t)}\right) dt \quad (60)$$

where, T(t) is the heating program used. For each α , Eq. (60) becomes,

$$(g(\alpha))_\alpha = A_\alpha \int_0^{t_\alpha} \exp\left(-\frac{E_{a\alpha}}{RT(t)}\right) dt \quad (61)$$

which can be generally expressed as,

$$(g(\alpha))_\alpha = A_\alpha J(E_{a\alpha}, T(t_\alpha)) \quad (62)$$

$$\text{where, } J(E_{a\alpha}, T(t_\alpha)) = \int_0^{t_\alpha} \exp\left(-\frac{E_{a\alpha}}{RT(t)}\right) dt$$

This method allows for use of linear (Eq. (17)) and nonlinear heating programs and also can be used for isothermal analysis ($\beta=0$, $T(t)=T_i$ according to Eq. (17)). For any heating program, the integral can be numerically evaluated using the trapezoidal method.

Using the same procedures that were employed for obtaining Eq. (59), it can be shown that all values of $g(\alpha)$ from Eq. (62) are equal, therefore, all $J(E_{a\alpha}, T(t_\alpha))$ values are equal. Thus, equating $J(E_{a\alpha}, T(t_\alpha))$ values and using the same logic as for Eqs. (48)-(59), we obtain:

$$\Omega = \left| \sum_{i=1}^n \sum_{j \neq i}^n \frac{J(E_{a\alpha}, T_i(t_\alpha))}{J(E_{a\alpha}, T_j(t_\alpha))} \right| \quad (63)$$

The activation energy at each α ($E_{a\alpha}$) is the value that minimizes Ω .

Vyazovkin's advanced isoconversional (AIC) method

Vyazovkin [63] introduced a further modification to his isoconversional method. This modification involved integration over smaller time intervals. Therefore, Eq. (61) was altered to give:

$$(g(\alpha))_{\alpha} = A_{\alpha} \int_{t_{\alpha-\Delta\alpha}}^{t_{\alpha}} e^{-\frac{E_{a\alpha}}{RT(t)}} dt \quad (64)$$

where, $\Delta\alpha = (1/m)$ and m is the number of segments (typically 10 – 50) into which the integration is divided. Eq. (64) can be generally expressed as,

$$(g(\alpha))_{\alpha} = A_{\alpha} J' [E_{a\alpha}, T(t_{\alpha})] \quad (65)$$

As with the methods for obtaining Eqs. (59) and (63), we can obtain:

$$\Omega = \left| \sum_{i=1}^n \sum_{j \neq i}^n \frac{J'(E_{a\alpha}, T_i(t_{\alpha}))}{J'(E_{a\alpha}, T_j(t_{\alpha}))} \right| \quad (66)$$

As in the previous methods, the activation energy ($E_{a\alpha}$) at each α is the value that minimizes Ω in the above equation. The advanced isoconversional method (AIC) is claimed to be superior to other isoconversional methods [63-65] because integration over smaller time segments can better account for systematic E_a variations.

Complementary model-free/modelistic approach

Khawam and Flanagan [21] have proposed a complementary approach (see Chapter 5) that uses both model-free and model-fitting methods for kinetic data analysis. This approach utilizes an isoconversional method (Vyazovkin's) to obtain E_a values which are compared to values obtained by a modelistic method (Coats-Redfern). The most accurate model is assumed to be the one which produces an activation energy

closest to that from the isoconversional analysis. This approach allows one to select models that might otherwise be indistinguishable based on quality of regression fit alone. Therefore, the strengths of both methods are used in the evaluation of solid-state kinetics to obtain A and E_a values as well as the best model.

Controversies in solid-state kinetics

Discussions over solid-state kinetic studies have caused numerous debates and controversies [66]. Disagreements include questioning whether such kinetic analysis have a good theoretical framework, [67, 68] as well as critiques of approximations or assumptions used [69-71]. Some of the controversies will be discussed below.

Varying activation energy in solid-state kinetics

Solid-state kinetics was developed from reaction kinetics in homogenous systems (i.e. gases and liquids). The Arrhenius equation (Eq. (14)) relates the rate constant of a simple one-step reaction to the temperature through the activation energy (E_a) and pre-exponential factor (A). It has been generally assumed that activation energy (E_a) and frequency factor (A) remain constant, however, it's been shown [72-74] in solid-state reactions these kinetic parameters may vary with the reaction progress (α). This variation can be detected by isoconversional methods. While this variation appears to be in conflict with basic chemical kinetic principles, in reality, it may not be.

Khawam and Flanagan [57, 75] have shown (Chapter 4) that activation energy variation is of two types – a true variation that results from the complex nature of the solid-state reaction or an artifactual one resulting from the use of some isoconversional methods.

True variation in activation energy

Many explanations have been suggested for the occurrence of a true variation in activation energy, both in homogenous [73] and heterogeneous phases [76]. In the solid-

state, a variation in activation energy could be observed for an elementary reaction due to the heterogeneous nature of the solid sample or due to a complex reaction mechanism.

Elementary reactions

If an elementary reaction shows variable activation energy during its progress, it may be attributed to a systematic change in the reaction kinetics. This is not usual for homogeneous reactions which occur between freely moving, identical reactant molecules with random collisional encounters that are usually unaffected by product formation. However, reacting entities in a solid sample are not isolated but interact strongly with neighboring molecules or particles. Therefore, during such a reaction, reactivity may change due to product formation (or disappearance), crystal defect formation, intra-crystalline strain or other similar effects [76].

Solid-state reactivity could also be affected by experimental variables that would change the reaction kinetics by affecting heat or mass transfer at a reaction interface. For example, temperature changes could affect the kinetics not only through the rate constant but also by mechanistic changes. Elementary reaction kinetics at one temperature could be different from that at another or complex reactions kinetics (described below) could vary with temperature due to changes in the contribution of each elementary step [76] or change in the rate-determining step. Purge gas flow rate, is another experimental variable that could affect reactivity when reactions produce or consume gaseous components. A low purge flow rate may not preclude the reversibility of a reaction compared to a higher flow rate which could reduce the reversibility and cause variability in the apparent activation energy and/or introduce errors in calculated reaction rates.

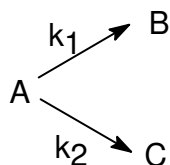
Complex reactions

If two or more elementary steps, each having a unique activation energy, affect the rate of product formation, the reaction is usually considered complex [9]. In such a reaction, a change in the activation energy as the reaction progresses would be observed.

This change will depend on the contribution of each elementary step, which gives an “effective” activation energy that varies with reaction progress. The effective activation energy can be mathematically derived from the nonisothermal reaction rate law (Eq. (15)), by taking the natural logarithm followed by differentiation to give:

$$\frac{d \ln \frac{d\alpha}{dt}}{d \frac{1}{T}} = -\frac{E_a}{R} \quad (67)$$

From this expression, the activation energy at each conversion ($E_{a\alpha}$) can be obtained. A reaction can be composed of two parallel steps according to the following scheme,



The overall reaction rate is,

$$\frac{d\alpha}{dt} = k_1 f_1(\alpha) + k_2 f_2(\alpha) = A_1 e^{-\frac{E_{a1}}{RT}} f_1(\alpha) + A_2 e^{-\frac{E_{a2}}{RT}} f_2(\alpha) \quad (68)$$

Taking the natural logarithm of both sides of Eq. (68) and differentiating gives:

$$\frac{d \ln \frac{d\alpha}{dt}}{d \frac{1}{T}} = -\frac{A_1 E_{a1} e^{-\frac{E_{a1}}{RT}} f_1(\alpha) + A_2 E_{a2} e^{-\frac{E_{a2}}{RT}} f_2(\alpha)}{R \left(A_1 e^{-\frac{E_{a1}}{RT}} f_1(\alpha) + A_2 e^{-\frac{E_{a2}}{RT}} f_2(\alpha) \right)} \quad (69)$$

Since the left-hand side of Eq. (69) is equal to $-(E_a)_{\text{apparent}}/R$ (which is also $-(E_a)_\alpha/R$ from Eq. (67)), Eq. (69) becomes:

$$E_{a_{\text{apparent}}} = E_{a_{\alpha}} = \frac{A_1 E_{a_1} e^{-\frac{E_{a_1}}{RT}} f_1(\alpha) + A_2 E_{a_2} e^{-\frac{E_{a_2}}{RT}} f_2(\alpha)}{A_1 e^{-\frac{E_{a_1}}{RT}} f_1(\alpha) + A_2 e^{-\frac{E_{a_2}}{RT}} f_2(\alpha)} \quad (70)$$

which can be generalized as:

$$E_{a_{\alpha}} = \frac{E_{a_1} k_1 f_1(\alpha) + E_{a_2} k_2 f_2(\alpha)}{k_1 f_1(\alpha) + k_2 f_2(\alpha)} \quad (71)$$

Eq. (71) shows that the effective activation energy ($E_{a\alpha}$) is a function of each E_a and α .

Kinetic complexities are not limited to multiple chemical steps. They may also include physical processes that have different activation energies such as:

- A. Nucleation and growth – the energy barrier for nucleation could be relatively large compared to growth. Once a nucleus is established, the rate of interface advance can be much lower than that for nucleation. There is no sharp demarcation where nucleation stops and growth starts, since the two are interdependent. The contribution of nucleation may diminish as the reaction progresses, leading to an effective activation energy that varies with the reaction progress.
- B. Imperfection distribution – different samples of the same material may have different imperfection distributions. Therefore, no two solid samples are identical, although they may be similar [77]. This could change the degradation kinetic profiles of each sample.
- C. Sublimation occurring simultaneously with other reaction processes.
- D. Surface adsorption-desorption processes on the reactants/products.
- E. Diffusion of a gaseous product through the sample.
- F. Rate of growth may vary along each crystallographic axis of a nucleus [74].

- G. Particle size – if a solid-state reaction occurs at surfaces or defect points, larger particles, which have a lower specific surface area, will be less reactive than smaller particles. Various particle sizes could have different kinetic behavior, therefore a variable particle-sized sample could show complex reaction behavior.
- H. Particle or solid morphology – degradation kinetics of a spherical particle or compact could differ from that of a cylindrical one. A non-homogenous sample that contains several solid shapes may show complex reaction behavior.
- I. Localized melting – melt degradation rates usually differ from that of the solid producing variable reactivity throughout the sample [76].

Artifactual variation in activation energy

Isoconversional methods, use several TGA or DSC data sets for kinetic analysis. Some of these methods are sensitive to experimental variables such that changes in these variables (Figure 7) produces errors in calculated kinetic parameters like activation energy. When performing isothermal experiments, care should be taken to ensure that every run is performed under the same experimental conditions (i.e., sample weight, purge rate, sample size distribution, particle morphology, etc.; Figure 7) so that temperature is the only variable for each run. Similarly, when performing nonisothermal experiments, care must be taken to ensure that each run is conducted under the same experimental conditions so that only the heating rate is the only variable. Experimental variation can be minimized, but not totally eliminated. For example, sample mass (Figure 7c) may vary from one run to the next and affect a reaction because [78],

1. Larger masses cause larger endothermic or exothermic (self-heating or self-cooling) effects, producing larger deviations from the programmed linear heating rate.
2. Diffusion rates through the sample will change; gas diffusion is faster through a lower mass compared to a higher mass.

3. Thermal gradients through the sample might vary, especially when a powder has a low thermal conductivity; larger samples could contain regions where the temperature differs significantly from other regions.

Similarly, sample packing (Figure 7d) could affect solid reaction kinetics where loosely packed powders contain air pockets that can reduce thermal conductivity or trap evolved gasses compared to a more densely packed powder which would minimize these effects. If any of the above effects occur, a thermogram can be altered such that it falls above or below the expected thermogram for isothermal studies. This would introduce errors in the calculated kinetic parameters obtained from some isoconversional methods.

Temperature dependence of the rate constant

The temperature dependence of the rate constant is almost universally expressed by the Arrhenius equation. However, historically, there has been controversy surrounding the temperature dependence of rate constants with many workers proposing several forms for rate constant temperature dependency, as summarized in Table 3.

These equations were empirically derived based on quality of fit. Selecting an equation because it gives a reasonable fit to the data is not a sufficient reason for its acceptance, as most of the cited equations will reasonably represent the same experimental data. This occurs because kinetic studies are most often conducted in a narrow temperature range, which makes $1/T$, T and $\ln T$ (i.e., independent variables in these equations) linearly related to one another. As kinetics developed, most of these equations, except for that of Arrhenius, disappeared because they were theoretically unsound [19]. As a result, the controversy over temperature dependency was finally put to rest, but the controversy and confusion surrounding reaction rate temperature dependence still affect researchers in heterogeneous kinetics [70, 79-84].

Galwey and Brown [6] have shown that use of the Arrhenius equation in heterogeneous kinetics is conceptually sound and theoretically well founded. However,

use of the Arrhenius equation in nonisothermal experiments is problematic because the temperature integral has no analytical solution. Use of the temperature integral can be avoided by performing kinetic studies isothermally, or using the differential form of the rate law [26]. However, with our current computational tools, approximating the temperature integral is no longer a serious problem because the approximations can be as exact as the kinetic data demands.

Kinetic Compensation Effect

A kinetic compensation effect (KCE) [85-87], is a relationship between the activation energy (E_a) and frequency factor (A) according to:

$$\ln A = bE_a + c \quad (72)$$

Where, b and c are constants. This relationship is called a “compensation” because a change in the activation energy (E_a) is partially or completely compensated by a change in the frequency factor (A). KCEs have been classified into three types [87, 88]:

1. Type-1 – due to a difference in the physicochemical properties of the sample which includes groups of different but related reactions. For example, groups of reactants that have different function substitutions on the same parent molecule, or different crystalline reactants of the same compound containing different defects and impurities [88].
2. Type-2 – due to a difference in the experimental conditions applied to a particular reactant’s kinetic studies which includes different atmospheres, sample masses, heating rate, etc.
3. Type-3 – due to using different computational methods for kinetic analysis of the same data set. The significance of this type of compensation has been questioned and is considered a mathematical artifact [87, 88]. Garn [79-83] considered that this effect results from using the Arrhenius equation.

Graphically, if a KCE exists, then each Arrhenius plot ($\ln k$ vs. $1/T$) gives a pair of A and E_a values. Several Arrhenius plots for a series of reaction studies will give an equal number of A , E_a pairs that can be used to construct a KCE plot (Figure 8a). If a KCE exists, then overlaying the Arrhenius curves reveals an isokinetic relationship (IKR) [87] as seen in Figure 8b. The IKR is characterized by a point called the “isokinetic point” where all Arrhenius curves intersect. The rate constant at this point (k_{iso}) is equal for all Arrhenius plots and the temperature at this point is called the “isokinetic temperature” (T_{iso}).

From the Arrhenius equation (Eq. (14)) and compensation effect (Eq. (72)), the isokinetic point can be determined as,

$$T_{iso} = \frac{1}{Rb} \quad (73)$$

$$\ln k_{iso} = c \quad (74)$$

Vyazovkin and Lesniovich [89] have used an IKR to calculate the frequency factor (A) which can not be obtained directly from isoconversional methods.

The compensation effect has been widely reported, both in homogenous and heterogeneous reactions [85]. However, it remains an empirical observation and has little theoretical justification. Galwey and Brown [86] have summarized the two extreme positions about the compensation effect – either it is an artifact or it has a real chemical significance. If it has real chemical significance, the Arrhenius relationship’s meaning is weakened and some basic principles of chemical kinetics may need to be reformulated.

ICTAC kinetic project

Solid-state kinetics has been associated with controversies and these issues needed to be addressed scientifically. One such approach was through the establishment

of a “kinetic project” by several researchers. A kinetics workshop was held during the 11th International Congress on Thermal Analysis and Calorimetry (ICTAC) in Philadelphia, in August, 1996. One of the suggestions of that workshop was to evaluate the various calculation methods in a consistent and scientific fashion by establishing a global kinetic project. The project distributed kinetic data sets to volunteer participants to perform their data analysis [90, 91]. Eight sets of kinetic data consisting of real and simulated isothermal and nonisothermal experiments were distributed. Experimental data were distributed in six sets for the decomposition of calcium carbonate and ammonium perchlorate under nitrogen and vacuum both isothermally and nonisothermally. Two data sets were simulated isothermally and nonisothermally using two equally-weighted, parallel, first-order reactions ($A_1=10^{10} \text{ min}^{-1}$, $E_{a1}= 80 \text{ kJ/mole}$; $A_2=10^{15} \text{ min}^{-1}$, $E_{a2}= 120 \text{ kJ/mole}$)

The purpose of the project was to evaluate the same data with different calculation methods and make judgments based on the kinetic analysis results. Participants were not limited to any particular calculation method. Many such methods were used to analyze the kinetic data sets including: Ozawa-Flynn-Wall, Kissinger, Friedman, Coats-Redfern, direct differential, and many others. Some of these methods were incorporated in software packages such as: TA-KIN[®], NETZSCH[®] thermokinetics, KINETICS[®] and AKTS-TA[®] [39].

Results for kinetic calculations showed that similar computational methods were in agreement among different laboratories. Analysis of simulated data showed that isoconversional methods produced results that were in general agreement with E_a values ranging from 80–120 kJ/mole; model-fitting results of simulated data gave single E_a values intermediate between the two E_a values used thus did not reveal the kinetic complexity of two parallel pathways [41]. Also, the kinetic results for the same reaction under various experimental conditions were different (i.e., comparing nitrogen and vacuum atmospheres for calcium carbonate and ammonium perchlorate).

The main conclusions from this project were that the kinetic description of a process strongly depends on the experimental conditions [92]. In addition, multi-heating rate methods should be employed to obtain reliable kinetic descriptions and any kinetic process must be described by the complete kinetic triplet [40, 92].

The project succeeded in bridging differences of data analysis in solid-state kinetics. The project was a first step in “standardizing” solid-state kinetic analysis methods. This project should be further expanded to cover other controversial areas in solid-state kinetics.

Summary

This chapter has demonstrated that solid-state reaction kinetics is both a unique and complex area of research.

It is unique because of its significant deviation from homogenous phase kinetic processes. Solid-state kinetics are affected by particle size, crystal defects, crystal strain and other solid properties not relevant to liquid or gas phase processes. One must carefully interpret solid-state kinetic results and incorporate interpretive caveats that reflect these perturbations. Generalizations are both easy and difficult. They are easy because the investigator can use straight forward extrapolation of activation energy, frequency factor and model to other temperatures or conditions. They are difficult because kinetic results can depend upon a myriad of solid-state characteristics making it risky to make such extrapolations without knowing how these factors interact to affect the reaction(s) of interest.

This area is complex because of the mathematical tools and models used to interpret solid-state kinetic data. There is a rich array of kinetic models that arise from the non-isotropic nature of the solid-state. Also, many kinetic studies are carried out under non-isothermal conditions which further complicates an already complex kinetic picture.

We have attempted to summarize the range of experimental methods (i.e., isothermal and non-isothermal) and the attendant mathematical approaches used to analyze such data. This review has not been exhaustive but rather representative of the common tools and models used. Even though the focus has been on reactions involving weight loss (i.e., TGA), many of the tools are applicable to other thermal methods such as DSC. The only requirement is the ability to convert collected data to degree of reaction (α) versus time or temperature.

For the pharmaceutical scientist, this summary serves as an introduction into the realm of solid-state reaction kinetics. The use of such results to make extrapolations or conclusions about solid drug stability under ambient conditions awaits further development. The question, “what can I do with these results?” is presently difficult to answer in a general sense. For specific cases, answers may be generated for narrow applications. Generality in solid-state kinetics of drug solids awaits further investigation of the factors affecting such processes and the successful extrapolation to predicting API or formulation stability characteristics.

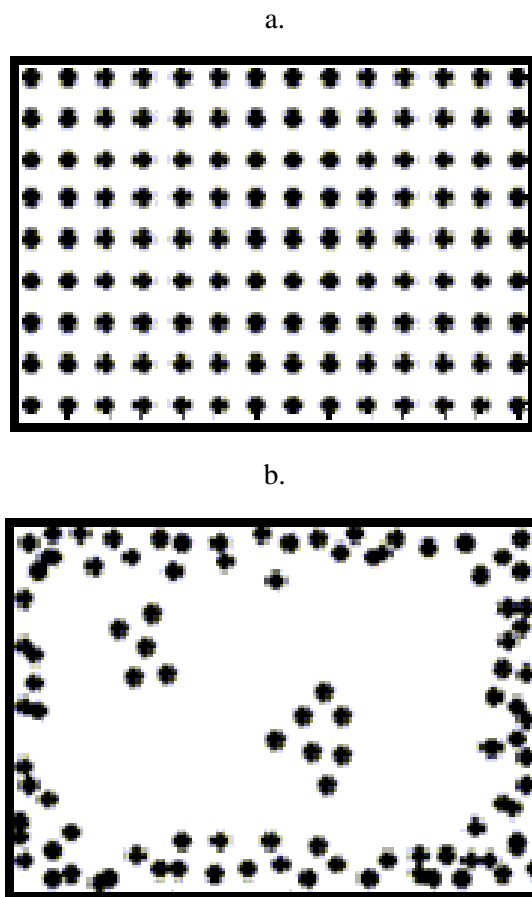


Figure 1. Schematic representation of reactivity: a. homogenous system; b. heterogeneous system. Black dots represent reaction sites.

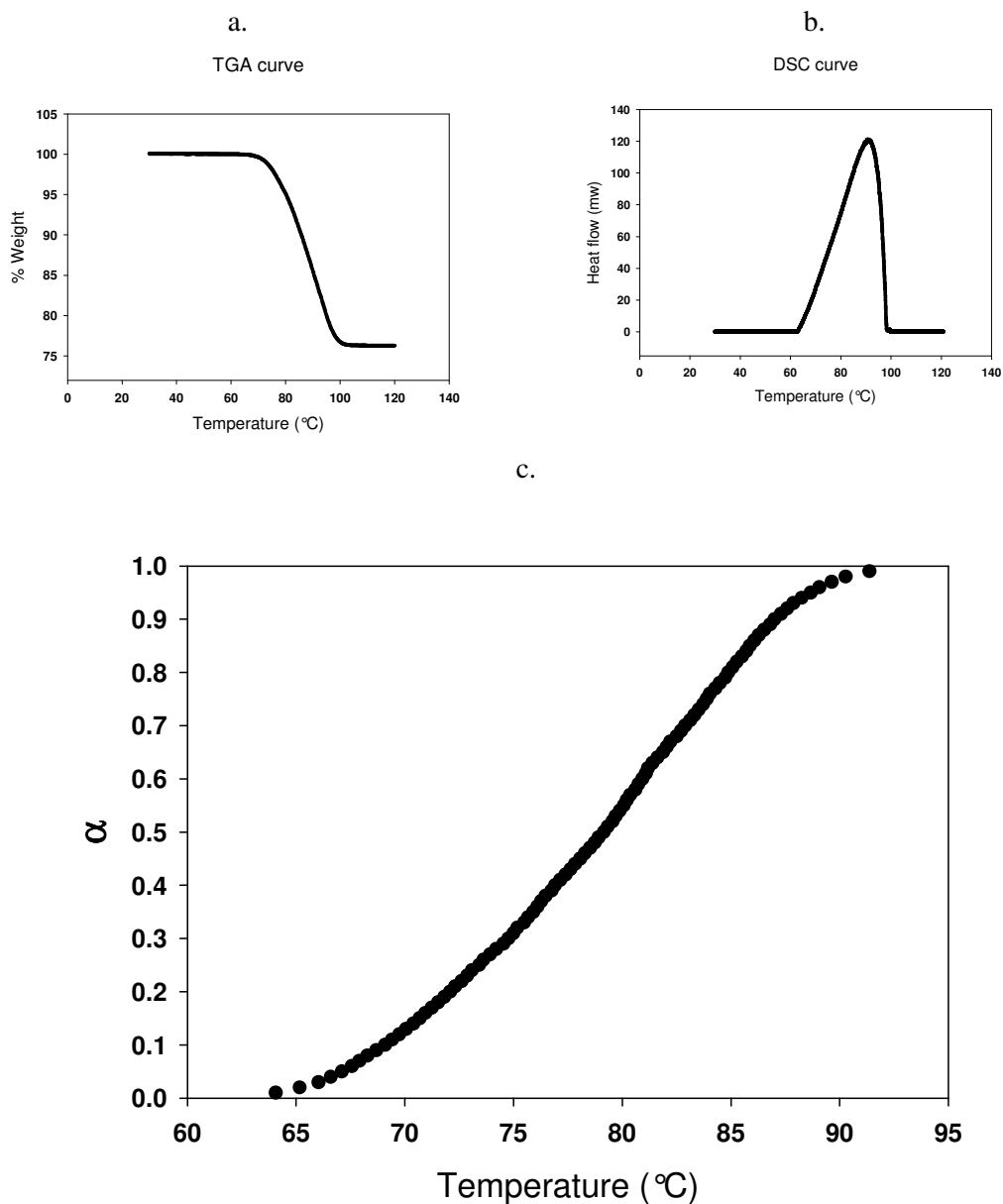


Figure 2. Transformations of TGA and DSC curves to conversion fraction curves: Desolvation thermogram of a solid solvate by TGA (a) and DSC (b); c. α -T plot for the desolvation process for both DSC and TGA results.

Table 1. Solid-state rate expressions for different reaction models, classifications and mathematical derivations are given in Chapter 2.

Model	Differential form $f(\alpha)=1/k \, d\alpha/dt$	Integral forma $g(\alpha)=kt$
Nucleation models		
Power law (P2)	$2 \alpha^{(1/2)}$	$\alpha^{(1/2)}$
Power law (P3)	$3 \alpha^{(2/3)}$	$\alpha^{(1/3)}$
Power law (P4)	$4 \alpha^{(3/4)}$	$\alpha^{(1/4)}$
Avarami-Erofeyev (A2)	$2(1-\alpha)[- \ln(1-\alpha)]^{1/2}$	$[- \ln(1-\alpha)]^{1/2}$
Avarami-Erofeyev (A3)	$3(1-\alpha)[- \ln(1-\alpha)]^{2/3}$	$[- \ln(1-\alpha)]^{1/3}$
Avarami-Erofeyev (A4)	$4(1-\alpha)[- \ln(1-\alpha)]^{3/4}$	$[- \ln(1-\alpha)]^{1/4}$
Prout-Tompkins (B1)	$\alpha (1-\alpha)$	$\ln[\alpha/(1-\alpha)]+c^b$
Geometrical contraction models		
Contracting area (R2)	$2(1-\alpha)^{1/2}$	$[1-(1-\alpha)^{1/2}]$
Contracting volume (R3)	$3(1-\alpha)^{2/3}$	$[1-(1-\alpha)^{1/3}]$
Diffusion models		
1-D Diffusion (D1)	$1/(2\alpha)$	α^2
2-D Diffusion (D2)	$[- \ln(1-\alpha)]^{-1}$	$[(1-\alpha)\ln(1-\alpha)]+ \alpha$
3-D Diffusion-Jander (D3)	$[3(1-\alpha)^{2/3}] / [2(1- (1-\alpha)^{1/3})]$	$[1-(1-\alpha)^{1/3}]^2$
Ginstling-Brounshtein (D4)	$3/[2((1-\alpha)^{-1/3} - 1)]$	$1-(2\alpha/3)-(1-\alpha)^{2/3}$
Reaction-order models		
Zero-order (F0/R1)	1	α
First-order (F1)	$(1-\alpha)$	$-\ln(1-\alpha)$
Second-order (F2)	$(1-\alpha)^2$	$(1-\alpha)^{-1} - 1$
Third-order (F3)	$(1-\alpha)^3$	$0.5 [(1-\alpha)^{-2} - 1]$

^a In some references $f(\alpha)$ and $g(\alpha)$ have opposite designations.

^b constant of integration.

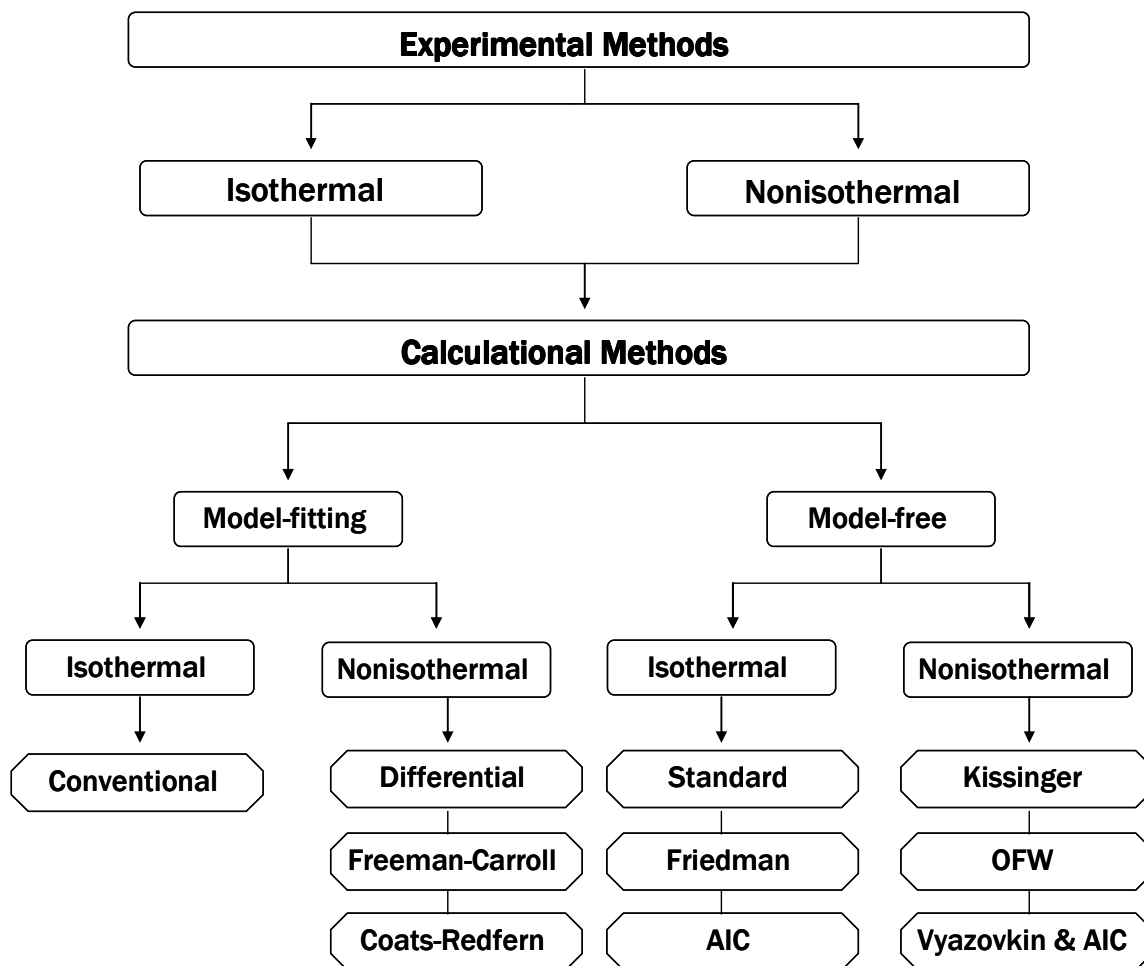


Figure 3. Methods for studying solid-state kinetics.

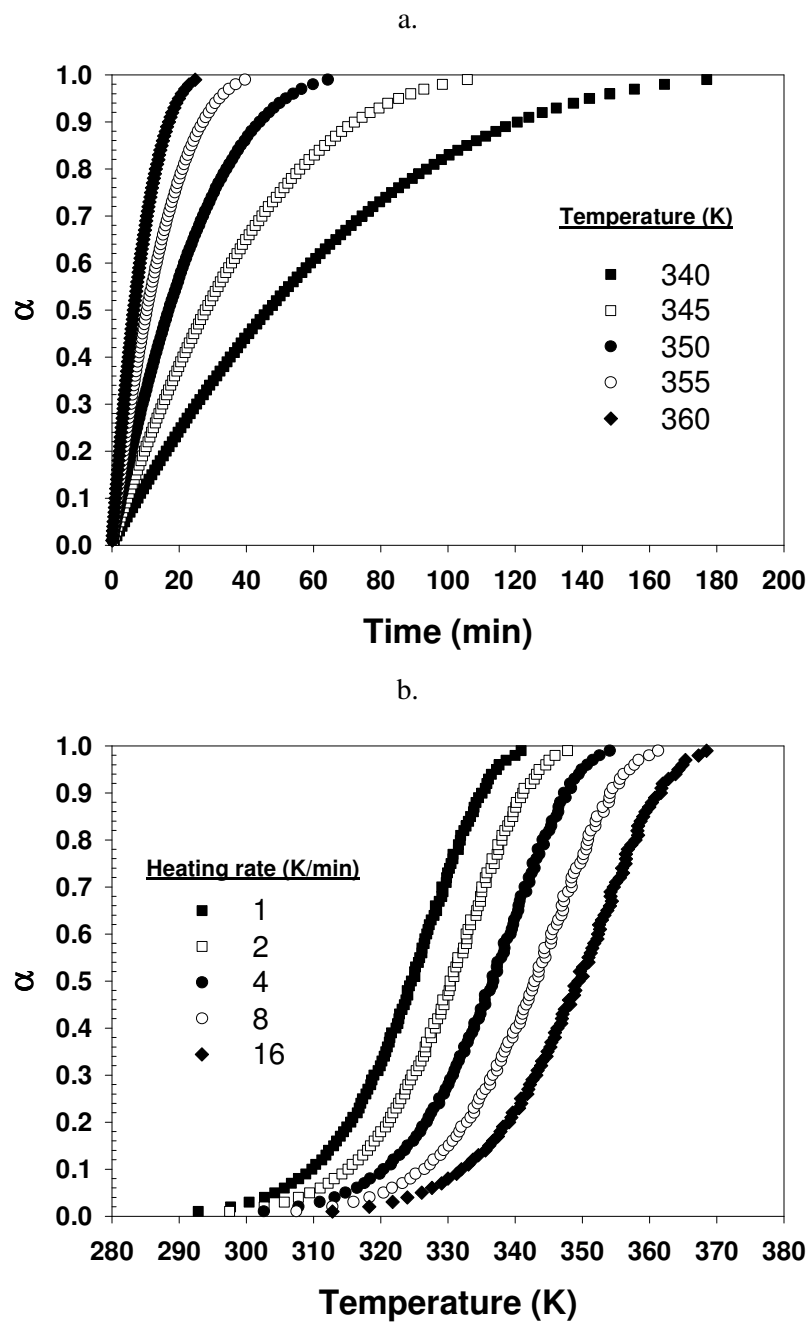


Figure 4. TGA data for a simulated dehydration reaction: a, isothermal; b, nonisothermal.

Table 2. Senum-Yang approximations of the temperature integral^a

Degree	p(x)
1	$\frac{e^{-x}}{x} \cdot \frac{1}{(x+2)}$
2	$\frac{e^{-x}}{x} \cdot \frac{(x+4)}{(x^2+6x+6)}$
3	$\frac{e^{-x}}{x} \cdot \frac{(x^2+10x+18)}{(x^3+12x^2+36x+24)}$
4 ^b	$\frac{e^{-x}}{x} \cdot \frac{(x^3+18x^2+86x+96)}{(x^4+20x^3+120x^2+240x+120)}$

^a Detailed derivation shown in the appendix section.

^b In Ref. [31], the 4th degree approximation is incorrectly calculated, It is 86x not 88x.

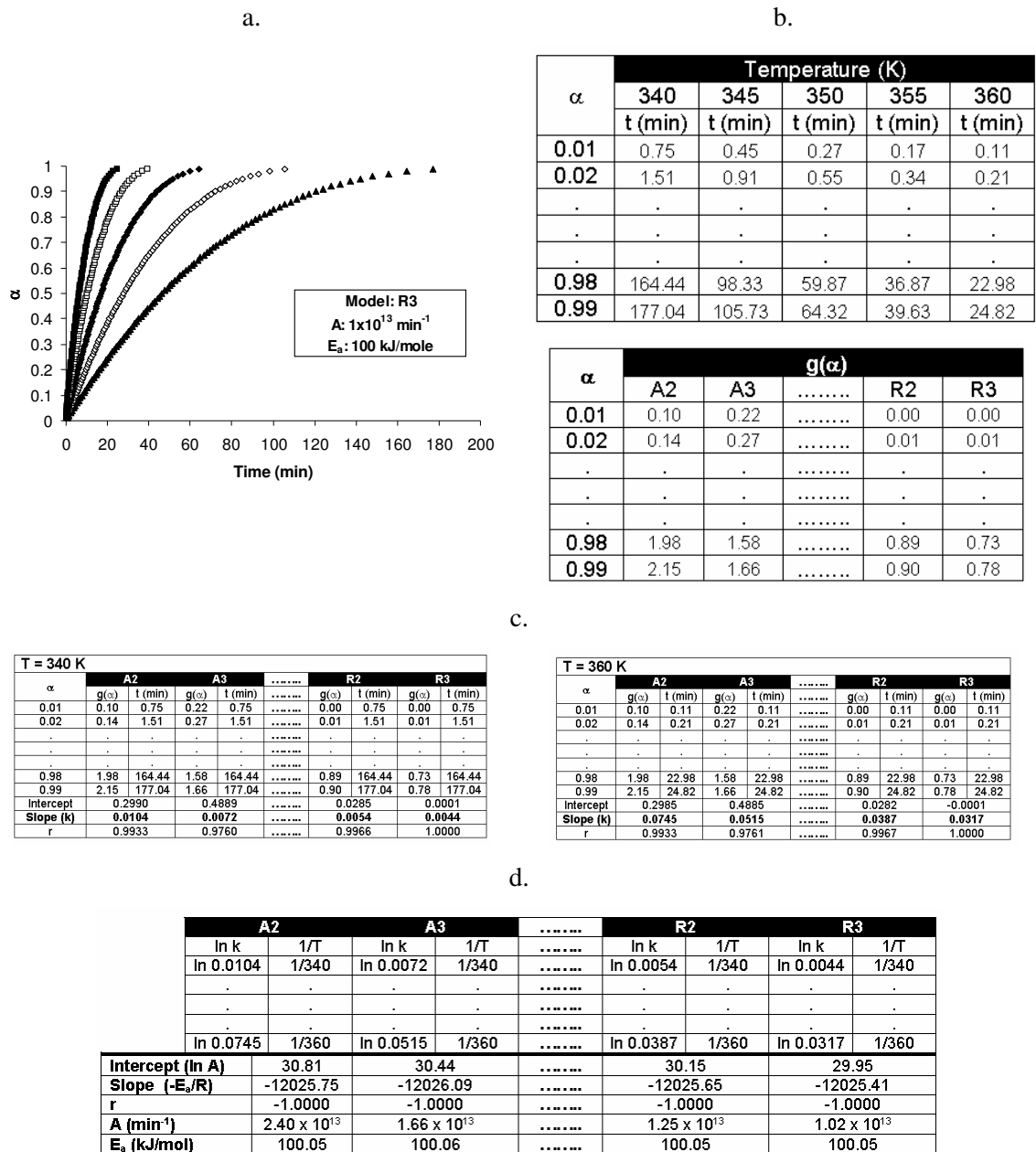


Figure 5. Isothermal model fitting method (conventional method): a, simulated α -time curves with 0.25% random error in time at: \blacktriangle , 340 K; \diamond , 345 K; \blacklozenge , 350 K; \square , 355 K and \blacksquare , 360 K. Inset shows simulation parameters: b, tabulated values obtained from the curve in addition to $g(\alpha)$ values for each model; c, first data fit ($g(\alpha)$ vs. t) for each model and temperature (only two temperature values are shown) and d, second data fit (Arrhenius plot) from which A and E_a can be calculated for each model.

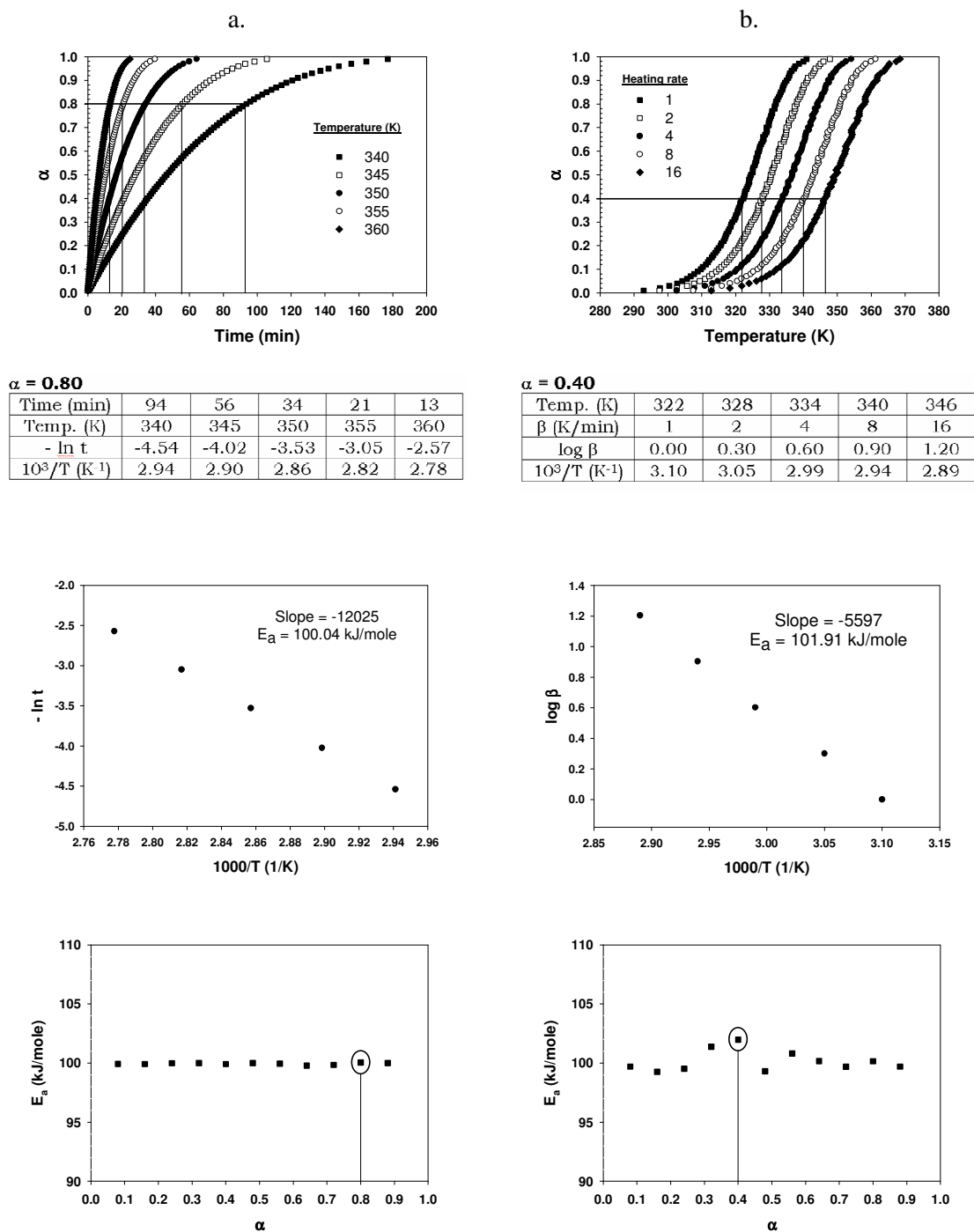


Figure 6. Isoconversational methods for evaluating solid-state kinetics: a, Standard method for a set of isothermal curves at: ■, 340 K; □, 345 K; ●, 350 K; ○, 355 K and ◆, 360 K; b, Ozawa-Flynn-Wall (OFW) method for a set of nonisothermal curves at: ■, 1 K/min; □, 2 K/min; ●, 4 K/min; ○, 8 K/min and ◆, 16 K/min.

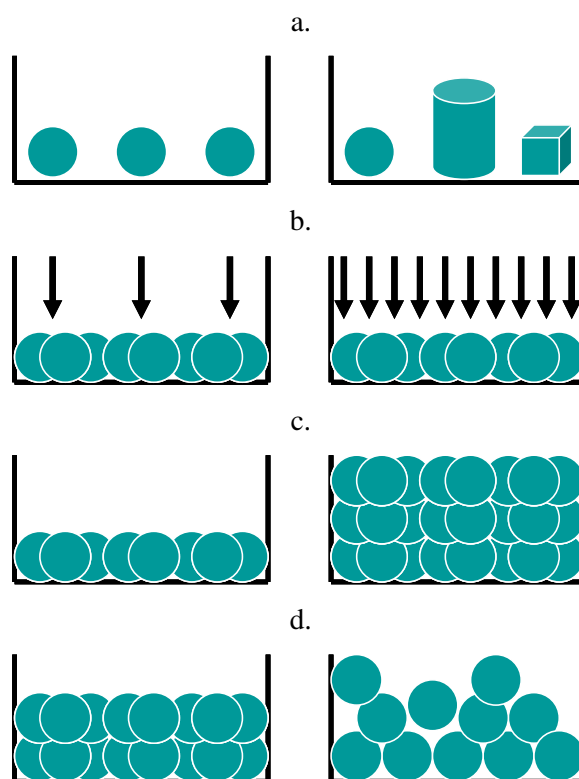


Figure 7. Examples of experimental variables that could affect thermograms obtained by TGA/DSC: a, particle shape; b, purge gas flow rate; c, sample mass and d, sample packing.

Table 3. Summary of temperature dependencies of rate constants [19]

Equation ^a	Year	Reference ^b
$k = A' F^T (1 + G'T)$	1850	Wilhelmy
$k = Ae^{DT}$	1862	Berthelot
$k = a'+b'T^2$	1881	Warder
$k = Ae^{-\frac{(B-DT^2)}{T}}$	1883	Schwab
$k = Ae^{-\frac{B}{T}}$	1889	Arrhenius
$k = AT^C e^{-\frac{B}{T}}$	1893	Kooij
$k = AT^C$	1895	Harcourt and Esson
$k = AT^C e^{-\frac{(B-DT^2)}{T}}$	1898	Van't Hoff

^a A, A', B, C, D, F, G', a' and b' are temperature independent constants.

^b Ref. [19] cites the original articles for these expressions.

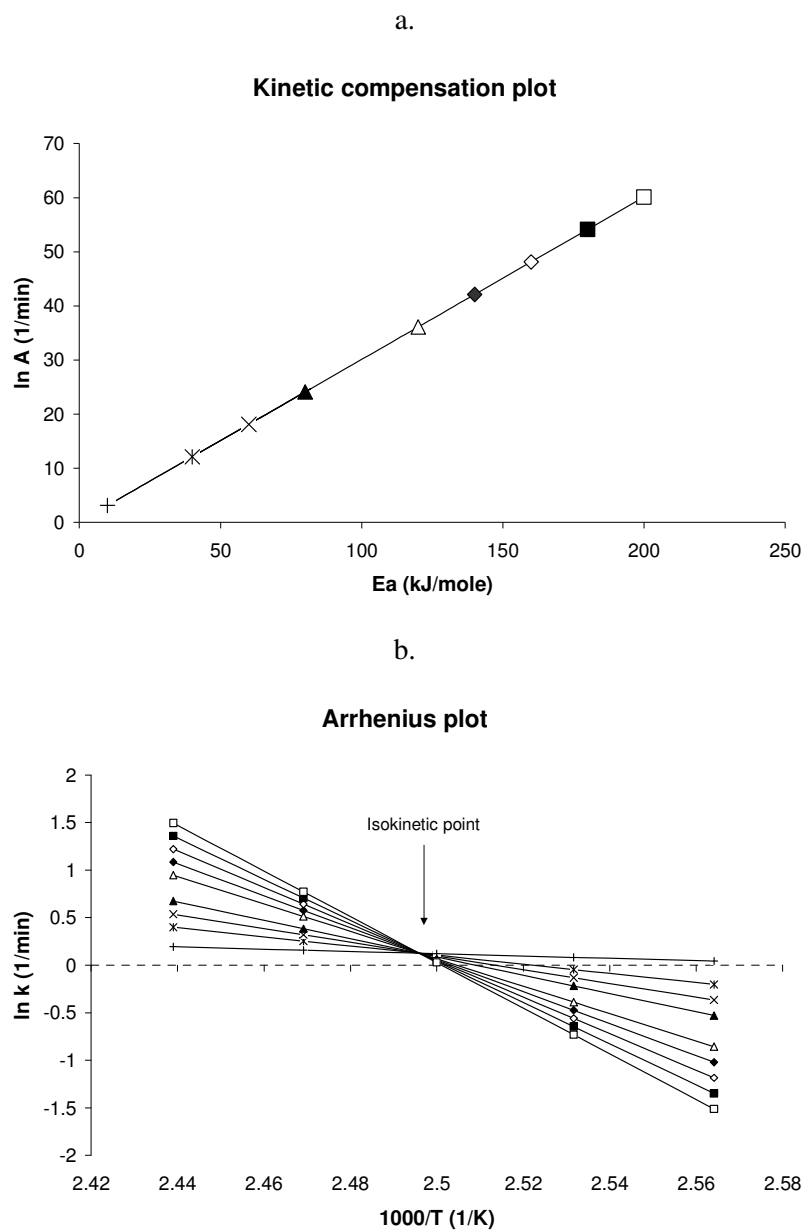


Figure 8. a, Kinetic compensation effect (KCE); b, isokinetic relationship (IKR). Each point in “a” results from an Arrhenius plot shown in “b”.

CHAPTER 2

MODELS IN SOLID-STATE KINETICS: BASICS AND MATHEMATICAL FUNDAMENTALS

Introduction

Fifty years have passed since the publication of “Chemistry of the Solid State” edited by W.E. Garner [93] which covered theories of the solid-state, including solid-state reaction kinetics. Jacobs and Tompkins [16] covered theories and derivations of some solid-state reaction models in Garner’s text; specifically, nucleation and nuclei growth models. The derivation of these and other models has also appeared in Volume 22 of the Chemical Kinetics Series entitled, “Reactions in the Solid State” by Brown et. al. [94] Later, Galwey and Brown [95] presented many of these same models. These and other older references are becoming less accessible because they have been out of print for many years. Researchers who seek the basis for these models and their mathematical foundations must find such old texts or access even older journal articles. Unfortunately, no single reference comprehensively presents the basics and mathematical development of these models. The lack of such a source causes authors to redundantly present reaction models in tabular forms [96-100] as shown in Table 1. It is rare to find a solid-state kinetic report that does not list such reaction models because of the lack of a general source to which reference can be made.

This chapter is intended to provide a summary and mathematical basis for commonly used reaction models in solid-state kinetics.

Model classification

Models are generally classified based on the graphical shape of their isothermal curves (α vs. t or $d\alpha/dt$ vs. α) or on their mechanistic assumptions. Based on their shape,

kinetic models can be grouped into: acceleratory, deceleratory, linear or sigmoidal models (Figure 9). Acceleratory models are those in which the reaction rate ($d\alpha/dt$) is increasing (e.g., accelerating) as the reaction proceeds (Figure 9a), similarly, deceleratory reaction rates decrease with reaction progress (Figure 9b–d) while the rate remains constant for linear models (Figure 9e) and sigmoidal models show a bell-shaped relationship between rate and α (Figure 9f). Nonisothermally, α -temperature plots are not as distinctive in their shapes as they are isothermally. Figure 10 shows the nonisothermal α -temperature and $d\alpha/dT$ vs. α plots generated using Eqs. (19) and (20).

Based on mechanistic assumptions, models are divided into: nucleation, geometrical contraction, diffusion or reaction-order (Table 1).

Model derivation

Model derivation is based on several proposed reaction mechanisms which include nucleation, geometric shape, diffusion, and reaction-order. Sestak and Berggren [101] have suggested a mathematical form that represents all models in a single general expression:

$$g(\alpha) = \alpha^m (1 - \alpha)^n (-\ln(1 - \alpha))^p \quad (75)$$

Where, m , n and p are constants. By assigning values for these three variables, any model can be expressed. Derivations and theoretical implications of specific models are discussed below.

Nucleation and nuclei growth models

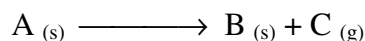
The kinetics of many solid-state reactions have been described by nucleation models; specifically, the Avrami models, these reactions include: crystallization [102-104], crystallographic transition [105], decomposition [106, 107], adsorption [108, 109], hydration [110], and desolvation [21]. Skrdla and Robertson [111] have recently

suggested a model that describes sigmoidal α -time curves based on the Maxwell-Boltzmann energy distribution and incorporates two rate constants – one for the acceleratory and one for the deceleratory region of the α -time curve.

Nucleation

Crystals have fluctuating local energies from imperfections due to impurities, surfaces, edges, dislocations, cracks and point defects [112]. Such imperfections are sites for reaction nucleation since the reaction activation energy is minimized at these points. Thus, they are called, nucleation sites [16, 105].

A common reaction in solid-state kinetics follows the scheme:



Where, a solid “A” decomposes thermally to produce a solid “B” and gas “C”.

Nucleation is the formation of a new product phase (B) at reactive points (nucleation sites) in the lattice of the reactant (A). Nucleation rates have been derived based on one of two assumptions [16]: nucleation is single or multi-stepped (Table 4).

Single-step nucleation assumes that nucleation and nuclei growth occur in a single step. For N_0 potential nucleation sites (having equal nucleation probability), once the nuclei (N) are formed, they grow and the rate of nucleation is a simple first-order process according to:

$$\frac{dN}{dt} = k_N (N_0 - N) \quad (76)$$

Where, N is the number of growth nuclei present at time, t, k_N is the nucleation rate constant. Separating variables and integrating Eq. (76) gives:

$$N = N_0 (1 - e^{-k_N t}) \quad (77)$$

Differentiation of Eq. (77) gives the exponential rate of nucleation:

$$\frac{dN}{dt} = k_N N_0 e^{-k_N t} \quad (78)$$

When k_N is small, the exponential term in Eq. (78) is ~ 1 and the rate of nucleation is approximately constant producing a linear rate of nucleation,

$$\frac{dN}{dt} = k_N N_0 \quad (79)$$

However, when k_N is very large, the rate of nucleation is very high indicating that all nucleation sites are rapidly or instantly nucleated producing an instantaneous rate of nucleation:

$$\frac{dN}{dt} = \infty \quad (80)$$

On the other hand, multi-step nucleation assumes that several distinct steps are required to generate a growth nucleus [113]. Accordingly, formation of product B will induce strain within the lattice of A rendering small aggregates of B unstable causing them to revert back to reactant A. Strain can be overcome if a critical number (m_c) of B nuclei are formed. Therefore, two types of nuclei can be defined – germ and growth nuclei. A germ nucleus is submicroscopic with B particles below the critical number ($m < m_c$) which will either revert back to reactant A or grow to a growth nucleus which is a nucleus with B particles exceeding the critical number ($m > m_c$) of particles allowing further reaction (i.e. nuclei growth). Therefore, a germ nucleus must accumulate a number of product molecules, “p”, before it is converted to a growth nucleus. The rate constant (k_i) for addition of individual molecules in a nucleus up to “p” molecules (e.g., $n < p$) is assumed to be constant or $k_0 = k_1 = k_2 = k_3 = \dots = k_{p-1} = k_i$. (i.e., rate constant for addition of each molecule). After “p” molecules have been accumulated (e.g. $n \geq p$), the rate constant (k_g) for further nucleus growth by addition of further molecules ($> p$)

becomes, $k_p=k_{p+1}=k_{p+2}=k_{p+4}=\dots=k_g$. It is assumed that the rate of nucleus growth is more than that of nucleus formation (i.e., $k_g > k_i$). Therefore, according to Bagdassarian [113], if β successive events are necessary to form the growth nucleus, and each event has a probability equal to k_i , then the number of nuclei formed at time, “t”, is:

$$N = \frac{N_0 (k_i t)^\beta}{\beta!} = D t^\beta \quad (81)$$

where, $D = \frac{N_0 (k_i t)^\beta}{\beta!}$. After differentiation, Eq. (81) becomes,

$$\frac{dN}{dt} = D \beta t^{\beta-1} \quad (82)$$

Equation (82) represents the power law of nucleation [16, 113] (Table 4).

Equation (82) was also derived by Allnatt and Jacobs [114] but they assumed unequal rate constants for addition of successive molecules to the growth nuclei before reaching the critical size ($n=p$).

Nuclei growth

The nuclei growth rate ($G(x)$) can be represented by the nuclei radius formed from growth. Nuclei growth rates usually vary with size [16, 95]. For example, growth rates of small nuclei (often, submicroscopic) would be different from that of large nuclei. Low growth rates are due to the instability of very small nuclei (germ nuclei) which revert to reactants. The radius of a stable nucleus (growth nucleus) at time, t, ($r(t, t_0)$), is:

$$r(t, t_0) = \int_{t_0}^t G(x) . dx \quad (83)$$

Where, $G(x)$ is the rate of nuclei growth and t_0 is the formation time of a growth nucleus.

In addition to nucleus radius, two important considerations in nuclei growth are also considered – nucleus shape (σ) and growth dimension (λ). When these are considered, they describe nuclei growth rate through the volume occupied by individual nuclei ($v(t)$). Therefore, a stable nucleus formed at time (t_0) occupies a volume $v(t)$ at time, t , according to:

$$v(t) = \sigma [r(t, t_0)]^\lambda \quad (84)$$

Where, λ is the number of growth dimensions (i.e., $\lambda=1, 2$ or 3), σ is the shape factor (i.e., $4\pi/3$ for a sphere) and r is the radius of a nucleus at time, t . Equation (84) gives the volume occupied by a single nucleus, the total volume occupied by all nuclei ($V(t)$) can be calculated by combining nucleation rate (dN/dt) and growth rate ($v(t, t_0)$) equations while accounting for different initial times of nucleus growth (t_0):

$$V(t) = \int_0^t v(t) \left(\frac{dN}{dt} \right)_{t=t_0} dt_0 \quad (85)$$

Where, $V(t)$ is the volume of all growth nuclei and dN/dt is the nucleation rate. Substituting Eq. (83) into (84) and Eq. (84) into (85) gives:

$$V(t) = \int_0^t \sigma \left(\int_{t_0}^t G(x) .dx \right)^\lambda \left(\frac{dN}{dt} \right)_{t=t_0} dt_0 \quad (86)$$

The above equation may be integrated for any combination of nucleation and/or growth rate laws to give a rate expression of the form ($g(\alpha) = kt$) as listed in Table 1. However, this is not always possible since there is no functional relationship [95] between the nucleation and growth terms. Therefore, assumptions about nucleation (dN/dt) and growth ($v(t)$) rate equations must be made, as described below.

Power law (P) models

For a simple case where nucleation rate follows the power law (Eq. (82)), and nuclei growth is assumed constant ($G(x)=k_G$), Eq. (86) becomes,

$$V(t) = \int_0^t \sigma (k_G (t-t_0))^\lambda (D \beta t_0^{\beta-1}) dt_0 \quad (87)$$

Evaluating the integral in Eq. (87) gives [16]:

$$V(t) = \sigma k_G^\lambda D \beta t^{\beta+\lambda} \left(1 - \frac{\lambda \beta}{\beta+1} + \frac{\lambda(\lambda-1)}{2!} \frac{\beta}{\beta+2} \dots \right), \quad \lambda \leq 3 \quad (88)$$

If $D' = D \beta \left(1 - \frac{\lambda \beta}{\beta+1} + \frac{\lambda(\lambda-1)}{2!} \frac{\beta}{\beta+2} \dots \right)$ and $n = \beta + \lambda$, Eq. (88) becomes,

$$V(t) = \sigma k_G^\lambda D' t^n \quad (89)$$

Since, $V(t)$ is directly proportional to the reaction progress (α), α can be represented as:

$$\alpha = V(t) \times C \quad (90)$$

Where, C is a constant equal to $1/V_0$ (V_0 -initial volume). From Eqs. (89) and (90) we obtain:

$$\alpha = \sigma k_G^\lambda C D' t^n \quad (91)$$

which can be rewritten as:

$$\alpha = \left(\left(\sigma k_G^\lambda C D' \right)^{\frac{1}{n}} \right)^n t^n \quad (92)$$

If $k = \left(\sigma k_G^\lambda C D' \right)^{\frac{1}{n}}$, Eq. (92) can be written as:

$$\alpha = (kt)^n \quad (93)$$

Equation (93) can be rearranged to:

$$(\alpha)^{\frac{1}{n}} = kt \quad (94)$$

Equation (94) represents the various power law (P) models (Table 1).

The Avrami-Erofeyev (A) models

In any solid-state decomposition, there are certain restrictions on nuclei growth.

Two such restrictions have been identified [95] (Figure 11):

- a. Ingestion – elimination of a potential nucleation site by growth of an existing nucleus; ingested sites never produce a growth nucleus due to their inclusion in a growth nucleus. Ingested nuclei are called “phantom” nuclei.
- b. Coalescence – loss of reactant/product interface when reaction zones of two or more growing nuclei merge.

An expression relating the number of nuclei sites is [115]:

$$N_1(t) = N_0 - N(t) - N_2(t) \quad (95)$$

Where, N_0 is the total number of possible nuclei-forming sites, $N_1(t)$ is the actual number of nuclei at time, t , $N_2(t)$ is the number of nuclei ingested and $N(t)$ is the number of nuclei activated (i.e., developed into growth nuclei). From Eq. (95), a nucleation rate (dN/dt) known as the modified exponential law can be developed [16]. However, if this nucleation rate is substituted into Eq. (85), the resulting expression does not have an analytical solution [16]. To deal with this issue, an extended conversion fraction (α') was proposed [116] which is the conversion fraction previously defined in Eq. (93) ($\alpha=[kt]^n$) that neglects ingestion (i.e., accounts for active and phantom nuclei) and nuclei coalescence. Therefore, $\alpha' \geq \alpha$. Values of α can be evaluated by determining their relation to values of α' .

The extended conversion fraction (α') was related to the actual conversion fraction (α) by Avrami [117] who obtained:

$$d\alpha' = \frac{d\alpha}{(1-\alpha)} \quad (96)$$

Which upon integration gives:

$$\alpha' = -\ln(1-\alpha) \quad (97)$$

Substituting the value of (α') from Eq. (93) into Eq. (97) gives:

$$(kt)^n = -\ln(1-\alpha) \quad (98)$$

which can be rearranged to:

$$[-\ln(1-\alpha)]^{1/n} = kt \quad (99)$$

Erofeyev (Erofe'ev or Erofeev) [118] followed a different approach to derive a special case of Eq. (99) for $n=3$. Therefore, Eq. (99) was attributed to both Avrami and Erofeyev and represents different Avrami-Erofeyev (A) models (Table 1) for different values of “n”. These “A” models are also called the JMAEK models which stands for: Johnson, Mehl, Avrami, Erofeyev and Kholmogorov, in recognition of the researchers that have contributed to their development [95].

Autocatalytic models

In homogenous kinetics, autocatalysis occurs when the products catalyze the reaction, this occurs when the reactants are regenerated during a reaction in what is called “branching”. The reactants will eventually be consumed and the reaction will enter a “termination” stage where it will cease. A similar observation can be seen in solid-state kinetics. Autocatalysis occurs in solid-state kinetics if nuclei growth promotes continued

reaction due to the formation of imperfections such as dislocations, or cracks at the reaction interface (i.e., branching). Termination occurs when the reaction begins to spread into material that has decomposed [119]. Prout and Tompkins [120] derived an autocatalysis model (B1) for the thermal decomposition of potassium permanganate which produced considerable crystal cracking during decomposition.

In autocatalytic reactions, the nucleation rate can be defined by,

$$\frac{dN}{dt} = k_N N_0 + (k_B - k_T)N \quad (100)$$

Where, k_B is the branching rate constant and k_T is the termination rate constant. If $k_N N_0$ is neglected, Eq. (100) becomes,

$$\frac{dN}{dt} = (k_B - k_T)N \quad (101)$$

This could occur in one of two cases:

1. k_N is very large – so that initial nucleation sites are depleted rapidly and calculations of dN/dt are valid for time intervals after N_0 sites are depleted.
2. k_N is very small so that $k_N N_0$ can be ignored.

The reaction rate is related to number of nuclei by,

$$\frac{d\alpha}{dt} = k' N \quad (102)$$

Where, k' is the reaction rate constant. Prout and Tompkins found that the shape of α vs. time plots for the degradation of potassium permanganate was sigmoidal.

Therefore, an inflection point exists (α_i, t_i) at which dN/dt will change signs. From the boundary conditions that need to be satisfied at that inflection point (i.e., $k_B = k_T$), the following can be defined:

$$k_T = k_B \left(\frac{\alpha}{\alpha_i} \right) \quad (103)$$

Substituting Eq. (103) into Eq. (101) gives,

$$\frac{dN}{dt} = k_B \left(1 - \frac{\alpha}{\alpha_i} \right) N \quad (104)$$

Since $\frac{dN}{d\alpha} = \frac{dN}{dt} \cdot \frac{dt}{d\alpha}$, Eq. (105) can be obtained:

$$\frac{dN}{d\alpha} = k'' \left(1 - \frac{\alpha}{\alpha_i} \right) \quad (105)$$

Where $k'' = k_B/k'$. Assuming k_B is independent of α , separating variables in Eq. (105) and integrating gives,

$$N = k'' \left(\alpha - \frac{\alpha^2}{2\alpha_i} \right) \quad (106)$$

Substituting Eq. (106) into (102) gives,

$$\frac{d\alpha}{dt} = k_B \left(\alpha - \frac{\alpha^2}{2\alpha_i} \right) \quad (107)$$

Since Prout and Tompkins assumed that $\alpha_i = 0.5$, Eq. (107) reduces to:

$$\frac{d\alpha}{dt} = k_B \alpha (1 - \alpha) \quad (108)$$

Separating variables and integrating Eq. (108) gives:

$$\ln \frac{\alpha}{1 - \alpha} = k_B t + c \quad (109)$$

where, c is the integration constant

Equation (109) is the Prout-Tompkins (B1) model (Table 1) which well fits the thermal degradation of solid potassium permanganate. It should be noted that unlike other models, the integration of Eq. (108) was performed without limits, simply because with a lower limit ($\alpha = 0$), the value is negative infinity. As a result, the integration constant appears in the Prout-Tompkins equation (Eq. (109)). One of the limitations in some literature on this equation is that it is reported without the constant term as:

$$\ln \frac{\alpha}{1-\alpha} = k_B t \quad (110)$$

This causes confusion since Eq. (110) will give negative time values for $\alpha < 0.5$ (Figure 12). To overcome this problem, an integration constant (c) in Eq. (109) is needed which shifts the curve towards positive time values. There is no general criterion for what the integration constant should be, however, Prout and Tompkins used t_{\max} which is the time needed for the maximum rate (i.e., the inflection point) which is approximately the same as $t_{1/2}$ used by Carstensen [121]. We have used a time equivalent to $\alpha=0.01$ (30.21 min) for our simulation (Figure 12) but other values would be equally valid.

The Prout-Tompkins model has been criticized because of the assumptions required for its derivation, other forms of it have been proposed [119, 122-124]. Skrdla [125] considered nucleation and branching as two separate processes (independent but coupled) having two different rate constants, and proposed an autocatalytic rate expression. The proposed expression gives the Prout-Tompkins model if the nucleation and branching rate constants are equal [125]. Guinesi et. al. [126] have shown that titanium(IV)-EDTA decarboxylates in two steps, the first being the B1 model while the second is the R3 model.

Geometrical contraction (R) models

These models assume that nucleation occurs rapidly on the surface of the crystal. The rate of degradation is controlled by the resulting reaction interface progress towards

the center of the crystal. Depending on crystal shape, different mathematical models may be derived. For any crystal particle the following relation is applicable:

$$r = r_0 - k t \quad (111)$$

Where, r is the radius at time, t , r_0 is the radius at time t_0 and k is the reaction rate constant. If a solid particle is assumed to have cylindrical or spherical/cubical shapes (Figure 13), the contracting cylinder (contracting area) or contracting sphere/cube (contracting volume) models [127], respectively, can be derived. Dehydration of calcium oxalate monohydrate was shown to follow geometrical contraction models [128-130].

The contracting cylinder (contracting area) model – R2

For a cylindrical solid particle, the volume is: $h\pi r^2$, where, h is the cylinder height and r is the cylinder radius. For “ n ” particles, the volume is $nh\pi r^2$. Since, weight = volume \times density (ρ), the weight of “ n ” cylindrical particles is $n\rho h\pi r^2$. From the earlier definition of conversion fraction (α , Eq. (6)) and assuming $m_\infty \approx 0$, we obtain:

$$\alpha = \frac{m_0 - m_t}{m_0} \quad (112)$$

Therefore, for “ n ” reacting particles:

$$\alpha = \frac{n \rho h \pi r_0^2 - n \rho h \pi r^2}{n \rho h \pi r_0^2} \quad (113)$$

Equation (113) reduces to:

$$\alpha = \left(1 - \frac{r^2}{r_0^2} \right) \quad (114)$$

Substituting the value of r from Eq. (111) gives:

$$\alpha = 1 - \left(\frac{r_0 - kt}{r_0} \right)^2 \quad (115)$$

which can be rearranged to,

$$1 - \alpha = \left(1 - \frac{k}{r_0} t \right)^2 \quad (116)$$

If $k_0 = k/r_0$, Eq. (116) becomes the contracting cylinder model:

$$1 - (1 - \alpha)^{1/2} = k_0 t \quad (117)$$

The contracting sphere/cube (contracting volume) model–

R3

If a solid particle has a spherical or cubical shape, a contracting sphere/cube model can be derived. A sphere has a volume of $4\pi r^3/3$. For “n” particles, the volume is: $4n\pi r^3/3$. Since weight = volume x density (ρ), the weight of “n” spherical particles is:

$$\text{Weight} = \frac{4}{3} n \rho \pi r^3 \quad (118)$$

Equation (112), for a reaction involving “n” particles becomes:

$$\alpha = \frac{\frac{4}{3} n \rho \pi r_0^3 - \frac{4}{3} n \rho \pi r^3}{\frac{4}{3} n \rho \pi r_0^3} \quad (119)$$

which reduces to:

$$\alpha = \left(1 - \frac{r^3}{r_0^3} \right) \quad (120)$$

Substituting for r from Eq. (111) gives:

$$\alpha = 1 - \left(\frac{r_0 - kt}{r_0} \right)^3 \quad (121)$$

which can be rearranged to:

$$1 - \alpha = \left(1 - \frac{k}{r_0} t \right)^3 \quad (122)$$

If $k_0 = k/r_0$, Eq. (122) becomes the contracting sphere model as:

$$1 - (1 - \alpha)^{1/3} = k_0 t \quad (123)$$

A similar approach for cubic crystals leads to the same general expression.

Diffusion (D) models

One of the major differences between homogenous and heterogeneous kinetics is the mobility of constituents in the system. While reactant molecules are usually readily available to one another in homogenous systems, solid-state reactions often occur between crystal lattices or with molecules that must permeate into lattices where motion is restricted and may depend on lattice defects [131]. A product layer may increase where the reaction rate is controlled by the movement of the reactants to or products from the reaction interface. Solid-state reactions are not usually controlled by mass transfer except for a few reversible reactions or when large evolution or consumption of heat occurs. Diffusion usually plays a role in the rates of reaction between two reacting solids, when reactants are in separate crystal lattices [94]. Wyandt and Flanagan [132] have shown that desolvation of sulfonamide-ammonia adducts follows diffusion models. A correlation was found between calculated desolvation activation energies of the ammonia adducts and the sulfonamide's intrinsic acidity. This finding was attributed to an acid-base-type interaction between the sulfonamide (acid) and ammonia (base) in the solid-state. The

pK_a of the drug was found to inversely relate to the strength of the ammonia-drug interaction which in turn affected desolvation activation energy.

In diffusion-controlled reactions, the rate of product formation decreases proportionally with the thickness of the product barrier layer. For metallic oxidation, this involves a moving boundary and is considered a “tarnishing reaction” [131, 133] which is depicted in Figure 14. According to Figure 14, the mass of B moving across P (unit area) in time, dt , to form product, AB, is:

$$\frac{dl}{dt} = -D \frac{M_{AB}}{M_B \rho} \frac{dC}{dx} \quad (124)$$

Where, M_{AB} and M_B are the molecular weights of AB and B, respectively, D is the diffusion coefficient, ρ is the density of the product (AB), l is the thickness of the product layer (AB), C is the concentration of B in AB and x is the distance from interface Q into AB. Assuming a linear concentration gradient of B in AB, $\left. \frac{dC}{dx} \right|_{x=l} = -\frac{C_2 - C_1}{l}$, where, C_2 and C_1 are the concentrations of B at interfaces P and Q, respectively, Eq. (124) becomes:

$$\frac{dl}{dt} = D \frac{M_{AB}}{M_B \rho} \frac{(C_2 - C_1)}{l} \quad (125)$$

Separating variables and integrating Eq. (125) gives:

$$l^2 = 2D \frac{M_{AB}}{M_B \rho} (C_2 - C_1) t \quad (126)$$

If $k = 2D \frac{M_{AB}}{M_B \rho} (C_2 - C_1)$, Eq. (126) becomes:

$$l^2 = kt \quad (127)$$

Equation (127) is known as the parabolic law [133]. The simplest rate equation is for an infinite flat plane that does not involve a shape factor (e.g., one-dimensional), where the conversion fraction (α) is directly proportional to product layer thickness, “ l ”. Therefore, Eq. (127) becomes:

$$\alpha^2 = k't \quad (128)$$

Where k' is a constant. Equation (128) represents the one-dimensional diffusion (D1) model.

The three-dimensional diffusional (D3) model is based on the assumption of spherical solid particles (Figure 15). The conversion fraction for a reaction involving “ n ” spherical particles using Eqs. (112) and (118) is:

$$\alpha = \frac{\frac{4}{3}n\rho\pi R^3 - \frac{4}{3}n\rho\pi(R-x)^3}{\frac{4}{3}n\rho\pi R^3} \quad (129)$$

Where, x , is the thickness of the reaction zone. Upon simplification, Eq. (129) becomes:

$$\alpha = 1 - \left(\frac{R-x}{R}\right)^3 \quad (130)$$

Equation (130) can be rearranged to:

$$x = R(1 - (1 - \alpha)^{1/3}) \quad (131)$$

Jander [134] used the parabolic law (Eq. (127)) to define x . Therefore, substituting Eq. (131) (after squaring x) into Eq. (127) gives:

$$R^2(1 - (1 - \alpha)^{1/3})^2 = kt \quad (132)$$

Assuming $k' = \frac{k}{R^2}$, Eq. (132) becomes the D3 (Jander) model:

$$\left(1 - (1 - \alpha)^{1/3}\right)^2 = k't \quad (133)$$

Ginstling and Brounshtein [135] have shown that the Jander model (Eq. (133)) which used the parabolic law (derived for a plane surface) is oversimplified and only holds at low conversion values (i.e., low x/R values). The steady-state solution of Fick's first law for radial diffusion in a sphere is [136]:

$$C_{(r)} = \frac{aC_1(b-r) + bC_2(r-a)}{r(b-a)} \quad (134)$$

Where $C(r)$ is the reactant concentration at a particular value of r ($a < r < b$), C_1 is the concentration of the diffusing species at surface $r=a$ and C_2 is the concentration of the diffusing species at surface $r=b$. The reaction at the interface is assumed to occur at a much faster rate than diffusion, therefore, $C_1 \approx 0$ and Eq. (134) becomes:

$$C_{(r)} = \frac{bC_2(r-a)}{r(b-a)} \quad (135)$$

Taking the derivative of the above equation with respect to r at $r=a$ gives:

$$\left. \frac{dC}{dr} \right|_{r=a} = \frac{(b-a)bC_2}{a(b-a)^2} \quad (136)$$

According to Figure 15, $a=R-x$ and $b=R$, so that Eq. (136) becomes:

$$\frac{dC}{dr} = \frac{RC_2}{(R-x)x} \quad (137)$$

The rate of reaction zone advance, dx/dt , can be related to dC/dr by [135]:

$$\frac{dx}{dt} = \frac{D}{\varepsilon} \frac{dC}{dr} \quad (138)$$

Where, D, is the diffusion coefficient, ε is a proportionality constant equal to $\rho n/\mu$ (ρ and μ are the specific gravity and molecular weight of the product, respectively and n is the stoichiometric coefficient of the reaction). Substituting Eq. (137) into Eq. (138) gives:

$$\frac{dx}{dt} = \frac{D}{\varepsilon} \frac{RC_2}{(R-x)x} \quad (139)$$

which can be rewritten as:

$$\frac{dx}{dt} = k \frac{R}{(Rx - x^2)} \quad (140)$$

Where, $k=DC_2/\varepsilon$. Separating variables and integrating Eq. (140) gives:

$$x^2 \left(\frac{1}{2} - \frac{x}{3R} \right) = kt \quad (141)$$

Substituting for x in Eq. (141) with the value of x in Eq. (131) and rearranging gives:

$$1 - \frac{2}{3}\alpha - (1 - \alpha)^{2/3} = kt \quad (142)$$

Equation (142) is the Ginstling-Brounshtein (D4) model. The D4 model is another type of three-dimensional model. Buscaglia and Milanese [137] have proposed a generalized form of the Ginstling-Brounshtein model and have discussed limitations related to the boundary conditions for this model. The reaction between manganese oxide (Mn_3O_4) and sodium carbonate was shown to follow the D4 model [138].

If solid particles are assumed to be cylindrical, and diffusion occurs radially through a cylindrical shell with an increasing reaction zone, a two-dimensional diffusion

(D2) model can be derived. The D2 model can be derived using the same general approach used for the D3 model. For a cylindrical particle, Eq. (131) is defined as:

$$x = R(1 - (1 - \alpha)^{1/2}) \quad (143)$$

If the Jander's approach is followed, the resulting equation is

$$(1 - (1 - \alpha)^{1/2})^2 = k't \quad (144)$$

Where, $k' = k/R^2$. Equation (144) is not the D2 model usually cited in the literature. The usual D2 model is derived following the Ginstling-Brounshtein approach. The steady-state solution of Fick's first law for radial diffusion in a cylinder is [139]:

$$C_{(r)} = \frac{C_1 \ln(b/r) + C_2 \ln(r/a)}{\ln(b/a)} \quad (145)$$

Where $C(r)$ is the reactant concentration at a particular value of r ($a < r < b$), C_1 is the concentration of the diffusing species at surface $r=a$ and C_2 is the concentration of the diffusing species at surface $r=b$. The reaction at the interface is assumed to occur at a much faster rate than diffusion making $C_1 \approx 0$. Therefore, Eq. (145) becomes:

$$C_{(r)} = \frac{C_2 \ln(r/a)}{\ln(b/a)} \quad (146)$$

Taking the derivative of the above equation with respect to r at $r=a$ gives:

$$\left. \frac{dC}{dr} \right|_{r=a} = \frac{C_2}{a \ln(b/a)} \quad (147)$$

According to Figure 16, $a=R-x$ and $b=R$, therefore, Eq. (147) becomes:

$$\frac{dC}{dr} = \frac{C_2}{(R-x) \ln(R/(R-x))} \quad (148)$$

Substituting Eq. (148) into (138) gives:

$$\frac{dx}{dt} = \frac{k}{(R-x)\ln(R/(R-x))} \quad (149)$$

Where $k=DC_2/\varepsilon$. Substituting for the value of x in Eq. (149) with x from Eq. (143) and rearranging gives:

$$\frac{dx}{dt} = -\frac{k}{(1-\alpha)^{1/2} \ln(1-\alpha)^{1/2}} \quad (150)$$

The derivative of Eq. (143) is:

$$dx = \frac{R}{2(1-\alpha)^{1/2}} d\alpha \quad (151)$$

Substituting Eq. (151) into Eq. (150) and rearranging gives:

$$\frac{d\alpha}{dt} = -\frac{k'}{\ln(1-\alpha)} \quad (152)$$

Where $k'=4k/R^2$. Equation (152) is the differential form of the D2 model. The integral form (Table 1) of the D2 model can be obtained by separating variables and integrating Eq. (152).

Order-based (F) models

Order-based models are the simplest models as they are similar to those used in homogenous kinetics. In these models, the reaction rate is proportional to concentration, amount or fraction remaining of reactant(s) raised to a particular power (integral or fractional) which is the reaction order. Some kinetic analysis methods force data into an order-based model which may not be appropriate [72, 95]. Order-based models are derived from the following general equation:

$$\frac{d\alpha}{dt} = k(1-\alpha)^n \quad (153)$$

Where, $d\alpha/dt$ is the rate of reaction, k is the rate constant and n is the reaction order.

If $n = 0$ in Eq. (153), the zero-order model (F0/R1) model is obtained and Eq. (153) becomes,

$$\frac{d\alpha}{dt} = k \quad (154)$$

After separating variables and integrating, Eq. (154) becomes:

$$\alpha = kt \quad (155)$$

If $n=1$ in Eq. (153), the first-order model (F1) model is obtained and Eq. (153) becomes,

$$\frac{d\alpha}{dt} = k(1-\alpha) \quad (156)$$

Separating variables and integrating Eq. (156) leads to the first-order integral expression:

$$-\ln(1-\alpha) = kt \quad (157)$$

The first-order model, also called the Mampel model [140, 141], is a special case of the Avrami-Erofeev (A) models where $n=1$. Similarly, second-order ($n=2$) and third-order ($n=3$) models can be obtained (Table 1). Lopes et.al. [142] have shown that decomposition of gadolinium(III) complexes follows a zero-order model. Thermal oxidation of porous silicon [143] and desorption of 2-phenylethylamine (PEA) from silica surfaces [144] were shown to follow a first-order model.

Summary

This chapter has summarized the assumptions and mathematical derivation of the most commonly used reaction models in solid-state kinetics. This review has not been exhaustive but rather representative of the common models used. Even though this review has focused on reactions involving weight loss ($A_{(s)} \rightarrow B_{(s)} + C_{(g)}$), many of the models are applicable to other solid-state reactions where, for example, evolution or consumption of heat is measured. Hopefully, this review has demonstrated that solid-state kinetic models have a theoretical physical meaning and are not merely based on goodness of fits of complex mathematical expressions to data.

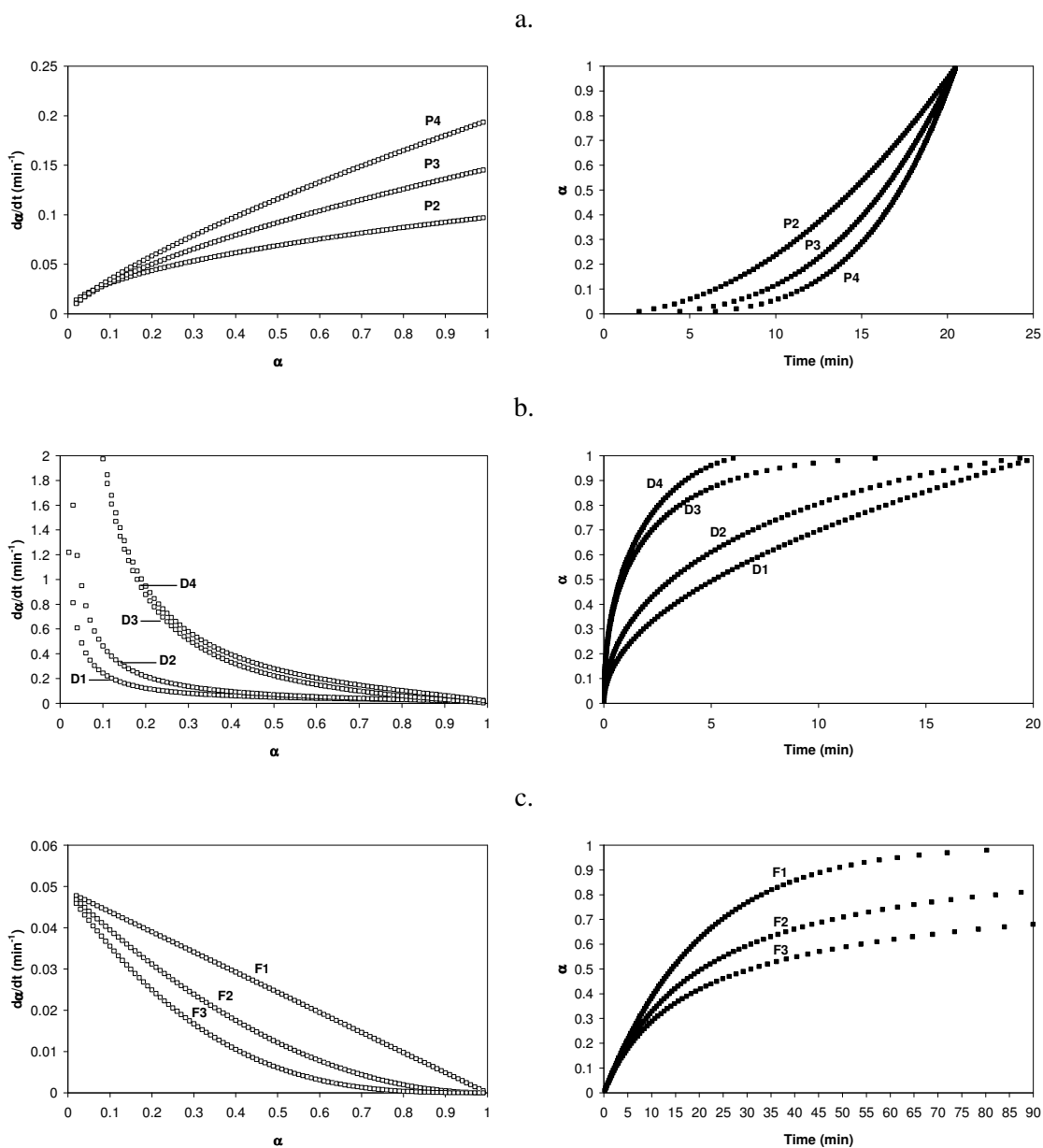
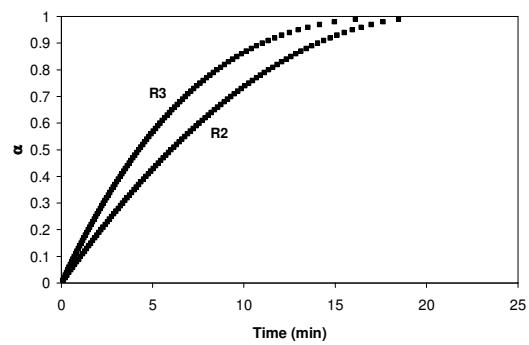
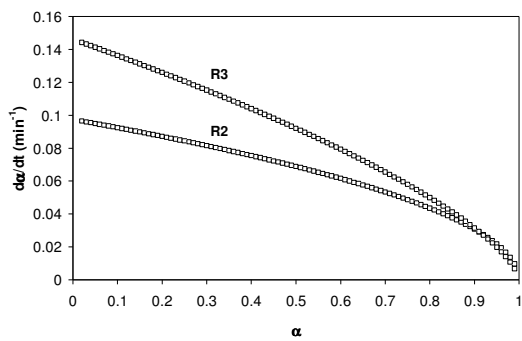
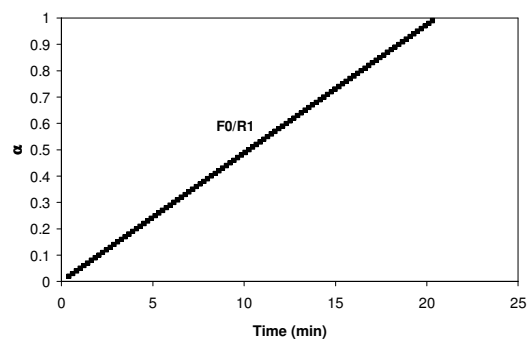
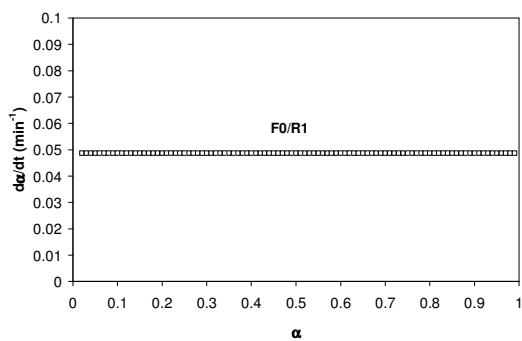


Figure 9. Isothermal $d\alpha/dt$ -time and α -time plots for solid-state reaction models (Table 1); data simulated with a rate constant of 0.049 min^{-1} : a, acceleratory; b–d, deceleratory; e, constant; f, sigmoidal.

d.



e.



f.

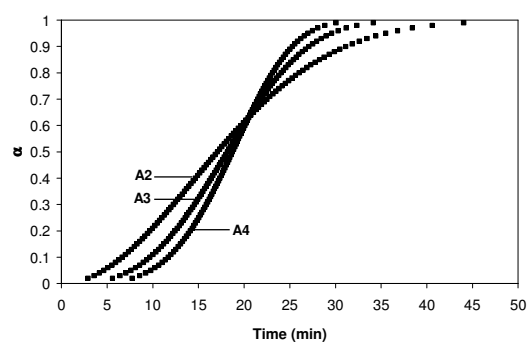
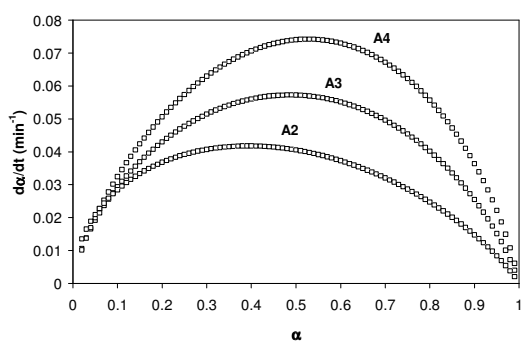


Figure 9, continued

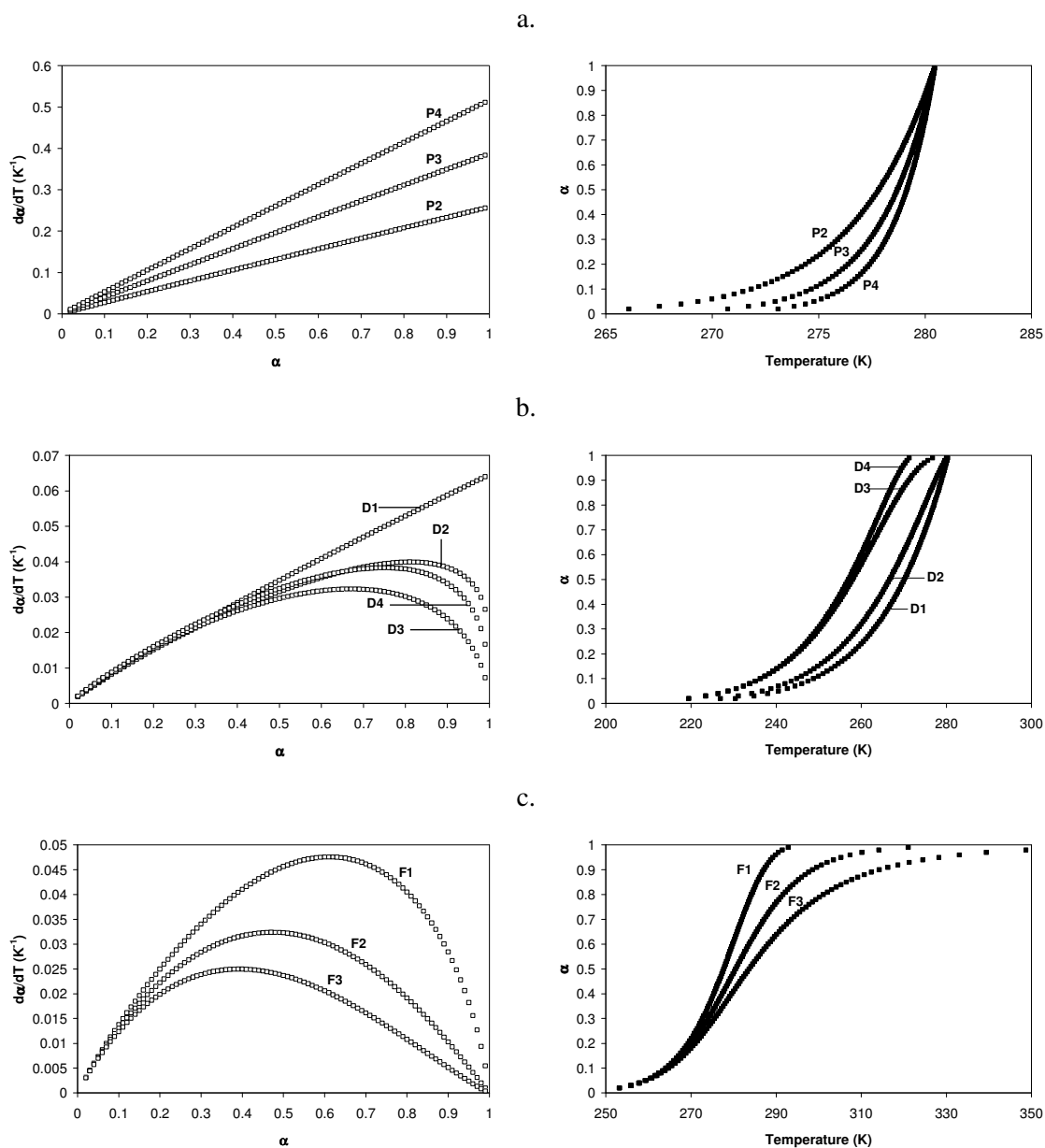
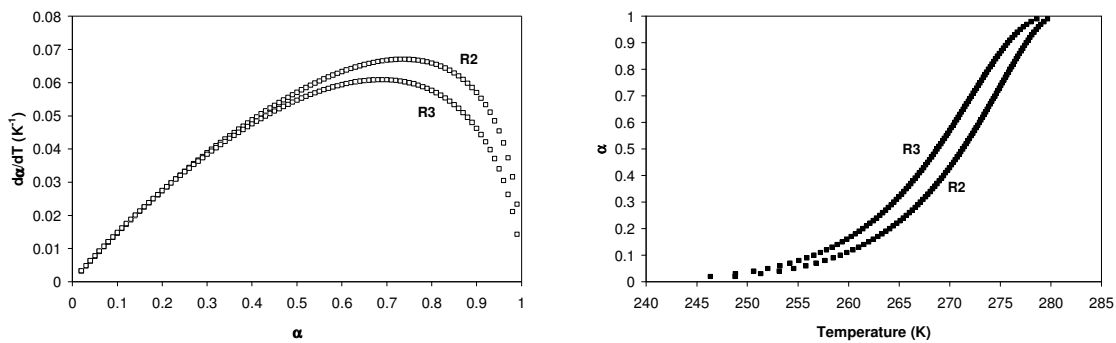
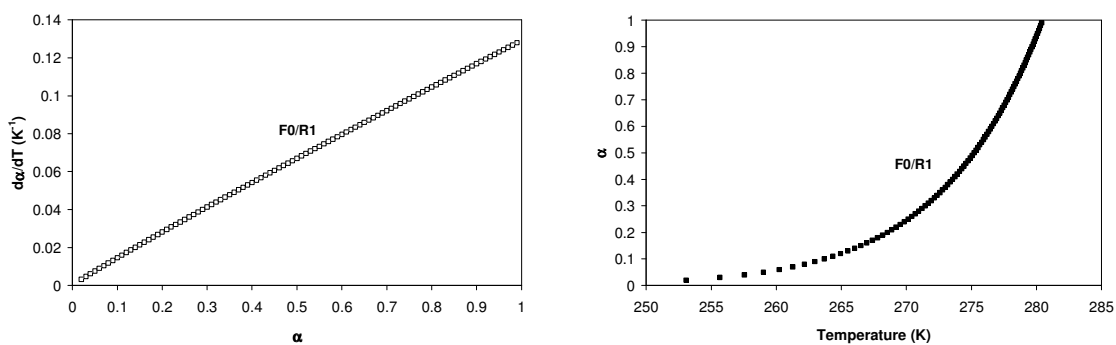


Figure 10. Nonisothermal $d\alpha/dT$ and α -temperature plots for solid-state reaction models (Table 1); data simulated with a heating rate of 10 K/min, frequency factor of $1 \times 10^{15} \text{ min}^{-1}$ and activation energy of 80 kJ/mole.

d.



e.



f.

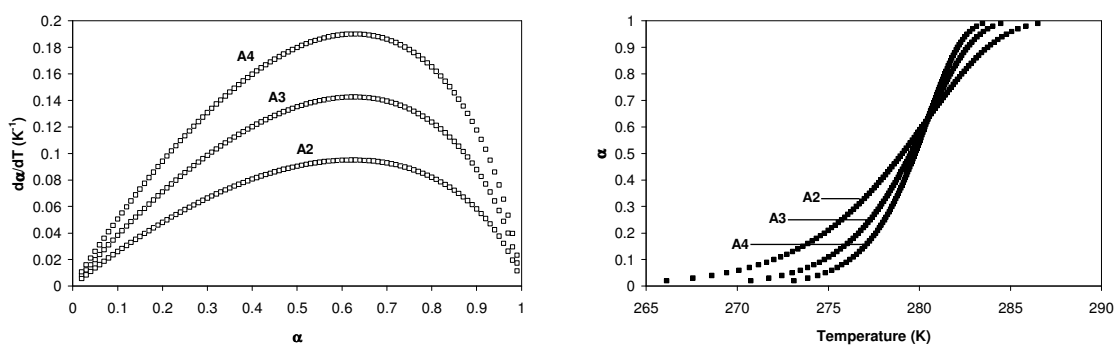


Figure 10, continued

Table 4. Mathematical expressions for nucleation rates.

Nucleation rate law	Differential form $\frac{dN}{dT}$	Integral form N
Exponential ¹	$k_N N_0 e^{-k_N t}$	$N_0 (1 - e^{-k_N t})$
Linear ¹	$k_N N_0$	$k_N N_0 t$
Instantaneous ¹	∞	N_0
Power ²	$D\beta t^{\beta-1}$	Dt^β

¹ Single-step nucleation.

² Multi-step nucleation.

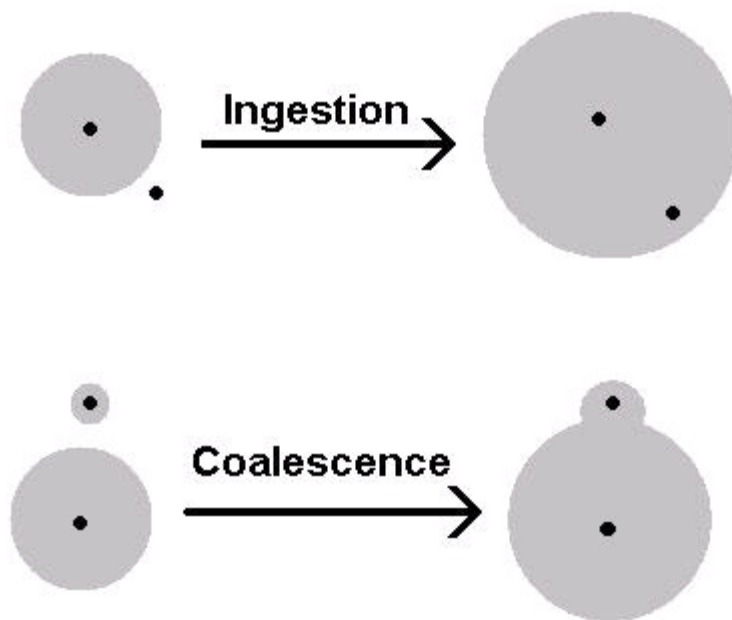


Figure 11. Two types of nuclei growth restrictions: black dots are nucleation sites and shaded areas are nuclei growth regions.

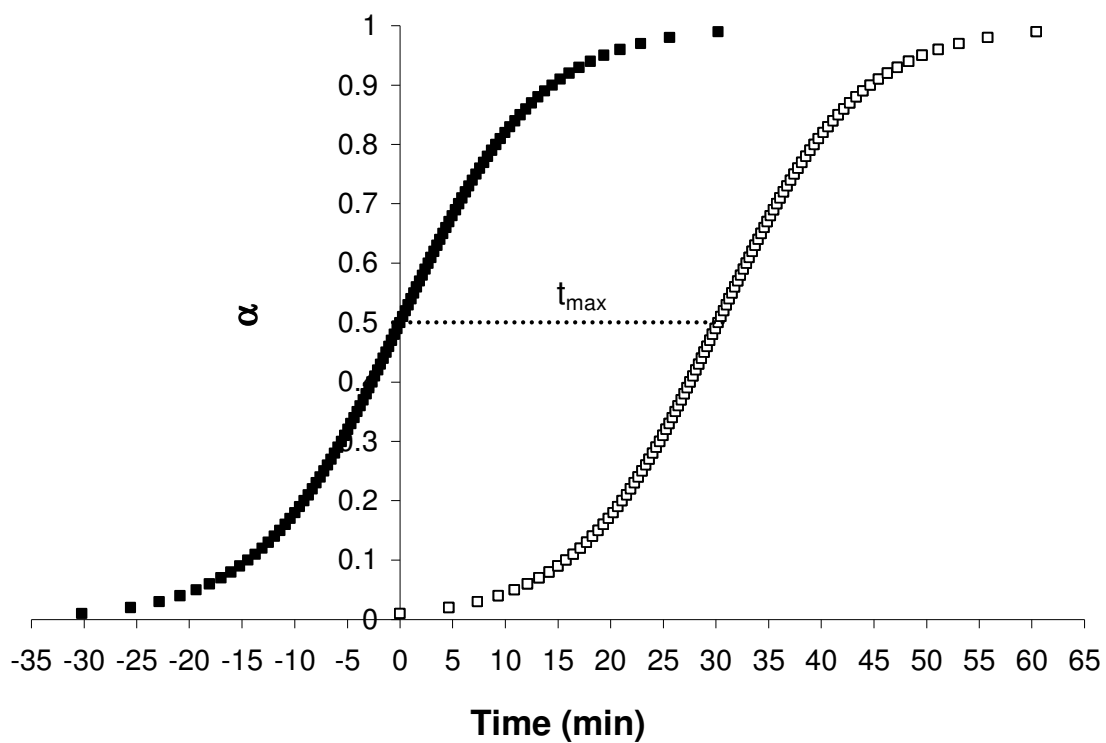


Figure 12. Isothermal α -time plots for the Prout-Tompkins reaction model (Table 1); data simulated with a rate constant of 0.152 min^{-1} : ■, data simulated according to Eq. (110); □, data simulated according to Eq. (109) where $c = t_{\max}$ (30.21 min.).

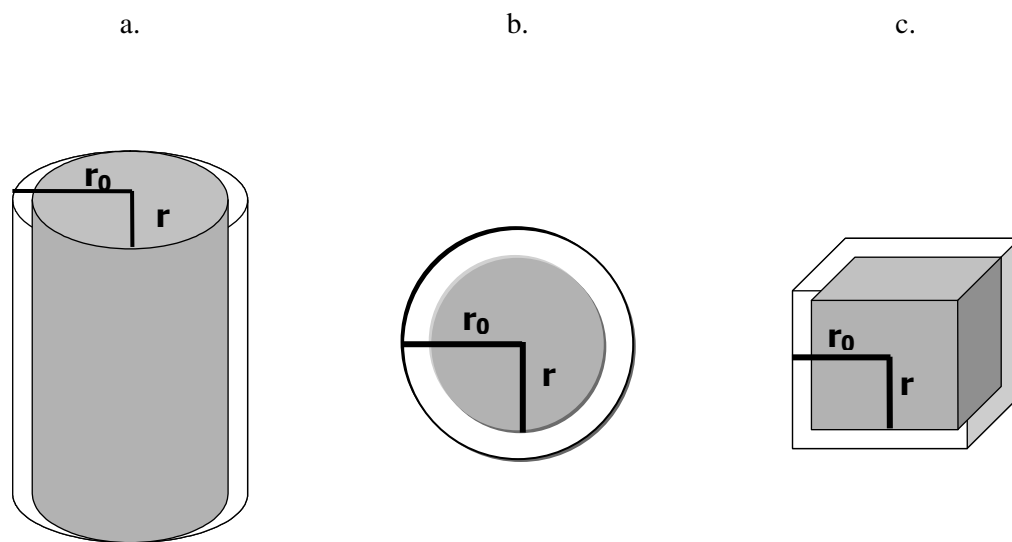


Figure 13. Geometrical crystal shapes: a, cylinder; b, sphere and c, cube.

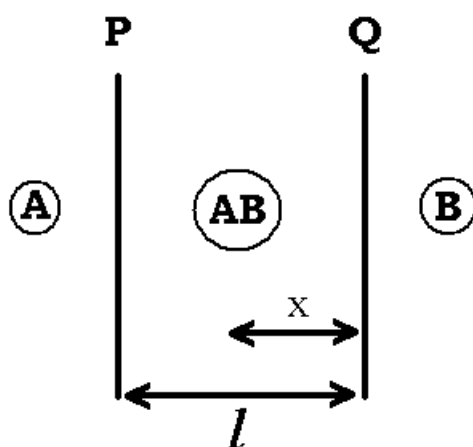


Figure 14. One-dimensional diffusion through a flat plane [133]. A and B are reactants, AB is the product interface, l is the thickness of the interface AB and x is the distance measured from interface Q into AB.

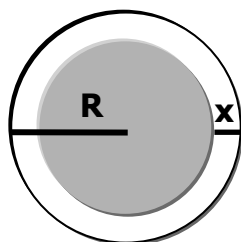


Figure 15. Schematic representation of a spherical particle reaction.

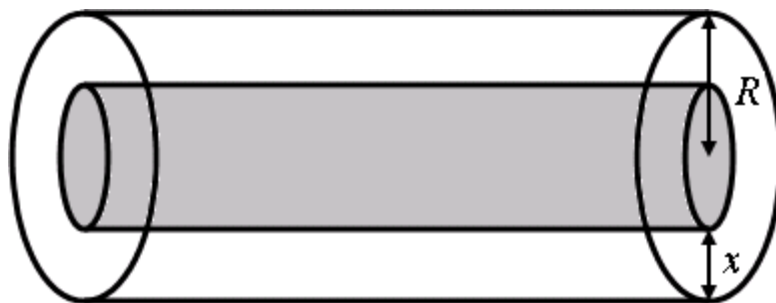


Figure 16. Schematic representation of a cylindrical particle reaction.

CHAPTER 3

EXPERIMENTAL METHODS

Solvates: description and identification.

A solvate crystal form (i.e., pseudopolymorphism) is a form in which solvent molecules (guest molecules) occupy specific positions within the crystal structure (host molecules). Solvates are usually generated during processing or purification of the crystal. Therefore, any solvent can be incorporated in a crystal during recrystallization, hydrates are usually the most common solvates as water is a common solvent in many purification systems. Solvent molecules usually exist in stoichiometric ratios with respect to the host molecules in solvates. Desolvation reactions are characterized by the removal of solvent molecules from the crystalline solvate below its melting point [7]. These reactions are best characterized by gravimetric analysis and/or microscopy. In this work, solvates were identified by:

1. Thermogravimetric analysis – weight loss with heating showed a stoichiometric ratio of a solvent to drug.
2. Hot stage microscopy – observed crystal changes (crystal fracture, changes in opacity or crystal movement [7]) during heating demonstrated a crystal transformation.

Thermal analysis (TGA and DSC) was also conducted on the parent drug (non-solvate), to show the lack of thermal history prior to melting.

Drug solvate screening

Many drug-solvate systems have been reported in the literature [145, 146], however, only a limited number of these systems have interesting characteristics. Characteristics of interest in a drug-solvate system include [147]:

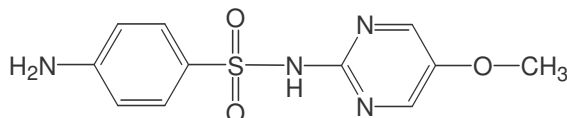
1. Mixed solvate systems, such as doxycycline hydrochloride [147] which forms a mixed ethanol–water solvate (i.e., hyclate) or triamterene [148] which forms mixed solvates of dimethylformamide and water.
2. Drugs with multiple solvates of different drug:solvent stoichiometries of the same drug and solvent such as the ouabain [149] and scopolamine HBr [150] hydrate systems.
3. Solvate polymorphism in which the drug-solvate of one stoichiometry shows two or more different crystal structures, such as the amiloride HCl [151] or nitrofurantoin hydrates [152].
4. Solvates that desolvate to give an amorphous form of the drug such as the carbamazepine hydrate [153].
5. Drug solvates having many structurally similar solvates, such as: cortisone acetate [147], erythromycin [154], spironolactone [155, 156] and sulfameter [157] solvates.

Solvates should be stable enough at room temperature for kinetic analysis to be performed. For example, the onset of desolvation should be relatively high (i.e., above room temperature) such that the solvate does not lose solvent molecules during preparation or storage.

Table 5 lists several drugs that were screened for solvate formation. Table 6 lists the commercial sources and batch/lot numbers of most chemicals used in this work.

The sulfameter solvate system

Sulfameter (structure below) was found to be the most suitable drug for kinetic analysis because it formed solvates that met the requirements for desolvation kinetic studies.



Sulfameter (5-methoxysulfadiazine)

MW – 280.3

Table 7 lists solvents screened for sulfameter solvate formation and Table 8 shows the drug:solvent stoichiometric ratios of some of the sulfameter solvates obtained. For solvents screened, guest molecules (i.e., solvents) were changed but the host molecule (sulfameter) was not, an attempt was made to change the host to other structurally similar structures (Table 9) and study the kinetics of desolvation of these new structures for the same guest molecules and compare it to that obtained from sulfameter. Results showed that although minimal changes were done in the structure, solvate forming ability and other physical properties such as solubility dramatically changed, therefore, each host structure should be explored as a separate system and a relationship between desolvation of structurally similar compounds can not be directly deduced.

Solvate preparation

Solvates were prepared by recrystallization from the neat solvents. A specific weight of drug (~ 0.5 g) was dissolved in an Erlenmeyer flask in a suitable volume of solvent and heated to the boiling point of the solvent. More solvent was then added drop wise until the drug completely dissolved and a saturated solution was formed at the boiling point. The solution was left to cool at room temperature and crystals formed. The precipitated solid was dried under suction on a Büchner funnel for 1–3 minutes. The solid was sieved to obtain a powder having the desired particle size. Sieved solid fractions were stored in small vials in a freezer below -10°C .

Drug and solvate characterization

Characterization methods

Drugs and their solvates were characterized by one or more of the following analytical methods:

1. Light microscopy.
2. Thermogravimetric analysis.
3. Differential scanning calorimetry.
4. Powder X-ray diffraction.

Light microscopy

An Olympus BX600 microscope system equipped with a Kodak MDS100 digital camera was used to examine crystal morphology under a 5X magnification.

Thermogravimetric analysis (TGA)

Thermogravimetric analysis was performed using a Perkin-Elmer TGA 7. Temperature calibration of the TGA was performed by a two-point calibration method through measuring the Curie point (C_p) of alumel ($C_p=163^\circ\text{C}$) and nickel ($C_p=354^\circ\text{C}$). The Curie point is a characteristic physical property of a metal, it represents the temperature above which the metal loses its ferromagnetic properties (i.e., the ability to spontaneously possess a net magnetization in the absence of an external magnetic field). Weight was calibrated using the supplied reference standard weight (100 mg). Nitrogen gas was used as a purge gas with a flow of 40-50 ml/min. A sample size of 3–5 mg was used for TGA analysis.

Differential Scanning Calorimetry (DSC)

Differential scanning calorimetry analysis was performed using a Perkin-Elmer DSC 7. The DSC was calibrated using indium. A sample size of 2–8 mg was used for DSC

analysis at 16 K/min. Analysis was done using open aluminum pans, a blank reference pan with the same composition to the sample pan was used in all DSC runs.

Powder X-ray diffraction (PXRD)

Powder X-ray diffraction was performed using a Bruker D-5000 diffractometer with a 2θ range of 5–40° (step size= 0.02°, step time = 2 sec and 50 kV, 30 mA). The wavelength used was 1.54056 Å (CuK α) which was incorporated in the Bragg equation to calculate crystal d-spacings.

Sulfameter characterization

Sulfameter was obtained from Sigma Chemical Co. (lot no. 107F0910). The drug was analyzed (as supplied) by thermogravimetry (Figure 24a), DSC (Figure 24b), PXRD (Figure 25, Table 10). Thermal analysis (Figure 24) confirmed the absence of any thermal events prior to melting (m.p. 212°C). Therefore, any event occurring for the solvated forms is expected to be from the desolvation reaction. Many solvents were screened for whether they formed solvates with sulfameter (Table 7). A total of 12 solvates were prepared from the 35 solvents investigated, seven solvates (Table 8) were further characterized and investigated kinetically; their stoichiometries were 1:1, as determined by TGA. Morphology of sulfameter and its seven solvates described in Table 8 is shown in Figure 26.

Sulfameter tetrahydrofuran solvate characterization

The tetrahydrofuran solvate of sulfameter was analyzed by TGA (Figure 27a), DSC (Figure 27b) and PXRD (Figure 28, Table 11). Thermal analysis shows that desolvation occurs in a single step with a maximum rate at 91°C.

Sulfameter dioxolane solvate characterization

The dioxolane solvate of sulfameter was analyzed by TGA (Figure 29a), DSC (Figure 29b) and PXRD (Figure 30, Table 12). Thermal analysis shows that desolvation occurs in a single step with a maximum rate at 89°C.

Sulfameter oxane solvate characterization

The oxane solvate of sulfameter was analyzed by TGA (Figure 31a), DSC (Figure 31b) and PXRD (Figure 32, Table 13). Thermal analysis shows that desolvation occurs in a single step with a maximum rate at 96°C.

Sulfameter dioxane solvate characterization

The dioxane solvate of sulfameter was analyzed by TGA (Figure 33a), DSC (Figure 33b) and PXRD (Figure 34, Table 14). Thermal analysis shows that desolvation occurs in a single step with a maximum rate at 104°C.

Sulfameter oxepane solvate characterization

The oxepane solvate of sulfameter was analyzed by TGA (Figure 35a), DSC (Figure 35b) and PXRD (Figure 36, Table 15). Thermal analysis shows that desolvation occurs in a single step with a maximum rate at 103°C.

Sulfameter chloroform solvate characterization

The chloroform solvate of sulfameter was analyzed by TGA (Figure 37a), DSC (Figure 37b) and PXRD (Figure 38, Table 16). Thermal analysis shows that desolvation occurs in a single step with a maximum rate at 91°C.

Sulfameter bromoform solvate characterization

The bromoform solvate of sulfameter was analyzed by TGA (Figure 39a), DSC (Figure 39b) and PXRD (Figure 40, Table 17). Thermal analysis shows that desolvation

occurred in two overlapping steps (peaks at 70°C and 110°C) as shown by the derivative TGA curve (DTG, Figure 39a).

Particle size effect on desolvation TGA analysis

Controlling experimental variables is important for solid-state kinetics. One such variable is particle size. Uncontrolled particle size can have a dramatic impact on TGA thermograms. Most importantly, lack of particle size control can lead to problems for data reproducibility, which significantly affects kinetics analysis (Chapter 4). Particle size effects were studied for the desolvation of sulfameter dioxane solvate both isothermally and nonisothermally (Figures 41–44). The results clearly show the effect of particle size control on data reproducibility which is further verified by the nonisothermal desolvation of the sulfameter oxane solvate (Figure 45).

Kinetic analysis of the desolvation reaction

Desolvation kinetics was evaluated isothermally and nonisothermally from several TGA thermograms. Isothermal TGA runs were performed at temperatures of 50, 55, 60, 65 and 70°C. Nonisothermal runs were performed at heating rates of 1, 2, 4, 8 and 16 K/min. Kinetic analysis methods have been described and derived previously (Chapter 1). Before these methods were applied, some pretreatment of the data was necessary to transform it into a suitable form for analysis. Kinetic analysis was in three steps:

1. Data collection.
2. Data pretreatment.
3. Data analysis.

Data collection

Thermal data were collected by the Perkin-Elmer v.4.0 thermal analysis software with a data set size of at least 3000 points for each TG run. The data were then exported as ANF files (Non-Pyris software files) which were transformed by the Windows-based

Perkin-Elmer Pyris software (version 5.0) to TGD files (Pyris software TGA files) which were then exported by the Pyris software as ASCII files each containing time, temperature and weight at each data point. ASCII files were imported into Microsoft Excel[®] to obtain spreadsheet formats which were further processed.

Data pretreatment

Data pretreatment involved two steps:

1. Data set reduction,
2. Determination of actual heating rates (nonisothermal reactions) and actual temperatures (isothermal reactions).

Data size reduction

The first step of data analysis was to convert each Excel[®] thermogram file of data points (time, temperature and weight) to one containing time, temperature and α (conversion fraction) according to Eq. (6). The larger set of α points was then reduced to one containing 99 points corresponding to α of 0.01-0.99 in 0.01 increments. This transformation was to obtain a standard set of α values for all TG runs which would enable calculation of kinetic parameters for the same α value across multiple thermograms (i.e., isoconversional), as described earlier (Chapter 1). To achieve this data reduction, three approaches can be pursued:

- a. Perform nonlinear regression on the TG curve to obtain a nonlinear equation that could be used to generate 99 α data points from the fitted equation.
- b. Perform multiple linear regressions (MLRs) over small regions of α values (i.e., linear fits at 0.01 α increments). Thus, 99 linear equations would result which could be used to generate 99 α points.
- c. Reduce (i.e., truncate) the number of data points in each file. This is done by rounding down (ROUND^{DOWN} function in Excel) each α in the original file to two significant figures, and taking the α value that rounds down to the next

0.01 increment, thus ignoring repeated α values (Table 18) until the next 0.01 increment in α is reached.

Of the above three methods, the last two (b and c) were tested on dehydration thermograms of calcium oxalate monohydrate at three heating rates: 2, 4 and 8 K/min (Figure 46).

According to Figure 46, both the MLR and truncation approaches gave the same results (points for both methods coincide). However, the MLR approach involves more computation, is slower and more sensitive to errors resulting from insufficient data points. Therefore, the truncation method was used in data analysis for pretreatment of all TGA data for kinetic analysis.

Calculating the actual nonisothermal heating rates.

The value of the heating rate is important in calculating kinetic parameters from non isothermal data in solid-state kinetics where errors in heating rate values could lead to erroneous kinetic parameters. One of the major sources of error in kinetic analysis involves miscalculating the heating rate (see Chapter 4). This is because the programmed heating rates are generally assumed to be the actual heating rates, whereas, in reality, this may not be the case as there are many factors (i.e., self-heating/cooling, purge gas cooling) that would change the actual heating rates of nonisothermal thermograms. To study this, thermograms for several linear heating rates were obtained from runs of empty TG pans and pans containing several compounds (Table 19). Actual heating rates were calculated from the slope of the linear relationship between time and temperature according to Eq. (17) as shown in Figure 47 for a nonisothermal run of an empty TG pan at 10 K/min giving an observed heating rate of 10.29 K/min. Results in Table 19 show that the programmed and calculated heating rates deviate from one another and the deviation depends on the type of compound heated, its quantity and the heating rate.

Calculating the actual isothermal temperature

The actual value of the isothermal temperature is important in kinetic analysis; the programmed temperature is usually different from the actual one which causes some errors in kinetic analysis if the incorrect value is used (see Chapter 4). The actual temperature was calculated by averaging the measured temperatures at which a significant rate of weight loss occurs (Figure 48).

The isothermal desolvation thermogram of sulfameter-tetrahydrofuran solvate ($T=55^{\circ}\text{C}$, Figure 48), where weight is plotted as a function of temperature, can be divided into two regions: A and B. Region A represents the heat up region and the time in this region is considered the heat up time (t_0), while region B is the actual experimental region. Averaging measured temperatures in region B gives the actual experimental temperature that should be used in kinetic analysis (53.61°C for the thermogram in Figure 48) rather than using the programmed value of 55°C .

Data analysis of pretreated data

Data analysis was performed with Microsoft Excel[®] for all kinetic analysis methods (Chapter 1). Direct calculations were used for the conventional, standard, Friedman, Ozawa-Flynn-Wall (OFW) and Coats-Redfern methods. Other methods such as the Vyazovkin and advanced isoconversional (AIC) methods required use of Excel's Solver[®] tool; the Solver[®] was used to iteratively find solutions for equations that required minimization (Eqs. (59) and (63)). Parameters used for the Solver[®] are shown in Figure 49.

Data simulation

Data simulation involved generating α , time (isothermal) or α , temperature (nonisothermal) data points for particular values of A , E_a and $g(\alpha)$ (model) in reaction rate laws (Eqs. (16) and (22)). A specific random error was usually introduced to time or temperature values. Percent random errors introduced in temperature was based on a

percentage of the temperature in °C. Data simulation was used to prove a hypothesis (Chapter 4) or to validate model-fitting results (i.e., curve reconstruction, see Chapter 5).

Isothermal simulation

Equation (16) can be rearranged to:

$$t = \frac{g(\alpha)}{Ae^{-\frac{E_a}{RT}}} \quad (158)$$

Isothermal simulation was performed by assigning values to the above parameters ($g(\alpha)$, E_a , A and T) and calculating the time (t) for α values between 0.01–0.99.

Nonisothermal simulation

Equation (22) can be rearranged to:

$$\Psi = \left| g(\alpha) \frac{\beta R}{AE_a} - p(x) \right| \quad (159)$$

Where, Ψ is a constant. The exponential integral ($p(x)$) in Eq. (159) was approximated by the 3rd degree Senum-Yang approximation (Chapter 1). Nonisothermal simulation was performed by assigning values to the above parameters ($g(\alpha)$, E_a , A and β) and using Microsoft Excel's Solver, the value of T at each α between 0.01-0.99 which minimizes Ψ was calculated. Parameters for the Solver utility are shown in Figure 49.

Validation of activation energy calculations

The activation energy represents the theoretical energy barrier that must be overcome for a reaction to occur. For physical processes, such as evaporation or sublimation, this could equal the enthalpy change (ΔH) of the process (i.e., ΔH_{vap} or ΔH_{sub}). Using TGA to study the kinetics of such phase transformations could serve as a means of validating activation energy values obtained by thermokinetic methods if both

E_a and ΔH values were comparable for such basic physical processes. Ideally, isoconversional methods would be a good candidate for such analysis since no model is assumed for the process.

Evaporation activation energies were calculated for several compounds by Vyazovkin's isoconversional method (Figure 50). Isoconversional plot shapes were deceleratory (i.e., not flat, Figure 50) which is expected for nonisothermal runs because enthalpies of vaporization are inversely related to temperature. Therefore, apparent activation energies are obtained by averaging E_a values calculated for α of 0.1–0.9.

Table 20 lists literature enthalpies of vaporization ΔH_{vap} compared to averaged evaporation activation energies (E_a) obtained from Figure 50 for five compounds. Results show a general agreement between enthalpy change and averaged E_a values for the compounds (Table 20), this general agreement is significant because it may give physical meaning to activation energies generated for desolvation kinetics. This procedure introduces another method of measuring enthalpies of vaporization. However, this method can not replace the more accurate physical methods for measuring vaporization enthalpies (i.e., calorimetry) because isoconversional methods are associated with many errors (see Chapter 4). Further refinements in both experimental procedures and data analysis are needed for TGA results to equal those of other methods.

Table 5. Drugs screened for solvate formation.

Drug	Solvents	Results
Doxycycline HCl ^a	Water and ethanol	Studied hydrate (water+ethanol) desolvation; desolvation, degradation and melting simultaneously occurred during heating (Figure 17)
Triamterene ^a	Dimethylformamide*, water	Only dimethylformamide formed a solvate (Figure 18)
Ouabain ^b	Water*	Unstable at room temperature; dehydrates at room temperature (Figure 19)
Nitrofurantoin ^c	Water*	Procedures in Ref. [152] claims two hydrate forms, but only Form II was produced. Form I was not obtained (Figure 20)
Carbamazepine ^d	Water*	Unstable; hydrate dehydrates at room temperature (Figure 21)
Cortisone acetate ^e	Acetic acid, acetonitrile, dimethylformamide*, dioxane and propanol.	Only dimethylformamide formed a solvate (Figure 22)
Erythromycin ^e	Acetone, methylethyl ketone, ethanol, propanol, isopropanol, chloroform.	No solvates formed.
Spironolactone ^e	Methanol, ethanol, ethyl acetate, benzene*	Only benzene formed a solvate (Figure 23).
Sulfameter ^e	See Table 7	12 solvates obtained and 7 studied kinetically.

^a Example of mixed solvate systems.

^b Example of a systems with multiple drug:solvent ratios of the same drug and solvent

^c Example of a solvate polymorphism systems.

^d Example of a solvate desolvating to form an amorphous drug.

^e Example of systems having structurally related drug solvates.

* Solvate formed.

Table 6. Sources for chemicals and their batch/lot numbers.

Substance	Supplier	Batch/Lot number
Carbamazepine	Sigma Chemical	053K0599
Doxycycline HCl	Sigma Chemical	063K1572
Hydrocortisone acetate	Sigma Chemical	078H0468
Nitrofurantoin	Sigma Chemical	104K1138
Ouabain	Sigma Chemical	56H2616
Sulfasoxazole	Sigma Chemical	071K1891
Sulfadiazine	Sigma Chemical	054K0837
Sulfameter	Sigma Chemical	107F0910
Triameterine	Sigma Chemical	81K1189
Calcium oxalate monohydrate	Fluka	452439/1
Dioxane	Fisher Scientific	023029
Bromoform	Aldrich	13107T0
Dioxolane	Aldrich	06210EC and LO14921KO
Oxane	Alfa Aesar	I6160A and 10100417
Dimethylformamide	Fisher Scientific	963127
Ethanolamine	Fisher Scientific	863303
1-propanol	Fisher Scientific	716121
Tetrahydrofuran	Fisher Scientific	011510
Methanol	J.T. Baker	X29B24
Oxepane	TCI	HAN01

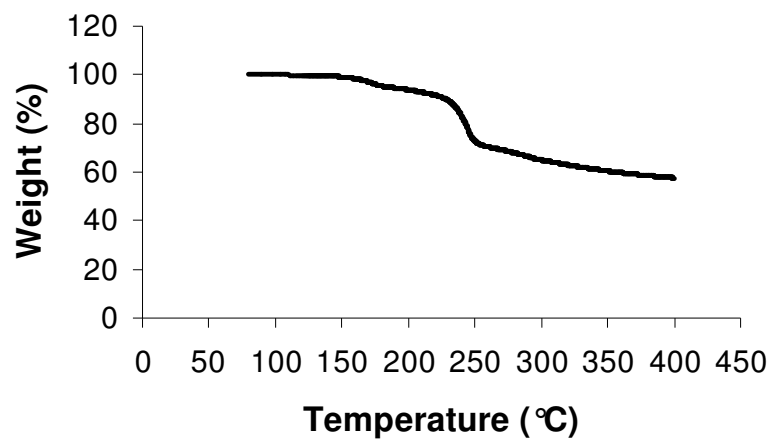


Figure 17. Desolvation TGA thermograms of doxycycline HCl hydrate at a heating rate of 5 K/min.

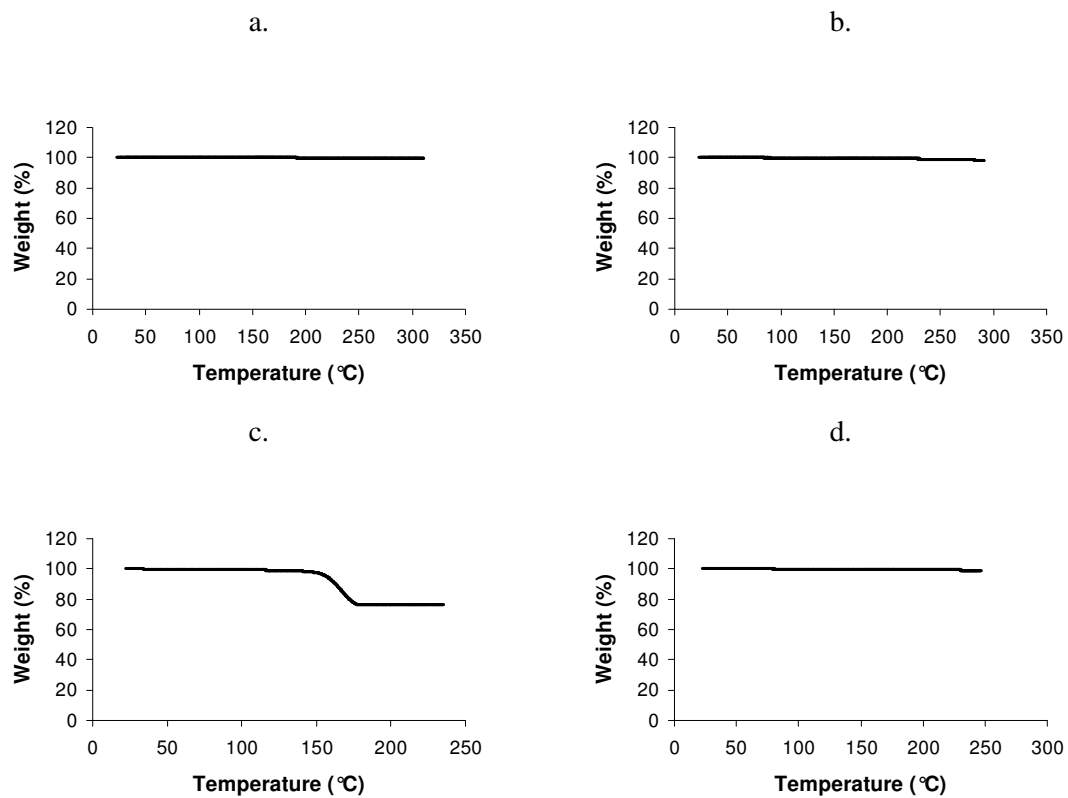


Figure 18. TGA thermograms of triamterene crystallized from different solvents: a, original material (10 K/min); b, butanol (10 K/min); c, dimethylformamide (10 K/min) and d, ethanol (20 K/min).

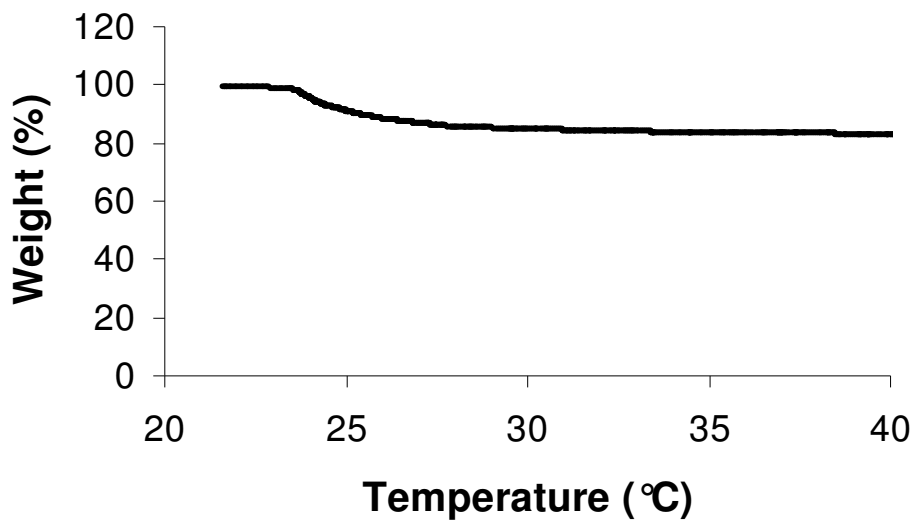


Figure 19. Dehydration TGA thermogram of ouabain octahydrate at 1K/min.

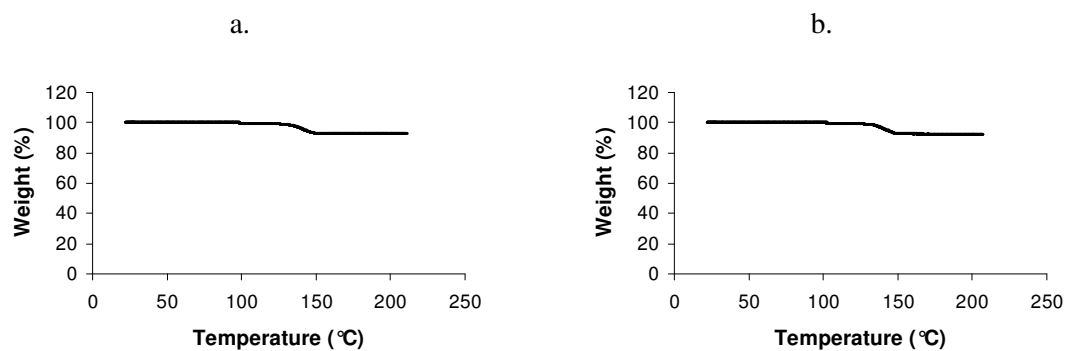


Figure 20. Dehydration TGA thermograms for two nitrofurantoin hydrates at 10 K/min, prepared according to ref. [152] to obtain: a. Form I; b. Form II.

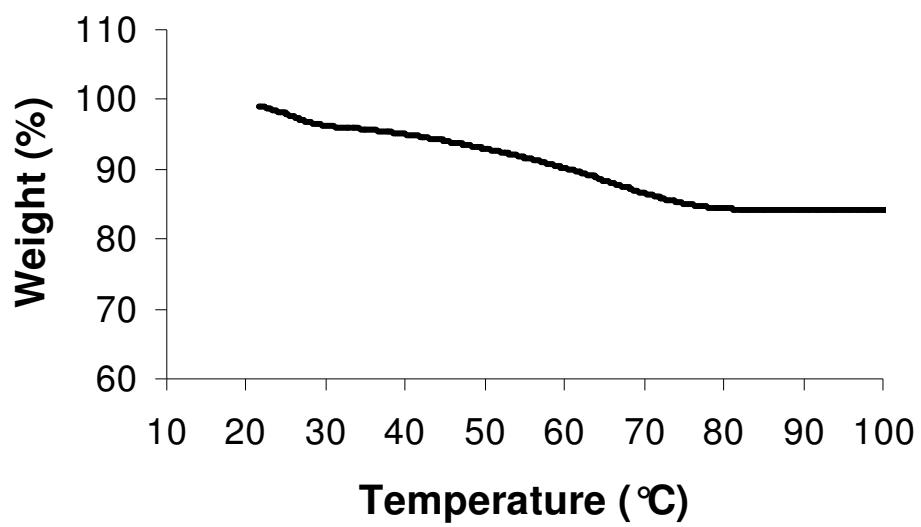


Figure 21. Dehydration TGA thermogram of carbamazepine hydrate at 16 K/min.

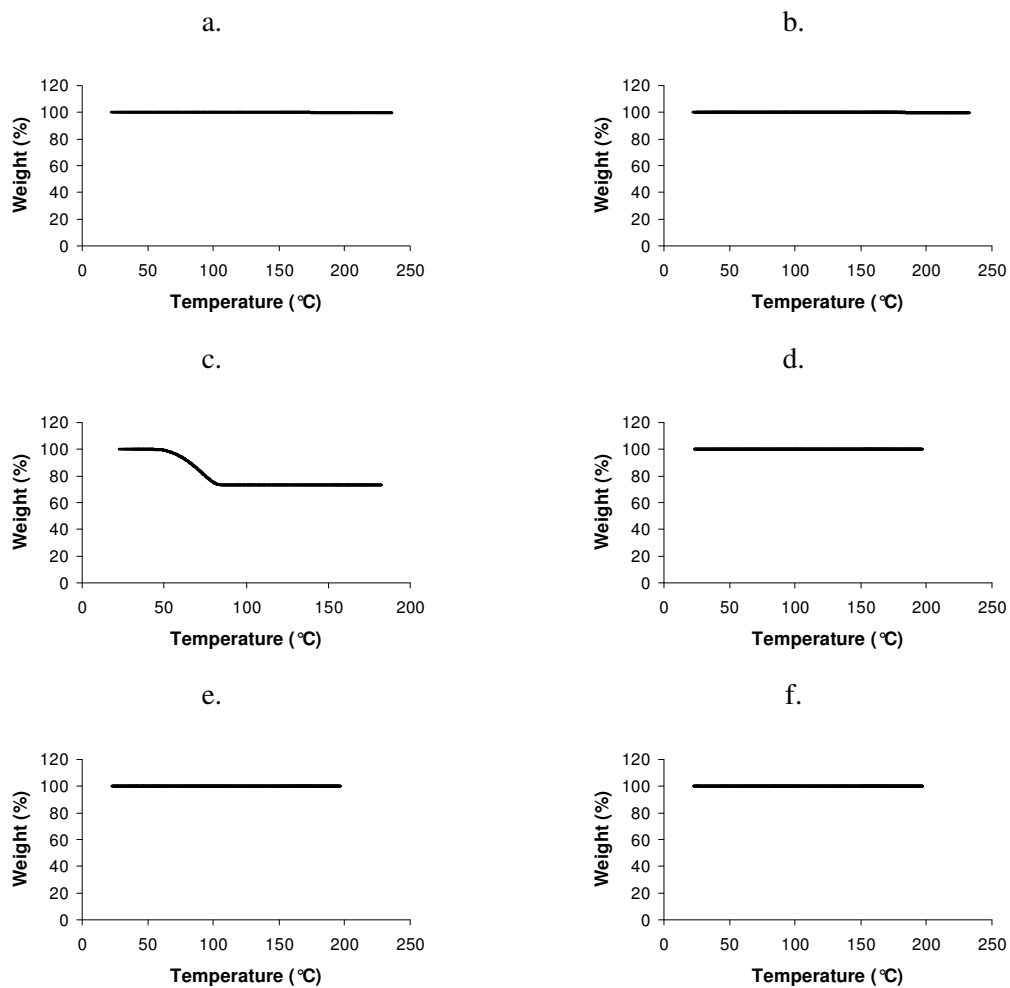


Figure 22. TGA thermograms of cortisolone acetate crystallized from different solvents: a, original material (10 K/min); b, acetonitrile (10 K/min); c, dimethylformamide (5 K/min); d, n-propanol (16 K/min); e, acetic acid (16 K/min) and f, dioxane (16 K/min).

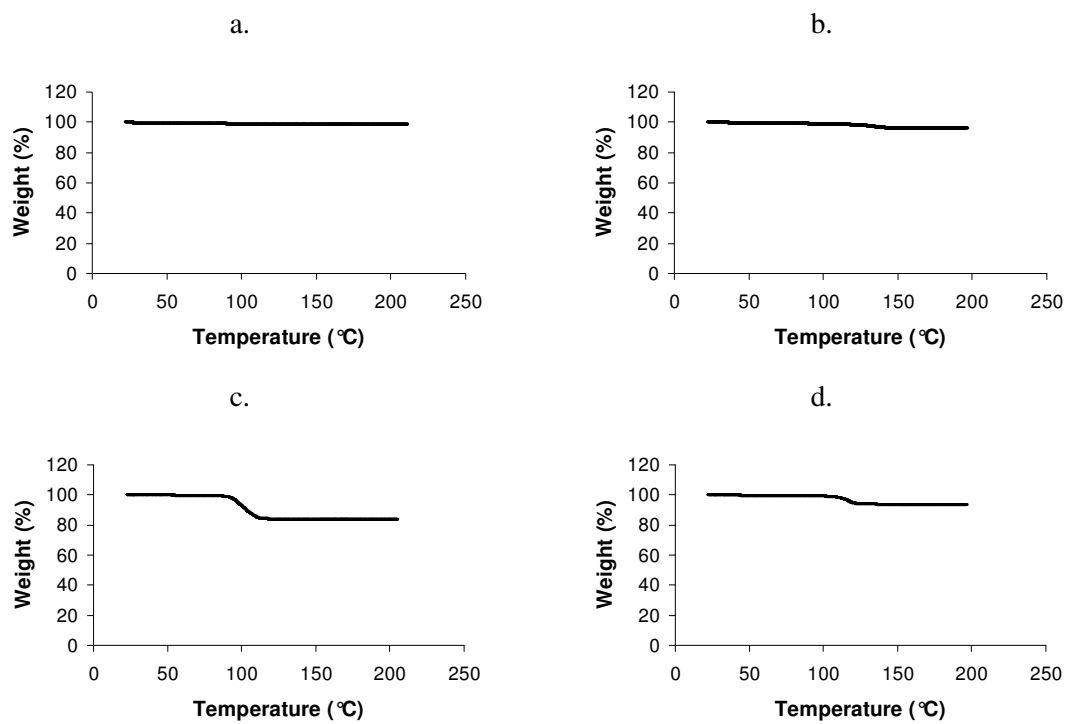


Figure 23. TGA thermograms of spironolactone crystallized from: a, methanol (10 K/min); b, ethanol (16 K/min); c, benzene (10 K/min) and d, ethyl acetate (16 K/min).

Table 7. Solvent screening for sulfameter solvate formation.

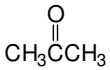
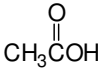
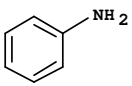
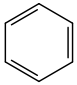
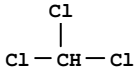
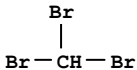
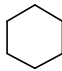
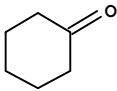
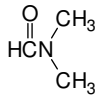
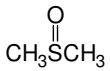
Solvent	Structure	Molecular weight	Solvate formed
Acetone		58.08	NO
Acetonitrile	$\text{CH}_3\text{C}\equiv\text{N}$	41.05	NO
Acetic acid		60.05	NO
Aniline		93.13	YES
Benzene		78.11	NO
Carbon tetrachloride	CCl_4	153.80	NO
Chloroform		119.40	YES
Bromoform		252.73	YES
Cyclohexane		84.16	NO
Cyclohexanone		98.14	NO
Diethyl ether	$(\text{C}_2\text{H}_5)_2\text{O}$	74.12	NO
Dimethylformamide		73.10	YES
Dimethylsulfoxide		78.13	NO

Table 7, continued

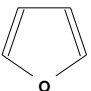
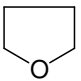
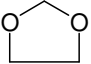
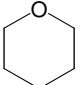
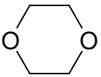
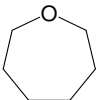
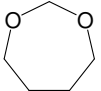
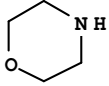
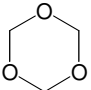
Solvent	Structure	Molecular weight	Solvate formed
Oxole		68.07	NO
Tetrahydrofuran		72.11	YES
Dioxolane		74.08	YES
Oxane		86.13	YES
Dioxane		88.11	YES
Oxepane		100.20	YES
Dioxepane		102.13	YES
Morpholine		87.12	NO
Trioxane		90.08	NO

Table 7, continued

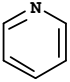
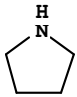
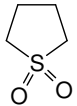
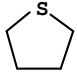
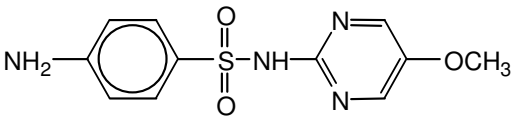
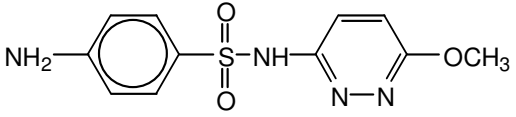
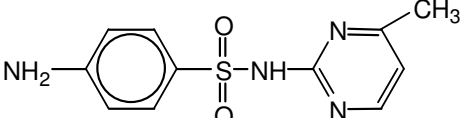
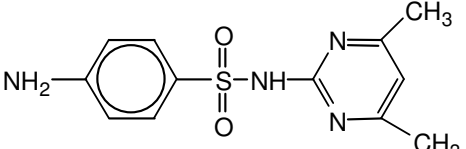
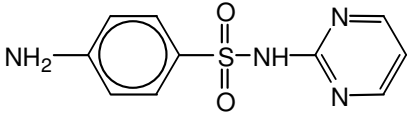
Solvent	Structure	Molecular weight	Solvate formed
Ethanol	C_2H_5OH	46.00	NO
Ethyl acetate	$CH_3\overset{O}{\parallel}COHC_2H_5$	88.11	NO
Hexane	$CH_3(CH_2)_4CH_3$	86.18	NO
Methanol	CH_3OH	32.00	NO
Methylene chloride (Dichloromethane)	CH_2Cl_2	84.93	NO
1- Propanol (n- propanol)	$H_3C-CH_2-CH_2-OH$	60.10	NO
2- Propanol (Iso- propanol)	$\begin{array}{c} OH \\ \\ H_3C-CH-CH_3 \end{array}$	60.10	NO
Pyridine		79.10	YES
Pyrrolidine		71.12	NO
Sulfolane		120.20	NO
Thiolane (Tetrahydrothiophen, Thiophane)		88.17	NO
Trichloroethylene	$\begin{array}{c} Cl \\ \\ Cl-C=CH-Cl \end{array}$	131.40	YES
Water	H_2O	18.00	NO

Table 8. Drug:solvent stoichiometries (1:1) by TGA for selected sulfamer solvates.

Solvate	% Theory (1:1)	% Actual ^a
THF	20.46	20.44 ± 0.12
Dioxolane	20.90	20.93 ± 0.20
Oxane	23.50	23.72 ± 0.07
Dioxane	23.92	23.94 ± 0.06
Oxepane	26.33	26.30 ± 0.06
Dioxepane	26.70	27.06 ^b
Chloroform	29.87	29.60 ± 0.10
Bromoform	47.41	47.42 ± 0.19

^a n=5.^b n=1.

Table 9. Solvent screening for solvate formation for various structurally related sulfonamides.

Substance	Solvents screened
 <p>Sulfameter</p>	See Table 7
 <p>Sulfamethoxypyridazine</p>	Acetone, Acetonitrile, Chloroform, Dimethylformamide, Dioxane, Ethanol, Methanol, Tetrahydrofuran, Water
 <p>Sulfamerazine</p>	Tetrahydrofuran ^a , dioxane ^a , chloroform ^a
 <p>Sulfamethazine</p>	Tetrahydrofuran, dioxane, chloroform
 <p>Sulfadiazine</p>	Dichloro methane, Dioxane ^b , Tetrahydrofuran ^b , chloroform ^a

^a Insoluble in this solvent.

^b Solvate formed.

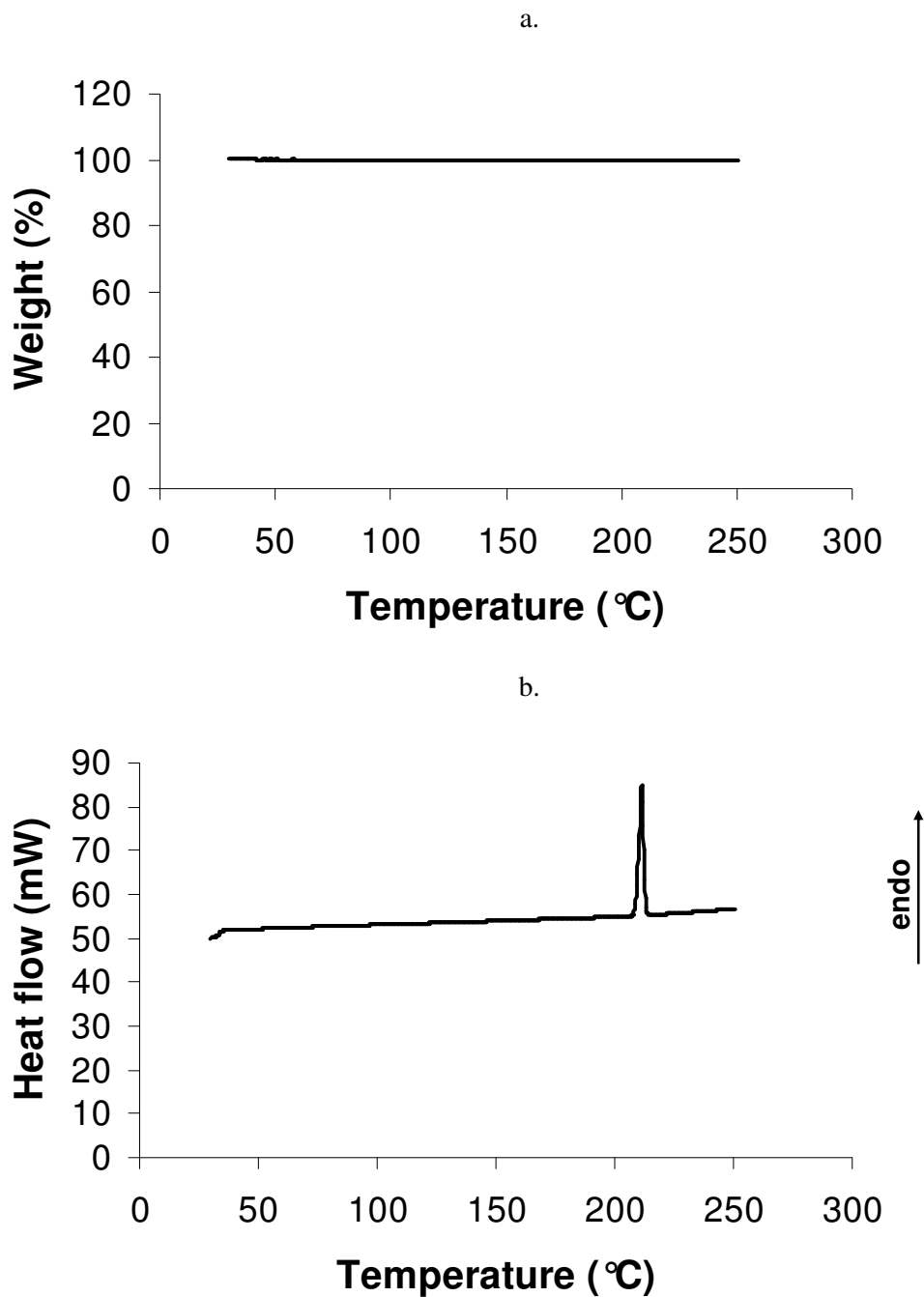


Figure 24. Thermal analysis of sulfameter from Sigma Chemical (lot no. 107F0910) by: a, TGA at a heating rate of 20 K/min and b, DSC at a heating rate of 10 K/min.

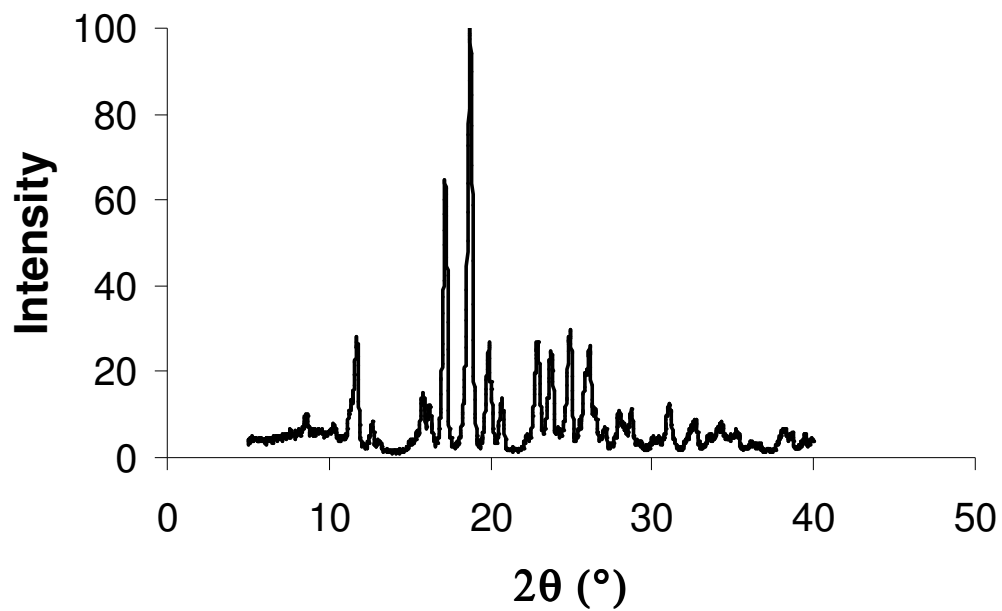


Figure 25. Powder X-ray diffraction pattern for sulfameter as supplied (Sigma Chemical, lot no. 107F0910).

Table 10. X-ray diffraction data ($I/I_0 \geq 20$) for sulfameter (Sigma Chemical, lot no. 107F0910).

d (Å)	I/I_0
7.57	28.12
5.15	64.78
4.73	100.00
4.45	26.82
3.89	26.82
3.87	27.02
3.76	22.60
3.74	24.97
3.73	20.64
3.58	27.95
3.57	29.73
3.43	20.47
3.41	24.76

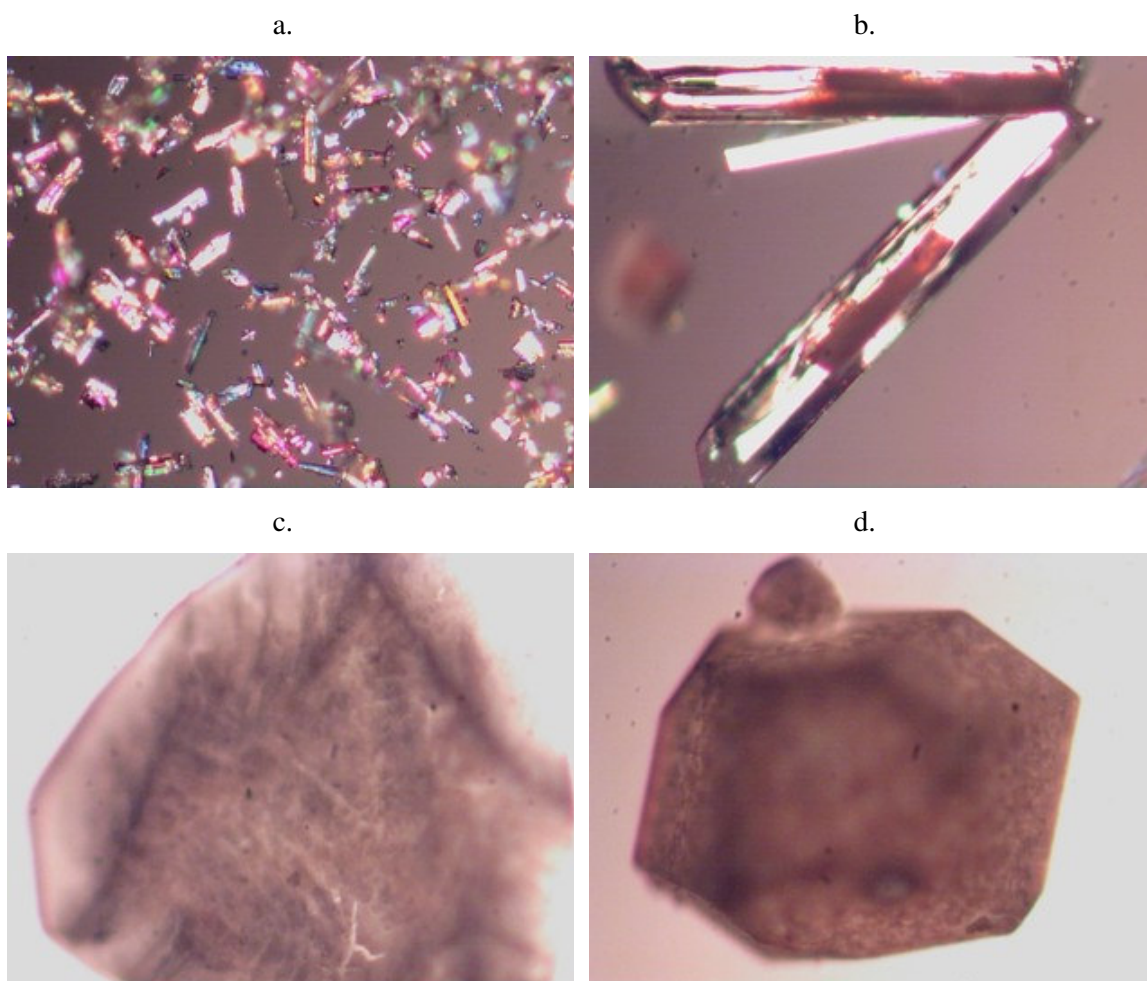
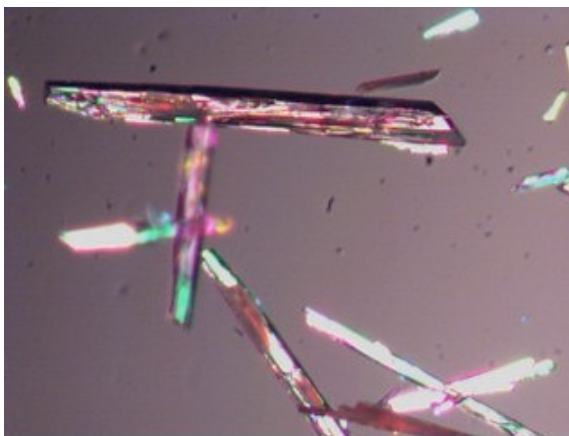
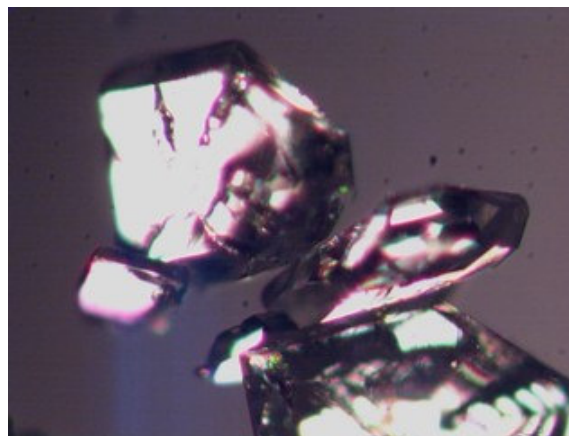


Figure 26. Light microscopy of sulfameter and different sulfameter solvates at 5X magnification: a, sulfameter; b, tetrahydrofuran; c, dioxolane; d, oxane; e, dioxane; f, oxepane; g, chloroform and h, bromoform.

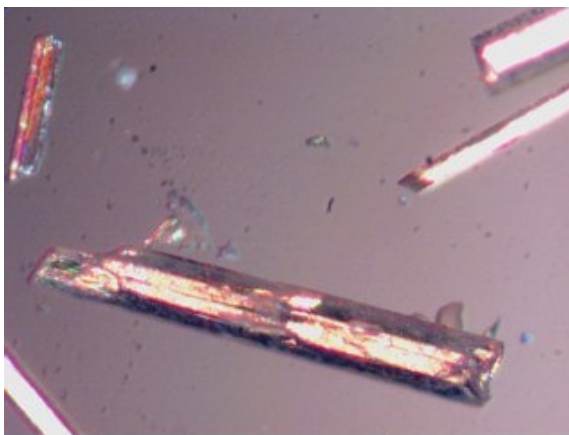
e.



f.



g.



h.

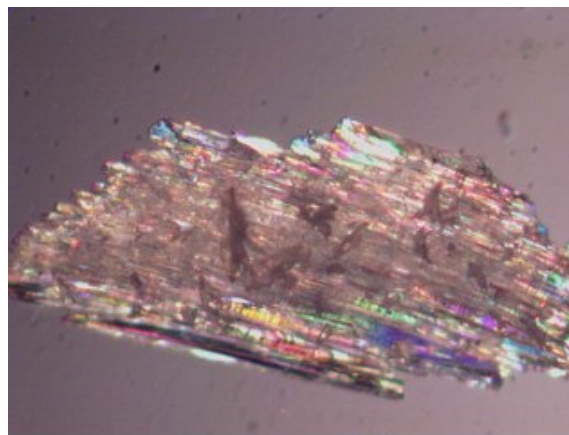


Figure 26, continued

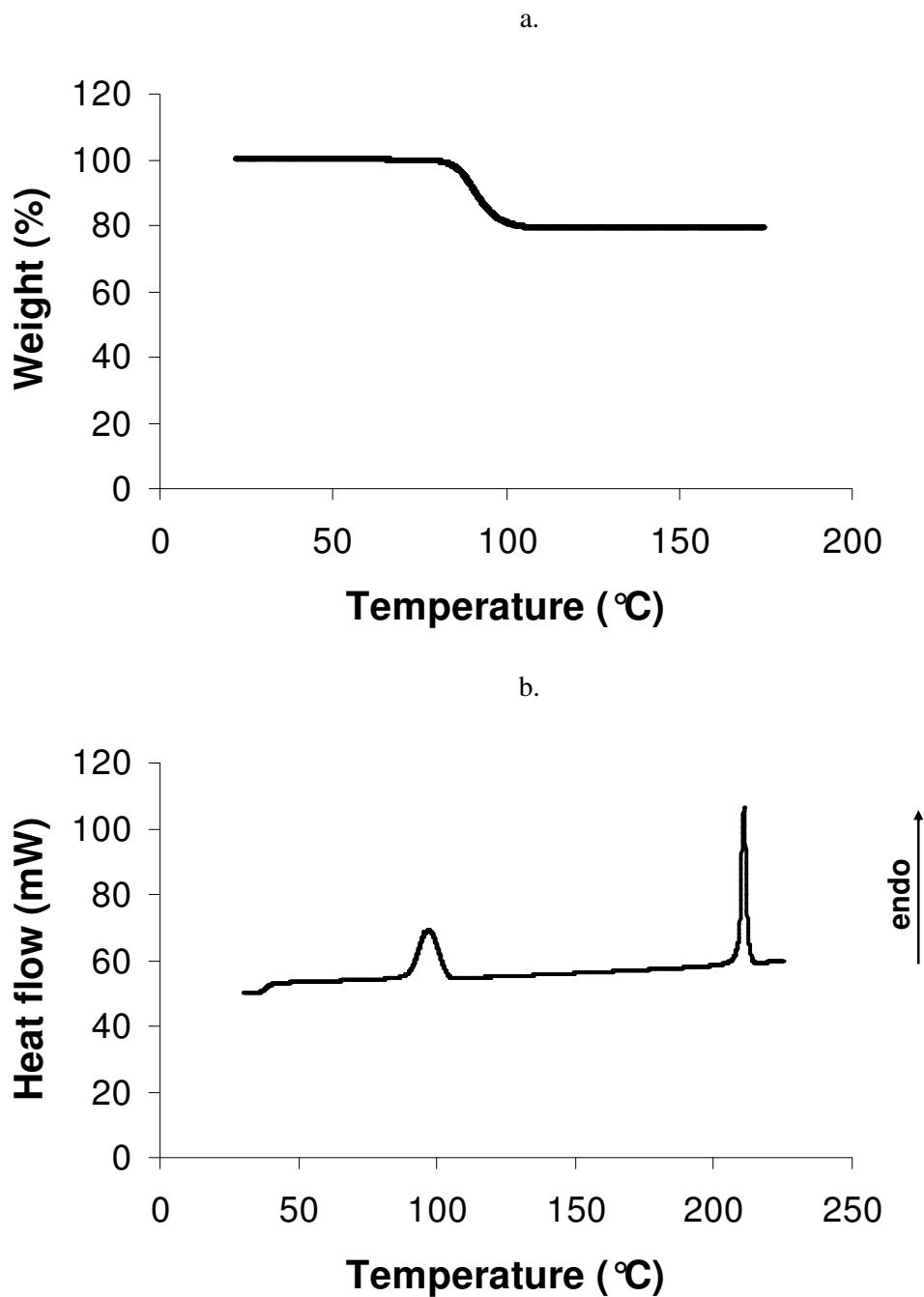


Figure 27. Thermal analysis of sulfameter tetrahydrofuran solvate at a heating rate of 16 K/min by: a, TGA and b, DSC.

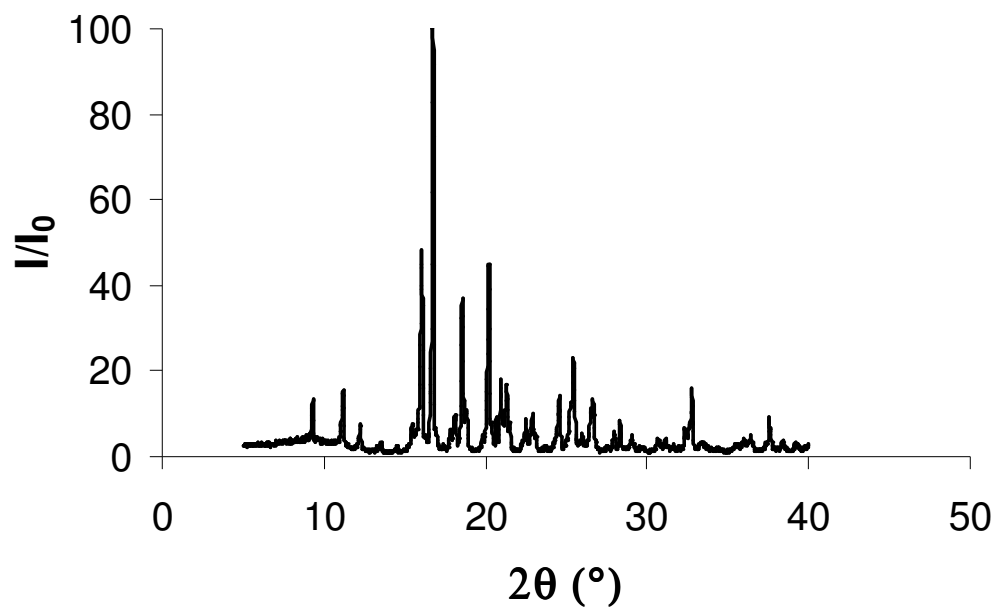


Figure 28. Powder X-ray diffraction pattern for sulfameter tetrahydrofuran solvate.

Table 11. X-ray diffraction data ($I/I_0 \geq 10$) for sulfameter tetrahydrofuran solvate.

d (Å)	I/I_0
9.48	13.35
7.89	15.69
5.52	48.19
5.29	100.00
4.78	37.03
4.72	11.03
4.39	44.78
4.24	17.99
4.18	11.07
4.16	16.83
3.62	14.18
3.52	11.84
3.50	23.20
3.35	11.29
3.34	13.37
2.73	15.85

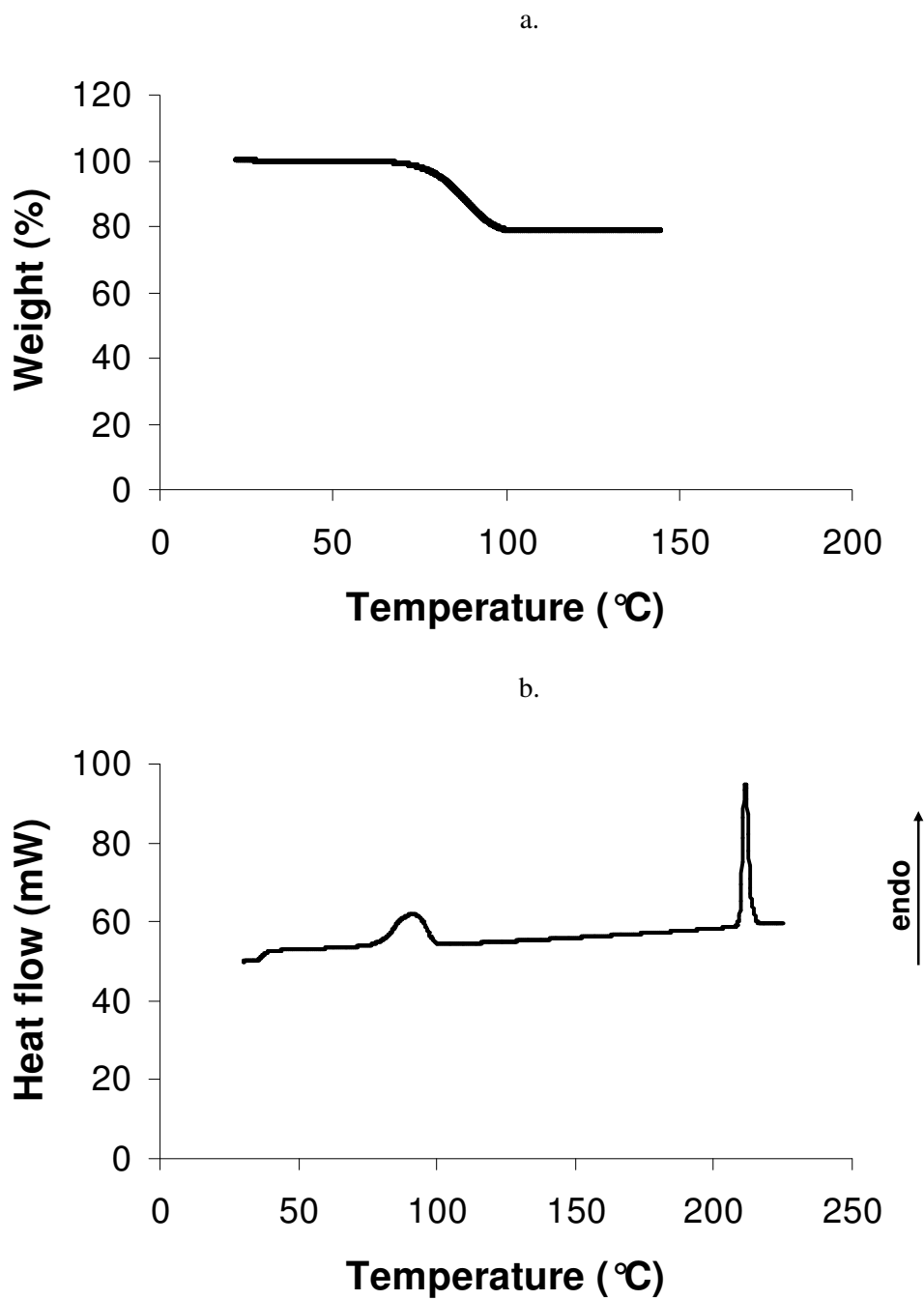


Figure 29. Thermal analysis of sulfameter dioxolane solvate at a heating rate of 16 K/min by: a, TGA and b, DSC.

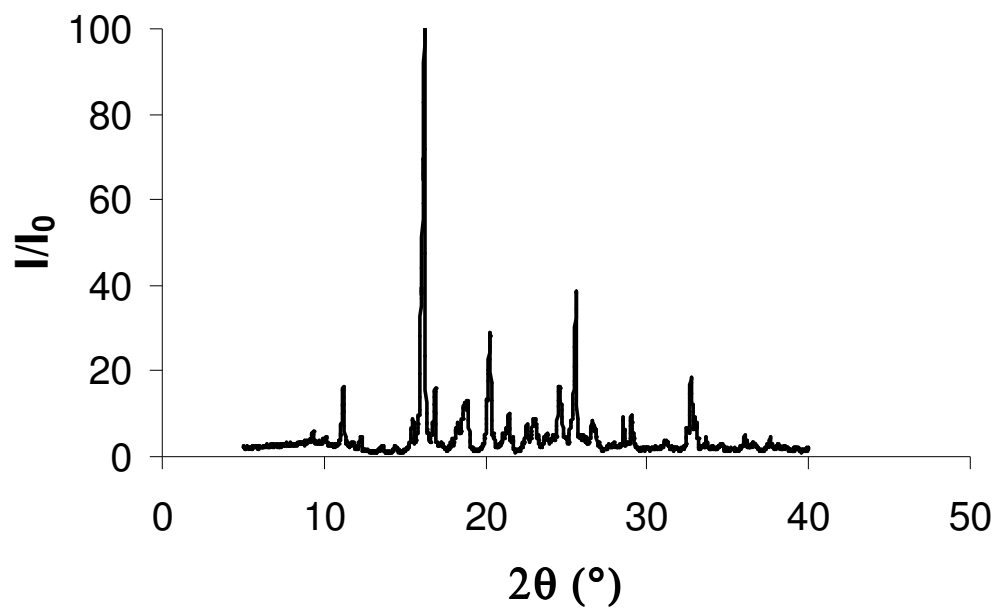


Figure 30. Powder X-ray diffraction pattern for sulfameter dioxolane solvate.

Table 12. X-ray diffraction data ($I/I_0 \geq 10$) for sulfameter dioxolane solvate.

d (Å)	I/I_0
7.89	16.29
5.53	39.55
5.49	69.50
5.45	100.00
5.27	12.39
5.24	16.15
4.75	12.09
4.74	12.44
4.70	13.18
4.41	13.63
4.38	28.30
3.62	16.36
3.48	38.06
2.73	18.60

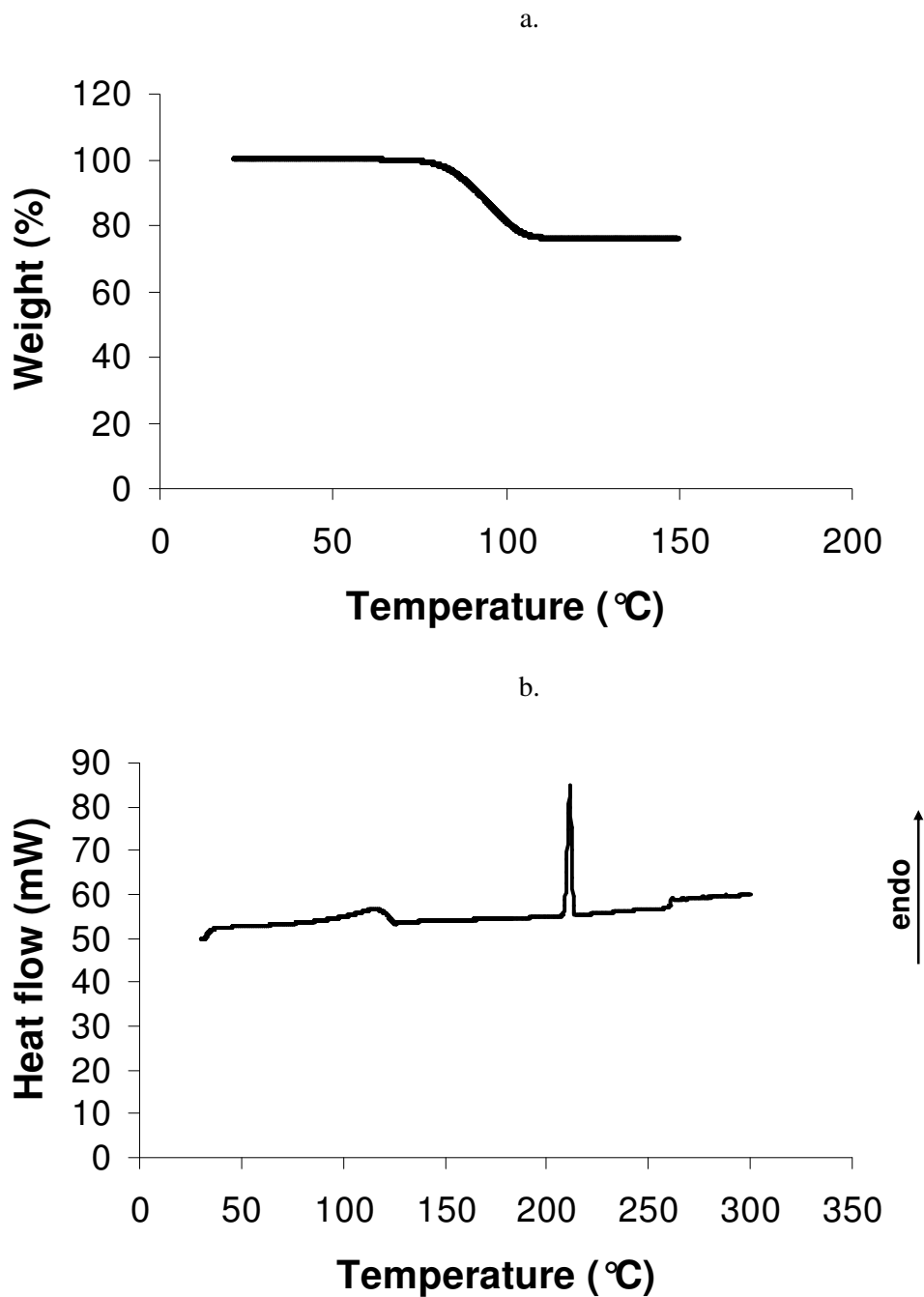


Figure 31. Thermal analysis of sulfameter oxane solvate at a heating rate of 16 K/min by:
a, TGA and b, DSC.

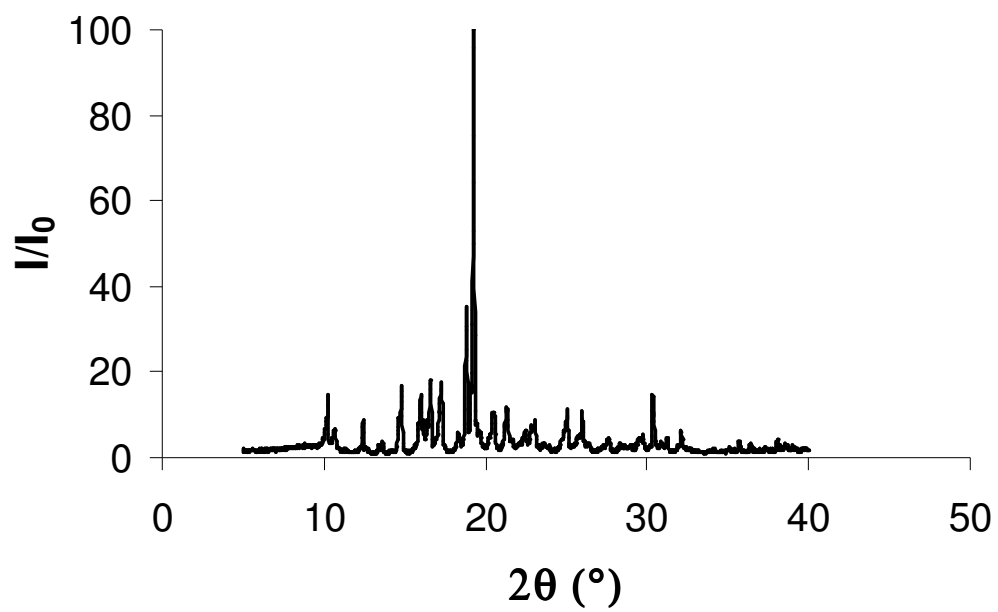


Figure 32. Powder X-ray diffraction pattern for sulfameter oxane solvate.

Table 13. X-ray diffraction data ($I/I_0 \geq 10$) for sulfameter oxane solvate.

d (Å)	I/I_0
8.63	14.91
5.98	16.65
5.54	14.58
5.34	18.13
5.13	17.62
4.71	35.26
4.65	17.11
4.60	100.00
4.18	10.99
2.94	14.85

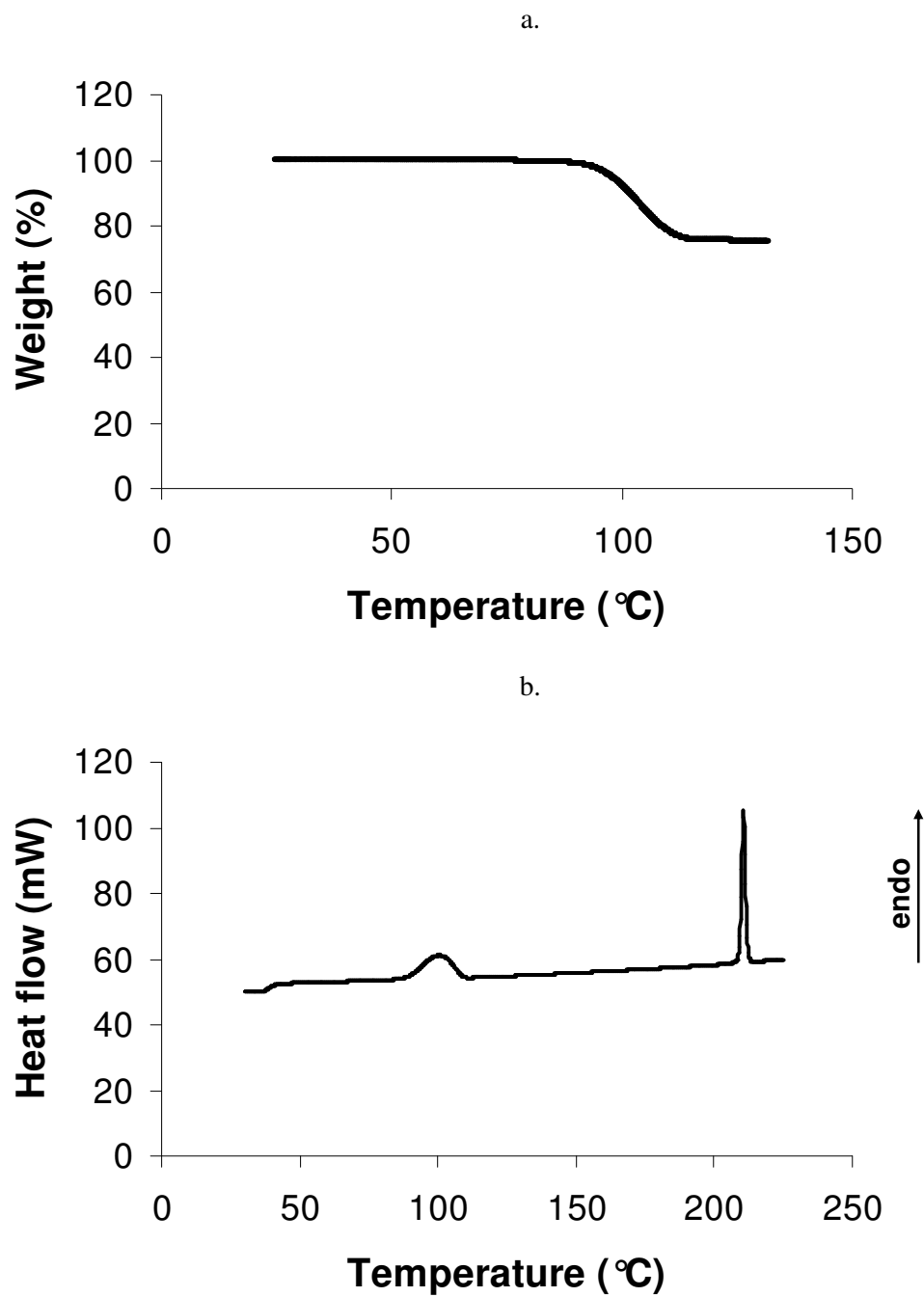


Figure 33. Thermal analysis of sulfameter dioxane solvate at a heating rate of 16 K/min by: a, TGA and b, DSC.

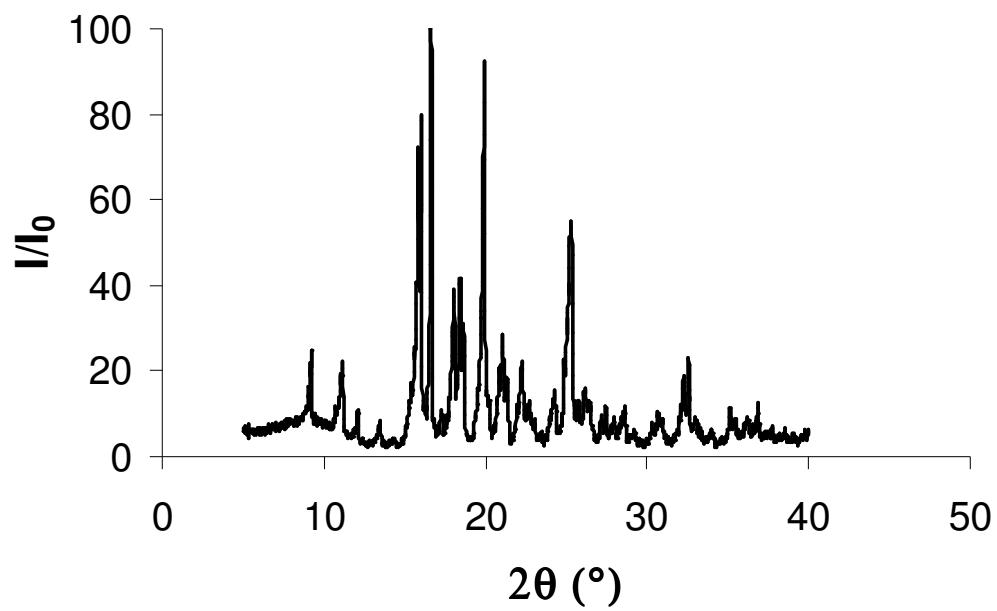


Figure 34. Powder X-ray diffraction pattern for sulfameter dioxane solvate.

Table 14. X-ray diffraction data ($I/I_0 \geq 20$) for sulfameter dioxane solvate.

d (Å)	I/I_0
9.58	24.90
5.63	40.94
5.59	72.25
5.53	79.90
5.32	100.00
4.91	38.91
4.81	41.45
4.78	24.02
4.76	30.89
4.46	92.62
4.21	28.63
3.99	22.45
3.58	22.50
3.55	32.27
3.54	40.25
3.53	52.24

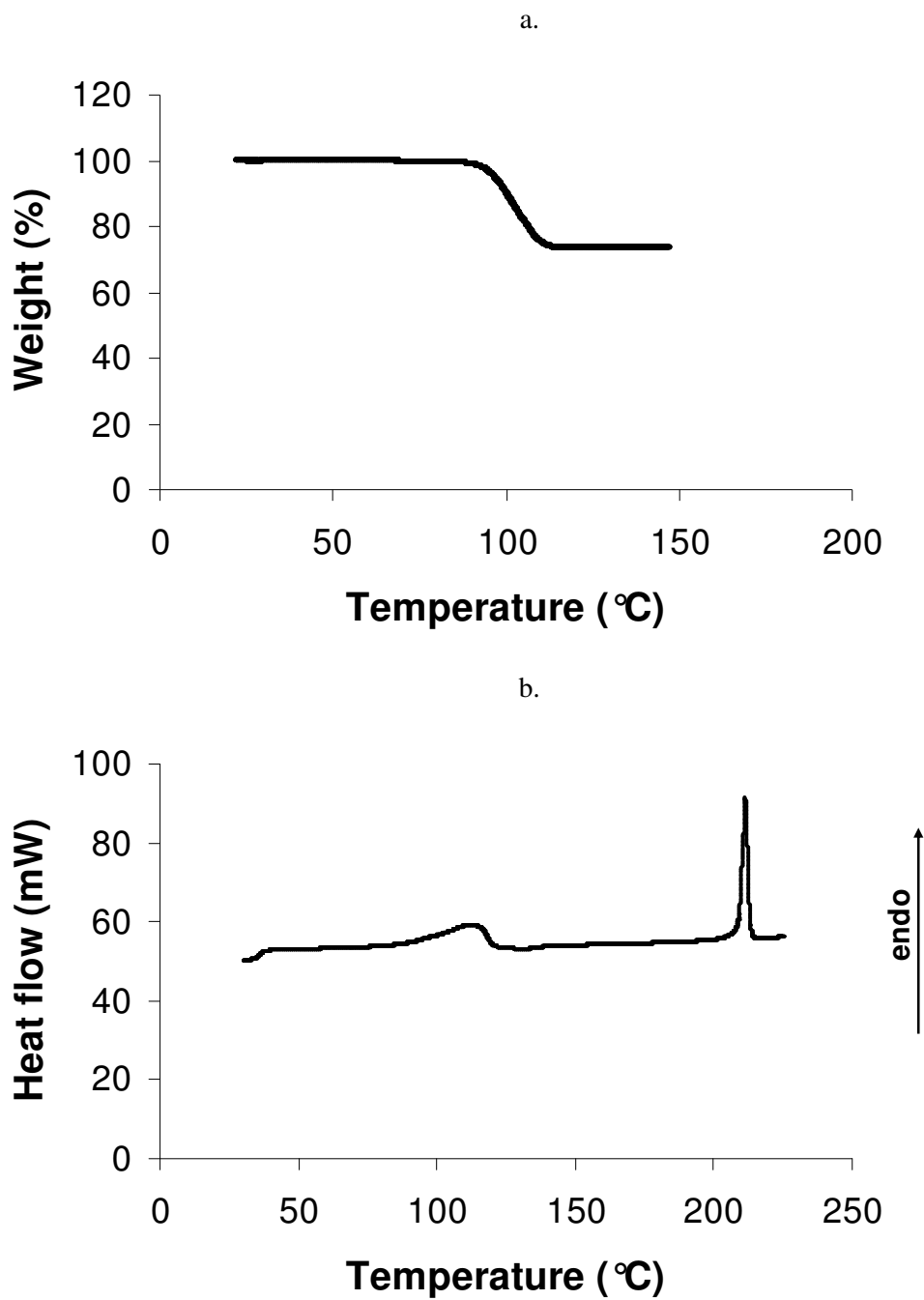


Figure 35. Thermal analysis of sulfameter oxepane solvate at a heating rate of 16 K/min by: a, TGA and b, DSC.

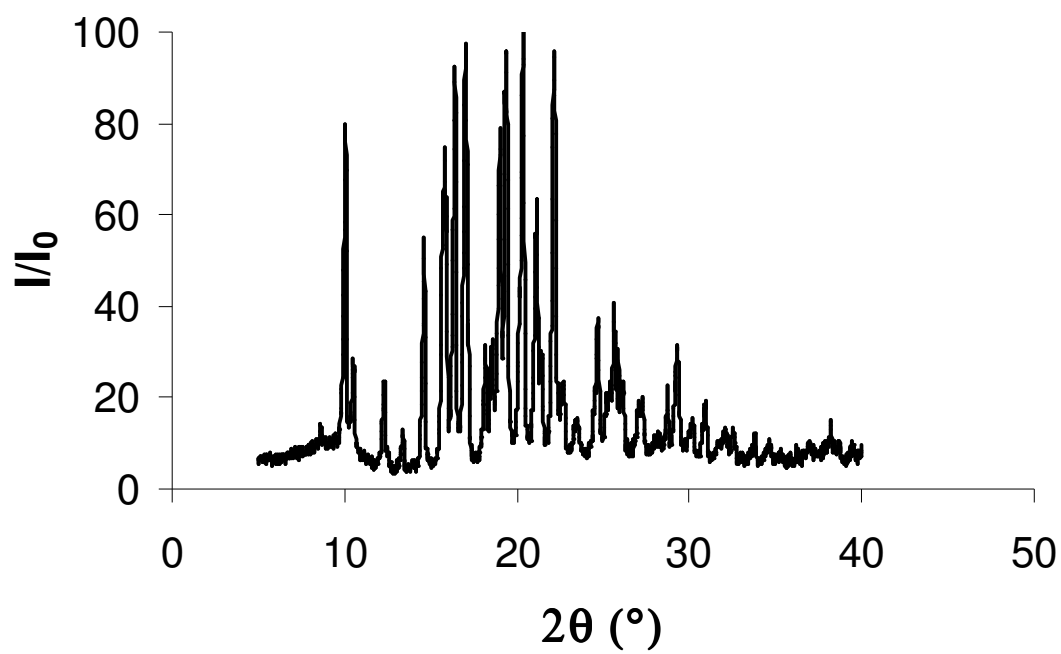


Figure 36. Powder X-ray diffraction pattern for sulfameter oxepane solvate.

Table 15. X-ray diffraction data ($I/I_0 \geq 20$) for sulfameter oxepane solvate.

d (Å)	I/I_0
8.79	79.81
8.40	28.38
7.19	23.72
6.05	55.02
5.64	60.40
5.61	74.71
5.39	92.32
5.20	97.53
5.15	36.29
4.88	31.41
4.79	30.90
4.72	21.48
4.66	78.86
4.59	86.37
4.58	95.51
4.40	43.97
4.36	100.00
4.21	55.75
4.20	63.04
4.16	27.43
4.01	95.68
3.92	23.44
3.62	22.99
3.60	37.46
3.51	23.44
3.47	40.66
3.44	30.57
3.42	21.99
3.05	31.52

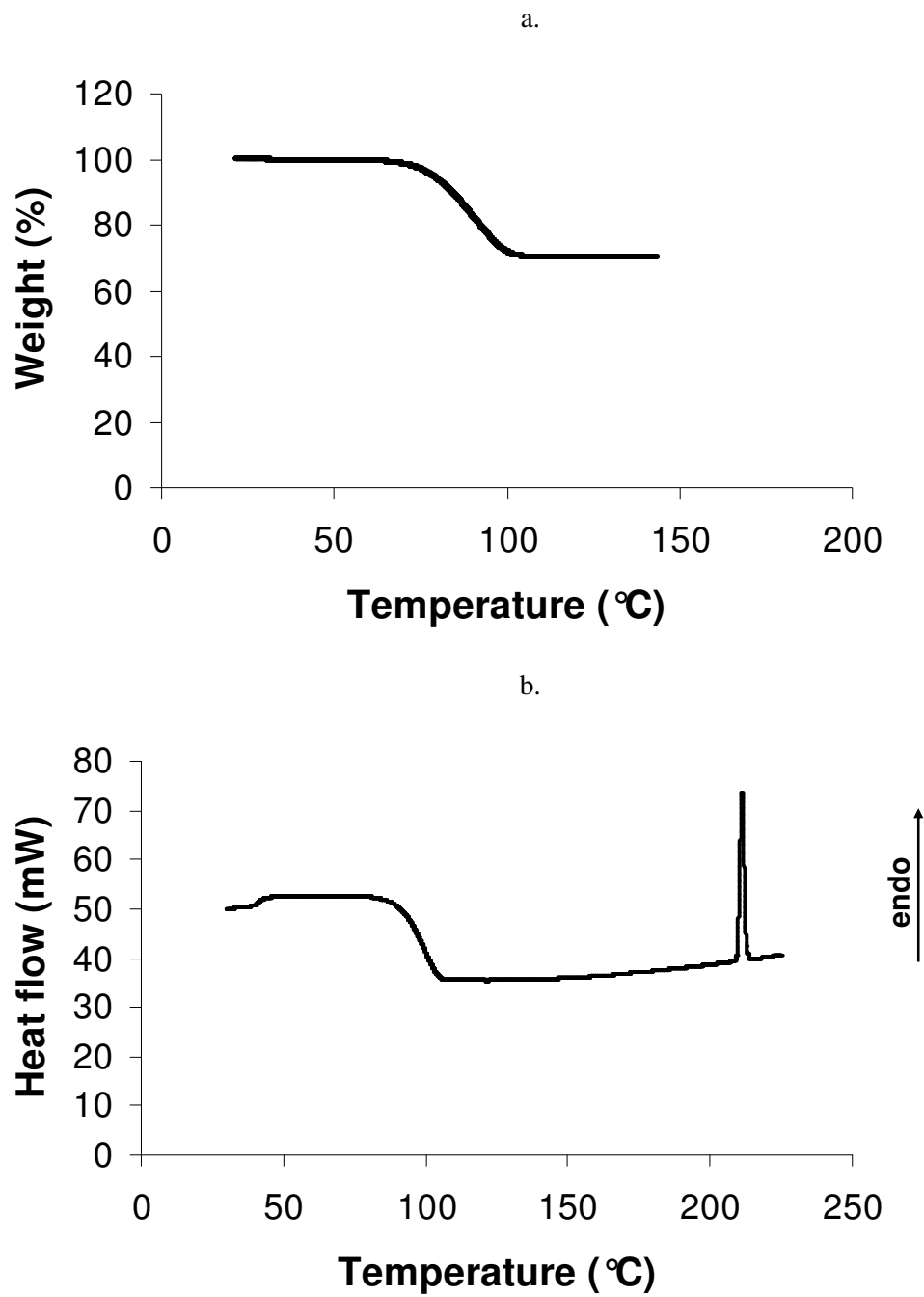


Figure 37. Thermal analysis of sulfameter chloroform solvate at a heating rate of 16 K/min by: a, TGA and b, DSC.

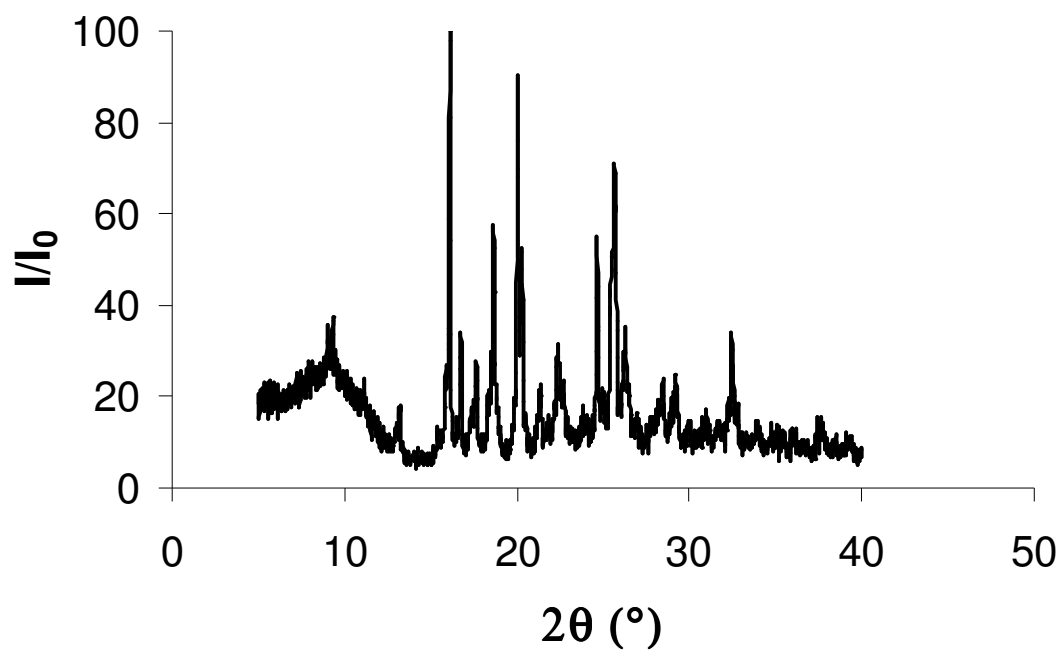


Figure 38. Powder X-ray diffraction pattern for sulfameter chloroform solvate.

Table 16. X-ray diffraction data ($I/I_0 \geq 25$) for sulfameter chloroform solvate.

d (Å)	I/I_0
10.02	28.71
9.71	31.81
9.34	30.32
5.50	100.00
5.29	33.83
4.76	57.55
4.42	90.16
4.39	41.37
4.37	52.70
3.98	28.98
3.97	31.54
3.61	54.85
3.51	39.35
3.49	50.94
3.47	71.16
3.40	29.78
3.39	35.18
2.76	33.96

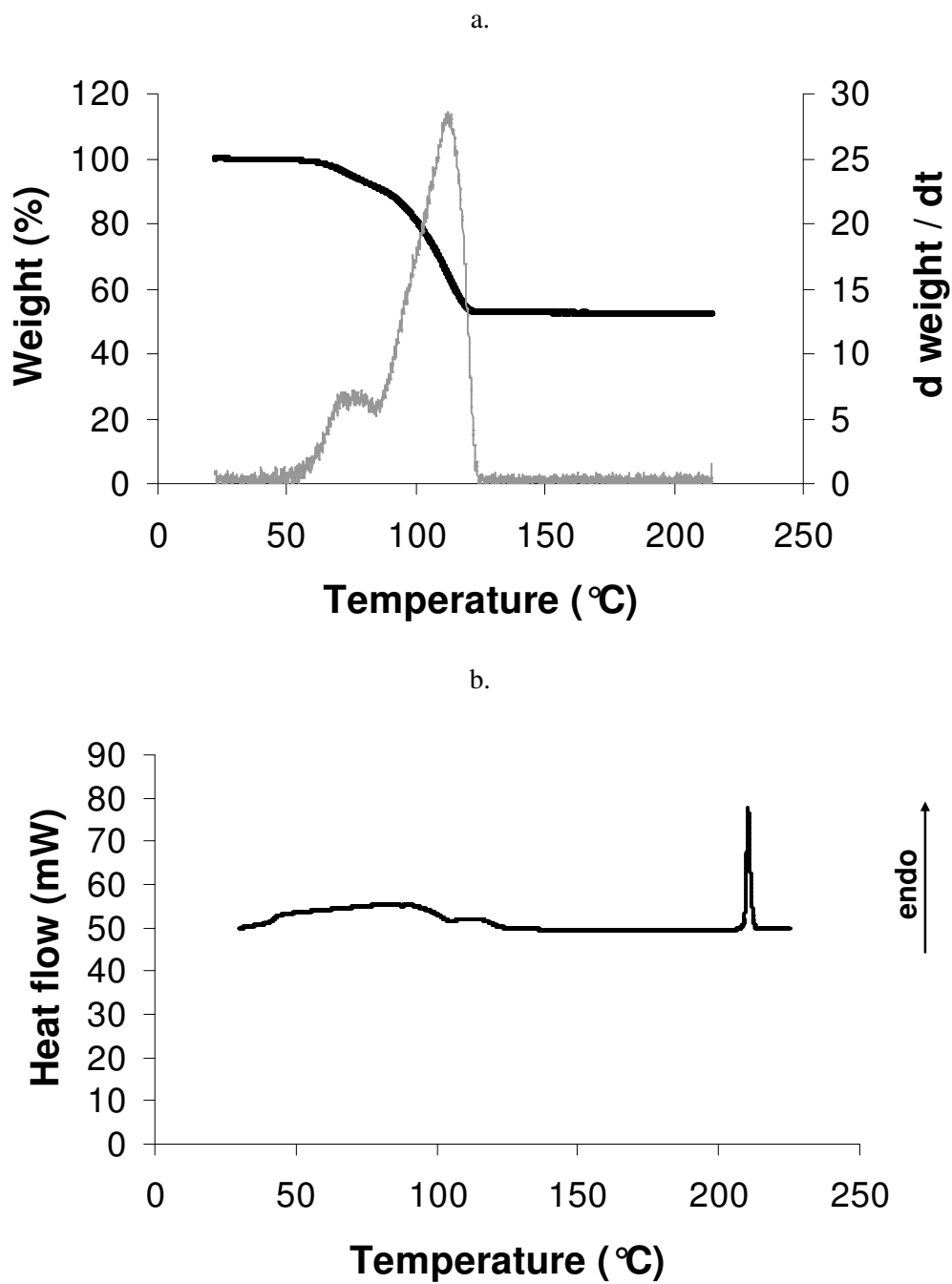


Figure 39. Thermal analysis of sulfameter bromoform solvate at a heating rate of 16 K/min by: a, TGA (black); DTG (gray) and b, DSC.

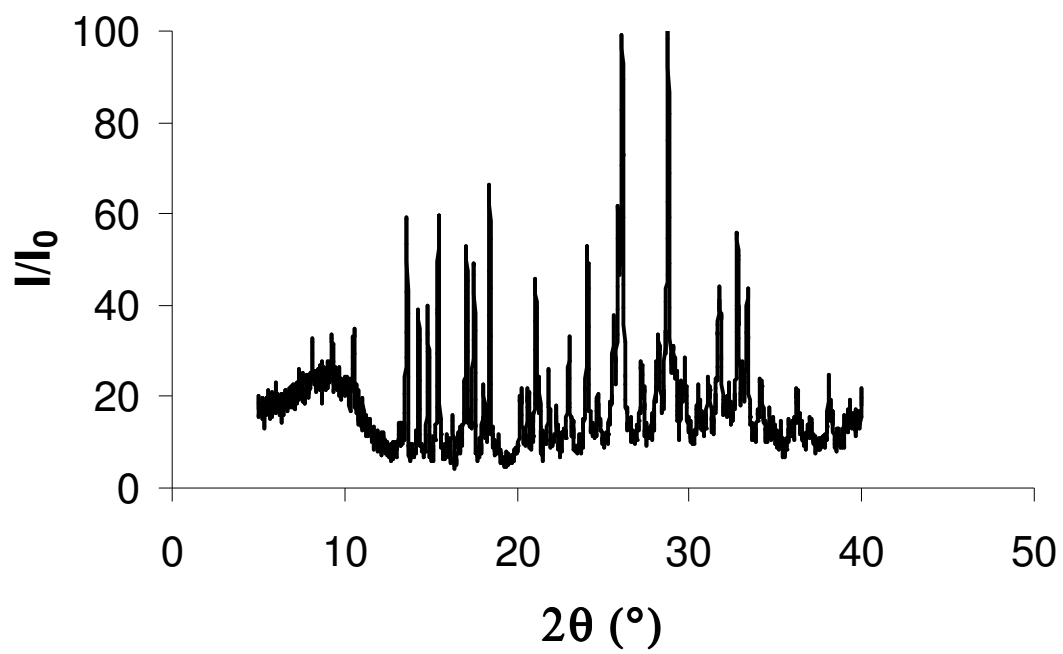


Figure 40. Powder X-ray diffraction pattern for sulfameter bromoform solvate.

Table 17. X-ray diffraction data ($I/I_0 \geq 30$) for sulfameter bromoform solvate.

d (Å)	I/I_0
9.54	33.51
8.37	34.84
6.49	59.04
5.96	40.03
5.73	59.04
5.19	52.93
5.06	48.54
4.81	66.22
4.21	45.74
3.69	52.66
3.48	37.77
3.44	61.70
3.41	99.07
3.12	34.44
3.10	100.00
3.07	30.98
2.82	44.28
2.81	41.36
2.73	55.32
2.68	43.62

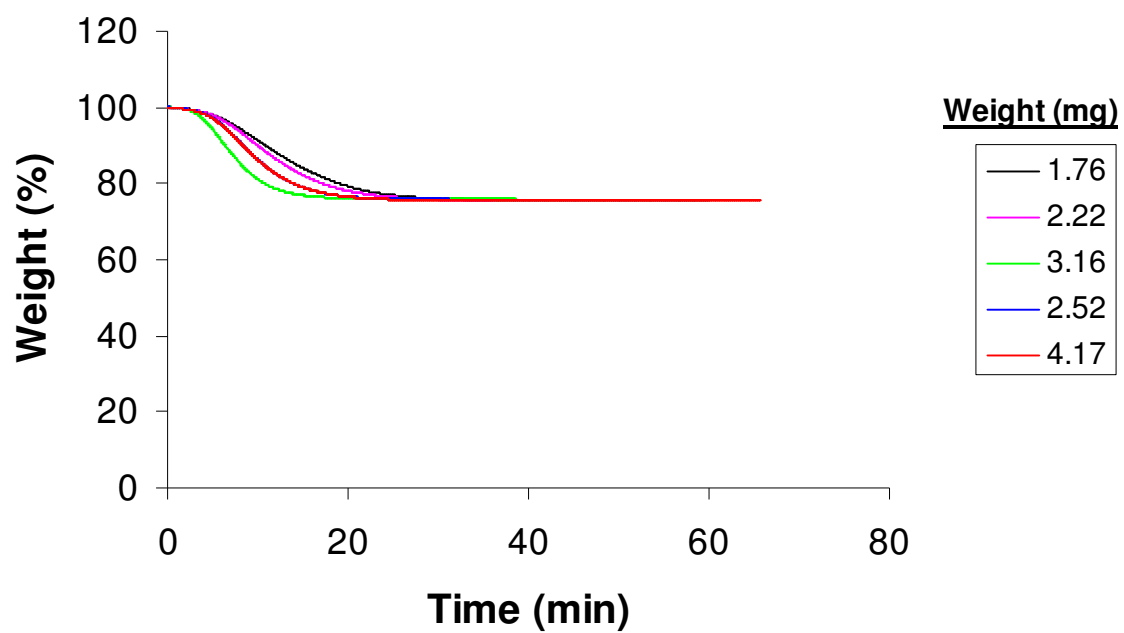


Figure 41. Isothermal desolvation thermograms at 70°C for sulfameter dioxane solvate having an uncontrolled particle size (i.e., unsieved sample).

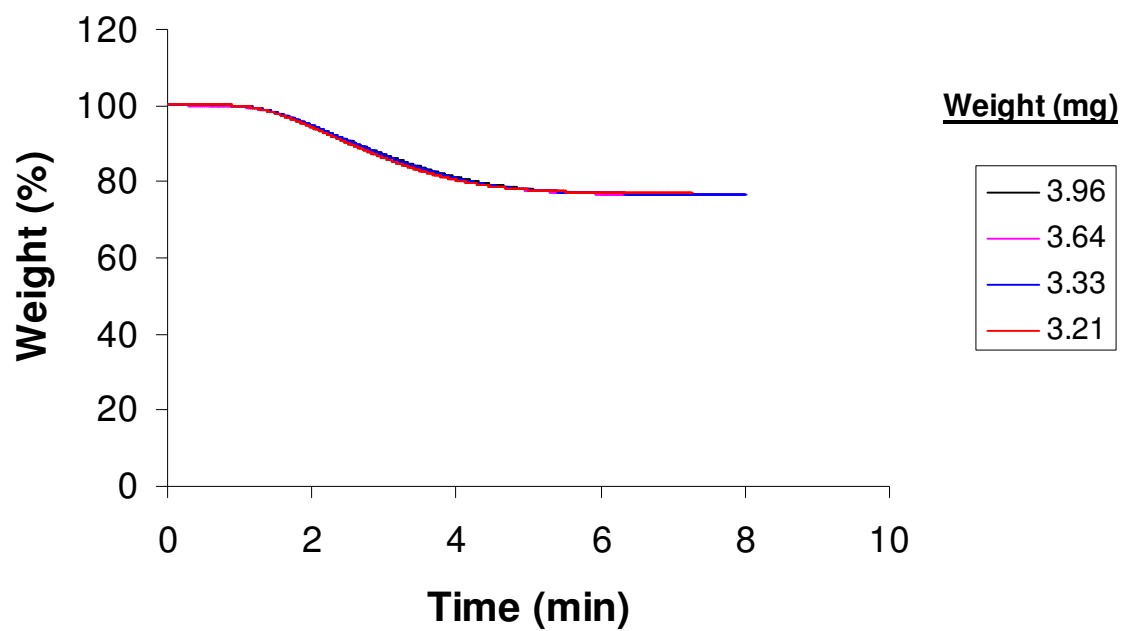


Figure 42. Isothermal desolvation thermograms at 75°C for sulfameter dioxane solvate having a particle size range of 90 – 300 μm .

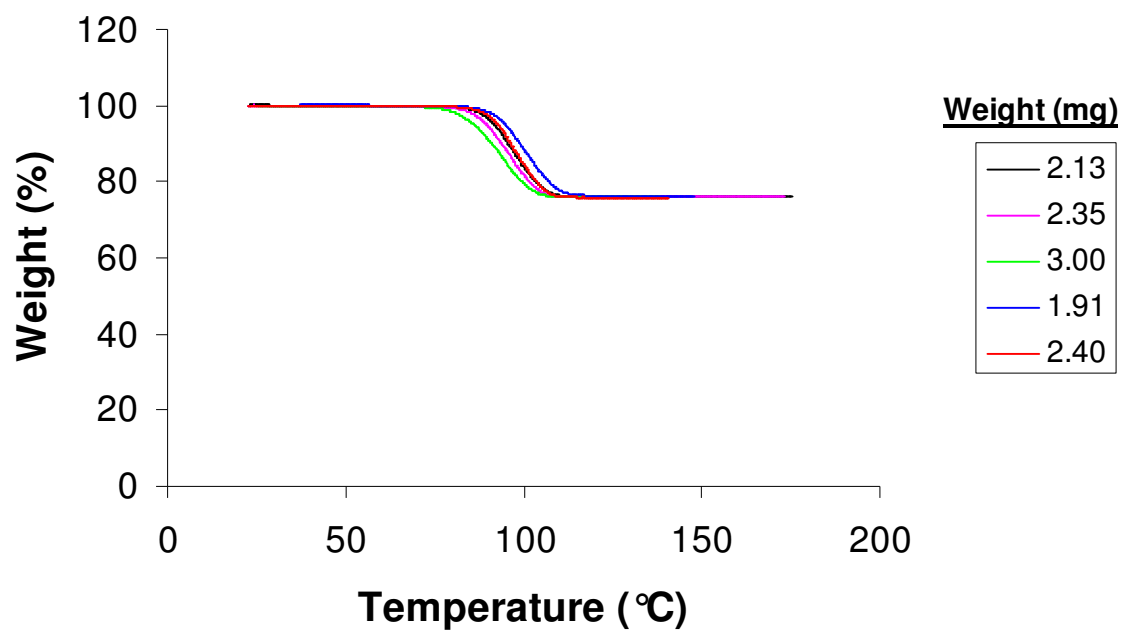


Figure 43. Nonisothermal desolvation thermograms at 16 K/min for sulfameter dioxane solvate having an uncontrolled particle size (i.e., unsieved sample).

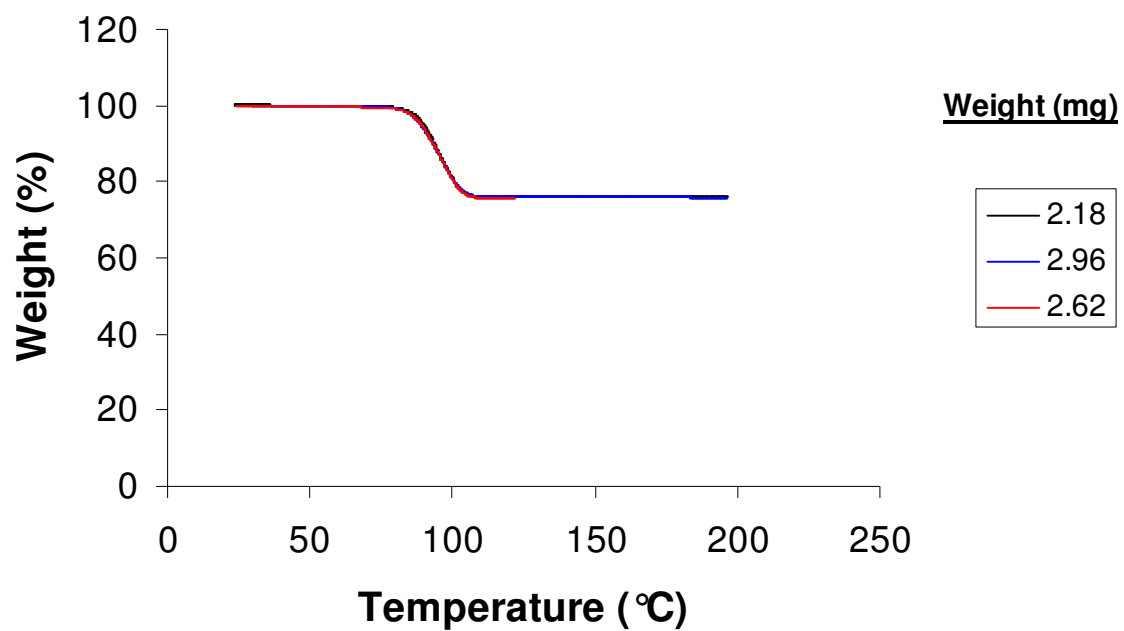


Figure 44. Nonisothermal desolvation thermograms at 16 K/min for sulfameter dioxane solvate having a particle size range of 90 – 300 μm .

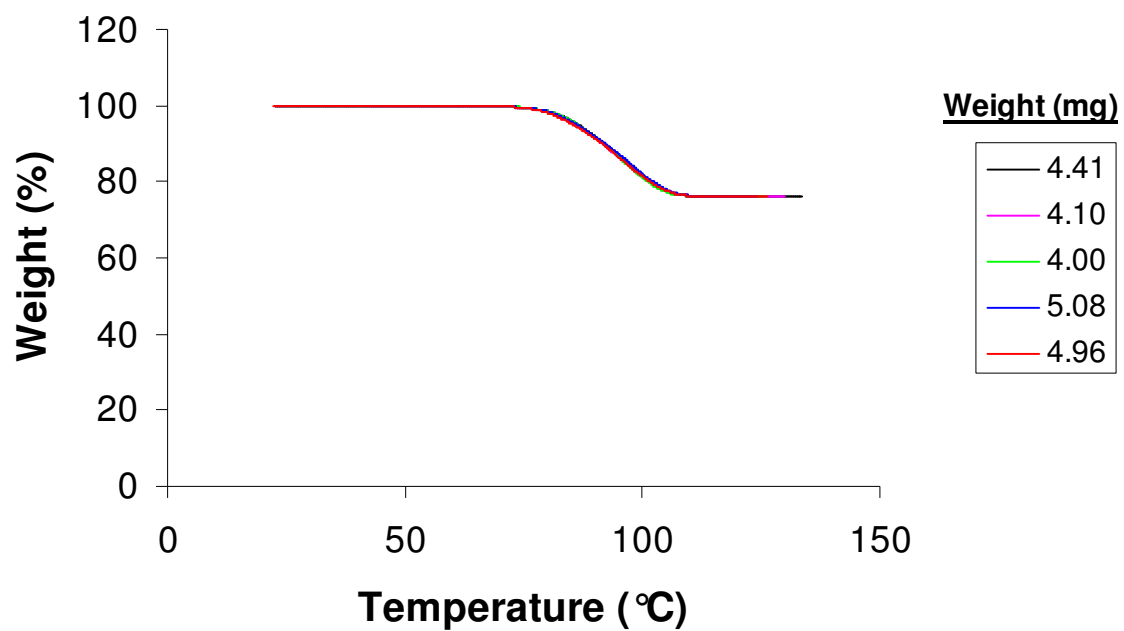


Figure 45. Nonisothermal desolvation thermograms at 16 K/min for sulfameter oxane solvate having a particle size range of 90 – 300 μm .

Table 18. Data reduction example using the truncation method by rounding down data. (11 data points reduced to 3).

Time (min)	Temperature (°C)	α	Rounded α	Result
14.10	69.647	0.102427903	0.10	0.10
14.12	69.728	0.104828610	0.10	Ignored
14.14	69.807	0.107496248	0.10	Ignored
14.16	69.880	0.109896954	0.10	Ignored
14.18	69.957	0.112829845	0.11	0.11
14.20	70.025	0.115764415	0.11	Ignored
14.22	70.081	0.118165122	0.11	Ignored
14.24	70.151	0.121099691	0.12	0.12
14.26	70.231	0.124034261	0.12	Ignored
14.28	70.250	0.126967152	0.12	Ignored
14.30	70.264	0.129901722	0.12	Ignored

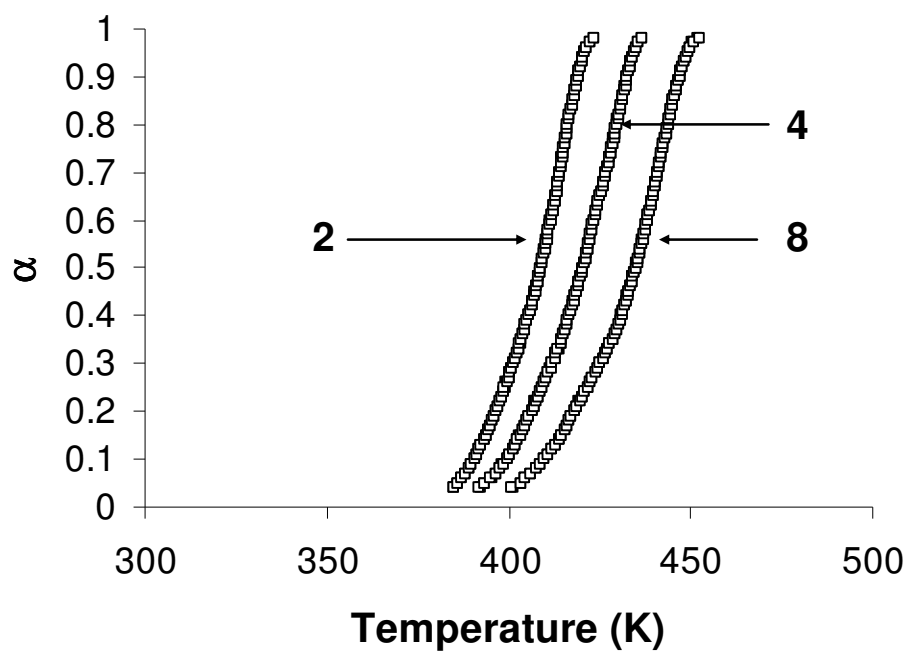


Figure 46. Calcium oxalate monohydrate dehydration thermograms at: 2, 4 and 8 K/min evaluated by two data reduction methods: ■, MLR and □, Truncation.

Table 19. Programmed and calculated heating rates for several nonisothermal TGA thermograms.

Sample	Programmed rate (K/min)	Calculated rate (K/min)	r ^a
Empty pan	5.00	5.15	0.9999
Empty pan	10.00	10.29	0.9999
Empty pan	20.00	20.50	0.9999
Empty pan	40.00	40.71	0.9998
Water evaporation	2.50	2.53	0.9953
Water evaporation	4.00	4.16	0.9912
Water evaporation	5.00	5.03	0.9984
Water evaporation	8.00	8.05	0.9989
Water evaporation	10.00	9.86	0.9993
Water evaporation	16.00	14.56	0.9977
Water evaporation	32.00	29.58	0.9973
Water evaporation	64.00	56.91	0.9988
n-Propanol evaporation	1.00	1.09	0.9939
n-Propanol evaporation	16.00	14.53	0.9998
n-Propanol evaporation	64.00	56.06	0.9998
Hexane evaporation	8.00	8.47	0.9999
Hexane evaporation	16.00	14.02	0.9999
Hexane evaporation	64.00	50.62	0.9997
Calcium oxalate dehydration	1.00	1.01	0.9999
Calcium oxalate dehydration	16.00	15.94	1.0000
Citric acid ^b	10.00	10.34	0.9997
Cortisone acetate ^b	10.00	10.12	0.9997
Brompheniramine maleate ^b	10.00	10.37	0.9999
Diphenhydramine HCl ^b	10.00	10.33	0.9998
Pramoxine HCl ^b	10.00	10.36	0.9998
Dibucaine HCl ^b	10.00	10.27	0.9998

^a Correlation coefficient of heating profile.

^b Heated until melting.

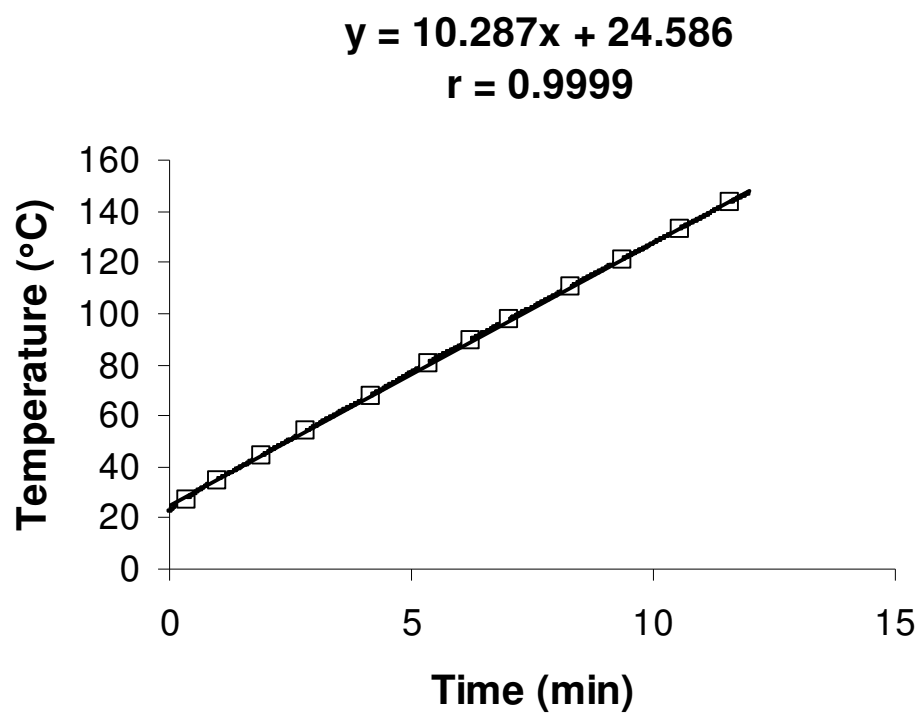


Figure 47. Linear heating rate profile of an empty TG pan for a nonisothermal run at a programmed heating rate of 10 K/min.

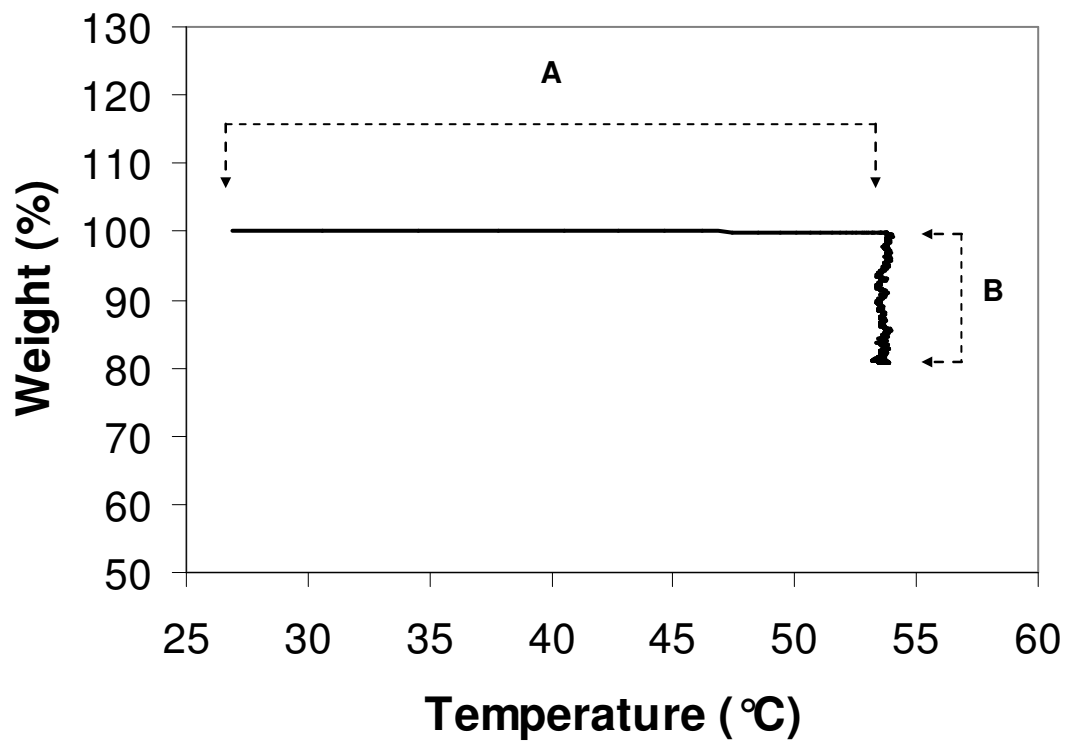
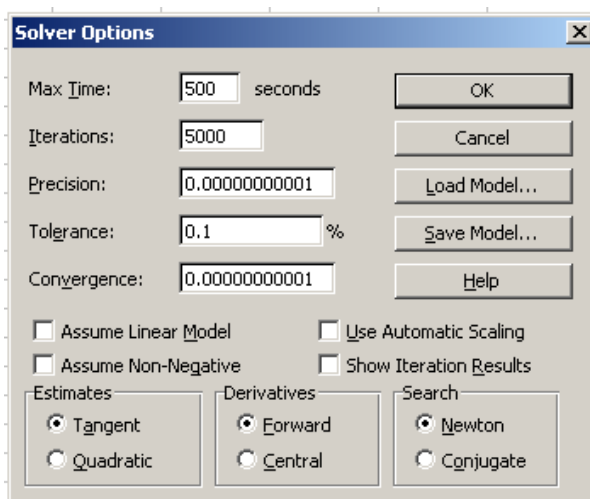


Figure 48. Determination of actual experimental temperature of an isothermal desolvation reaction (sulfameter-tetrahydrofuran solvate at $T=55^{\circ}\text{C}$). Region A represents the heat up period, while region B is the portion where the desolvation reaction occurs at a rapid rate.

a.



b.

SolverOptions MaxTime:=500, Iterations:=5000, Precision:=0.00000000001,
 AssumeLinear:=False, StepThru:=False, Estimates:=1, Derivatives:=1, SearchOption:=1,
 IntTolerance:=0.1, Scaling:=False, Convergence:=0.00000000001,
 AssumeNonNeg:=False

Figure 49. Microsoft Excel's Solver[®] parameters used for iterative solving of kinetic equations: a, graphical interface and b, Visual Basic[®] code used in Excel's Macros.

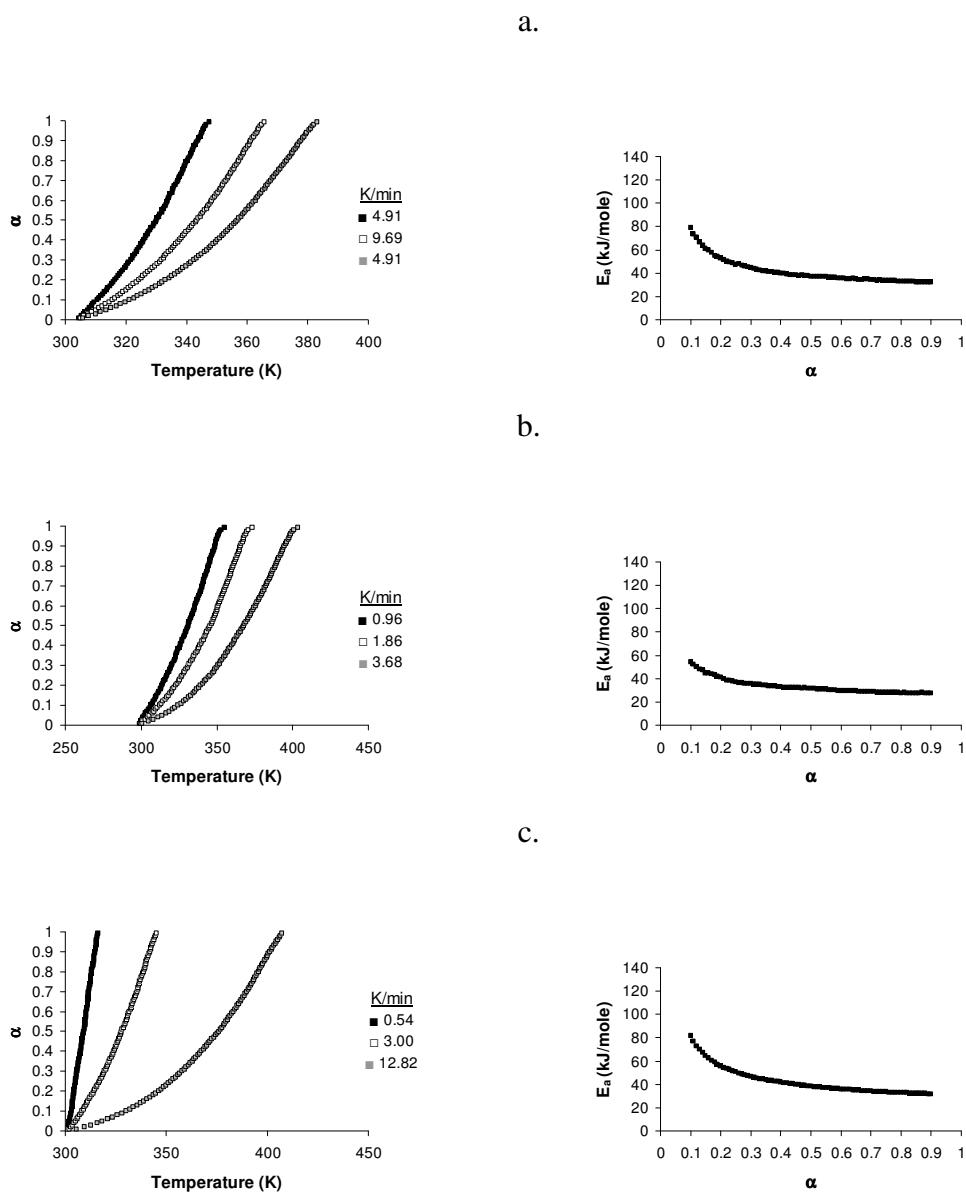
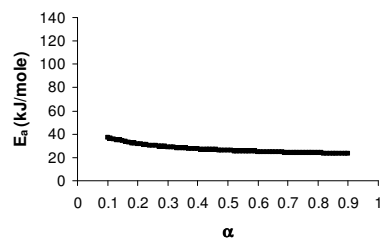
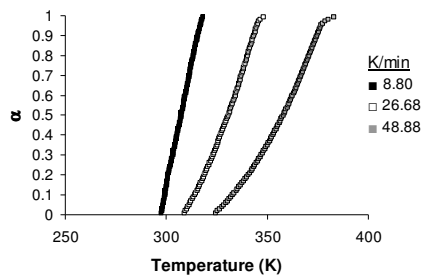


Figure 50. Nonisothermal thermograms for the evaporation of five substances and their isoconversional plots: a, water; b, deuterium oxide; c, propanol; d, hexane and e, naphthalene.

d.



e.

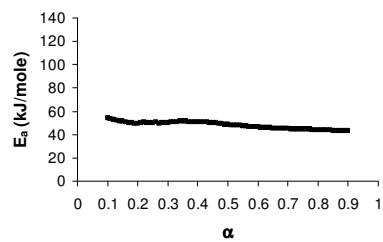
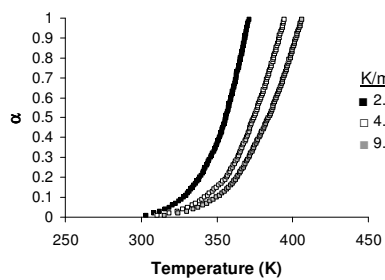


Figure 50, continued

Table 20. Heats of vaporization (literature) compared to averaged vaporization activation energies (E_a) for five substances; activation energies calculated by the Vyazovkin isoconversional method for conversion values (α) of 0.1–0.90.

Substance	ΔH_{vap} (kJ/mole)	Average E_a (kJ/mole)
Water	40.68	41.33
Deuterium oxide	41.52	33.31
Propanol	41.44	42.48
Hexane	28.64	27.15
Naphthalene	43.85	47.95

CHAPTER 4

ROLE OF ISOCONVERSIONAL METHODS IN VARYING ACTIVATION ENERGIES OF SOLID-STATE KINETICS

Introduction

Solid-state kinetic studies have caused numerous debates and controversies [66, 68]. One controversial issue is the variation of activation energy as a function of reaction progress. In a recent article, Galwey [76] questioned the meaning of variable activation energy in solid-state decompositions and proposed several explanations for this observation.

Vyazovkin [158], in reply, provided alternative explanations for this behavior. Most explanations focus on the complexities inherent in solid-state kinetics with little consideration being given to secondary effects such as the effects of mathematical or computational methods. The aim of this work is to test the sensitivity of some of these methods, which will be done through kinetic analysis of simulated isothermal and nonisothermal data, in addition to actual experimental kinetic results.

Varying activation energy

Solid-state kinetics was developed from reaction kinetics in homogenous systems (i.e. gases and liquids). The Arrhenius equation (Eq. (14)) relates the rate constant of a simple one-step reaction to the temperature through the activation energy (E_a) and pre-exponential factor (A). It has been generally assumed that activation energy (E_a) and frequency factor (A) remain constant, however, it's been shown [72-74] that in solid-state reactions these kinetic parameters may vary with the progress of the reaction (α). This variation can be detected by isoconversional methods. While this variation appears to be in conflict with basic chemical kinetic principles, in reality, it may not be. Such behavior

may show that solid-state kinetics are more complex and/or multi-step compared to reactions in homogenous phases. There are several proposed explanations for varying E_a with reaction progress. Vyazovkin [73] has shown this behavior in homogenous phases. Possible explanations for such variation in solid-state reactions have been summarized by Galwey [76]. Explanations for this variation usually focus on the complexities inherent in solid-state kinetics with little consideration being given to secondary effects such as artifacts from mathematical or computational methods. Solid-state reactivity of an elementary reaction could also be affected by experimental variables that could change the reaction kinetics by affecting heat or mass transfer at a reaction interface [76].

If two or more elementary steps, each having a unique activation energy, control the rate of product formation, the reaction is usually called a complex reaction [9]. In such a reaction, a change in the activation energy as the reaction progresses would be observed. This change will depend on the contribution of each elementary step, which gives an “effective” activation energy that varies with reaction progress. Kinetic complexities are not limited to multiple chemical steps. They may also include physical processes (e.g. sublimation, localized melting, adsorption-desorption, diffusion of a gaseous product, particle size and morphology effects, etc.) that have different activation energies [76], as discussed in Chapter 1.

Isoconversional methods, use several TGA or DSC data sets for kinetic analysis. When performing isothermal experiments, care should be taken to ensure that every run is done under the same experimental conditions (i.e., sample weight, purge rate, sample size distribution, particle morphology, etc.) so that only the temperature varies for each run. Similarly, when performing nonisothermal experiments, care must be taken to ensure that each run is conducted under the same experimental conditions so that only the heating rate is the only variable.

Experimental variation can be minimized, but not totally removed which alters a thermogram such that it falls above or below its expected location. This could introduce errors in the calculation of the activation energy obtained from isoconversional methods.

We propose that the observed variation in activation energy, as detected by isoconversional methods could be an artifact that results from the sensitivity of these methods to different experimental variables. This sensitivity was tested through kinetic analysis of simulated and actual experimental data. Actual experimental data was based on studying desolvation reaction kinetics of sulfameter dioxolane solvate (Chapter 3) isothermally and nonisothermally.

The sulfameter solvate system was selected for this study because it has been previously shown [157] that desolvation of sulfameter solvates is a simple process because solvent molecules fill channels within the crystal structure and desolvation involves the removal of solvent from such channels. Although desolvation does not reflect the inherent complexities observed in many other solid-state systems, it does represent simple solid-state reactions that occur in many pharmaceutical solids.

Experimental

There are two parts to this investigation: an isothermal and a nonisothermal part. Each part involves mathematical analysis of simulated and actual experimental data of the desolvation of sulfameter-dioxolane solvate.

The methods for evaluating isothermal kinetic data include the standard isoconversional method [41], Friedman's isoconversional method [58], Vyazovkin's advanced isoconversional (AIC) method [25, 63] and the conventional model-fitting method (see Chapter 1). Nonisothermal data were analyzed by model-fitting methods (Coats-Redfern) [48, 49] in addition to isoconversional methods which include the Ozawa-Flynn-Wall (OFW) method [59, 60] and Vyazovkin's (VYZ) isoconversional [62] and advanced isoconversional (AIC) [25, 63] methods (see Chapter 1).

Data simulation

A simple, one-step reaction was simulated. Fifteen isothermal and twenty four nonisothermal simulations were generated, as described in Chapter 3.

The first isothermal simulation (A1) consisted of five isothermal (α -t) curves which were simulated (error-free) at five temperatures (323, 328, 333, 338 and 343 K) using a first-order model ($g(\alpha)=-\ln(1-\alpha)$) with $A=1 \times 10^{15} \text{ min}^{-1}$ and $E_a=100 \text{ kJ/mole}$ as seen in Figure 51. Fourteen additional simulations (A2–15) were generated from A1 using the same kinetic parameters and model but introducing different perturbations in each (Table 21). These perturbations included shifting one or more curves and/or changing the temperature of a curve. A curve shift simulates a thermal lag in a sample, while a temperature change simulates possible self cooling/heating effects or the effect of using an apparent sample temperature rather than the true temperature.

Nonisothermal runs were simulated in two data sets (sets B and C). The first simulation in set B (B1) consisted of five error-free nonisothermal (α -T) curves generated at five heating rates (2, 4, 8, 16 and 32 K/min) using a first-order model ($g(\alpha)=-\ln(1-\alpha)$) with $A=1 \times 10^{15} \text{ min}^{-1}$ and $E_a=100 \text{ kJ/mole}$ (Figure 52). Thirteen additional simulations (B2–14) were generated from B1 using the same kinetic parameters and model but with perturbations in temperature or heating rate (Table 22).

The first simulation in set C (C1) consisted of five error-free nonisothermal (α -T) curves which were generated using the same parameters for simulation B1 except the heating rates (0.5, 1, 1.5, 2 and 2.5 K/min) (Figure 53) covered a narrower range. Nine additional simulations (C2-C10) were generated from C1 using the same kinetic parameters and model but with different perturbations in each (Table 23). The use of low heating rates as in simulation set C has been previously suggested [37] to narrow the temperature range of nonisothermal experiments. Narrow temperature ranges may reduce differences between isothermal and nonisothermal experiments [37]. Perturbations introduced into each nonisothermal simulation set included shifting one or more curves or

changing their nominal heating rate. A curve shift simulates thermal lag in a sample, while a change in the nominal heating rate simulates possible self cooling/heating effects or the effect of using the programmed heating rate rather than the actual one.

Kinetic analysis of each isothermal simulation was done by the conventional model-fitting method and several isoconversional methods (i.e. standard method [41], Friedman's method [58] and the advanced isoconversional method, AIC [25, 63]).

Nonisothermal kinetic analysis was done by the Coats-Redfern model-fitting method [48, 49] in addition to several isoconversional methods: Ozawa-Flynn-Wall (OFW) [59, 60]; Vyazovkin's isoconversional (VYZ) [62]; and, the advanced isoconversional (AIC) [25, 63].

All kinetic analysis was done with Microsoft Excel[®], as discussed in Chapter 3. The differential ($d\alpha/dt$) in Friedman's method was numerically evaluated without smoothing.

Sulfameter solvate desolvation

Sulfameter was obtained from Sigma[®] Chemical Co. while dioxolane was obtained from Aldrich[®] Chemical Co. These chemicals were used as supplied. A dioxolane solvate of sulfameter was prepared by recrystallizing sulfameter from the neat solvent, as described in Chapter 3. Samples were sieved and a particle size range of 90 – 355 μm was used for isothermal experiments and a range of 850–1700 μm was used for nonisothermal experiments.

Desolvation kinetics for this solvate was followed by thermogravimetry using a Perkin-Elmer TGA 7, as explained in Chapter 3.

Isothermally, four different batches of sulfameter dioxolane solvate were separately prepared, a sample from each batch was analyzed (samples 1 – 4). Samples 1 and 2 were run without controlling particle size or weight while samples 3 and 4 were sieved and a particle size range of 90 – 355 μm was used and weights were within 5% of

each other. Runs were performed at nominal temperatures of 323, 328, 333, 338 and 343 K, the exact sample temperature was obtained by averaging observed sample temperatures over the time of the TGA run as explained in Chapter 3.

Nonisothermally, five data sets, each containing five samples of sulfameter-dioxolane were desolvated at different heating rates, within each set, sample weights were within 5% of each other. Runs were performed at nominal heating rates of 1, 1.5, 2, 2.5 and 3 K/min for two sets while nominal heating rates for the remaining three sets were 1, 2, 4, 8 and 16 K/min. The exact heating rate was obtained from the slope of the linear heating curve of the TGA run during the time period of significant weight loss, as explained in Chapter 3.

Kinetic analysis for desolvation data was done by model-fitting and isoconversional methods, as described in Chapter 3.

Results and Discussion

Figure 54 shows four isothermal desolvation thermograms for sulfameter-dioxolane samples (samples 1 –4) while Figure 55 shows five sets of nonisothermal desolvation thermograms for sulfameter-dioxolane samples. Gravimetric weight loss for these solvates showed a 1:1 drug – solvent ratio (~ 21% w/w). Kinetic analysis for simulated and real data sets is described below.

Kinetic analysis of simulated data

Isothermal data

Isoconversional methods

Isoconversional analysis (Figures 56–61) showed that changing the temperature in isothermal runs does not affect the shape (i.e. linearity or slope) of the isoconversional ($E_a-\alpha$) plot. However, it does significantly change calculated E_a values, as seen in

simulations A7–8 (Figure 58). A change in the shape of an isoconversional plot represents an artificial variation in activation energy.

Shifting one or more curves had different effects based on the type of curve shift introduced. Systematic curve shifts (moving a curve by a constant percent, (A2–6)) had no effect on the shape of the isoconversional plot, but considerably altered calculated values of E_a from all three isoconversional calculation methods (Figure 57). On the other hand, shifting a curve by a fixed time (A9–13) significantly changed the shape of isoconversional plots calculated from the standard isoconversional method while those calculated from the Friedman and AIC methods were unaffected (Figures 58–60). Changes in the shape of isoconversional plots (i.e. the artifactual variation in activation energy), are due to variation of introduced errors at each α , the highest error being at low α values, which accounts for the observed deviation in E_a from 100 kJ/mole in some simulations. For example, A9 and A10 (Figure 58) show opposite deviations in E_a values that result from a ± 0.016 minute curve shift (Table 21), which occur up to $\alpha = 0.5$. A similar result is seen for A11–14 (Figures 59–60) where larger E_a deviations are seen compared to A9–10 due to larger introduced curve shifts (Table 21). Traditionally, researchers [132] have suggested analyzing solid-state kinetics over selected conversion values (i.e. 0.1 – 0.9) because errors are usually highest at extreme conversion values (i.e., $\alpha < 0.1$ and $\alpha > 0.9$).

Our results also show that some simulated runs were more sensitive to the same perturbation than others. Perturbations affecting the middle curve (third of five) introduced less error than those affecting extreme curves (i.e. first or fifth curve). For example, when curves were systematically shifted by -10% minutes in A2–6 (Figure 57), calculated values of E_a increased by about 0.6% in A4 where the third curve was shifted compared to a change of about 4% in A2 and A6 that involved shifting the first or last curve. Similarly, curves shifted by a fixed time as in A9–12 (Figures 58–59) showed variable effects in the results calculated from the standard isoconversional method. For

example, when the fifth curve (343 K curve) was shifted by ± 0.016 minutes as seen in A9–10 (Figure 58), deviations in calculated E_a values as large as 25% were seen, however when the curve shift was six times higher (curve shifted by ± 0.1 minutes) on the middle curve (333 K curve) as in A11–12 (Figure 59), the deviation in calculated E_a values did not exceed 0.6%.

Model-fitting results

Kinetic analysis of each simulation was done by the conventional model-fitting method where several kinetic triplets (model, A and E_a) were obtained (Table 24). Model selection (i.e., the first fit) was not affected by any introduced perturbation. The correct model (F1) was selected for all isothermal simulations (A1–15) and essentially perfect first-order plots were obtained ($r=1.000$). Model-fitting results agreed with those obtained from the Friedman and AIC methods which showed that the model-fitting method is less sensitive to some of the perturbations (namely, curve shifts by a fixed time) compared to the standard isoconversional method. While the shape of the standard isoconversional plot changed for A9–13 (Figures 58–60). Kinetic parameters obtained by the model-fitting method for these simulations were not affected (Table 24). Both isoconversional and model-fitting results were similarly affected by either changing the isothermal temperature as in A7–8 (Figure 58) or systematically shifting one or more curves as in A2–6 (Figure 57).

Nonisothermal data

Isoconversional methods

Kinetic results for nonisothermal data (Figures 62–68) show the sensitivity of isoconversional methods to introduced perturbations. This sensitivity is manifested either as an inaccurate value of E_a or as an artifactual variation of E_a as a function of α .

Perturbations involving curve shifts had two effects on kinetic analysis. First, calculated E_a values were significantly affected and second, the linearity of isoconversional plots was affected producing an artifactual variation in E_a . These effects were seen for both simulation sets B (B2–7, Figure 63; B13, Figure 64) and C (C2–9, Figure 67).

Perturbations which changed the heating rate did not affect the shape (i.e., linearity) of the isoconversional (E_a - α) plot. However, they significantly changed calculated E_a values, as seen in simulations B8–12 (Figure 64).

Analysis of simulation results also showed that the same perturbation had different effects on each curve, which has been previously shown isothermally. In simulation set B, perturbations affecting the middle curve (3rd of five) produced less error than those affecting the outer curves (i.e. 1st or 5th curve). For example, in simulations B3 and B7 (Figure 63), shifting an outer curve (1st or 5th) by -2 K produced a larger error in E_a compared to simulation B5 with the same shift on a middle curve ($\sim 6\%$ versus 0.8%). A similar observation is seen for simulations B8 and B12 where a larger error in E_a was produced when an outer curve was shifted compared to less error for B10 which involved a shift in the middle curve ($\sim 3\%$ versus $<0.1\%$, Figure 64). The maximum error in E_a was produced in simulation B13 where more than one curve was shifted ($\sim 18\%$, Figure 64). For simulation set C, fitted results also showed that perturbations affecting outer curves (i.e., 1st or 5th) produced higher E_a variation than those affecting the middle curve (i.e., 3rd). However, errors in E_a differed if the direction of the perturbation changed (Figure 67). For example, simulations C2 and C6, involved shifting the first (C2) and fifth (C6) curves by $+2$ K or -2 K, respectively, gave $\sim 16\%$ error in E_a (C2) compared to $\sim 10\%$ error (C6). Similarly, C2 and C7 involved shifting the first curve (0.5 K/min curve) by $+2$ K and -2 K, respectively, producing $\sim 16\%$ (C2) compared to $\sim 14\%$ (C7) errors in E_a . Also, C4 and C8 involved shifting the third curve (1.5 K/min curve) by $+2$ K and -2 K, respectively, producing errors of $\sim 4.5\%$ (C4) or $\sim 0.7\%$ (C8).

Errors produced in simulation set C were generally higher than those in set B. For example, a curve shift of -2K for the first curve in simulations B7 and C7 produced an E_a error of $\sim 7\%$ (B7) versus $\sim 14\%$ (C7). Shifting the last curve by $+2\text{K}$ and -2K in B2 and B3 produced $\sim 6\%$ error in E_a for each. However, these shifts ($+2\text{K}$ and -2K in the last curve) produced E_a errors $\sim 10\%$ (C6) and 8% (C9) in set C. Larger errors in simulations C are probably due to the experimental design. In this simulation set (set C), heating rates were selected to yield curves that cover a narrower temperature range, which produced curves less separated than those over the wider temperature range in simulation set B. For example, C1 curves were closely spaced (Figure 53) with each curve separated by the 0.5 K/min difference in heating rate (i.e., $0.5, 1, 1.5, 2$ and 2.5 K/min), whereas, curves in simulation B1 (Figure 52) were separated by a twofold heating rate difference (i.e., $2, 4, 8, 16$ and 32 K/min). As a result, any curve shift is likely to affect closely spaced curves (set C) more than widely spaced ones (set B).

Because narrow temperature-range curves are so closely spaced, any shift within these curves may cause a curve to shift to a position where it overlaps the curve that follows it (i.e., curve having a higher heating rate) or overlaps the curve that precedes it (i.e., curve having a lower heating rate). This overlap was observed in simulations C4 (1.5 and 2 K/min curves), C5 and C9 (2 and 2.5 K/min curves) as seen in Figure 69a–c, but this effect is less likely in wider temperature-range curves as they are more widely spaced. Even when maximal curve shifts were introduced (B13), simulated curves remained well separated (Figure 69d).

Data analysis also showed that the AIC method was slightly more accurate in calculating E_a than the OFW or VYZ methods, however, it was more sensitive to random errors (Figures 65 and 68). The higher random error is probably due to integration over small α intervals ($\Delta\alpha=0.05$) in Eq. (66); the scatter could be reduced by smoothing but experimental information could be lost if too much smoothing is done.

Model-fitting methods

Kinetic analysis of simulated data by the Coats-Redfern model-fitting method show that perturbations introduced had little effect on calculated kinetic parameters (Table 25) as A and E_a were calculated with little error. However, two problems were encountered: all models gave acceptable fits ($r > 0.93$); some models were indistinguishable (A2, A3, A4 and F1) based on quality of the fit (i.e., all r -values equal). Therefore, quality of fit is a poor indicator of the best model when using model-fitting methods, as other authors have reported [37] and is further explained in Chapter 5.

Kinetic analysis of sulfameter desolvation

Isothermal data

Kinetic analysis of sulfameter-dioxolane desolvation using the standard isoconversional method showed that shapes of isoconversional plots are substantially different. For the first two samples (Figure 70a–b), this variation was anticipated since experimental variables were not as carefully controlled. However, for the second two samples (Figure 70c–d), experimental conditions were nearly identical but the isoconversional plot still showed large differences at low conversion values, whereas at $\alpha > 0.4$ both isoconversional plots obtained from the standard method are almost identical for these samples. This finding resembles results obtained for the same method for simulations A9–10 (Figure 58) and A11–12 (Figure 59).

Kinetic analysis done with the Friedman and advanced isoconversional (AIC) methods showed less variable activation energy compared to the standard isoconversional method (Figure 71). However, calculated activation energies were highly scattered with the Friedman's method which was also seen in simulation A15 (Figure 61) which is common with differential methods, the scatter could be reduced by smoothing but experimental information could be lost if this is not done carefully. There was also some scatter in the isothermal desolvation results obtained by the AIC method for both

simulated (Figure 61) and experimental data (Figure 71), which can also be seen in some other AIC results [63]. This scatter is probably due to integration over small α intervals.

Kinetic analysis done with the model-fitting method (Table 26) gave E_a values that agreed with those obtained from the AIC method. Results obtained from the model-fitting method also showed an agreement with those obtained from the standard isoconversional method for $\alpha > 0.4$. Model-fitting results also showed that calculated activation energies were not very dependent upon the kinetic model (Table 26). This means that for the same run, any model gives very comparable activation energies which agrees with previous reports [38, 159].

Comparison of activation energies obtained from different methods suggests that the observed variation in E_a in the standard isoconversional method for samples 3–4 is artifactual, which could be due to a less controlled experimental variable that may have shifted any of the α -time curves for these two samples (Figure 54). These two samples gave widely varying E_a values up to $\alpha \sim 0.4$. It seems that desolvation of sulfameter dioxolane solvate having a particle size of 90–355 μm (samples 3–4) has an activation energy of 75–85 kJ/mol if the results of the standard method for $\alpha > 0.4$ are to be believed, which agrees with the results obtained from the AIC (Figure 70c–d) and model-fitting (Table 26) methods.

Nonisothermal data

Figure 72 shows E_a - α plots for the desolvation of five experimental data sets for sulfameter-dioxolane solvate desolvation. The isoconversional plots of all sets show variation in E_a . Sample sets 1–2 (Figure 72a–b) show the highest random scatter (AIC method) and systematic variation in E_a . The isoconversional plots for the two sets were also significantly different, especially for $\alpha < 0.5$ (Figure 73). On the other hand, sample sets 3–5 (Figure 72c–e) showed less systematic E_a variation and random scatter.

However, the isoconversional plots for all three data sets were comparable (Figure 73) indicating better consistency of more widely spaced heating rates.

Isoconversional plots for sets 1–2 are comparable to those for simulation set C as they involve heating rates that produce closely spaced curves (i.e., cover a narrow temperature range) while plots for sets 3–5 are comparable to those obtained from simulation set B as they involve heating rates that produce widely spaced curves (i.e., cover a wider temperature range). Large errors seen in sample sets 1–2 compared to sets 3–5 are perhaps due to the nature of the experimental protocol as was seen for simulation set C. Like simulation C1, curves in sample sets 1–2 were closely spaced where small curve shifts in these sets caused their positions to move above or below their expected positions (Figure 74a) which dramatically affects the shape of isoconversional plots (Figure 73). Similarly, simulation B1 resembles those of sample sets 3–5 as they were widely spaced and curve shifts due to experimental variation had less effect on curve positions (Figure 74b) and the shape of isoconversional plots (Figure 73).

Also, experimental TGA curves are generally expected to produce more errors in the isoconversional kinetic analysis because, in addition to any observed curve shift that might occur, actual heating rates are usually different from those programmed due to self heating/cooling effects. Therefore, in reality, curves are more tightly spaced than expected in the experimental protocol.

Model-fitting results of sample sets showed that kinetic parameters (A and E_a) of all sets gave comparable values for each model (Table 27). Therefore, curve shifts that occurred from different experimental variables had less effect on kinetic parameters calculated by the Coats-Redfern method. This finding was also substantiated by the analysis of simulated data. Problems encountered with the Coats and Redfern model-fitting method were similar to those seen for simulated data which included excellent fits for all models ($r > 0.94$, Figure 75) with some models being indistinguishable (A2, A3, A4 and F1) based on a statistical criterion (see variation in r for each model, Figure 75).

Confidence intervals for activation energies

To minimize experimental errors encountered, it is often necessary for experimental conditions to be rigorously controlled. For solid-state kinetic studies, this can be achieved by sieving the sample, using the same weight for each run ($\pm 5\%$), controlling purge gas flow rate as well as other variables. However, such variations can not be totally eliminated and random experimental errors could produce significant variation in calculated kinetic parameters. Therefore, replicate samples should be analyzed, which permits calculating an average value of the activation energy with a confidence interval. The 95% confidence interval of the activation energy was calculated for the isothermal desolvation of sulfameter dioxolane solvate (Figure 76) by averaging all four previous runs (samples 1 – 4) even though two runs had less well controlled particle size and weights. For the standard isoconversional method (Figure 76a), this average showed the widest confidence intervals ($\pm 40\%$) for low α ($\alpha \leq 0.2$) while the smallest were $\pm 8\text{--}12\%$ for $\alpha > 0.2$. On the other hand, averaging all four runs for the AIC method (Figure 76b) showed uniform confidence intervals of $\pm 10\text{--}20\%$ at all values of α .

Judging from the simulation results, plot (Figure 76b) is probably more representative of the actual activation energy than that in (Figure 76a).

The systematic decrease of confidence intervals with reaction progress seen in the standard isoconversional method further supports the somewhat artifactual activation energy variation at low α .

Conclusions

The debate over variable activation energy is most often due to viewing heterogeneous solid-state kinetics from a homogenous perspective. However, explanations are necessary for this behavior to better understand solid-state reaction mechanisms.

Activation energy variation could be real or artifactual. A true variation in activation energy is one that occurs because of the inherent complexity of the solid sample which includes different reactivity of individual particles due to particle size variations or crystal imperfections. Artifactual variations arise from the kinetic calculation methods employed. Our results showed the sensitivity of some calculation methods to introduced experimental variables. This sensitivity is manifested by an artifactual variation in activation energy as a function of α . Methods do not equally contribute to the observed variation in activation energy.

Isothermally, the standard isoconversional method gives the most activation energy variation, which does not occur with Friedman's or AIC methods. However, both methods show some data scattering, which is quite significant in Friedman's method such that it is far less useful for analyzing real experimental data if no data smoothing is employed. Activation energy calculated from the model-fitting method like the Friedman and AIC methods, is apparently least affected by experimental variables. The AIC method appears to be a superior isoconversional method and its use should be encouraged in isothermal experiments. Results from this method should be used in conjunction with those from the model-fitting method to determine the most accurate values of E_a and A .

Nonisothermally, results showed that all tested isoconversional methods produced artifactual variation in E_a . While the magnitude of this variation appears to be small in some experiments where curves were well separated, the magnitude of artifactual variation was quite high in others which had little separation between curves. Artifactual E_a variation can be attributed to various experimental variables that can shift thermogravimetric curves from their expected positions (e.g., less systematic shift with increasing heating rate) which are manifested as variations in E_a with isoconversional analysis methods. Such variations in E_a will be observed in all nonisothermal isoconversional methods. Therefore, such a variation can not be reduced or prevented in any isoconversional method unless more careful control of experimental variables and

better experimental design are applied. Nonisothermal experiments should be designed so that curves are widely separated. A twofold difference in heating rates between curves produced more consistent E_a values in our experimental work. Model fitting methods were least affected by experimental variables that cause curve shifts. Inaccurate determination of heating rates affects all calculation methods in solid-state kinetic analyses. Therefore, the actual heating rate of each run rather than that programmed should be used in kinetic analyses.

Generally, care should be taken when interpreting kinetic results from isoconversional methods, if the variation in activation energy is artificial, this variation can lead to a false mechanistic conclusion about a reaction being complex while, in fact, it is not.

Finally, variation in activation energy could be a combination of the two aforementioned sources of variation (i.e., true and artificial), making the resolution into individual contributions difficult or impossible. There seems to be no ideal method for evaluating solid-state kinetics because calculated values of activation energy could be in error, even when results from isoconversional and the model-fitting methods agree. To overcome this, experimental variables should be adequately controlled and experiments replicated, so that averaged kinetic parameters and their confidence intervals can be estimated.

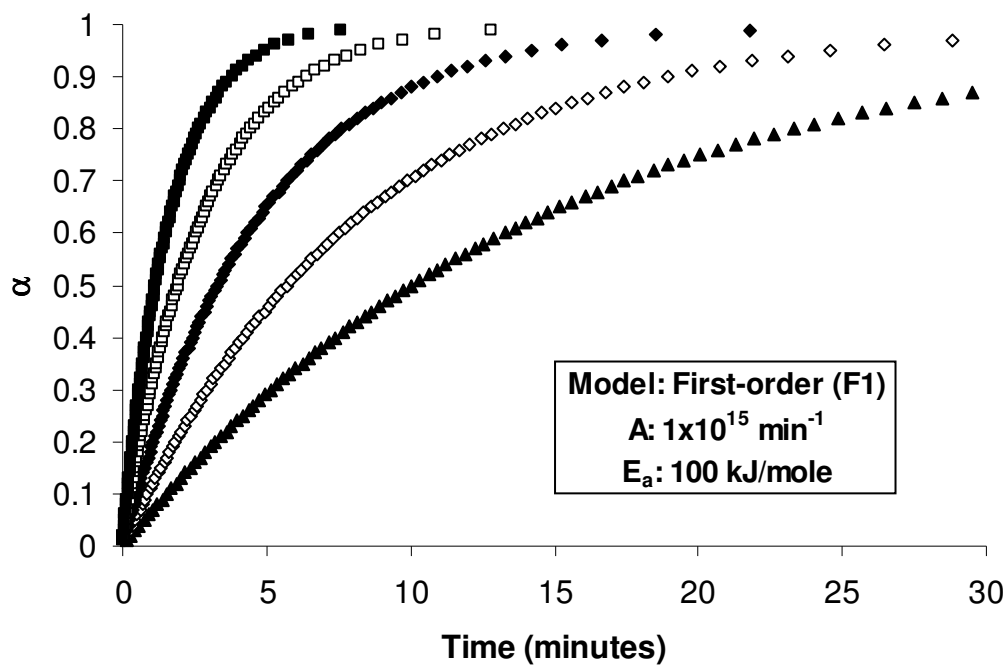


Figure 51. Error-free simulation (A1) of α versus time for several isothermal kinetic runs at: \blacktriangle , 323 K; \diamond , 328 K; \blacklozenge , 333 K; \square , 338 K; and \blacksquare , 343 K. The inset gives the simulation model, pre-exponential factor (A) and activation energy (E_a).

Table 21. Variations in isothermal simulations generated from simulation A1 (error-free), produced using a first-order reaction model (F1) with $A=1 \times 10^{15} \text{ min}^{-1}$ and $E_a=100 \text{ kJ/mole}$.

Simulation	Simulation characteristics
A1	Error-free simulation of five isothermal curves at 323, 328, 333, 338 and 343 K.
A2	323 K curve of simulation A1 shifted by -10% in time.
A3	328 K curve of simulation A1 shifted by -10% in time.
A4	333 K curve of simulation A1 shifted by -10% in time.
A5	338 K curve of simulation A1 shifted by -10% in time.
A6	343 K curve of simulation A1 shifted by -10% in time.
A7	Temperature of 343 K curve in simulation A1 taken as 340 K.
A8	Temperature of 333 K and 343 K curves in simulation A1 taken as 335 K and 340 K, respectively.
A9	343 K curve of simulation A1 shifted by -0.016 min .
A10	343 K curve of simulation A1 shifted by $+0.016 \text{ min}$.
A11	333 K curve of simulation A1 shifted by -0.1 min .
A12	333 K curve of simulation A1 shifted by $+0.1 \text{ min}$.
A13	333 K and 343 K curves of simulation A1 shifted by $+0.2$ and -0.1 min , respectively.
A14	Simulations A7 and A9 combined.
A15	0.5% random error in time introduced to each curve in simulation A1

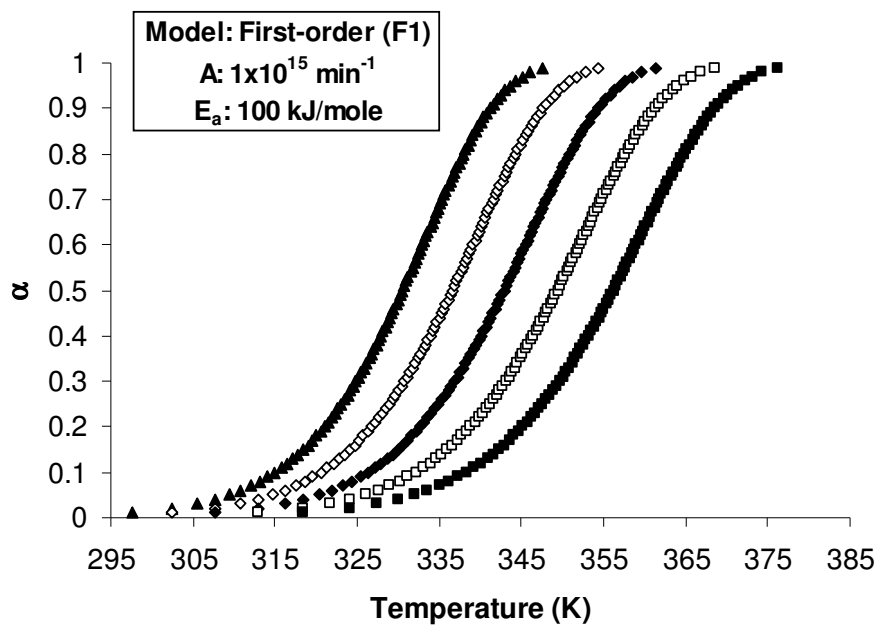


Figure 52. Error-free simulations (B1) of α versus temperature for nonisothermal kinetic runs at: \blacktriangle , 2 K/min; \diamond , 4 K/min; \blacklozenge , 8 K/min; \square , 16 K/min and \blacksquare , 32 K/min. The inset gives the model, pre-exponential factor (A) and activation energy (E_a) for these simulations.

Table 22. Nonisothermal simulations generated from simulation B1 (error-free), produced using a first-order reaction model with (F1) with $A=1 \times 10^{15} \text{ min}^{-1}$ and $E_a=100 \text{ kJ/mole}$. Simulations B2–B13 are perturbations of B1.

Simulation	Simulation characteristics
B1	Five nonisothermal curves at heating rates of 2, 4, 8, 16 and 32 K/min.
B2	32 K/min curve shifted by + 2 K
B3	32 K/min curve shifted by – 2 K
B4	16 K/min curve shifted by – 2 K
B5	8 K/min curve shifted by – 2 K
B6	4 K/min curve shifted by – 2 K
B7	1 K/min curve shifted by – 2 K
B8	Heating rate of 32 K/min curve taken as 28.2 K/min.
B9	Heating rate of 16 K/min curve taken as 14.4 K/min.
B10	Heating rate of 8 K/min curve taken as 7.2 K /min.
B11	Heating rate of 4 K/min curve taken as 3.6 K /min.
B12	Heating rate of 2 K/min curve taken as 1.8 K /min.
B13	2 K/min and 32 K/min curves shifted by +3 K and –2 K respectively.
B14	0.5% random error in temperature (°C) added to each curve.

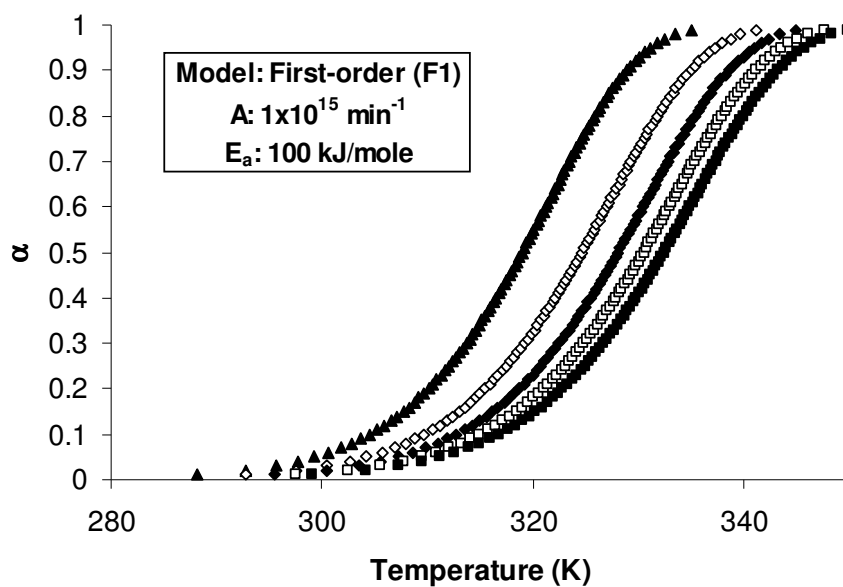


Figure 53. Error-free simulations (C1) of α versus temperature for nonisothermal kinetic runs at: \blacktriangle , 0.5 K/min; \diamond , 1 K/min; \blacklozenge , 1.5 K/min; \square , 2 K/min and \blacksquare , 2.5 K/min. The inset gives the model, pre-exponential factor (A) and activation energy (E_a) for these simulations.

Table 23. Nonisothermal simulations generated from simulation C1 (error-free), produced using a first-order reaction model with (F1) with $A=1 \times 10^{15} \text{ min}^{-1}$ and $E_a=100 \text{ kJ/mole}$. Simulations C2–C10 are perturbations of C1.

Simulation	Simulation characteristics
C1	Five nonisothermal curves at heating rates of 0.5, 1, 1.5, 2 and 2.5 K/min.
C2	0.5 K/min curve shifted by + 2 K
C3	1 K/min curve shifted by + 2 K
C4	1.5 K/min curve shifted by + 2 K
C5	2 K/min curve shifted by + 2 K
C6	2.5 K/min curve shifted by + 2 K
C7	0.5 K/min curve shifted by – 2 K
C8	1.5 K/min curve shifted by – 2 K
C9	2.5 K/min curve shifted by – 2 K
C10	0.5% random error in temperature (°C) added to each curve.

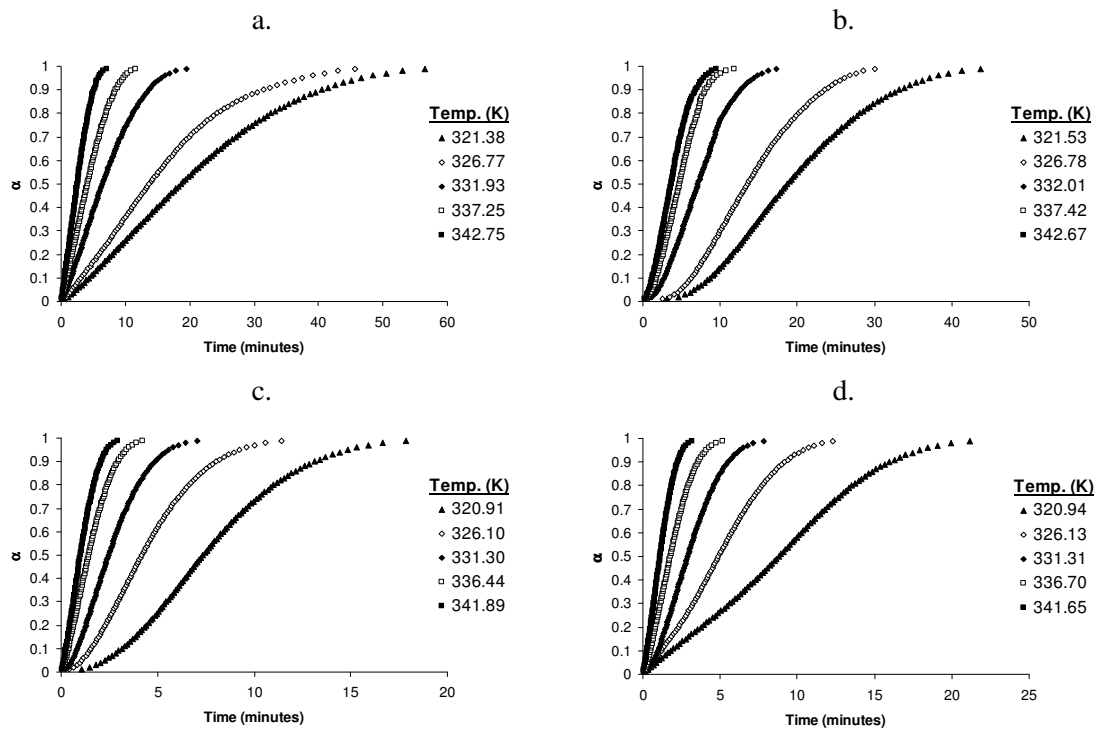


Figure 54. α versus time plots for the isothermal desolvation of sulfameter-dioxolane solvate samples: a, sample 1; b, sample 2; c, sample 3 and d, sample 4.

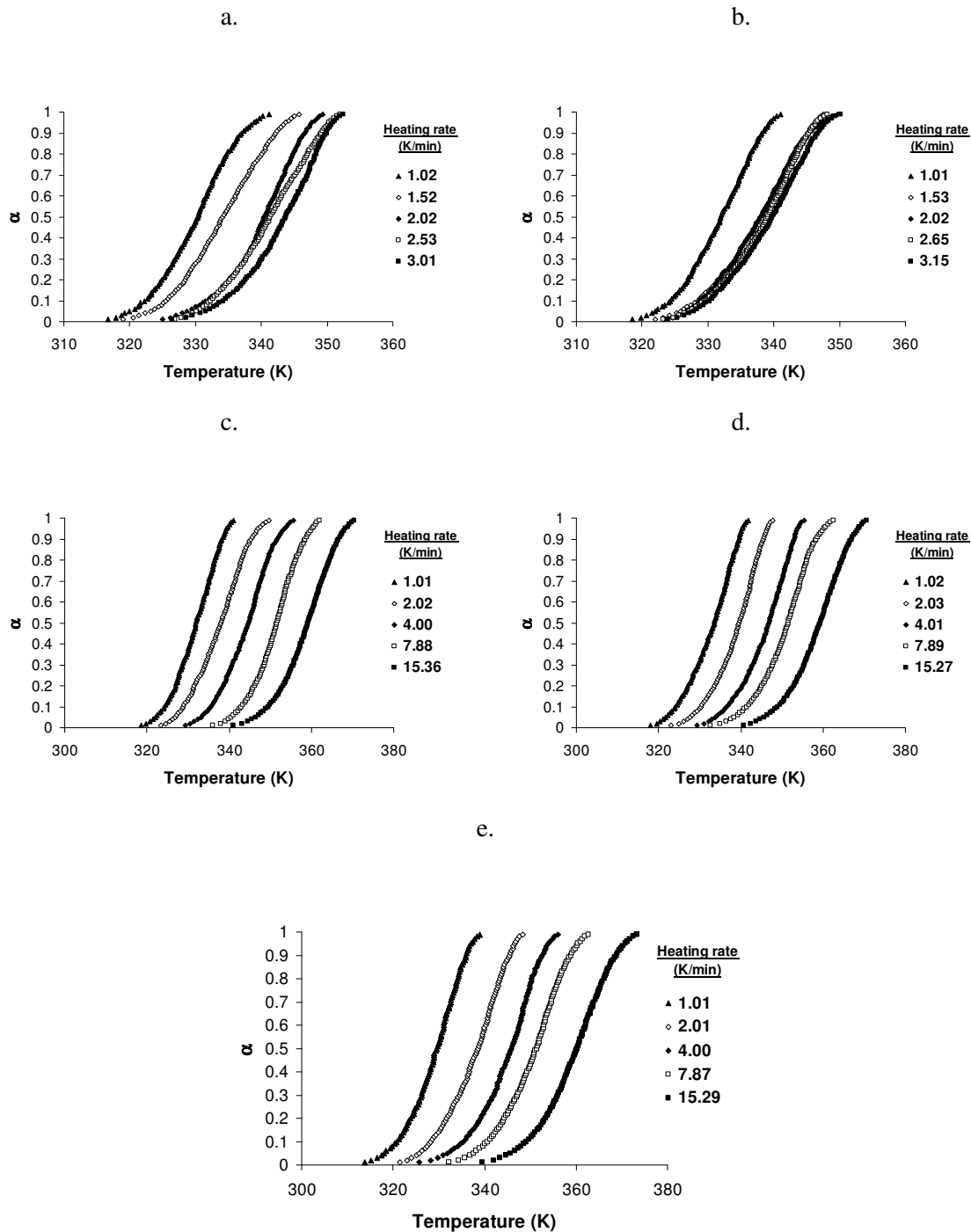


Figure 55. α versus temperature plots for the nonisothermal desolvation of sulfameter-dioxolane solvate sets: a, set 1; b, set 2; c, set 3; d, set 4 and e, set 5.

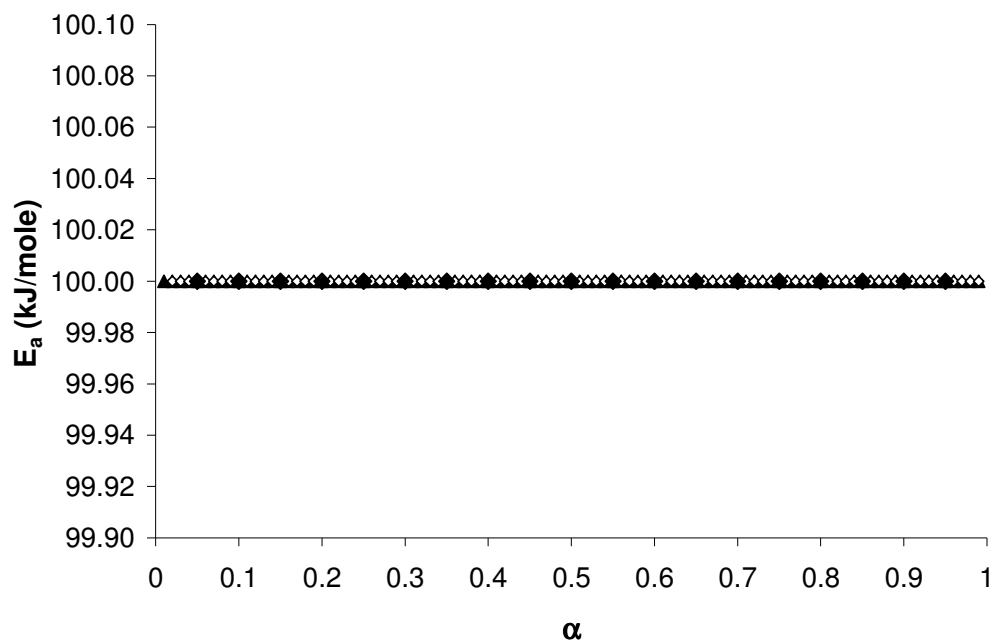


Figure 56. E_a versus α plots of simulated isothermal runs (A1), evaluated by three isoconversional methods: \blacktriangle , standard; \diamond , Friedman and \blacklozenge , AIC.

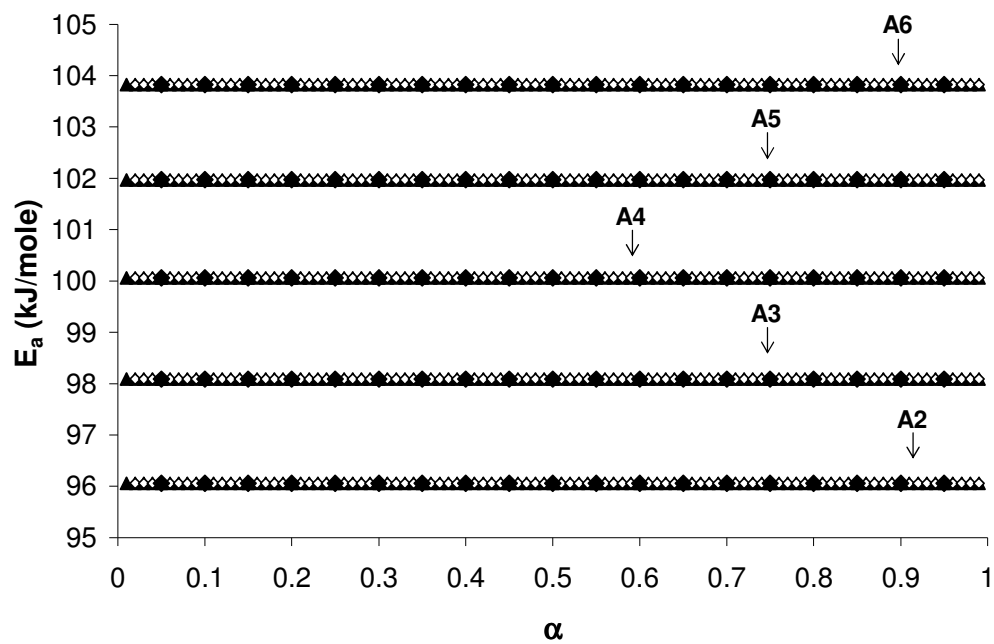


Figure 57. E_a versus α plots of simulated isothermal runs (A2–6), evaluated by three isoconversional methods: \blacktriangle , standard; \diamond , Friedman and \blacklozenge , AIC.

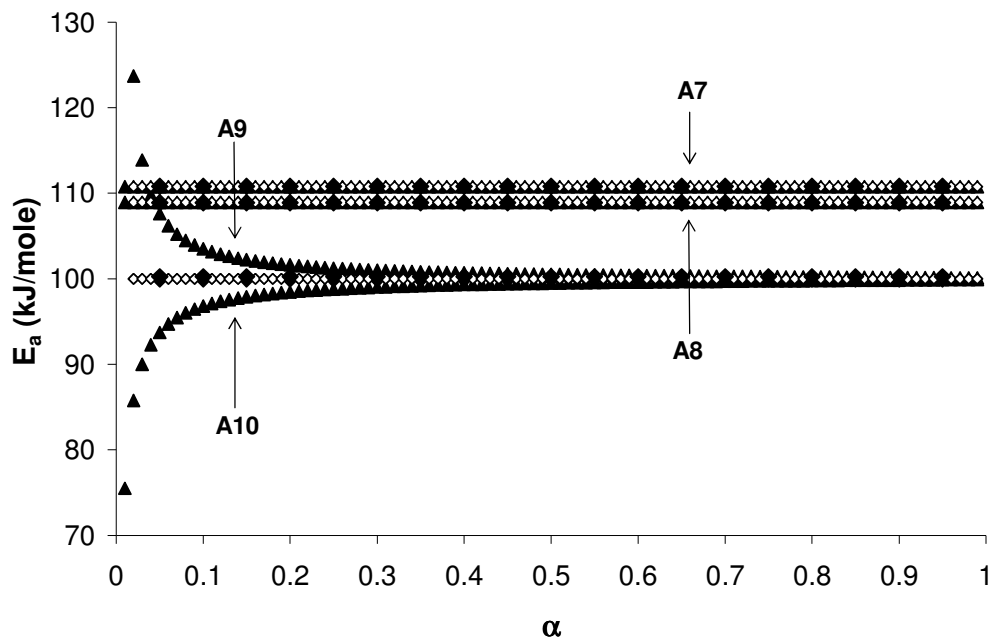


Figure 58. E_a versus α plots of simulated isothermal runs (A7–10), evaluated by three isoconversional methods: \blacktriangle , standard; \diamond , Friedman and \blacklozenge , AIC.

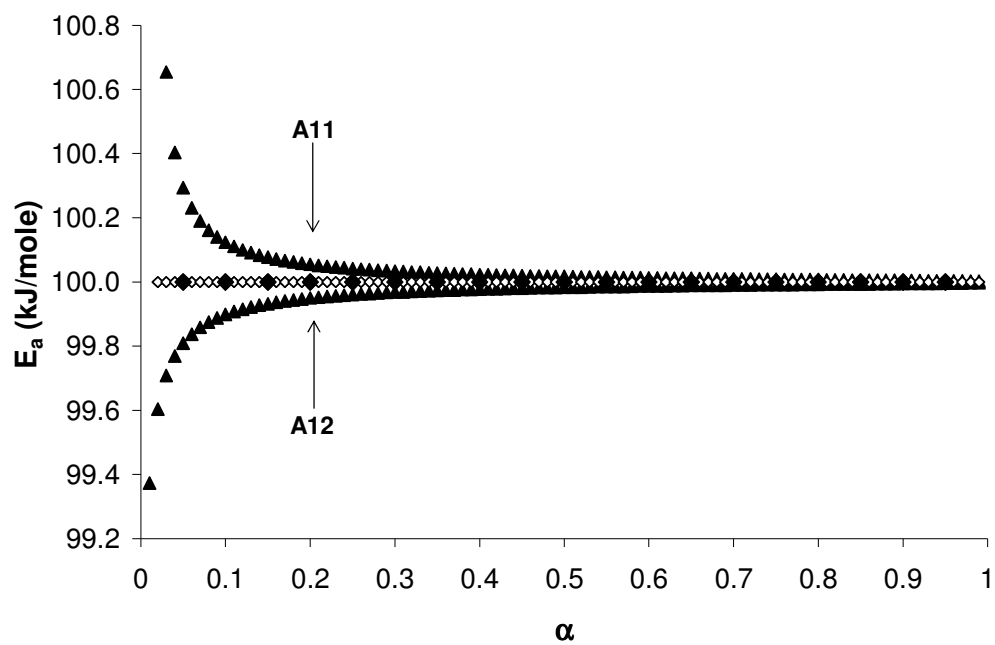


Figure 59. E_a versus α plots of simulated isothermal runs (A11–12), evaluated by three isoconversional methods: ▲, standard; ◇, Friedman and ◆, AIC.

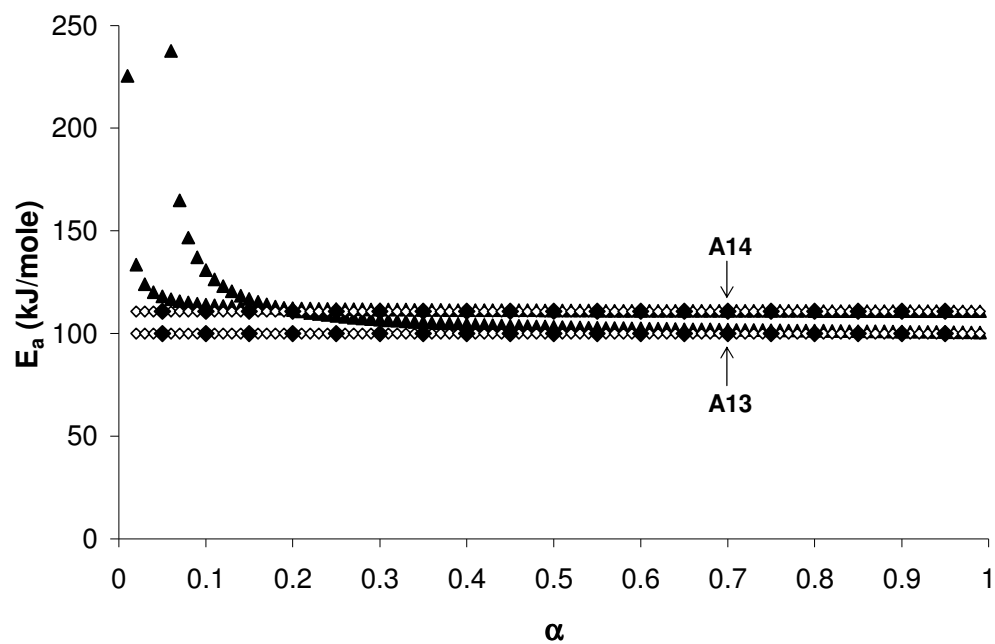


Figure 60. E_a versus α plots of simulated isothermal runs (A13–14), evaluated by three isoconversional methods: \blacktriangle , standard; \diamond , Friedman and \blacklozenge , AIC.

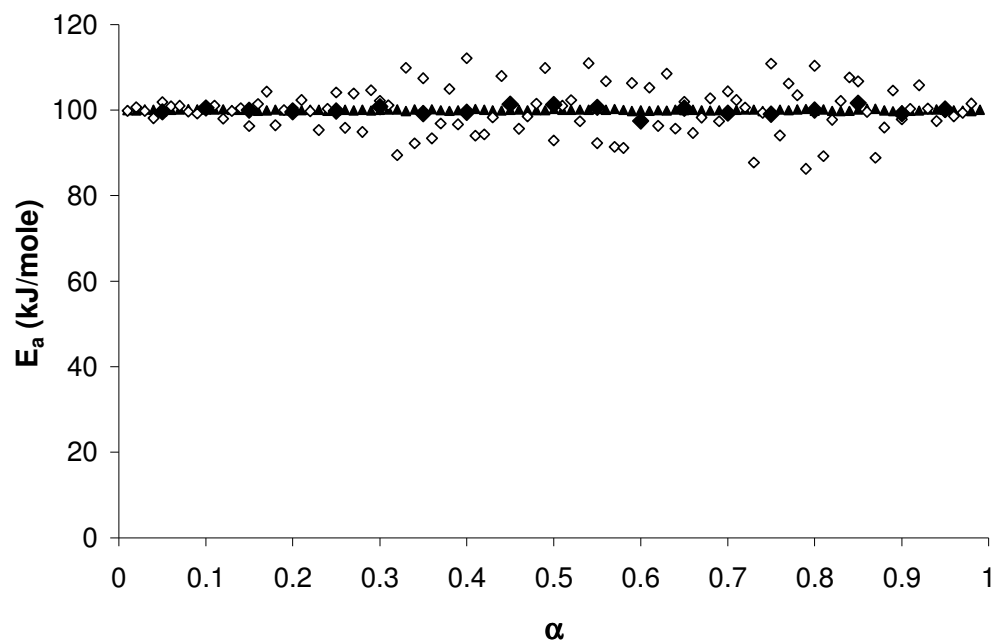


Figure 61. E_a versus α plots of simulated isothermal runs (A15), evaluated by three isoconversional methods: \blacktriangle , standard; \diamond , Friedman and \blacklozenge , AIC.

Table 24. Fitted kinetic parameters for simulated isothermal data (Table 21) using model-fitting methods.*

Simulation	A (min ⁻¹)	E _a (kJ/mole)	r **
A1	1.00 × 10 ¹⁵	100.00	- 1.0000
A2	2.46 × 10 ¹⁴	96.06	- 0.9992
A3	5.12 × 10 ¹⁴	98.09	- 0.9986
A4	1.04 × 10 ¹⁵	100.06	- 0.9985
A5	2.08 × 10 ¹⁵	101.97	- 0.9987
A6	4.07 × 10 ¹⁵	103.83	- 0.9993
A7	5.23 × 10 ¹⁶	110.77	- 0.9916
A8	2.89 × 10 ¹⁶	108.93	- 0.9824
A9	1.00 × 10 ¹⁵	100.00	- 1.0000
A10	1.00 × 10 ¹⁵	100.00	- 1.0000
A11	1.00 × 10 ¹⁵	100.00	- 1.0000
A12	1.00 × 10 ¹⁵	100.00	- 1.0000
A13	1.02 × 10 ¹⁵	100.06	- 1.0000
A14	5.23 × 10 ¹⁶	110.77	- 0.9916
A15	9.85 × 10 ¹⁴	99.96	- 1.0000

* Results shown for the F1 (i.e., first-order) model.

** Correlation coefficient for ln k vs. 1/T plot.

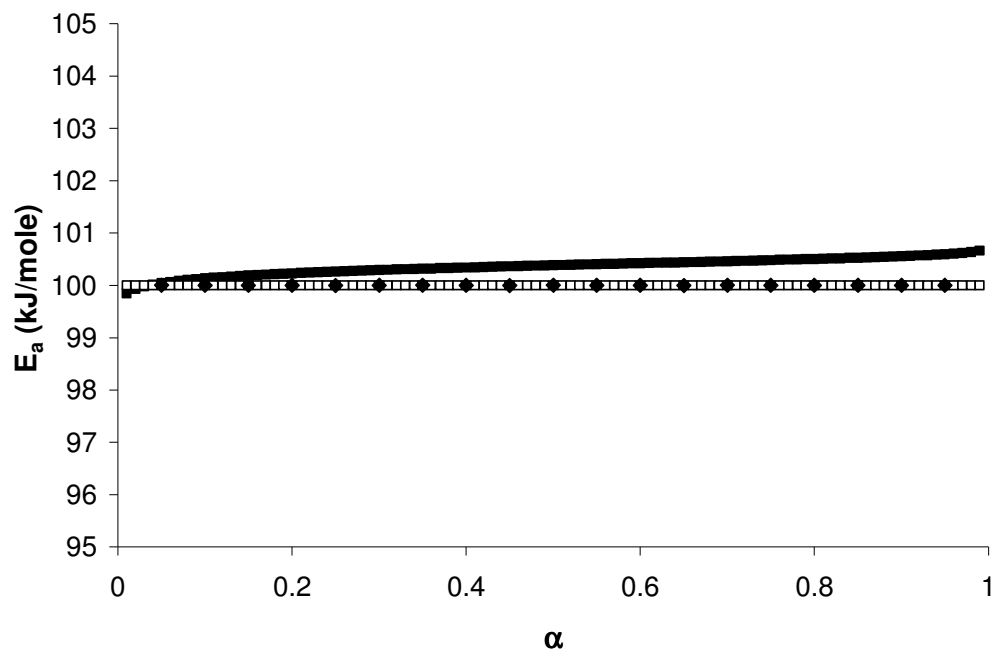


Figure 62. E_a versus α plots of simulated nonisothermal runs (Simulation B1), evaluated by three isoconversional methods: \square , VYZ; \blacksquare , OFW and \blacklozenge , AIC.

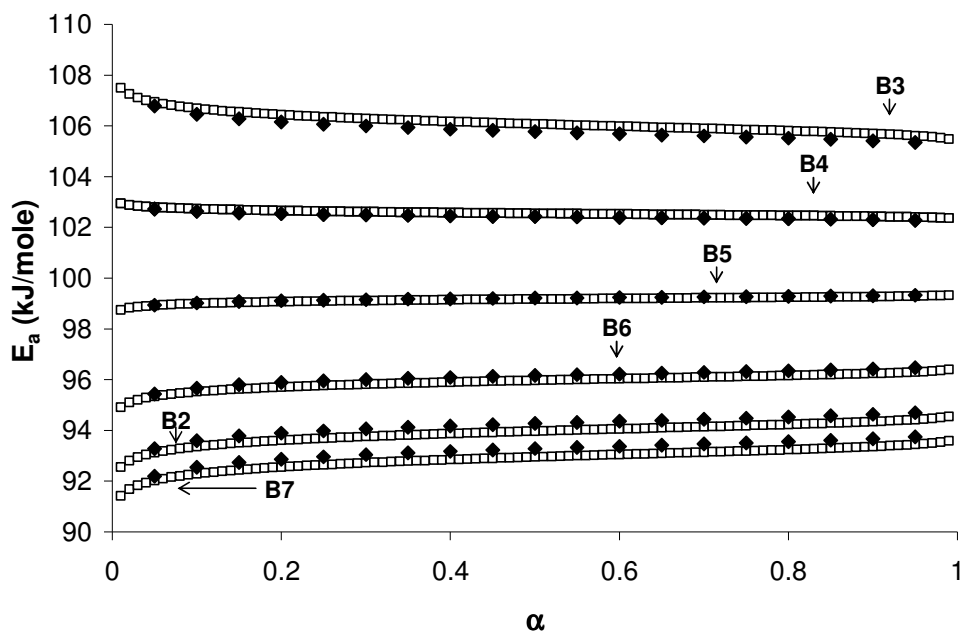


Figure 63. E_a versus α plots of simulated nonisothermal runs (Simulations B2–7), evaluated by two isoconversional methods: \square , VYZ and \blacklozenge , AIC.

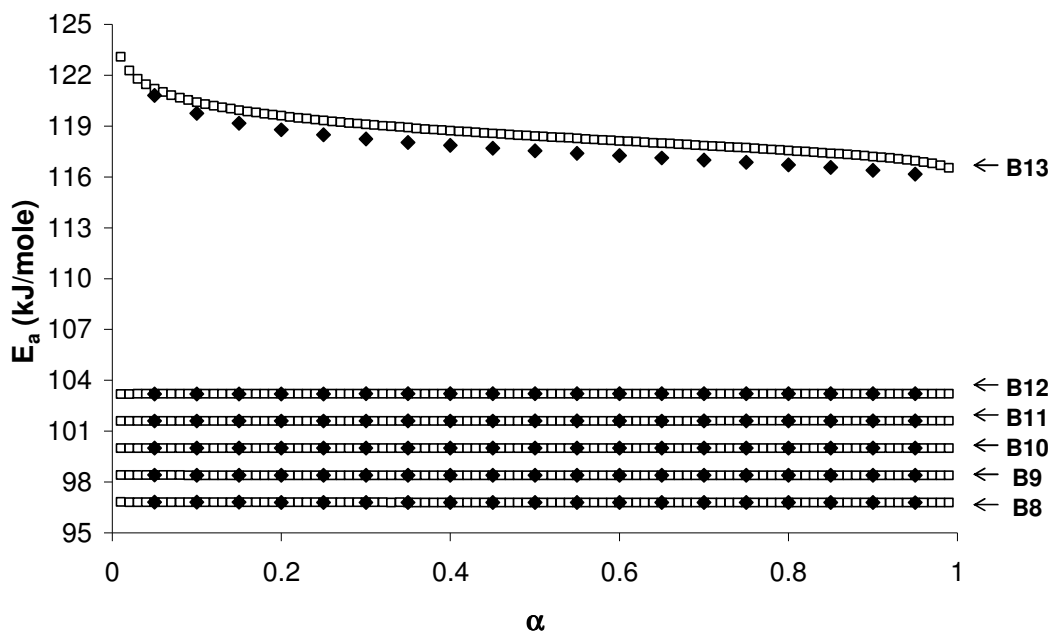


Figure 64. E_a versus α plots of simulated nonisothermal runs (Simulations B8–13), evaluated by two isoconversional methods: \square , VYZ and \blacklozenge , AIC.

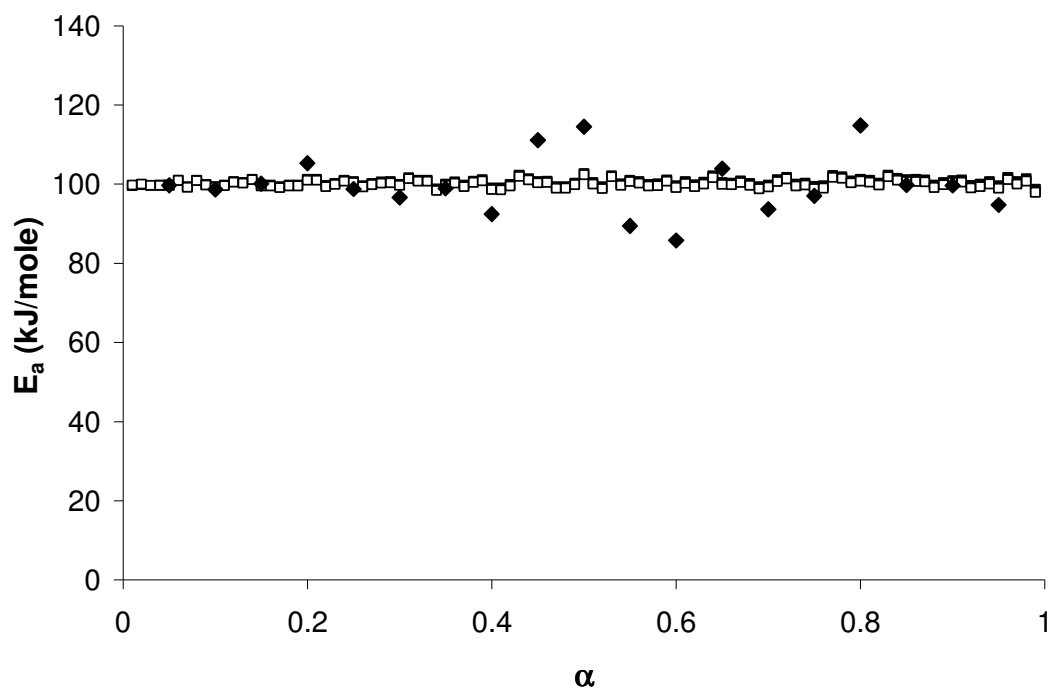


Figure 65. E_a versus α plots of simulated nonisothermal runs (Simulation B14), evaluated by three isoconversional methods: \square , VYZ; \blacksquare , OFW and \blacklozenge , AIC.

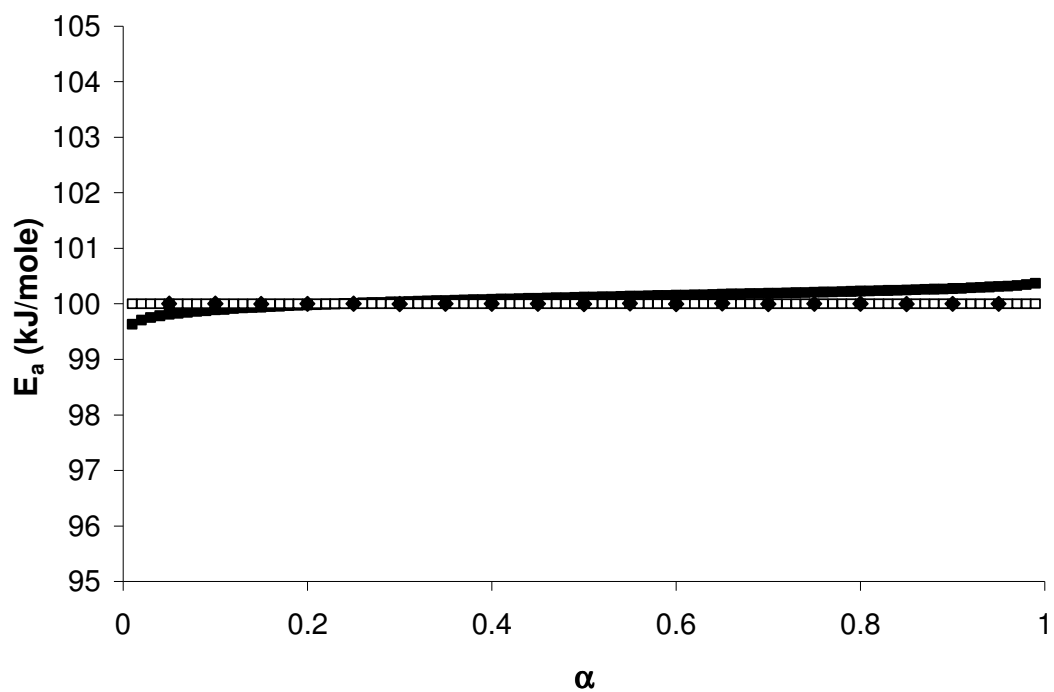


Figure 66. E_a versus α plots of simulated nonisothermal runs (Simulation C1), evaluated by three isoconversional methods: \square , VYZ; \blacksquare , OFW and \blacklozenge , AIC.

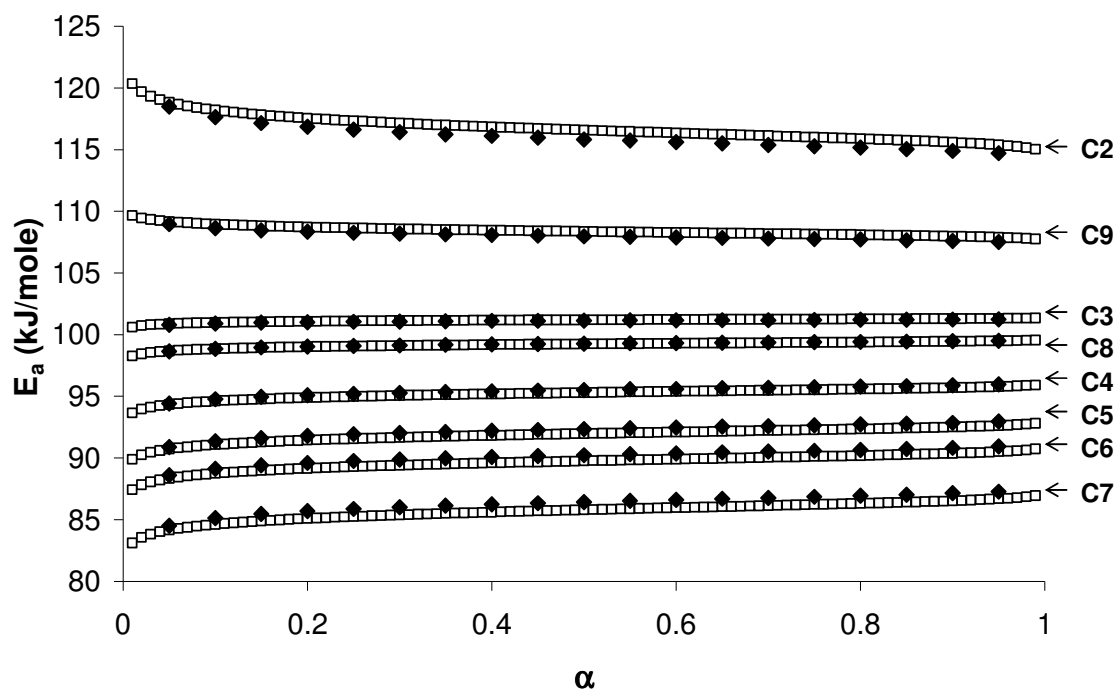


Figure 67. E_a versus α plots of simulated nonisothermal runs (Simulations C2–9), evaluated by two isoconversional methods: □, VYZ and ◆, AIC.

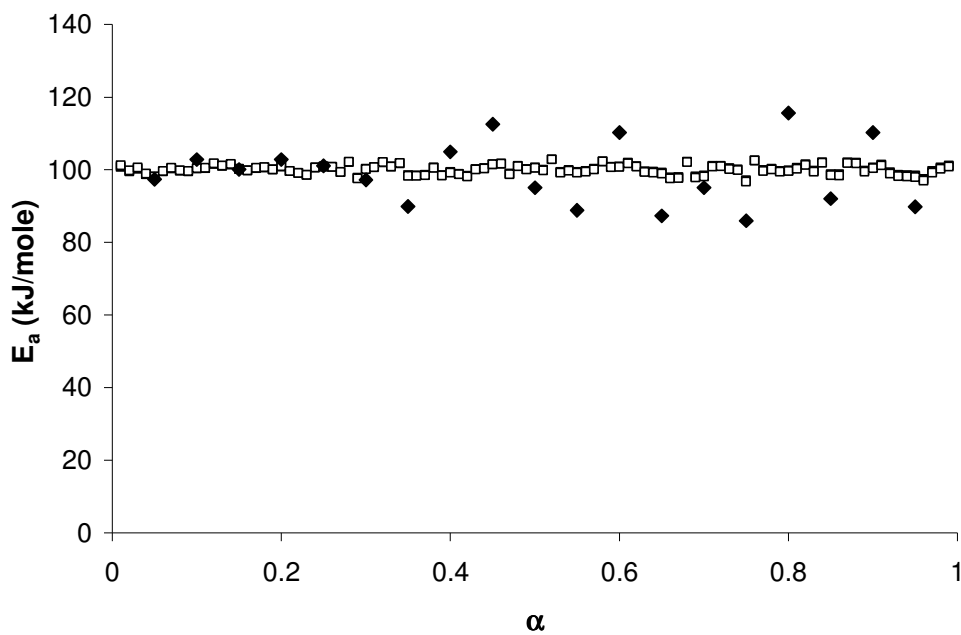


Figure 68. E_a versus α plots of simulated nonisothermal runs (Simulation C10), evaluated by three isoconversional methods: \square , VYZ; \blacksquare , OFW and \blacklozenge , AIC.

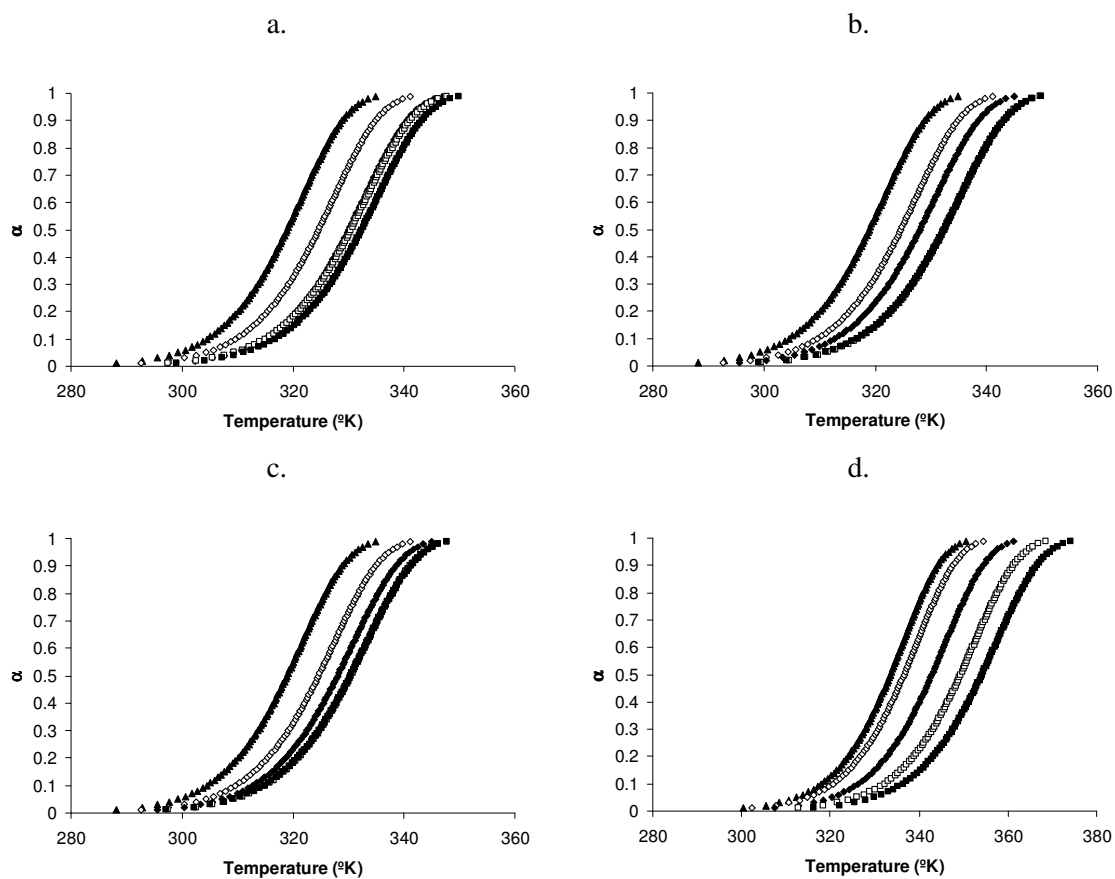


Figure 69. α versus temperature curves for simulations C4, C5 and C9 (a-c) at nominal heating rates of: \blacktriangle , 0.5 K/min; \diamond , 1 K/min; \blacklozenge , 1.5 K/min; \square , 2 K/min; \blacksquare , 2.5 K/min and simulation B13; (d) at: \blacktriangle , 2 K/min; \diamond , 4 K/min; \blacklozenge , 8 K/min; \square , 16 K/min and \blacksquare , 32 K/min.

Table 25. Fitted kinetic parameters for simulated nonisothermal data (B and C), using the Coats-Redfern method.^{*†}

Simulation	A (min ⁻¹) × 10 ¹⁴	E _a (kJ/mole)
B1	9.5	99.9
B2	10.0	100.1
B3	9.2	99.6
B4	9.1	99.6
B5	9.1	99.6
B6	9.1	99.6
B7	9.1	99.6
B8	9.3	99.9
B9	9.3	99.9
B10	9.3	99.9
B11	9.3	99.9
B12	9.3	99.9
B13	9.8	100.0
B14	9.7	99.9
C1	9.6	99.9
C2	10.1	100.1
C3	10.0	100.1
C4	10.0	100.1
C5	10.0	100.1
C6	10.0	100.1
C7	9.1	99.6
C8	9.1	99.6
C9	9.1	99.6
C10	9.4	99.8

* Results shown for first-order (F1) model.

† Results averaged from five heating rate curves using the geometric mean of A and E_a.

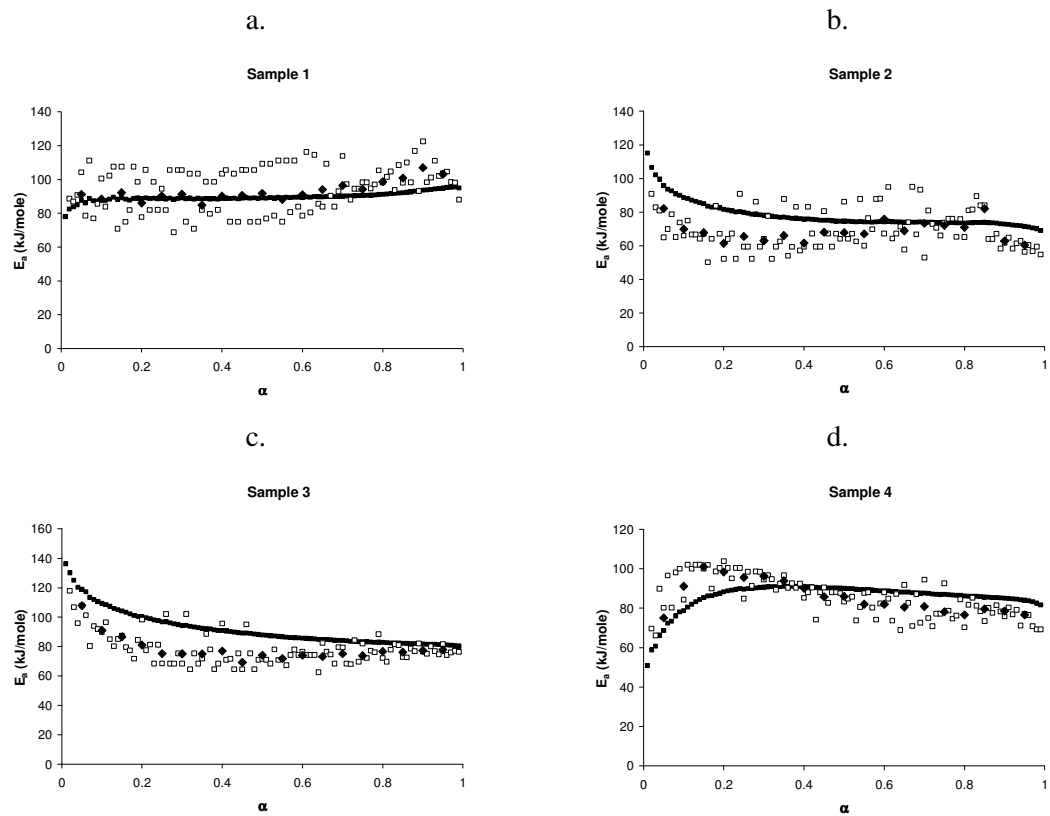


Figure 70. E_a versus α plots for isothermal sulfameter-dioxolane solvate desolvation runs (samples 1–4), evaluated by three isoconversional methods: ■, standard; □, Friedman and ◆, AIC.

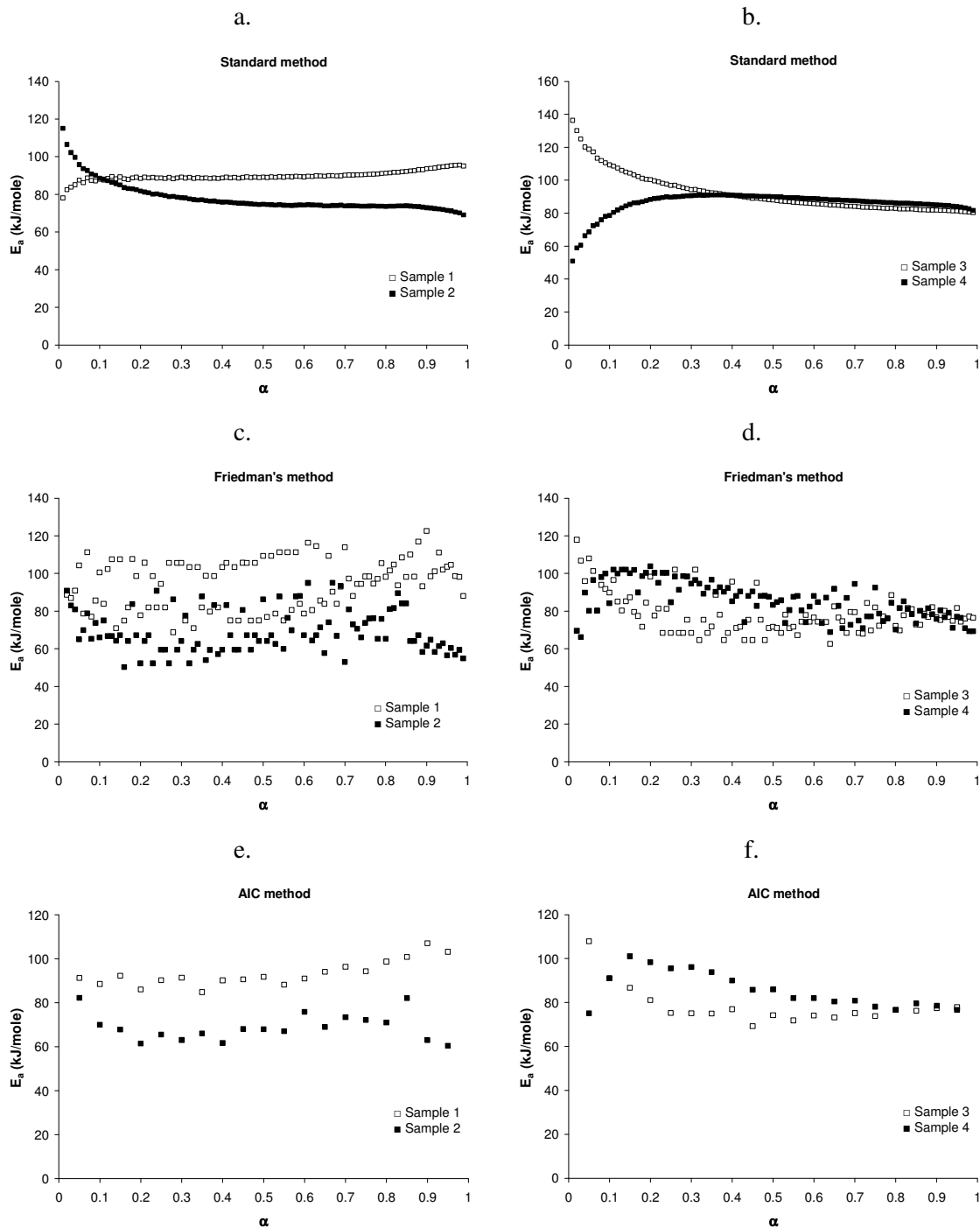


Figure 71. E_a versus α plots for isothermal sulfameter-dioxolane solvate desolvation runs of four samples. Plots a, c and e are for samples 1–2. Plots b, d and f are for samples 3–4.

Table 26. Fitted kinetic parameters for sulfameter-dioxolane isothermal desolvation kinetics by model-fitting methods.

Model	Sample 1			Sample 2		
	A (min ⁻¹)	E _a (kJ/mole)	r	A (min ⁻¹)	E _a (kJ/mole)	r
A2	6.89 x 10 ¹³	94.61	0.9980	5.26 x 10 ⁹	67.90	0.9992*
A3	5.36 x 10 ¹³	94.92	0.9890	3.67 x 10 ⁹	67.88	0.9954
A4	4.39 x 10 ¹³	95.07	0.9790	2.84 x 10 ⁹	67.88	0.9884
D1	4.34 x 10 ¹³	94.51	0.9879	3.09 x 10 ⁹	67.63	0.9805
D2	3.13 x 10 ¹³	94.04	0.9785	2.71 x 10 ⁹	67.70	0.9676
D3	1.15 x 10 ¹³	93.33	0.9275	1.43 x 10 ⁹	68.01	0.9136
D4	8.13 x 10 ¹²	93.80	0.9674	7.88 x 10 ⁸	67.79	0.9552
F1	1.03 x 10 ¹⁴	93.80	0.9666	1.09 x 10 ¹⁰	68.02	0.9576
F2	4.56 x 10 ¹⁴	92.11	0.6227	1.46 x 10 ¹¹	69.39	0.6130
F3	1.04 x 10 ¹⁶	91.61	0.3870	6.38 x 10 ¹²	70.69	0.3821
P2	4.91 x 10 ¹³	95.67	0.9377	2.52 x 10 ⁹	67.81	0.9520
P3	4.13 x 10 ¹³	95.83	0.9125	2.02 x 10 ⁹	67.83	0.9310
P4	3.50 x 10 ¹³	95.91	0.8968	1.67 x 10 ⁹	67.84	0.9176
R1	5.39 x 10 ¹³	95.22	0.9783	3.12 x 10 ⁹	67.74	0.9825
R2	3.56 x 10 ¹³	94.61	0.9981*	2.60 x 10 ⁹	67.78	0.9954
R3	2.65 x 10 ¹³	94.36	0.9962	2.15 x 10 ⁹	67.83	0.9913

* Best fit model.

Table 26, continued

Model	Sample 3			Sample 4		
	A (min ⁻¹)	E _a (kJ/mole)	r	A (min ⁻¹)	E _a (kJ/mole)	r
A2	2.67 x 10 ¹¹	75.91	0.9995*	5.12 x 10 ¹²	84.55	0.9983*
A3	1.78 x 10 ¹¹	75.78	0.9915	3.04 x 10 ¹²	84.09	0.9943
A4	1.34 x 10 ¹¹	75.70	0.9822	2.17 x 10 ¹²	83.86	0.9871
D1	1.96 x 10 ¹¹	76.24	0.9846	3.82 x 10 ¹²	84.92	0.9818
D2	1.67 x 10 ¹¹	76.23	0.9761	3.98 x 10 ¹²	85.49	0.9672
D3	7.82 x 10 ¹⁰	76.17	0.9278	2.59 x 10 ¹²	86.37	0.9103
D4	4.71 x 10 ¹⁰	76.22	0.9657	1.25 x 10 ¹²	85.78	0.9538
F1	5.71 x 10 ¹¹	76.09	0.9675	1.55 x 10 ¹³	85.72	0.9554
F2	4.45 x 10 ¹²	75.92	0.6315	3.18 x 10 ¹⁴	88.29	0.6069
F3	1.17 x 10 ¹⁴	75.76	0.3981	1.51 x 10 ¹⁶	89.82	0.3772
P2	1.19 x 10 ¹¹	75.66	0.9402	1.49 x 10 ¹²	83.08	0.9528
P3	8.92 x 10 ¹⁰	75.50	0.9167	1.07 x 10 ¹²	82.80	0.9307
P4	7.1 x 10 ¹⁰	75.40	0.9019	8.37 x 10 ¹¹	82.66	0.9166
R1	1.72 x 10 ¹¹	75.99	0.9774	2.49 x 10 ¹²	83.83	0.9846
R2	1.47 x 10 ¹¹	76.07	0.9971	2.75 x 10 ¹²	84.65	0.9959
R3	1.2 x 10 ¹¹	76.09	0.9955	2.51 x 10 ¹²	84.98	0.9909

* Best fit model.

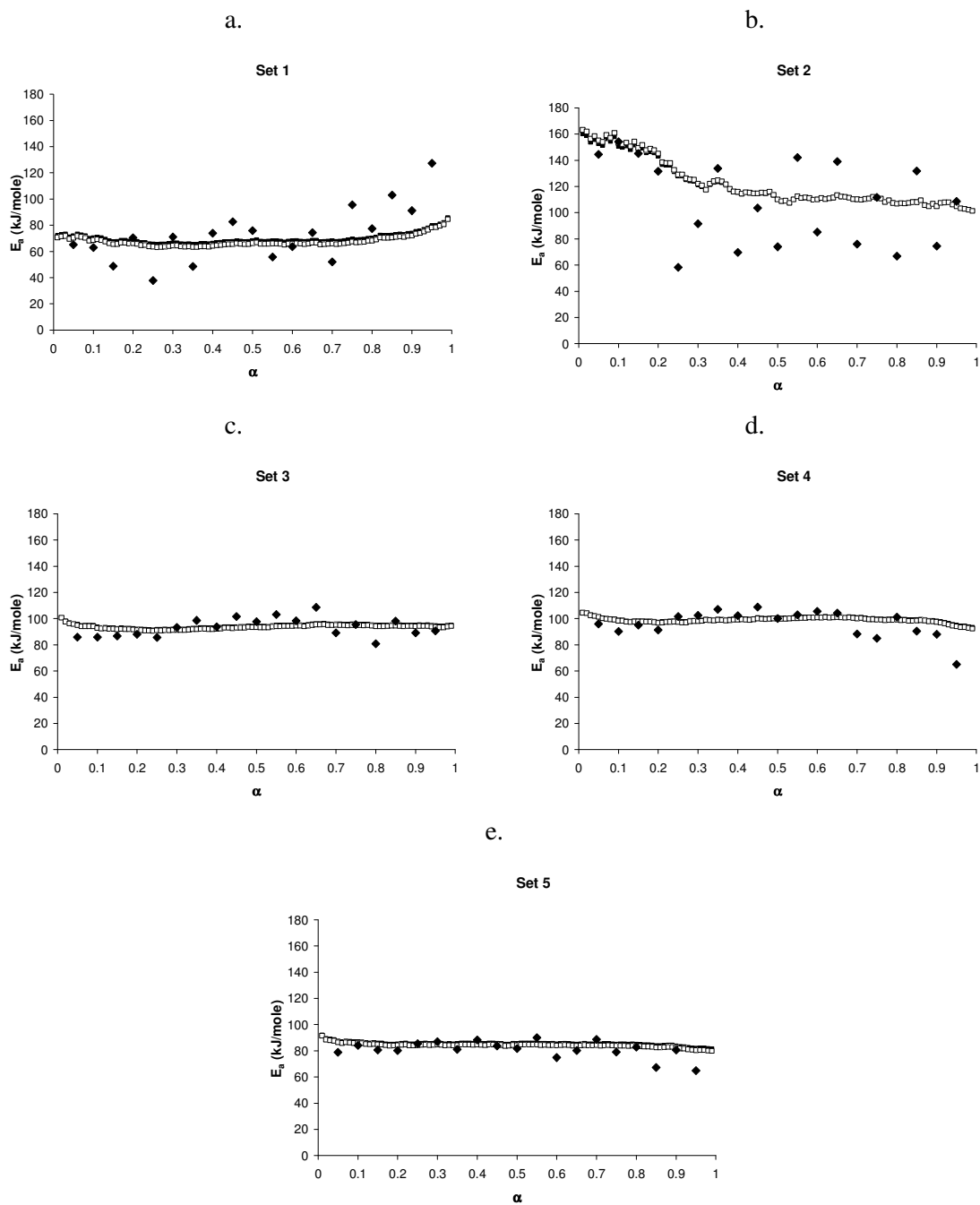


Figure 72. E_a versus α plots for nonisothermal sulfameter-dioxolane solvate desolvation runs (sets 1–5), evaluated by three isoconversional methods: ■, OFW; □, VYZ and ◆, AIC.

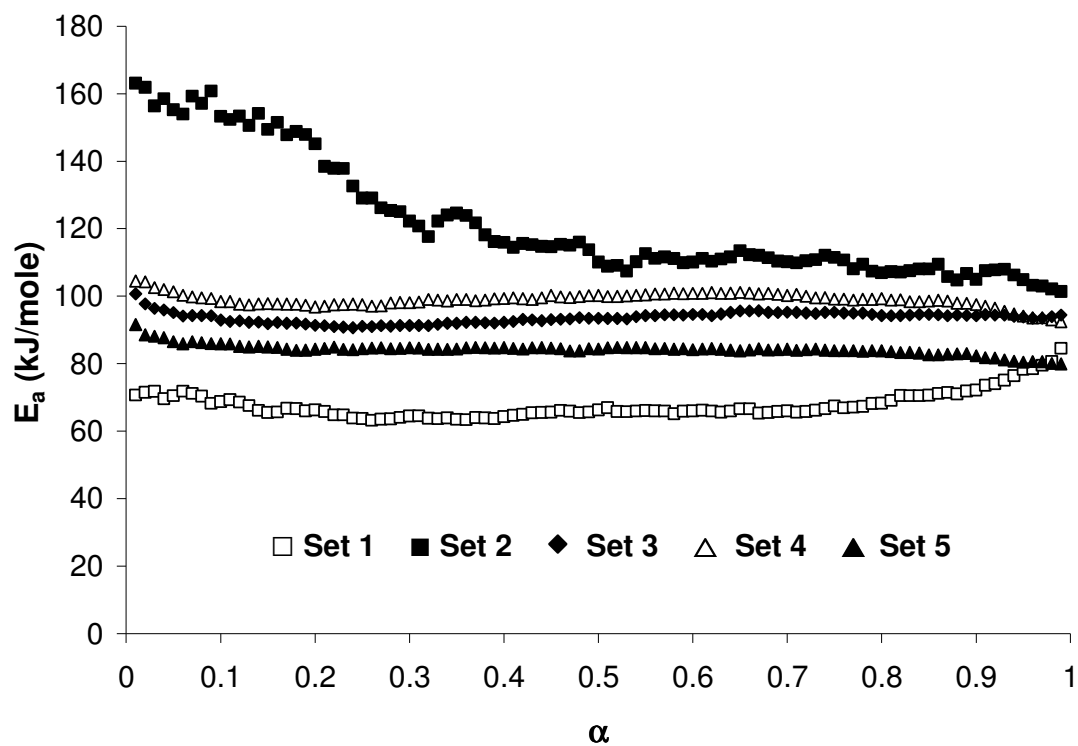


Figure 73. E_a versus α plots for nonisothermal sulfameter-dioxolane solvate desolvation evaluated by the Vyazovkin (VYZ) method.

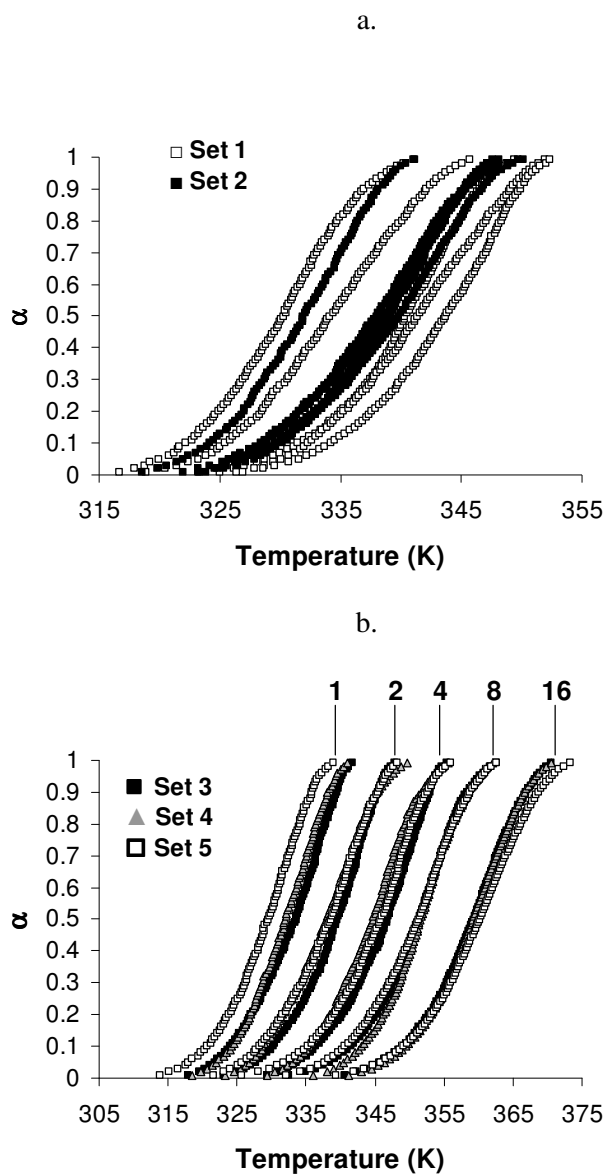


Figure 74. α versus temperature plots for the nonisothermal desolvation of sulfameter-dioxolane solvate for five experimental sets: a. sets 1–2 with nominal heating rates of 1, 1.5, 2, 2.5 and 3K/min; b. sets 3–5 with nominal heating rates of 1, 2, 4, 8 and 16 K/min.

Table 27. Fitted kinetic parameters for nonisothermal sulfameter-dioxolane desolvation data sets (Figure 55), using the Coats-Redfern method.*

Model	ln A (min ⁻¹)					E _a (kJ/mol)				
	Set-1	Set-2	Set-3	Set-4	Set-5	Set-1	Set-2	Set-3	Set-4	Set-5
A2	30.5	30.1	31.9	30.6	28.4	91.0	89.6	94.5	91.2	84.7
A3	18.7	18.5	19.9	19.0	17.5	58.8	57.9	61.1	58.9	54.5
A4	12.8	12.6	13.8	13.1	12.0	42.7	42.0	44.4	42.7	39.5
D1	97.3	96.2	99.6	97.1	90.3	279.8	276.0	289.8	283.6	263.3
D2	106.3	105.0	108.7	105.7	98.3	305.9	301.8	317.1	309.2	287.3
D3	117.7	116.3	120.5	116.5	108.5	341.3	336.4	354.0	343.6	319.7
D4	109.0	107.7	111.5	108.2	100.6	317.4	313.0	329.1	320.4	297.8
F1	65.4	64.6	67.3	64.8	60.4	187.6	184.8	194.8	188.1	175.0
F2	94.0	92.7	96.7	91.8	86.1	265.2	260.8	276.3	263.0	245.8
F3	129.7	127.8	133.5	125.5	118.1	362.7	356.2	378.7	356.9	334.7
P2	21.0	20.8	22.1	21.5	19.8	65.7	64.8	68.2	66.6	61.6
P3	12.3	12.1	13.3	12.9	11.7	42.0	41.3	43.5	42.5	39.1
P4	7.9	7.8	8.8	8.5	7.6	30.1	29.6	31.2	30.5	27.9
R1	46.7	46.1	48.2	46.9	43.5	137.1	135.2	142.0	139.0	128.8
R2	54.2	53.5	55.9	54.1	50.2	159.1	156.9	165.0	160.5	149.0
R3	57.0	56.3	58.8	56.7	52.7	167.8	165.4	174.1	168.9	157.0

* Results in each data set are averaged from five heating rate curves (geometric mean of E_a and A).

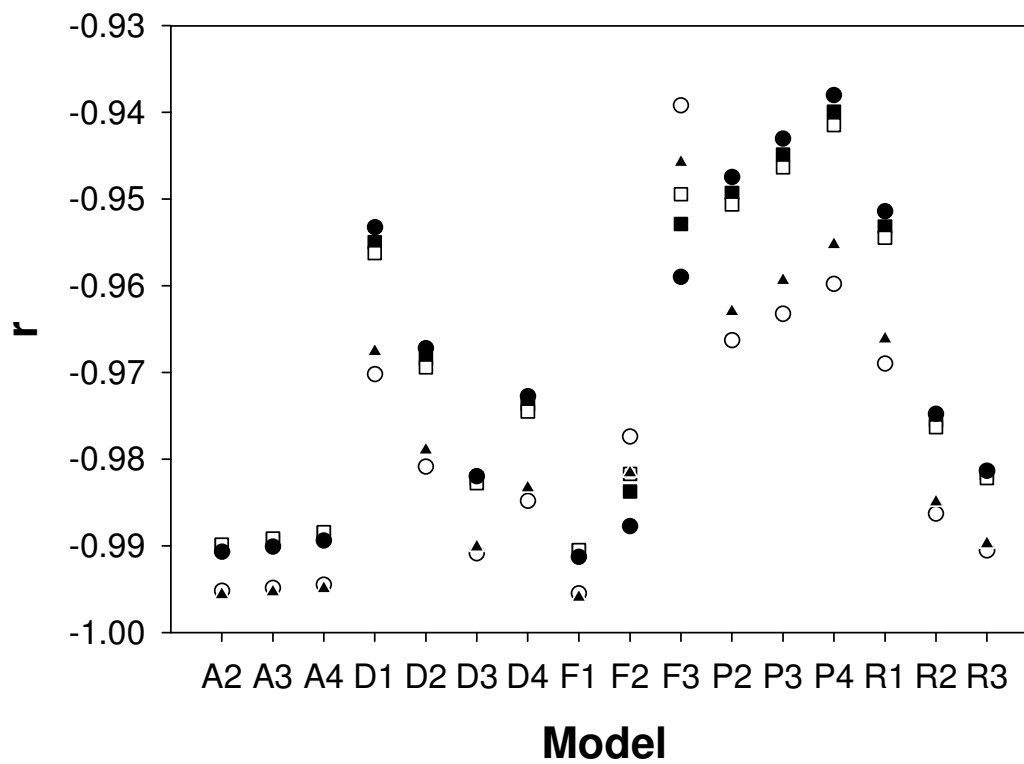


Figure 75. Model-fitting correlation coefficients (r) for nonisothermal sulfameter-dioxolane solvate desolvation evaluated by the Coats-Redfern method: ■, set 1; □, set 2; ●, set 3; ○, set 4 and ▲, set 5. Values from each set are averages from five curves.

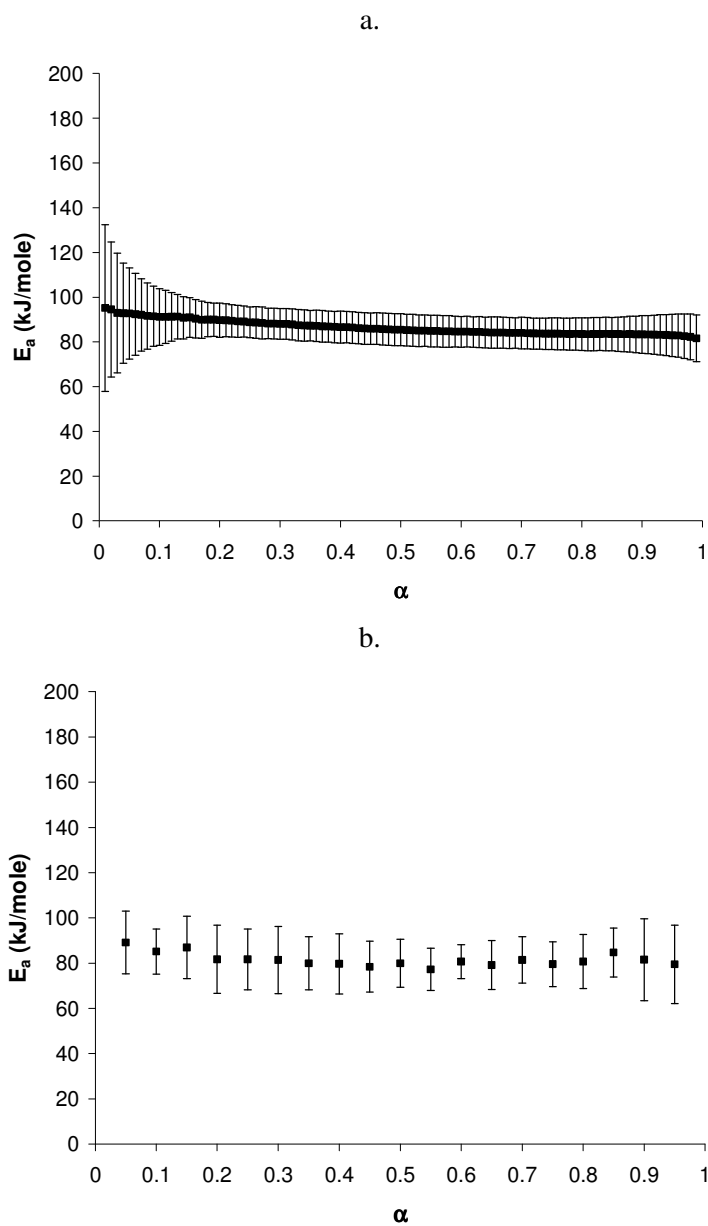


Figure 76. E_a versus α plots for isothermal sulfameter-dioxolane solvate desolvation using the average of samples 1–4 with 95% confidence intervals, evaluated by the: a, standard method and b, AIC method.

CHAPTER 5
COMPLEMENTARY USE OF MODEL-FREE AND MODELISTIC
METHODS IN THE ANALYSIS OF SOLID-STATE KINETICS

Introduction

Many methods have been developed for studying solid-state kinetic data. These methods can be classified according to the experimental conditions selected and the mathematical analysis performed. Experimentally, either isothermal or nonisothermal methods are employed. The mathematical approaches employed can be divided into model-fitting and isoconversional (model-free) methods. Model-fitting methods were amongst the first and most popular methods to be used in evaluating solid-state kinetics, especially for nonisothermal experiments. The popularity of these methods has recently declined in favor of isoconversional methods which can compute kinetic parameters without modelistic assumptions. However, these methods, like the model-fitting methods, have some limitations, as described in Chapter 4.

Results obtained from different mathematical analysis methods have been viewed as conflicting rather than complementary. Selection of the best model for experimental data is problematic because a statistical fit parameter (i.e., r) may be quite high for a number of fitted models [37]. The aim of this work is to show the utility of a model-free method to obtain activation energy (E_a) and a modelistic approach to obtain frequency factor (A). We feel that such an approach gives the highest probability of selecting the most accurate kinetic triplet (A , E_a and model). The kinetic triplet is essential for accurate kinetic description of any solid-state reaction since the reaction rate expression (Eq. (22)) requires all three. If only one or two of the triplet are known, an incomplete kinetic picture is generated [40, 92, 160]. Just as in homogenous phase kinetics, obtaining all kinetic parameters for a solid-state reaction is essential for understanding reaction

dynamics. In this chapter, we will demonstrate how such a complete analysis can be accomplished using simulated kinetic data and real data for a desolvation reaction.

Modelistic and model-free methods

The use of modelistic methods has been criticized in nonisothermal studies [39-43, 159] because regression methods may lead to indistinguishable fits or mathematical expressions with high correlation because of the form of the equation. This casts serious doubt on using these methods to obtain mechanistic information (A , E_a and model). Model-fitting problems are especially evident with the Coats and Redfern method in which the ordinate ($\ln(g(\alpha)/T^2)$) and abscissa ($1/T$) axes are correlated because of the form of each variable which violates a basic assumption of linear regression [161]. As a result, all models would show relatively good fits (i.e. high r) even though they may be poor descriptors of the mechanism. Another problem with the Coats-Redfern method is that some models are indistinguishable. For example, the F1, A2, A3 and A4 models are indistinguishable when linear regression is performed as they all show very similar correlation coefficients.

Vyazovkin and Wight [159] reviewed several alternative non-statistical approaches for model selection. These include using predictions of the activated complex to obtain the frequency factor, selecting a model from an isothermal experiment [162] or choosing a reaction model from the extent of the reaction at the maximum reaction rate (α_{\max}) [163]. These approaches have not gained wide use. Therefore, Vyazovkin and Wight have recommended using isoconversional methods instead of modelistic approaches.

Isoconversional methods calculate E_a values at progressive degrees of conversion without modelistic assumptions.

Despite concerns over use of model-fitting methods, these methods have the advantage of directly calculating E_a and A from a single non-isothermal kinetic run. This

is not seen in isoconversional methods as they require multiple kinetic runs at different heating rates and do not allow direct calculation of A. An indirect method has been suggested [164] to calculate A for isoconversional methods, however, this procedure utilizes an artificial isokinetic relationship that is not fully supported theoretically [86].

This work utilizes isoconversional methods to obtain E_a values which are compared to values obtained by modelistic methods. The most accurate model is assumed to be the one which produces an activation energy closest to that from the isoconversional analysis. This allows one to select models that might otherwise be indistinguishable based on quality of the regression fit alone. We demonstrate the utility of this approach by analyzing both simulated and experimental data.

Experimental data were obtained for the desolvation kinetics of three sulfameter solvates of cyclic ether solvents. These solvents were tetrahydrofuran, dioxolane and dioxane, as detailed in Chapter 3).

Experimental

Simulated data were isothermally and nonisothermally generated and then analyzed. Sulfameter desolvation was followed nonisothermally by TGA, as described in Chapter 3. Isothermal calculation methods included the conventional model-fitting method (modelistic) and the standard isoconversional method (model-free). Nonisothermal calculation methods included the Coats and Redfern method (modelistic) in addition to Vyazovkin's method (model-free).

Data simulation

A simple, one-step reaction was isothermally and nonisothermally simulated using Microsoft Excel[®], as described in Chapter 3.

The isothermal simulation (S1) consisted of five isothermal (α -time) curves which were simulated at five temperatures (340, 345, 350, 355 and 360 K) using a contracting volume (R3) model ($g(\alpha)=[1-(1-\alpha)^{1/3}]$) with $A=1\times 10^{13} \text{ min}^{-1}$ and $E_a=100$

kJ/mole. A 0.25% random error in time was introduced to each curve in the simulation (Figure 77).

The nonisothermal simulation (S2) consisted of five nonisothermal (α -T) curves which were simulated at five heating rates (1, 2, 4, 8 and 16 K/min) using the same kinetic parameters (model, E_a and A) used for simulation S1. A 0.25% random error in temperature ($^{\circ}$ C) was introduced to each curve in the simulation (Figure 78).

Sulfameter solvate desolvation

Three sulfameter solvates were prepared from the following solvents: tetrahydrofuran, dioxolane and dioxane, as described in Chapter 3.

The prepared solvates were sieved and a particle size range of 355–710 μ m was used for desolvation studies.

Desolvation kinetics was followed nonisothermally by TGA as explained in Chapter 3. Nonisothermal runs were performed at nominal heating rates of 1, 2, 4 and 8 K/min. The exact heating rate was obtained from the slope of the linear heating curve of the TGA run during the time period of significant weight loss, as discussed in Chapter 3.

Kinetic analysis

Kinetic analysis of data was conducted by model-fitting and isoconversional methods. Simulated isothermal data were analyzed by the conventional model-fitting method and the standard isoconversional method while nonisothermal data were analyzed by the Coats-Redfern model-fitting method in addition to Vyazovkin's isoconversional method.

Model selection was done by means of an isoconversional-model (IM) plot in which a plot of E_a for each model, as calculated from the Coats-Redfern method, was plotted along with E_a calculated from Vyazovkin's isoconversional method as a function of α . The model for which E_a matched that from the isoconversional plot was selected as the model of choice.

Curve reconstruction and stability prediction

TGA curves were reconstructed to verify that the most accurate kinetic triplet (A , E_a and model) was selected by the isoconversional method for each heating rate. A sum of squares plot ($(T_{\text{actual}} - T_{\text{reconstructed}})^2$) for each solvate was created to show the sum of squared difference between experimental and reconstructed curves for each kinetic triplet obtained from the modelistic method. For each α -T thermogram, $(T_{\text{actual}} - T_{\text{reconstructed}})^2$ values were calculated at each α in 0.01 increments (i.e., 0.01-0.99) and these values summed for that thermogram. $(T_{\text{actual}} - T_{\text{reconstructed}})^2$ values were averaged for all five α -T thermograms. The choice of a kinetic triplet is that which gives the lowest sum of squared values which would further validates the triplets selected by the isoconversional-model (IM) plot.

The selected kinetic triplet was also used to predict the stability of solvates at three different heating rates that were not used in the kinetic analysis. The exact heating rate was obtained from the slope of the linear heating curve of the TGA run during the time period of significant weight loss, as described in Chapter 3. Equation (159) was used to reconstruct/predict each curve.

Results and Discussion

Thermogravimetric results for sulfamer desolvation are shown in Figures 79–81. Gravimetric weight loss for these solvates showed a 1:1 drug–solvent ratio, as described in Table 8 (Chapter 3). Kinetic analysis for the simulated and real data sets is described below.

Simulated data

Model-fitting methods produced several kinetic triplets (A , E_a and model) for each simulation. The conventional model fitting results for simulation S1 are given in Table 28, while results obtained by the Coats-Redfern method for simulation S2 are in Table 29.

Isoconversional-model (IM) plots containing activation energies calculated by model-fitting along with that calculated from an isoconversional method are shown in Figures 82 - 83. IM plots of isothermal data (S1, Figure 82) show that no particular model can be selected because all models give comparable values of E_a (~100 kJ/mole, Table 28). Previous reports have demonstrated similar constancy of E_a [37, 38, 159] which is the reason that the desolvation reaction was not further studied isothermally.

IM plots of nonisothermal data (S2, Figure 83) show that the R3 model is selected as the best model because E_a for R3, calculated by the Coats-Redfern method, is almost the same as that calculated by Vyazovkin's isoconversional method (~99.7 kJ/mole, Table 29). If model selection is to be based on the correlation coefficient (r), no single model can be chosen because several models are equivalent (A2, A3, A4, D2, D3, D4, F1, R2 and R3) as indicated in Table 29. This shows that, model selection based on IM plots is more appropriate than that using the correlation coefficient.

Sulfameter desolvation

Several kinetic triplets were calculated from the Coats-Redfern model-fitting method for each solvate (Tables 30–32). Results based on curve fitting clearly show that using the correlation coefficient (r), several models were indistinguishable, namely the A2, A3, A4 and F1 models. On the other hand, IM plots of desolvation data (Figures 84–86) show that the A3 model can be selected for both the tetrahydrofuran and dioxane solvates while the A2 model is the model of choice for the dioxolane solvate, these selection were further verified by sum of squares plots (Figures 87–89). Model selection is not as clear for the dioxane solvate as it is for tetrahydrofuran and dioxolane solvates. For dioxane, another model (P2) can also be selected because the isoconversional curve intersects E_a values for both the A3 and P2 models (Figure 86). This could be due to small variations in the isoconversional curve as the reaction progresses or because these models are mechanistically similar (i.e. both are nucleation models), which in turn results

in similar values of E_a . To better judge which is the most accurate model, TGA curve reconstructions from E_a and A values for both models were conducted and compared.

Figures 90–92 show reconstructed α – T plots for the nonisothermal desolvation of the different sulfameter solvates. For each solvate, the kinetic triplet (A , E_a and model) was selected based on isoconversional-model plots (Figures 84–86). There is good correlation between the reconstructed and actual experimental data in most cases. In some cases, there is less correlation between reconstructed and experimental curves which may be due to using average values of E_a and A from the Coats and Redfern analysis. Figure 92 shows reconstructed α – T plots for the nonisothermal desolvation of the dioxane solvate for two models, A3 (Figure 92a) and P2 (Figure 92b). It is clear that the A3 model accurately predicts while the P2 model less accurately predicts experimental curves, especially at $\alpha > 0.5$.

If a mechanistic model is selected based on the correlation coefficient, the model of choice for the dioxane solvate (Table 32) would be a first-order (F1) model. However, when α – T curves are reconstructed with the F1 model, they poorly correlate with experimental α – T results, as seen in Figure 93. Therefore, such an approach is not satisfactory compared to model selection based on isoconversional methods. Figures 94–96 show predicted and experimental α – T plots for the nonisothermal desolvation of sulfameter solvates. These plots show that nonisothermal curves have been reasonably well predicted from the kinetic triplet (A , E_a and model). These results also agree with those of Cairra and Mohamed [29] for the tetrahydrofuran solvate where they reported an activation energy of 103 kJ/mole by a model-independent method which is similar to the value of 104.5 kJ/mole we obtained for the same solvate.

Conclusions

The large number of methods for evaluating solid-state kinetics has created some debate over the appropriate method or group of methods that should be used for

analyzing such data. Different kinetic analysis methods have been treated by some investigators as competing rather than complementary. The increasing popularity of isoconversional methods has been at the expense of model-fitting methods. However, to fully study any kinetic process, it should be adequately described by a kinetic triplet (A , E_a and model), which is not directly obtained from isoconversional methods. Yet, model-fitting methods suffer from severe shortcomings that limit their sole use for analyzing and understanding solid-state reactions.

Kinetic analysis of simulated data, in addition to that for the desolvation of sulfameter solvates, has shown that, selecting a model based on statistical methods using a common model-fitting method (i.e., Coats and Redfern) can produce misleading results, as shown by other investigators [37, 159].

Our approach combines the power of isoconversional and model-fitting methods for the evaluation of solid-state kinetics. This has produced promising results for simulated and real experimental data but, as with any kinetic method, this approach has some limitations. One is the assumption of a simple reaction or a flat isoconversional plot (i.e., constant activation energy throughout the reaction). This assumption seems to be applicable to the sulfameter-solvate system where solvent molecules fill channels within the crystal structure and desolvation involves the removal of solvent from such channels [157]. This approach is also not applicable to isothermal experiments where different models yield comparable values of the activation energy. The success of this approach also depends on careful control of experimental variables because poorly executed experimental protocols can lead to inaccurate isoconversional results which in turn can lead to inappropriate model selection. One must be able to carefully and reproducibly generate TGA data for accurate comparison of results at different heating rates as explained in Chapter 4. When more than one model is selected using this approach, α - T curve reconstruction can be further used to select the most appropriate model.

Results from both modelistic and model-free approaches have been separately reported and compared in the literature [36, 165, 166]. Our approach represents a complementary means for using the strengths of both methods in the evaluation of solid-state kinetics.

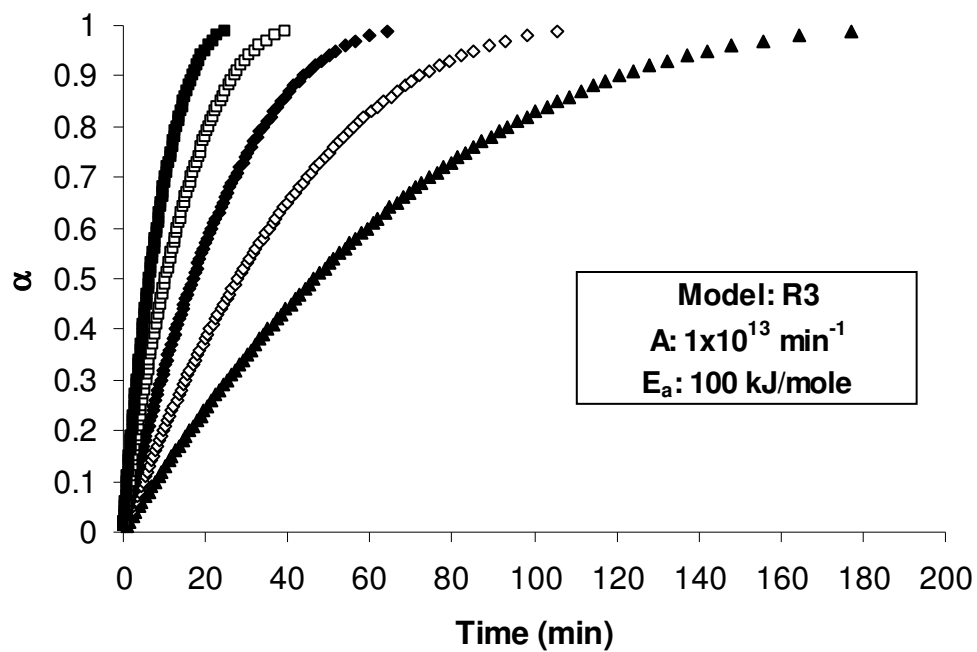


Figure 77. Simulations of α versus time for isothermal kinetic runs with 0.25% random error in time at: \blacktriangle , 340 K; \diamond , 345 K; \blacklozenge , 350 K; \square , 355 K and \blacksquare , 360 K (simulation S1). The inset gives the simulation model, pre-exponential factor (A) and activation energy (E_a).

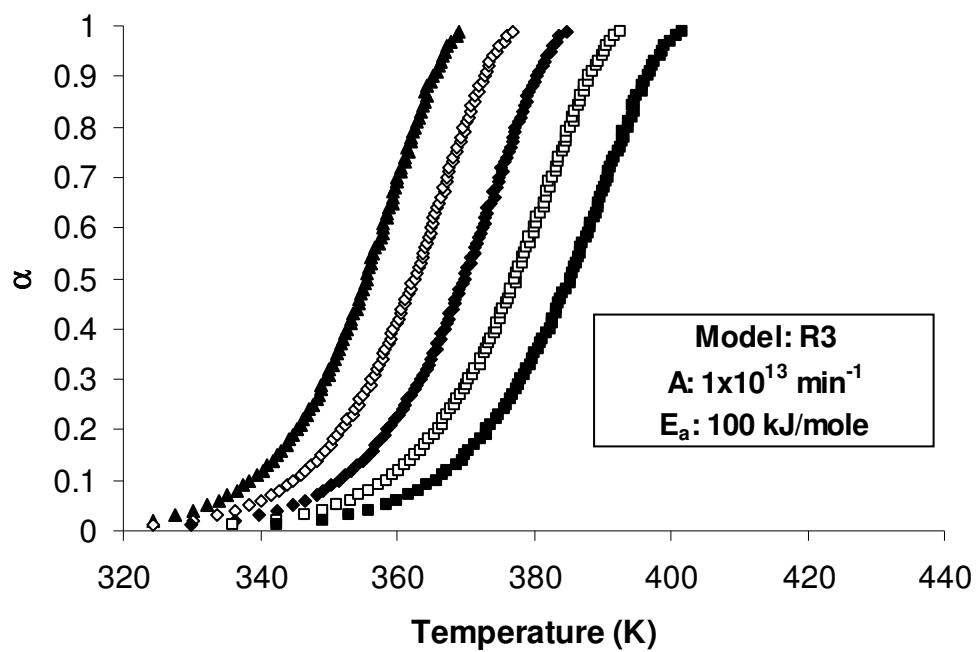


Figure 78. Simulated α -temperature plots with 0.25% random error in temperature ($^{\circ}\text{C}$) for nonisothermal kinetic runs at: \blacktriangle , 1 K/min; \diamond , 2 K/min; \blacklozenge , 4 K/min; \square , 8 K/min and \blacksquare , 16 K/min (simulation S2). The inset gives the simulation model, pre-exponential factor (A) and activation energy (E_a).

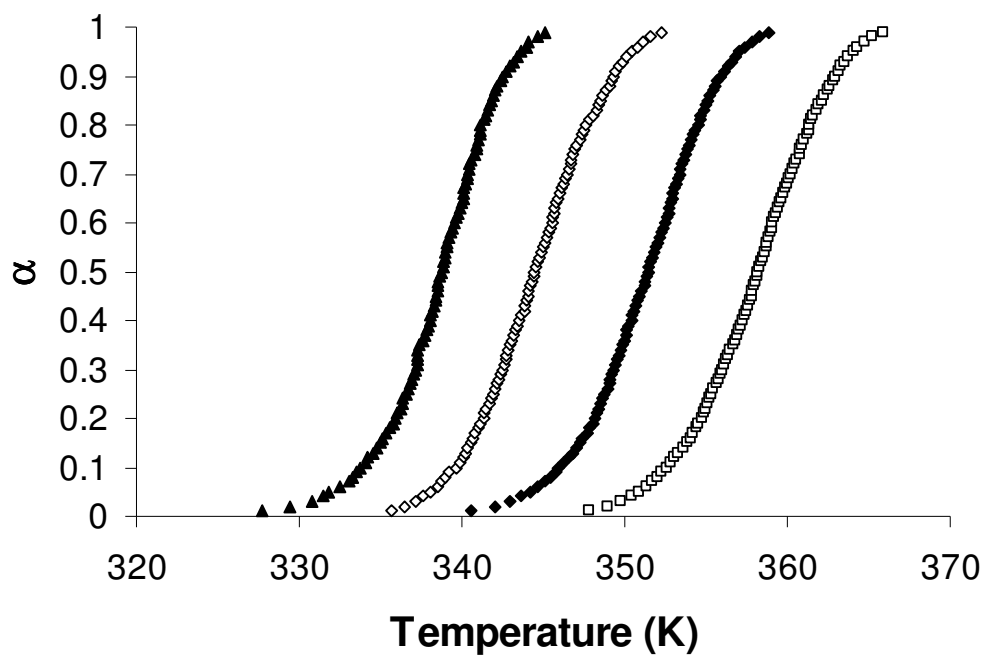


Figure 79. α versus temperature plots for the nonisothermal desolvation of sulfameter-tetrahydrofuran solvate at: ▲, 0.95; ◇, 1.93 ◆, 3.86 K and □, 7.61 K/min.

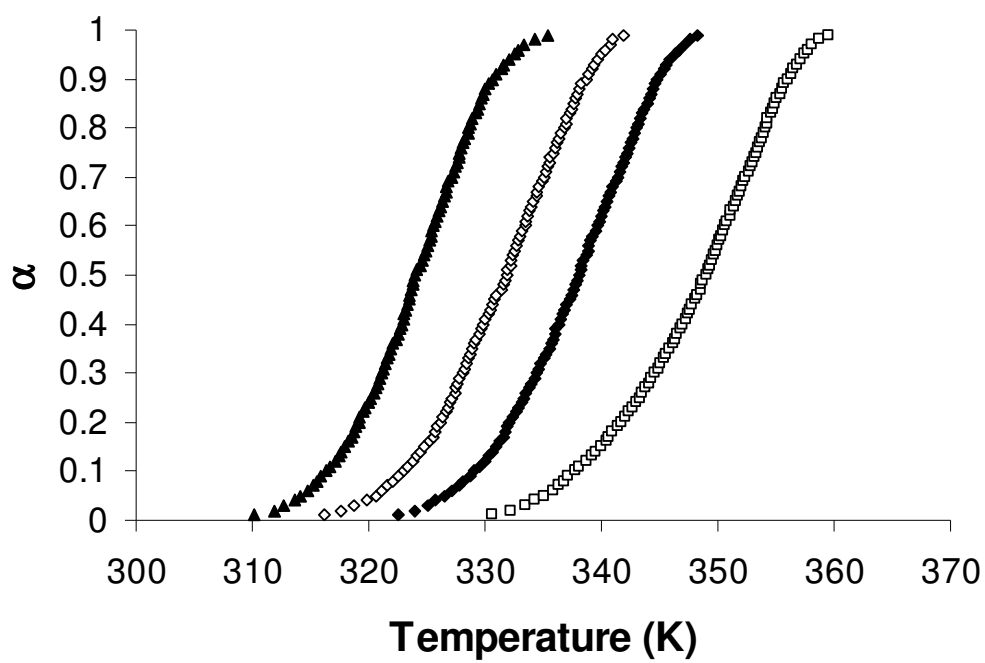


Figure 80. α versus temperature plots for the nonisothermal desolvation of sulfameter-dioxolane solvate at: ▲, 0.96; ◇, 1.92 ◆, 3.80 K and □, 7.62 K/min.

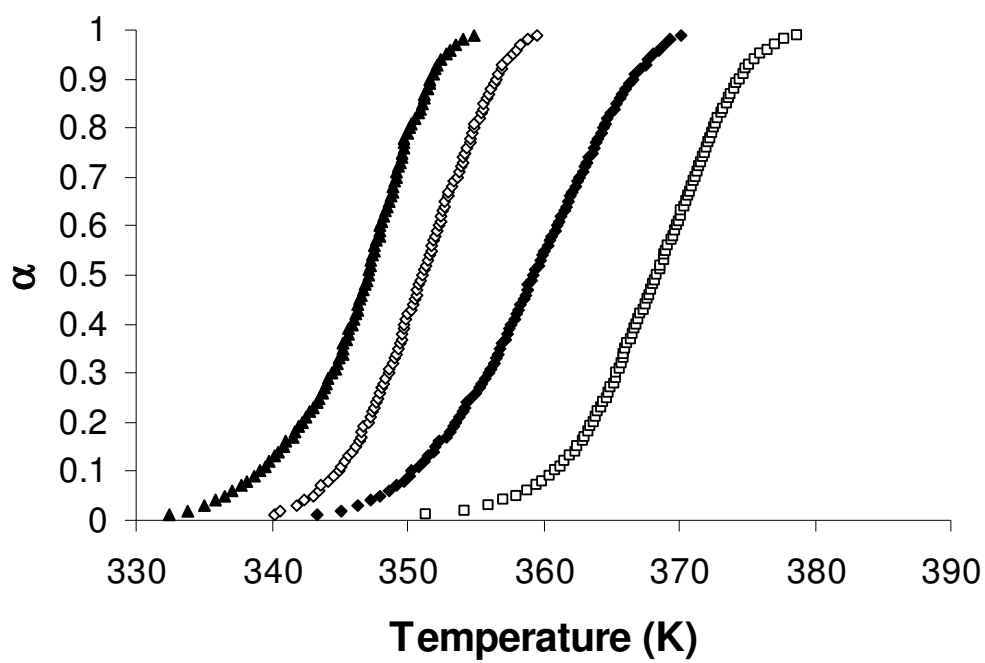


Figure 81. α versus temperature plots for the nonisothermal desolvation of sulfameter-dioxane solvate at: ▲, 0.98; ◇, 1.99 ◆, 3.94 K and □, 7.71 K/min.

Table 28. Fitted kinetic parameters for simulated isothermal data (S1) using the conventional model-fitting method.

Model	A (min ⁻¹)	E _a (kJ/mole)	r *
A2	2.40×10^{13}	100.05	0.9933
A3	1.66×10^{13}	100.06	0.9761
A4	1.28×10^{13}	100.06	0.9618
D1	1.58×10^{13}	100.05	0.9922
D2	1.36×10^{13}	100.05	0.9917
D3	6.56×10^{12}	100.04	0.9514
D4	3.87×10^{12}	100.05	0.9846
F1	4.88×10^{13}	100.05	0.9809
F2	4.10×10^{14}	100.04	0.6506
F3	1.13×10^{16}	100.04	0.4084
P2	1.14×10^{13}	100.06	0.9090
P3	8.99×10^{12}	100.07	0.8790
P4	7.38×10^{12}	100.07	0.8610
R1	1.49×10^{13}	100.06	0.9631
R2	1.25×10^{13}	100.05	0.9967
R3**	1.02×10^{13}	100.05	1.0000

* Correlation coefficient for g(α) vs. t plot.

** Best fit model.

Table 29. Fitted kinetic parameters for simulated nonisothermal data (S2) using the Coats-Redfern method.*

Model	A (min ⁻¹)	E _a (kJ/mole)	r
A2	4.18×10^{06}	52.21	-0.9970†
A3	5.46×10^{03}	32.80	-0.9967†
A4	1.86×10^{02}	23.10	-0.9963†
D1	2.06×10^{23}	171.44	-0.9924
D2	1.67×10^{25}	186.01	-0.9974†
D3	3.07×10^{27}	205.38	-0.9999†
D4	3.31×10^{25}	192.31	-0.9988†
F1	1.18×10^{15}	110.44	-0.9972†
F2	2.45×10^{21}	152.26	-0.9576
F3	1.69×10^{29}	204.49	-0.9059
P2	2.80×10^{04}	38.35	-0.9903
P3	1.82×10^{02}	23.56	-0.9883
P4	1.44×10^{01}	16.16	-0.9858
R1	6.78×10^{10}	82.71	-0.9918
R2	2.52×10^{12}	94.90	-0.9993†
R3**	9.02×10^{12}	99.68	-0.9999†

* Results averaged from five curves, using the geometric mean of A and E_a and arithmetic mean of r.

** Model selected based on isoconversional-model (IM) plots.

† Equivalent models based on goodness of fit.

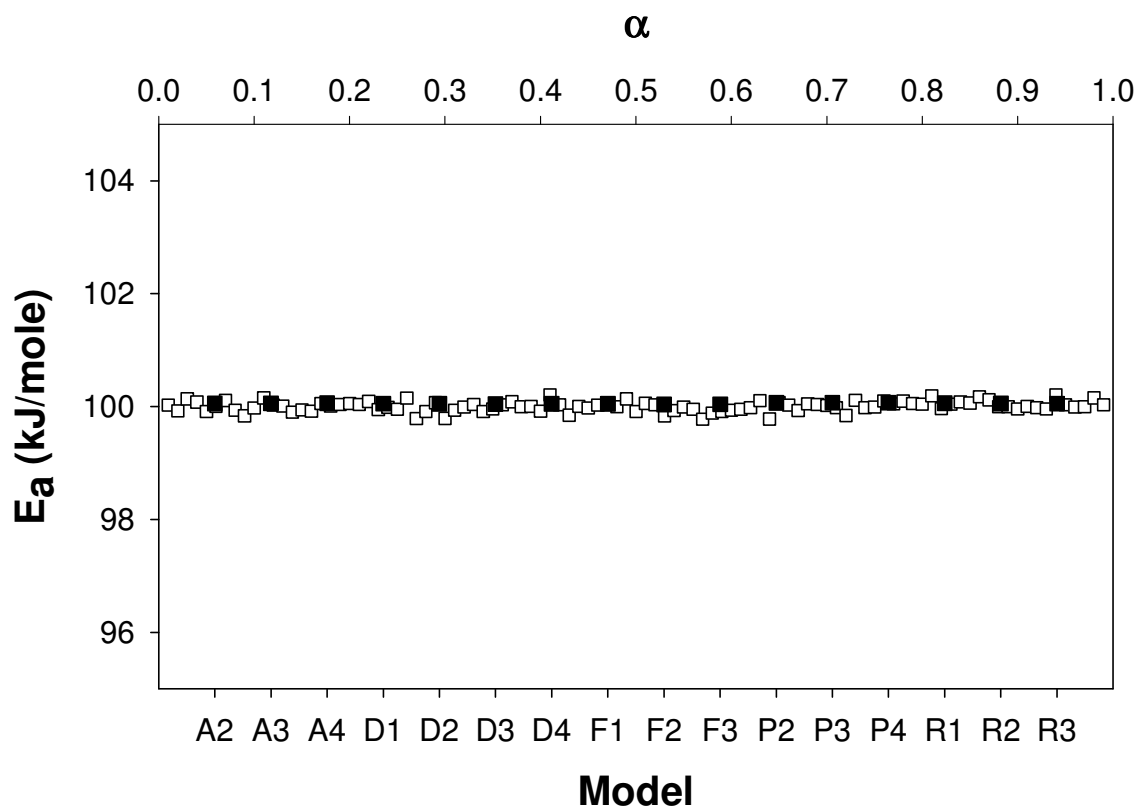


Figure 82. Isoconversional-model plot of activation energies for simulation S1 calculated by: ■, conventional model-fitting method and □, standard isoconversional method.

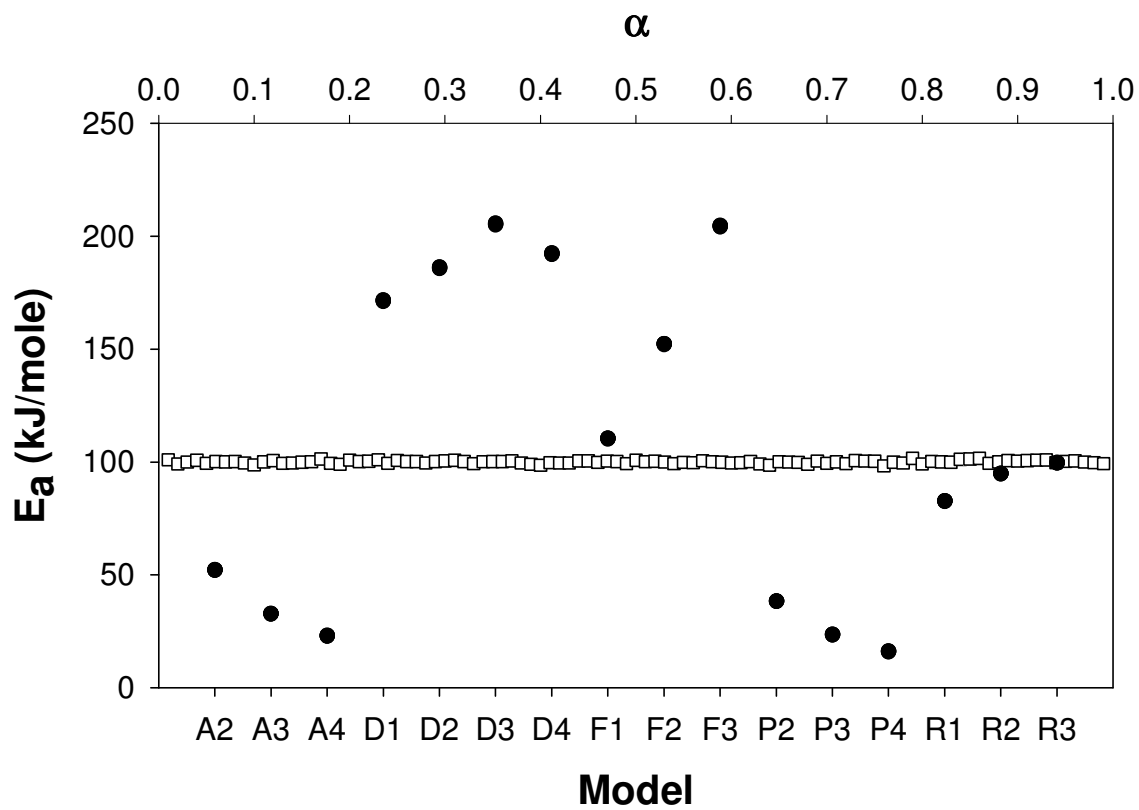


Figure 83. Isoconversional-model plot of activation energies for simulation S2 calculated by: ●, Coats-Redfern's modelistic method and □, Vyazovkin's isoconversional method.

Table 30. Fitted kinetic parameters for the nonisothermal desolvation of sulfameter-tetrahydrofuran solvate using the Coats-Redfern method*

Model	A (min ⁻¹)	E _a (kJ/mole)	r
A2	3.12×10^{23}	159.64	-0.9916†
A3**	1.21×10^{15}	104.50	-0.9913†
A4	6.90×10^{10}	76.93	-0.9909†
D1	3.07×10^{71}	480.96	-0.9527
D2	1.17×10^{78}	525.89	-0.9665
D3	5.96×10^{86}	587.13	-0.9817
D4	2.84×10^{80}	545.76	-0.9721
F1	3.21×10^{48}	325.07	-0.9919†
F2	2.18×10^{69}	461.28	-0.9921†
F3	3.09×10^{95}	632.71	-0.9663
P2	5.11×10^{16}	115.90	-0.9493
P3	3.27×10^{10}	75.34	-0.9468
P4	2.41×10^{07}	55.06	-0.9442
R1	1.17×10^{35}	237.59	-0.9516
R2	4.09×10^{40}	275.58	-0.9746
R3	5.68×10^{42}	290.68	-0.9813

* Results averaged from four curves using the geometric mean of A and E_a and arithmetic mean of r.

** Model selected based on isoconversional-model (IM) plots.

† Equivalent models based on goodness of fit.

Table 31. Fitted kinetic parameters for the nonisothermal desolvation of sulfameter-dioxolane solvate using the Coats-Redfern method.*

Model	A (min ⁻¹)	E _a (kJ/mole)	r
A2**	1.26×10^{13}	88.30	-0.9918†
A3	1.22×10^{08}	57.01	-0.9913†
A4	3.48×10^{05}	41.37	-0.9907†
D1	3.13×10^{41}	271.90	-0.9572
D2	1.98×10^{45}	297.26	-0.9704
D3	1.48×10^{50}	331.53	-0.9841
D4	2.75×10^{46}	308.40	-0.9756
F1	8.57×10^{27}	182.15	-0.9924†
F2	1.30×10^{40}	257.57	-0.9854
F3	2.23×10^{55}	352.29	-0.9544
P2	1.13×10^{09}	63.81	-0.9517
P3	2.22×10^{05}	40.68	-0.9475
P4	2.88×10^{03}	29.12	-0.9427
R1	9.27×10^{19}	133.17	-0.9555
R2	1.41×10^{23}	154.54	-0.9775
R3	2.22×10^{24}	162.98	-0.9836

* Results averaged from four curves using the geometric mean of A and E_a and arithmetic mean of r.

** Model selected based on isoconversional-model (IM) plots.

† Equivalent models based on goodness of fit.

Table 32. Fitted kinetic parameters for the nonisothermal desolvation of sulfameter-dioxane solvate using the Coats-Redfern method.*

Model	A (min ⁻¹)	E _a (kJ/mole)	r
A2	7.00×10^{16}	118.22	-0.9942†
A3**	4.03×10^{10}	76.84	-0.9939†
A4	2.82×10^{07}	56.14	-0.9935†
D1	3.74×10^{52}	362.15	-0.9623
D2	2.06×10^{57}	395.38	-0.9744
D3	2.93×10^{63}	440.35	-0.9871
D4	7.45×10^{58}	409.99	-0.9793
F1	2.19×10^{35}	242.38	-0.9945†
F2	2.33×10^{50}	341.57	-0.9858
F3	1.52×10^{69}	466.14	-0.9539
P2	7.66×10^{11}	86.09	-0.9585
P3	1.81×10^{07}	55.41	-0.9556
P4	8.12×10^{04}	40.07	-0.9523
R1	3.52×10^{25}	178.11	-0.9611
R2	3.33×10^{29}	206.12	-0.9812
R3	1.08×10^{31}	217.21	-0.9867

* Results averaged from four curves using the geometric mean of A and E_a and arithmetic mean of r.

** Model selected based on isoconversional-model (IM) plots.

† Equivalent models based on goodness of fit.

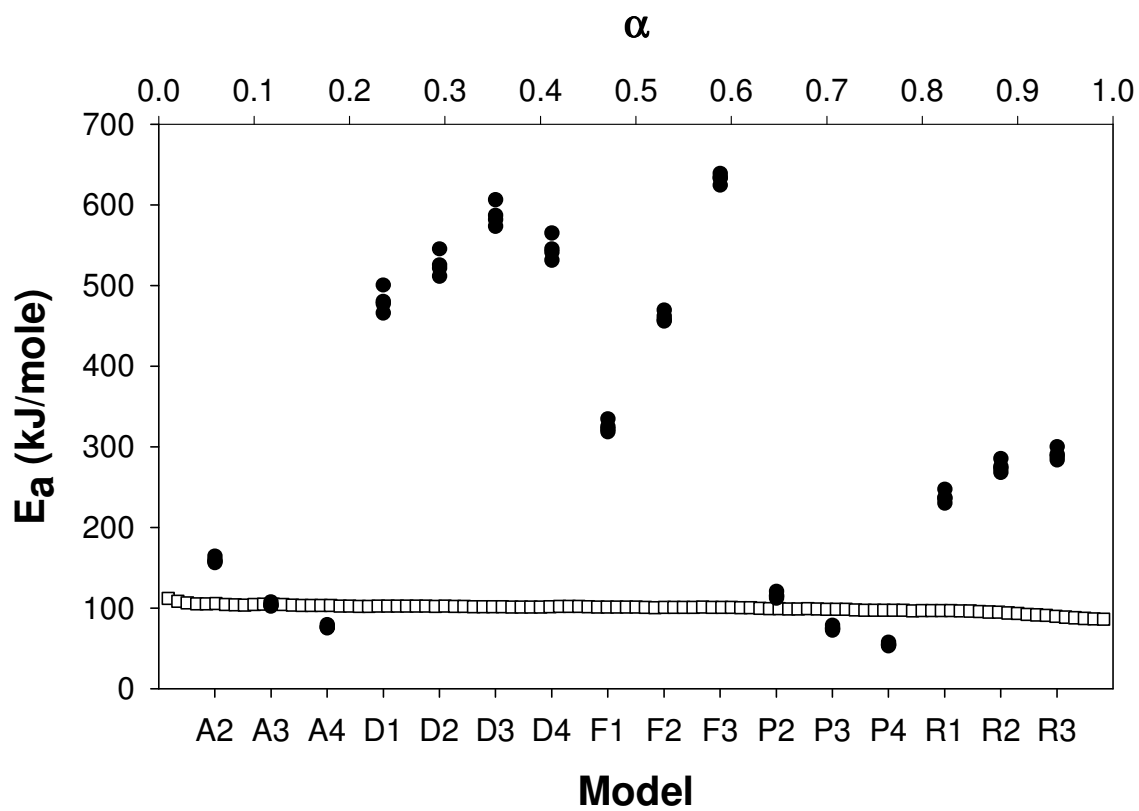


Figure 84. Isoconversional-model plot of activation energies for the nonisothermal desolvation of sulfameter-tetrahydrofuran solvate calculated by: ●, Coats-Redfern's modelistic method and □, Vyazovkin's isoconversional method.

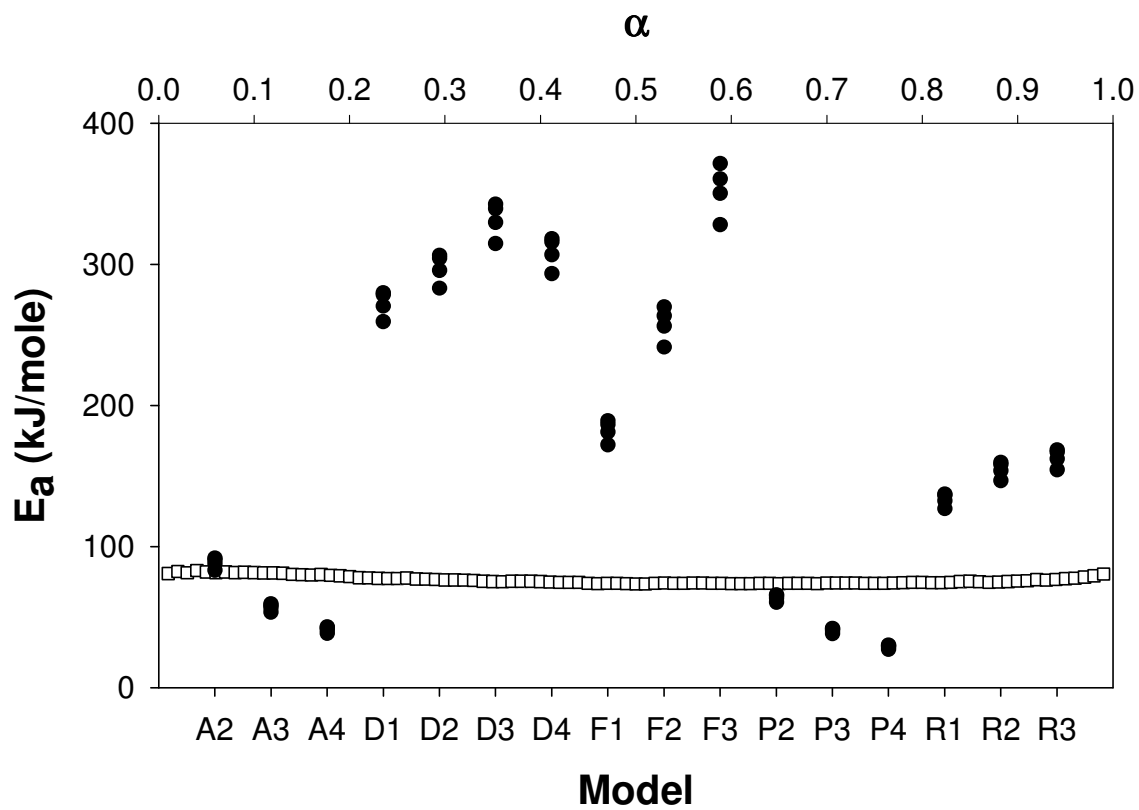


Figure 85. Isoconversional-model plot of activation energies for the nonisothermal desolvation of sulfameter-dioxolane solvate calculated by: ●, Coats-Redfern's modelistic method and □, Vyazovkin's isoconversional method.

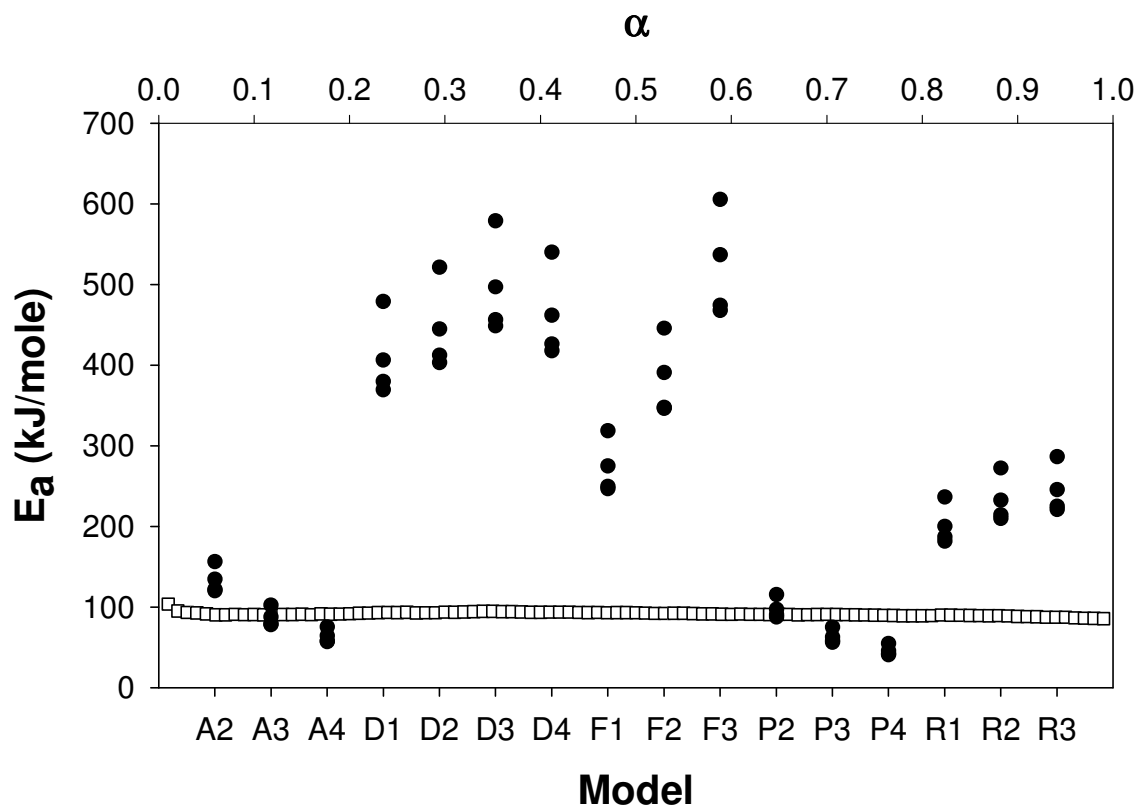


Figure 86. Isoconversional-model plot of activation energies for the nonisothermal desolvation of sulfameter-dioxane solvate calculated by: ●, Coats-Redfern's modelistic method and □, Vyazovkin's isoconversional method.

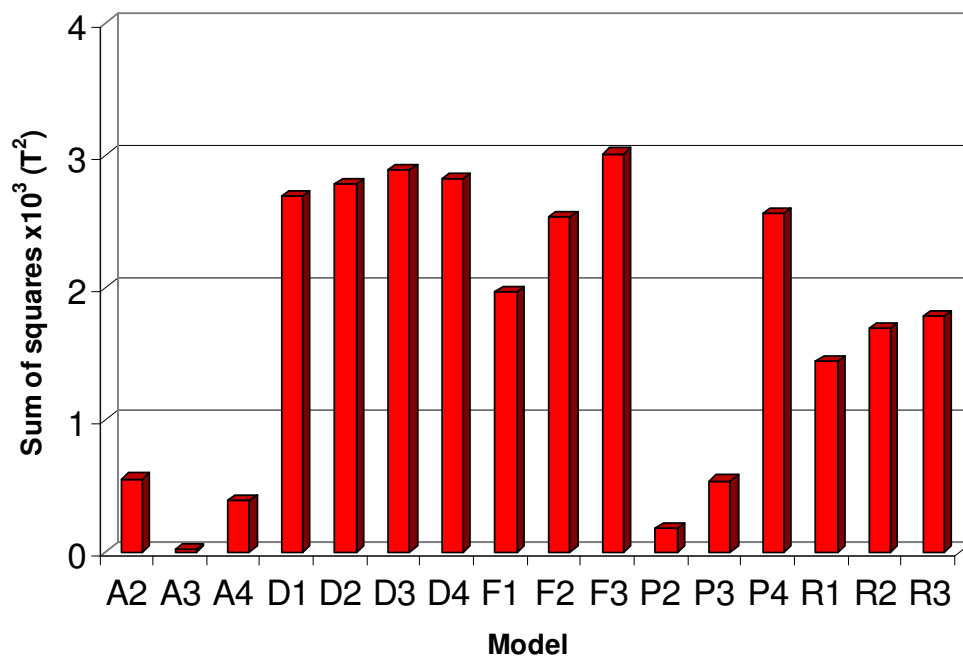


Figure 87 Sum of squared differences between actual and reconstructed nonisothermal desolvation curves ($(T_{\text{actual}} - T_{\text{reconstructed}})^2$) of sulfameter tetrahydrofuran solvate.

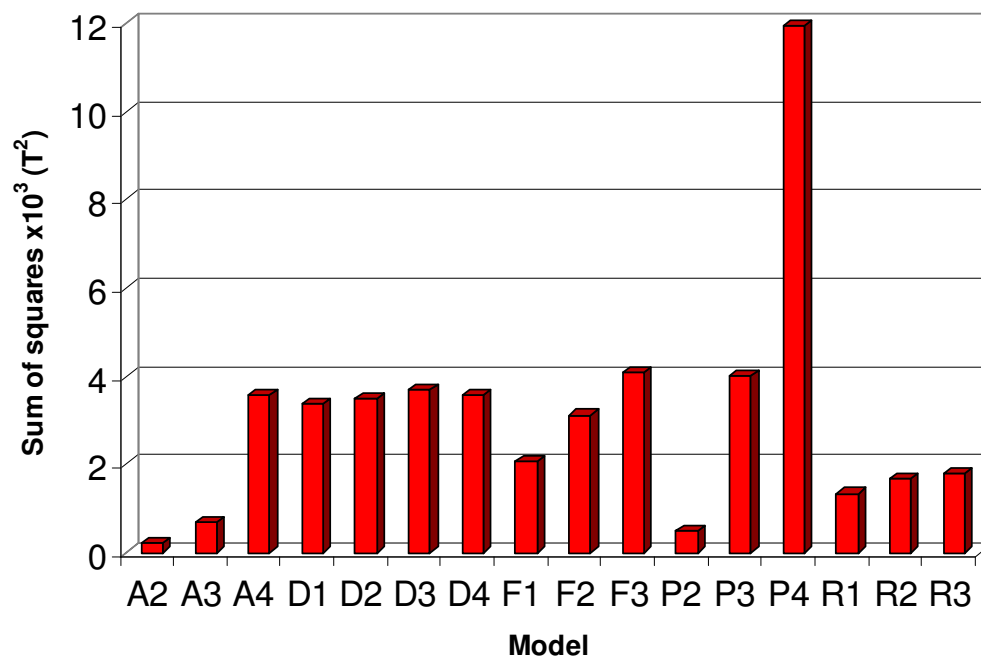


Figure 88. Sum of squared differences between actual and reconstructed nonisothermal desolvation curves ($(T_{\text{actual}} - T_{\text{reconstructed}})^2$) of sulfameter dioxolane solvate.

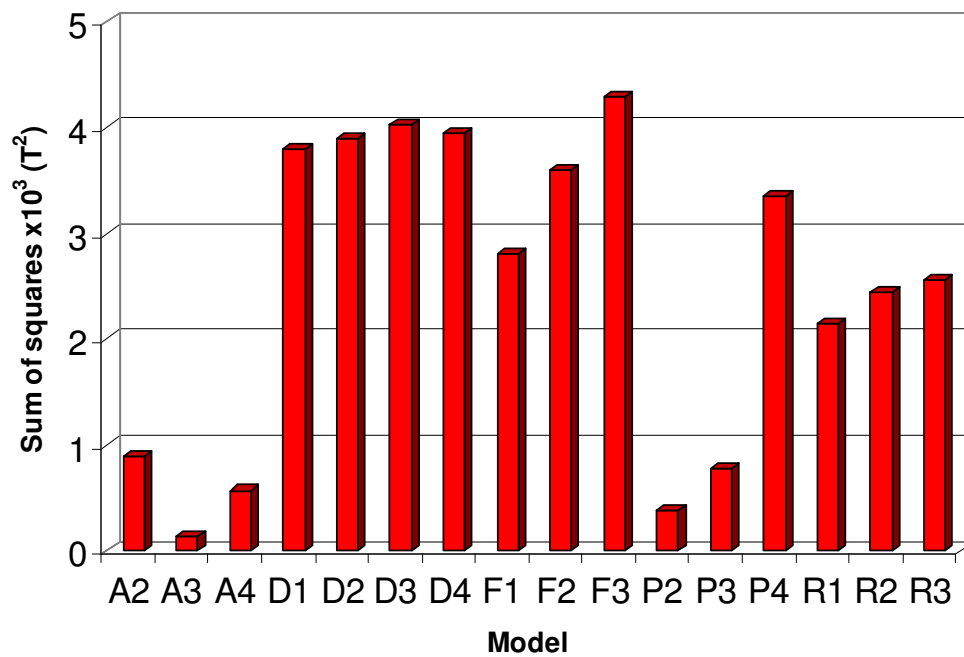


Figure 89. Sum of squared differences between actual and reconstructed nonisothermal desolvation curves ($(T_{\text{actual}} - T_{\text{reconstructed}})^2$) of sulfameter dioxane solvate.

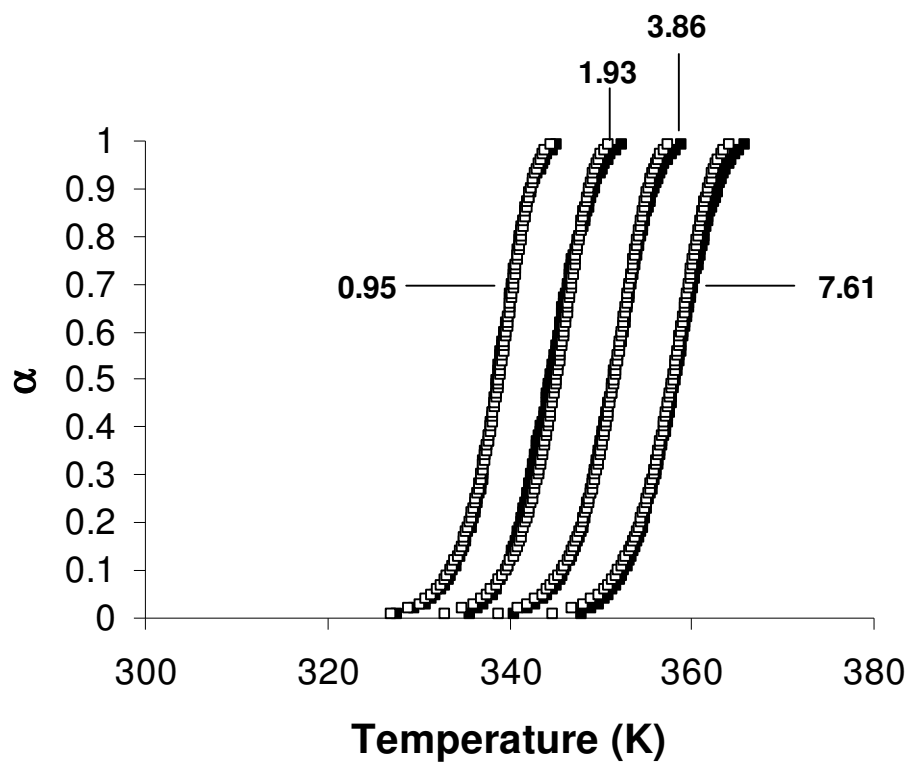


Figure 90. Reconstructed α -T plots for nonisothermal desolvation of sulfameter-tetrahydrofuran solvate for four heating rates (0.95, 1.93, 3.86, 7.61 K/min): ■, experimental curves and □, reconstructed curves (A3).

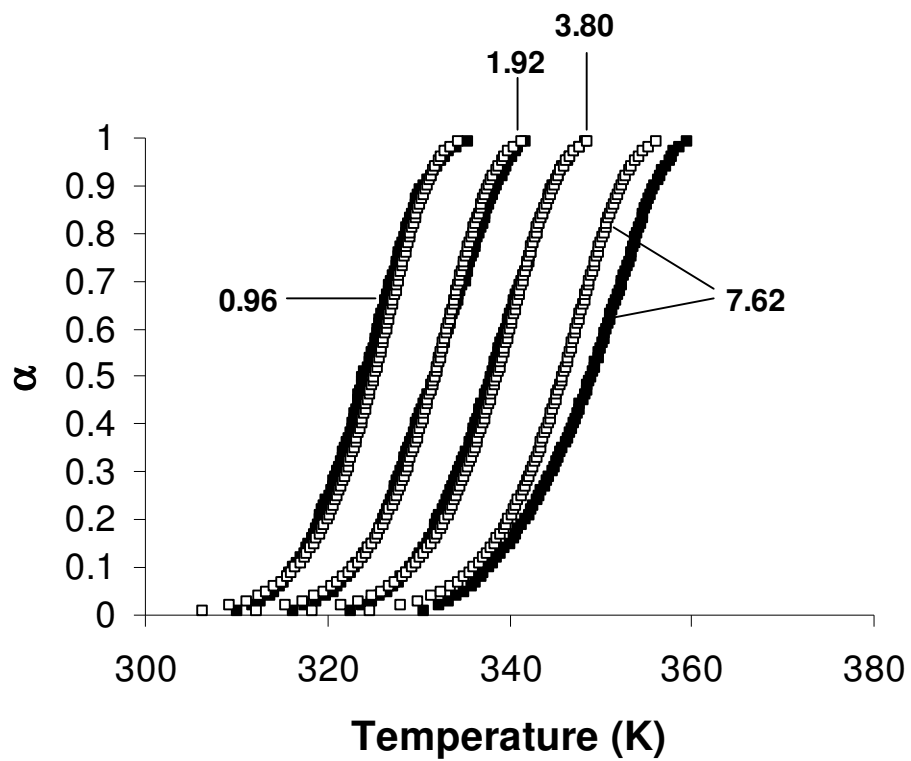


Figure 91. Reconstructed α -T plots for nonisothermal desolvation of sulfamer-dioxolane solvate for four heating rates (0.96, 1.92, 3.80, 7.62 K/min): ■, experimental curves and □, reconstructed curves (A2).

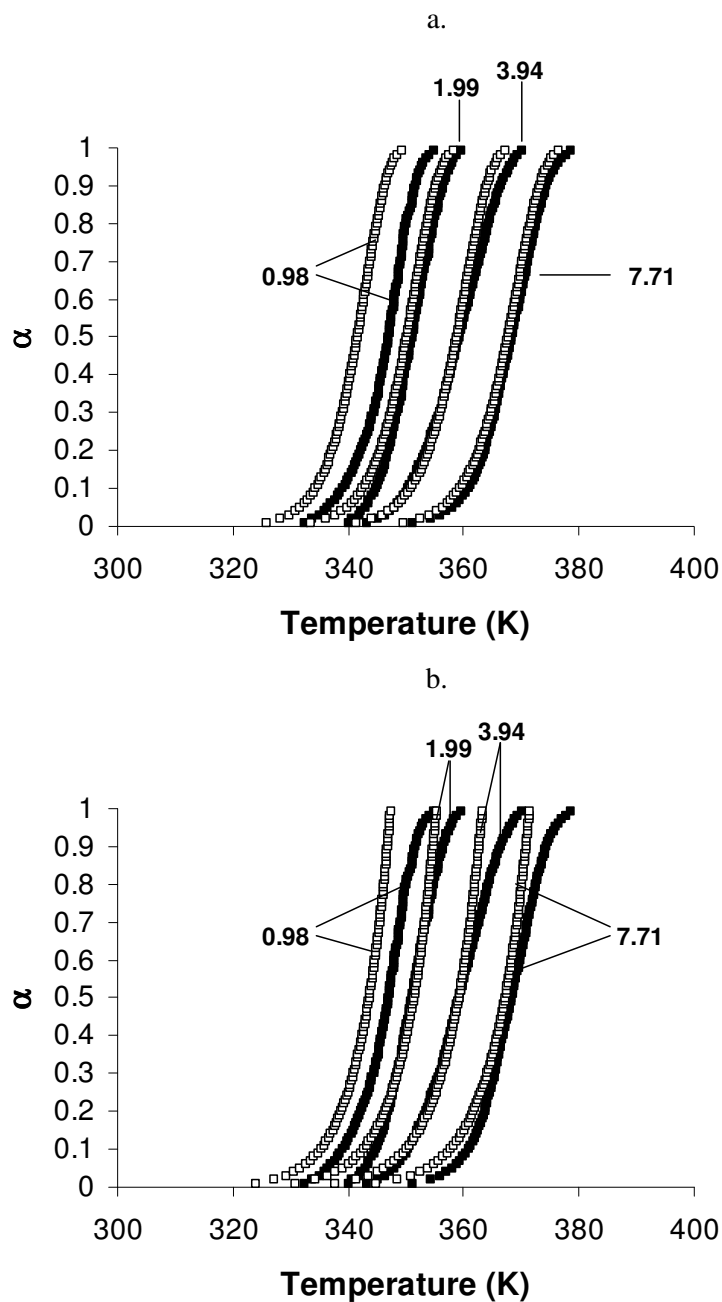


Figure 92. Reconstructed α -T plots for nonisothermal desolvation of sulfameter-dioxane solvate for four different heating rates (0.98, 1.99, 3.94, 7.71 K/min): ■, experimental curves and □, reconstructed curves (a. A3; b. P2)

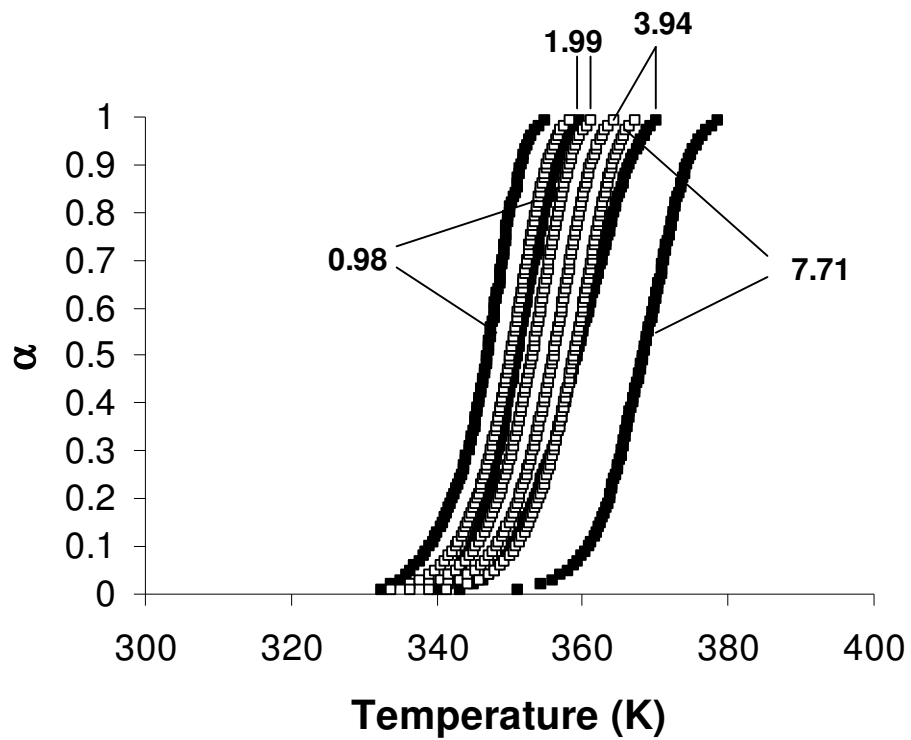


Figure 93. Reconstructed α -T plots for nonisothermal desolvation of sulfameter-dioxane solvate for four heating rates (0.98, 1.99, 3.94, 7.71 K/min): ■, experimental curves and □, reconstructed curves (F1).

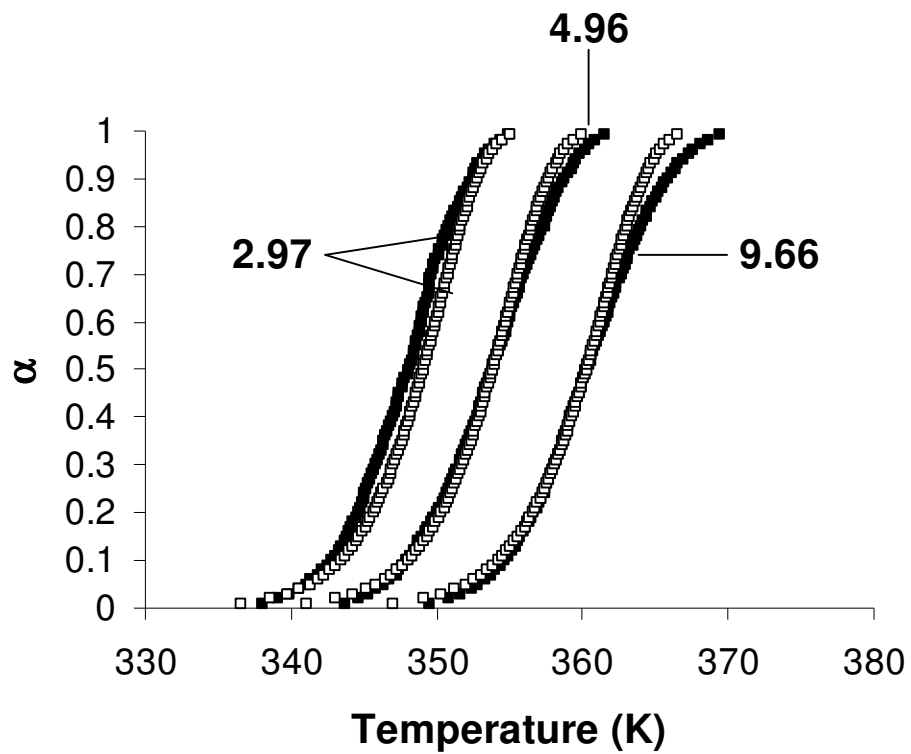


Figure 94. Predicted α -T plots for nonisothermal desolvation of sulfameter-tetrahydrofuran solvate at three heating rates (2.97, 4.96, 9.66 K/min): ■, experimental and □, predicted (A3).

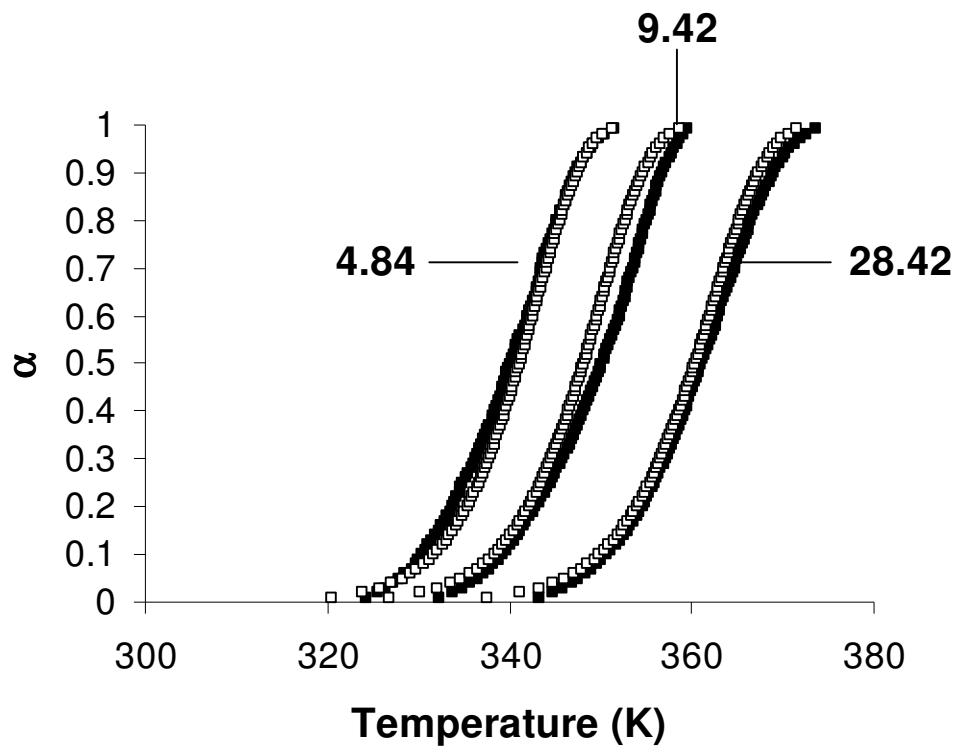


Figure 95. Predicted α -T plots for the nonisothermal desolvation of sulfameter-dioxolane solvate at three heating rates (4.84, 9.42, 28.42 K/min): ■, experimental and □, predicted (A2).

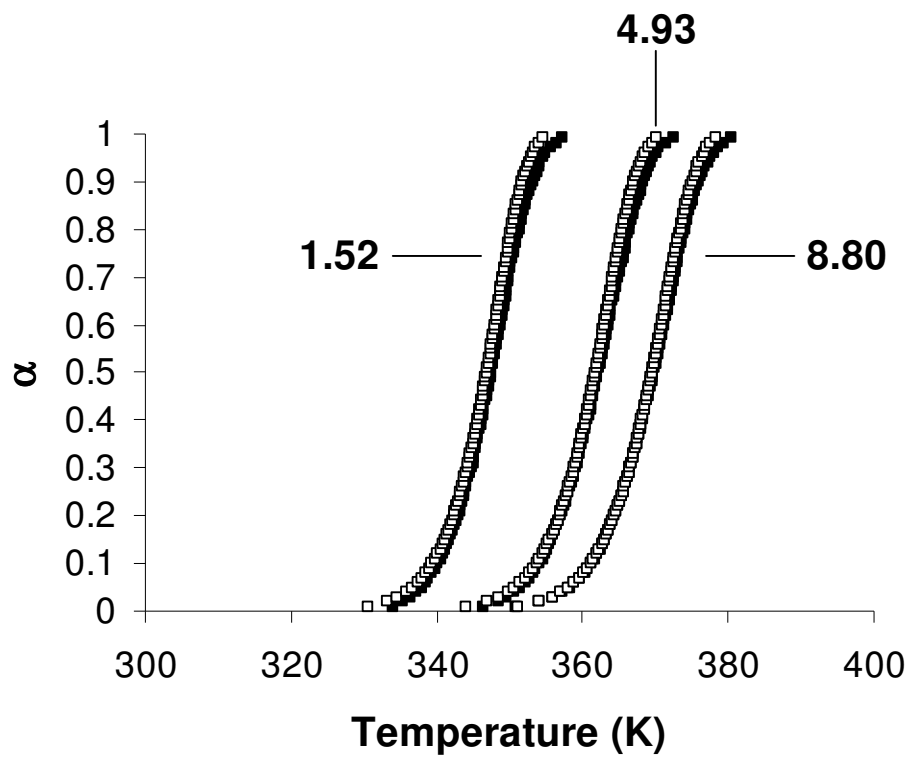


Figure 96. Predicted α -T plots for the nonisothermal desolvation of sulfameter-dioxane solvate at three heating rates (1.52, 4.93, 8.80 K/min): ■, experimental and □, predicted (A3).

CHAPTER 6
AVERAGING KINETIC PARAMETERS IN SOLID-STATE STUDIES

Introduction

Statistically, measures of central tendency for multiple data points are measures of the location of the middle or the center of a distribution, the most common of these measures are the: mean, median and mode. The mean is the most common measure of central tendency. Traditionally, the mean or “average” usually refers to an arithmetic mean. For a set of n values (X_1, X_2, \dots, X_n), the arithmetic mean (\bar{X}_A) [167] can be calculated by summing the values and dividing by n as shown below:

$$\bar{X}_A = \frac{X_1 + X_2 + \dots + X_n}{n} \quad (160)$$

Mathematically, there are several types of means. The geometric mean (\bar{X}_G) [168] is defined by Eq.(161),

$$\bar{X}_G = (X_1 \times X_2 \times \dots \times X_n)^{\frac{1}{n}} \quad (161)$$

The harmonic mean (\bar{X}_H) [169] is a reciprocal of the arithmetic mean that is defined by Eq.(162),

$$\bar{X}_H = \frac{n}{\frac{1}{X_1} + \frac{1}{X_2} + \dots + \frac{1}{X_n}} \quad (162)$$

The arithmetic, geometric and harmonic means are usually called the Pythagorean means [170]. Pythagorean means are usually expressed in a general expression called the generalized mean (M_t) also known as power mean or Hölder mean [171] defined by,

$$M_t = \left(\frac{1}{n} \sum_{i=1}^n X_i^t \right)^{\frac{1}{t}} \quad (163)$$

Where, t is a number that specifies the type of mean.

The arithmetic mean (M_1) is obtained when $t=1$, the geometric mean is obtained as $\lim_{t \rightarrow 0} (M_0)$ and the harmonic mean is obtained when $t = -1$ (M_{-1}). The order of these means is: $M_1 \geq M_0 \geq M_{-1}$. Equality of these means is achieved only when all X_i values are equal.

Kinetically, if several nonisothermal thermograms are analyzed by model-fitting methods, such as the Coats-Redfern method, a range of A and E_a values will be calculated for each model. Therefore, it is necessary to find the appropriate mean that would properly “average” these A and E_a values. By default, researchers assume the arithmetic mean to be the mean that would achieve this, however, this may not always be true. This chapter will investigate use of different means for averaging kinetic parameters obtained from nonisothermal model-fitting methods.

Solvates (particle size of 355–710 μm)

Desolvation data of three sulfameter solvates (tetrahydrofuran, dioxolane and dioxane) with particle sizes of 355–710 μm previously reported in Chapter 5, were investigated. The complementary approach led to the A3 (tetrahydrofuran and dioxane) and A2 models (dioxolane) as the models of choice for the three sulfameter solvates. For each solvate, four nonisothermal curves (four different heating rates) were analyzed by the Coats-Redfern method (Tables 33–35). E_a and A values of each solvate were averaged by the arithmetic, geometric and harmonic means. Nine different combinations of means are possible for each solvate as shown in Table 36. Each combination was used to reconstruct experimental curves for each solvate, the sum of squared differences $((T_{\text{actual}} - T_{\text{reconstructed}})^2)$ between actual and reconstructed desolvation curves for each combination were computed for each solvate. The combination that gave the least sum of

squared differences between experimental and reconstructed curves was taken as the combination that best averaged A and E_a values.

Table 37 shows the sum of squared differences between actual and reconstructed curves for the nine possible A and E_a mean combinations of each solvate, Figure 97 also shows plots of actual sulfameter dioxolane desolvation data at 1.92 K/min and reconstructed data from each of the nine possible combinations in Table 36. It can be seen that the least sum of squares occurs when the geometric mean of frequency factors and the arithmetic mean of activation energies were taken as the average.

Dioxolane solvates (particle size of 850–1700 μm)

Desolvation data of sulfameter-dioxolane solvate with a particle size of 850–1700 μm was also investigated. Twenty three nonisothermal thermograms (Figure 98) were analyzed by the Coats-Redfern method (Table 38). All possible combinations of A and E_a means (Table 36) were used to reconstruct experimental curves for this solvate. The sum of squared differences ($(T_{\text{actual}} - T_{\text{reconstructed}})^2$) between actual and reconstructed desolvation curves for each combination of means were computed for this solvate and are given in Table 39. The results agreed with those obtained for the previous solvates in that the least sum of squares occurs when frequency factors were averaged by the geometric mean while the activation energies were averaged by the arithmetic mean.

Conclusions

Results show that kinetic parameters calculated for the dioxolane solvate were comparable for the two particle sizes tested, indicating a minimal effect of particle size tested on the kinetic parameters. Results also show that the geometric mean should be used to average preexponential factor values while the arithmetic mean should be used for averaging activation energies. An example recently introduced in the literature [172] averages kinetic parameters from four thermograms and attempts to reconstruct the experimental curves from these averaged values, the mean used for averaging the results

was not specified but was assumed to be the arithmetic mean, reconstructed values disagreed with experimental ones. Authors concluded that this deviation was “inevitable” and that “much work needs to be done in solid-state kinetics”. Use of appropriate means to average the kinetic results could have reduced such deviation between experimental and reconstructed curves.

Table 33. Fitted kinetic parameters (A3 model) for the nonisothermal desolvation of sulfameter-tetrahydrofuran solvate (Figure 79) using the Coats-Redfern method.

Heating rate	A (min ⁻¹)	E _a (kJ/mole)
0.95	3.93×10^{15}	107.76
1.93	5.97×10^{14}	102.47
3.86	8.10×10^{14}	103.42
7.61	1.11×10^{15}	104.43
Arithmetic mean	1.61×10^{15}	104.52
Geometric mean	1.21×10^{15}	104.50
Harmonic mean	9.84×10^{14}	104.48

Table 34. Fitted kinetic parameters (A2 model) for the nonisothermal desolvation of sulfameter-dioxolane solvate (Figure 80) using the Coats-Redfern method.

Heating rate	A (min ⁻¹)	E _a (kJ/mole)
0.96	5.22×10^{13}	91.85
1.92	1.06×10^{13}	87.87
3.80	2.91×10^{13}	90.47
7.62	1.59×10^{12}	83.23
Arithmetic mean	2.34×10^{13}	88.36
Geometric mean	1.26×10^{13}	88.30
Harmonic mean	5.15×10^{12}	88.23

Table 35. Fitted kinetic parameters (A3 model) for the nonisothermal desolvation of sulfameter-dioxane solvate (Figure 81) using the Coats-Redfern method.

Heating rate	A (min ⁻¹)	E _a (kJ/mole)
0.98	3.59×10^{10}	77.72
1.99	1.75×10^{12}	87.79
3.94	6.97×10^{08}	65.32
7.71	6.02×10^{10}	78.21
Arithmetic mean	4.62×10^{11}	77.26
Geometric mean	4.03×10^{10}	76.84
Harmonic mean	2.71×10^{09}	76.40

Table 36. Possible combinations of means of A and E_a .

Combination Number	Possible combinations	
	Frequency factor (A)	Activation energy (E_a)
1	Arithmetic	Arithmetic
2	Arithmetic	Geometric
3	Arithmetic	Harmonic
4	Geometric	Arithmetic
5	Geometric	Geometric
6	Geometric	Harmonic
7	Harmonic	Arithmetic
8	Harmonic	Geometric
9	Harmonic	Harmonic

Table 37. Sum of squared differences between actual and reconstructed curves for possible A and E_a mean combinations for each solvate.

Mean used		Sum of squared differences (K^2) ($(T_{\text{actual}} - T_{\text{reconstructed}})^2$)		
(A)	(E_a)	Tetrahydrofuran	Dioxolane	Dioxane
Arithmetic	Arithmetic	3,140	17,265	329,098
Arithmetic	Geometric	3,274	18,419	369,799
Arithmetic	Harmonic	3,410	19,631	413,913
Geometric	Arithmetic	120	1,018	1,606
Geometric	Geometric	127	1,108	3,278
Geometric	Harmonic	137	1,242	7,885
Harmonic	Arithmetic	1,322	31,497	566,589
Harmonic	Geometric	1,238	29,886	506,404
Harmonic	Harmonic	1,158	28,296	448,330

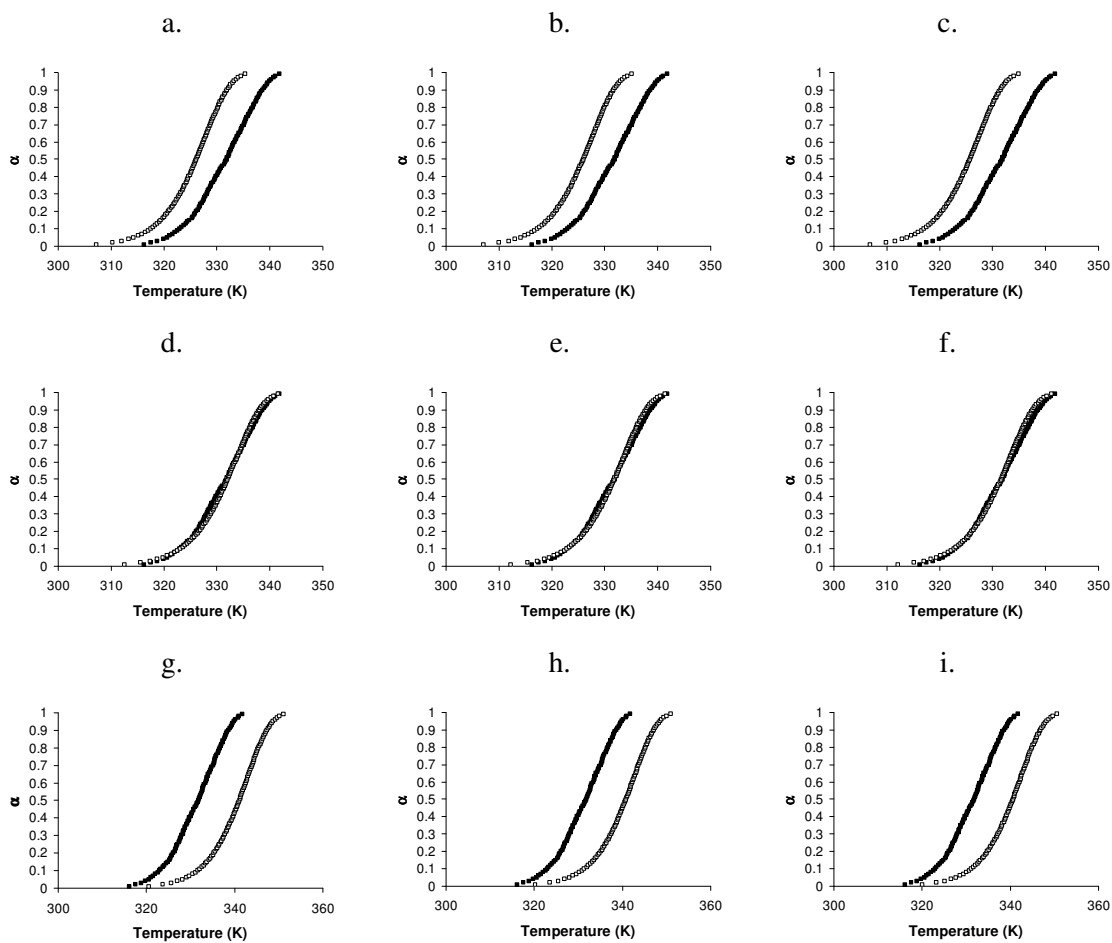


Figure 97. Actual (■) and reconstructed (□) curves for the desolvation of sulfamer dioxolane solvate at 1.92 K/min. Curves reconstructed according to possible combinations of means of A and E_a given in Table 36: a, 1; b, 2; c, 3; d, 4; e, 5; f, 6; g, 7; h, 8 and i, 9

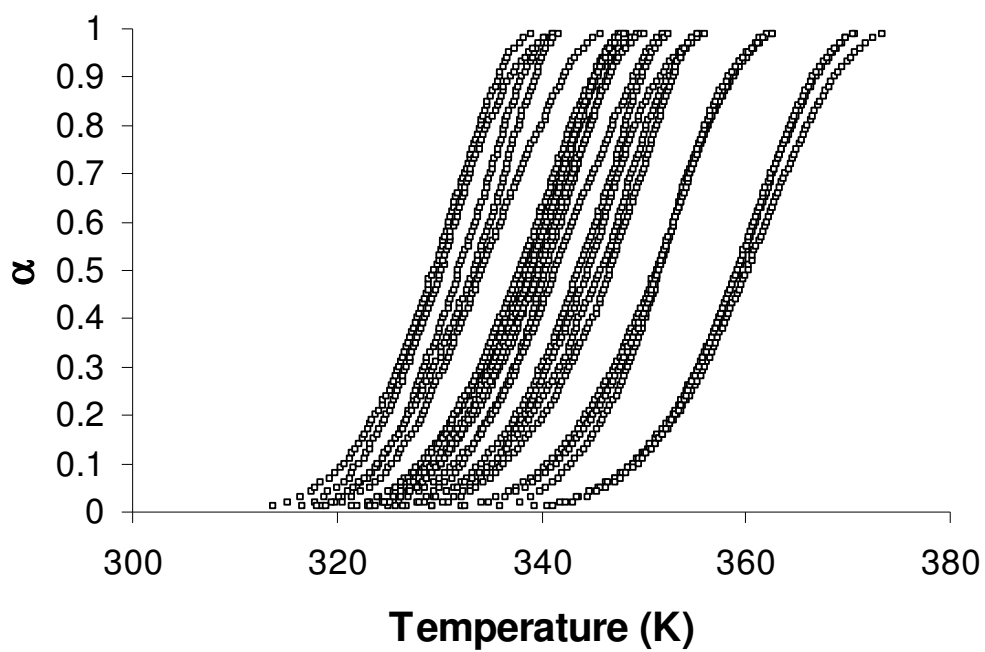


Figure 98. α versus temperature plots for the nonisothermal desolvation of sulfameter-dioxolane for 23 samples having a particle size of 850–1700 μm at various heating rates.

Table 38. Fitted kinetic parameters (A2 model) for the nonisothermal desolvation of sulfameter-dioxolane solvate (Figure 98) with a particle size of 850–1700 μm using the Coats-Redfern method.

Heating rate	A (min^{-1})	E_a (kJ/mole)
1.01	1.22×10^{13}	89.31
1.01	3.40×10^{14}	99.01
1.02	4.25×10^{13}	92.89
1.02	1.30×10^{13}	90.47
1.52	1.25×10^{12}	83.5
1.53	1.35×10^{12}	84.6
2.01	1.40×10^{12}	83.96
2.02	1.77×10^{14}	97.81
2.02	4.11×10^{12}	86.86
2.03	6.24×10^{13}	94.61
2.53	5.58×10^{12}	88.03
2.65	2.49×10^{13}	91.23
3.01	3.83×10^{13}	93.37
3.15	5.76×10^{12}	86.98
4.00	3.12×10^{13}	92.32
4.00	1.52×10^{12}	84.11
4.01	1.94×10^{13}	91.46
7.87	2.03×10^{12}	84.45
7.88	8.52×10^{14}	101.79
7.89	1.43×10^{13}	90.03
15.27	1.09×10^{13}	89.43
15.29	6.87×10^{11}	81.66
15.36	4.41×10^{13}	93.47
Arithmetic mean	7.42×10^{13}	90.06
Geometric mean	1.32×10^{13}	89.91
Harmonic mean	3.83×10^{12}	89.77

Table 39. Sum of squared differences between actual and reconstructed curves for possible A and E_a mean combinations for sulfameter-dioxolane solvate with a particle size of 850–1700 μm .

Mean used		Sum of squared differences (K^2) $((T_{\text{actual}} - T_{\text{reconstructed}})^2)$
(A)	(E_a)	
Arithmetic	Arithmetic	654,303
Arithmetic	Geometric	694,155
Arithmetic	Harmonic	734,673
Geometric	Arithmetic	5,564
Geometric	Geometric	6,377
Geometric	Harmonic	8,465
Harmonic	Arithmetic	392,208
Harmonic	Geometric	359,933
Harmonic	Harmonic	329,445

CHAPTER 7

DESOLVATION AND POLYMORPHIC TRANSFORMATIONS OF SULFAMETER SOLVATES

Solid-state kinetic principles were introduced and discussed in previous chapters. Chapter 5 introduced a method to obtain reliable kinetic data nonisothermally by combining modelistic and model-free approaches in a complementary approach which was tested on three sulfameter solvates (tetrahydrofuran, dioxolane and dioxane). Although kinetic parameters needed to characterize the desolvation reactions were obtained, general mechanistic conclusions about sulfameter solvate desolvation can not be drawn due to the limited number of solvates studied. Through the study of more such sulfameter solvates we hope that a correlation of kinetic parameters with solvent structure/size will emerge. Therefore, this chapter expands nonisothermal solvate analysis to four more sulfameter solvates including: oxane, oxepane, chloroform and bromoform. In addition, five solvates (tetrahydrofuran, dioxolane, oxane, dioxane and oxepane) were isothermally desolvated and their desolvation kinetics analyzed. The isothermal and nonisothermal kinetic parameters will be compared in the next chapter. Finally, polymorphic transformations of the tetrahydrofuran, dioxolane, oxane, dioxane, oxepane, chloroform and bromoform solvates after desolvation, melting and recrystallization were studied and will be discussed.

Experimental

Sulfameter solvates were prepared from the following solvents: tetrahydrofuran, dioxolane, oxane, dioxane, oxepane, chloroform and bromoform, as described in Chapter 3. The prepared solvates were sieved and a particle size range of 355–710 μm was used for desolvation studies.

Sulfameter solvate desolvation

Desolvation kinetics of the tetrahydrofuran, dioxolane, oxane, dioxane and oxepane solvates was followed isothermally by TGA, as described in Chapter 3. Isothermal runs were done at nominal temperatures of 323, 328, 333, 338 and 343 K for the five solvates. An additional sample of the dioxane solvate was desolvated at the following nominal temperatures: 328, 333, 338, 343 and 348 K. The exact reaction temperature was calculated by averaging measured reaction temperatures during the time period of significant weight loss, as discussed in Chapter 3.

Additionally, desolvation kinetics of the oxane, oxepane, chloroform and bromoform solvates was followed nonisothermally by TGA, as described in Chapter 3. Nonisothermal runs were performed at nominal heating rates of 1, 2, 4, 8 and 16 K/min. Runs were done in duplicate for the oxane solvate (i.e., 10 curves total). The exact heating rate was obtained from the slope of the linear heating curve of the TGA run during the time period of significant weight loss, as discussed in Chapter 3.

Kinetic analysis of desolvation

Kinetic analysis of isothermal data was done by the conventional (model-fitting) method and the advanced isoconversional (model-free) method, as described in Chapter 1. Model-fitting results were displayed on a reduced time plot which is an α -time plot where the time axis has been normalized (i.e., reduced) by the time required for 90% conversion ($t_{0.9}$) for each model. Instead of time (minutes) on the x-axis, the reduced time ($t/t_{0.9}$) which is unitless is displayed. The advantage of reduced time plots is that the experimental data and all models can be displayed in a single figure and the best fitting model appears to closely follow the actual data.

Kinetic analysis of nonisothermal data was done by the complementary method (see Chapter 5) from which a model was selected, the choice of model was verified by reconstructing the original experimental TGA curves from the parameters (A and E_a)

obtained with the selected model. Reconstruction results were shown as the sum of squared differences between experimental and reconstructed models for each possible kinetic triplet. The model of choice was that which had the least sum of squared differences.

Polymorphic transformation of sulfameter solvates

Sulfameter has been reported to occur in several polymorphic forms [173-178]. Bettinetti et. al. [178] have investigated and compared these polymorphic forms and reported an amorphous and three crystalline forms of sulfameter (see Table 40).

Sulfameter characterization (DSC; Figure 24b and PXRD; Figure 25) shows that the crystal form supplied by Sigma (lot no. 107F0910) is form I. This chapter discusses the transformations of the parent drug and seven of the sulfameter solvates (tetrahydrofuran, dioxolane, oxane, dioxane, oxepane, chloroform and bromoform) upon heating, cooling and reheating. Sulfameter and its solvates were nonisothermally heated at 16 K/min. up to 220°C in the DSC and then immediately allowed to cool (uncontrolled) to room temperature (10-20 minutes) and then re-heated at 16 K/min. to 220°C. The objective was to determine the resulting crystal forms after solvate desolvation and sulfameter melting.

Results and Discussion

Isothermal desolvation results

Thermogravimetric results for the isothermal desolvation of the tetrahydrofuran, dioxolane, oxane, dioxane and oxepane solvates are shown in Figures 99–103. Gravimetric weight loss for these solvates showed a 1:1 drug–solvent ratio (Table 8, Chapter 3).

The conventional model-fitting results (Tables 41–45) showed that the A2 model was the model of choice for the desolvation of the tetrahydrofuran, dioxolane, dioxane

and oxepane solvates while the R3 model was the model of choice for the oxane solvate which is also shown in the reduced time plots (Figures 104–108). Model-free analysis results (Figures 109–113) show that E_a values calculated by the advanced isoconversional (AIC) method are comparable to those obtained from model-fitting methods.

Nonisothermal desolvation results

Thermogravimetric results for the nonisothermal desolvation of the oxane, oxepane, chloroform and bromoform solvates are shown in Figures 114–117. Gravimetric weight loss for these solvates showed a 1:1 drug–solvent ratio (Table 8, Chapter 3).

Several kinetic triplets were calculated from the Coats-Redfern model-fitting method for each solvate (Tables 46–49). Sum of squares ($(T_{\text{actual}} - T_{\text{reconstructed}})^2$) plots (Figures 118–120) and α –temperature reconstruction plots (Figures 121–123) show that the A2 is the model of choice for the oxane and chloroform solvates while the A3 model is the model for the oxepane solvate. The bromoform solvate shows two overlapping weight loss steps (Figures 39 and 117) which is further confirmed from its desolvation isoconversional plot (Figure 124) that does not show a flat isoconversional plot. However, it can be fairly described by a single kinetic triplet (R3 model) as seen in the sum of squares plot (Figure 125) and α –temperature reconstruction plot (Figure 126).

Results of sulfameter solvate desolvation isothermally and nonisothermally are examined and further discussed in the next chapter.

Polymorphic transformations of sulfameter solvates

Figure 127 shows two successive DSC thermograms for sulfameter: the first heating cycle (black thermogram) shows sulfameter melting at around 209°C indicating the presence of Form I and no evident thermal event prior to the melting peak. After slowly cooling the melt to room temperature, an amorphous form is produced (Figure 128a) which agrees with literature reports [177, 178]. Upon heating the amorphous form (gray thermogram), an exothermic peak is observed at 120°C which represents

crystallization of form I, which subsequently melts at 209°C. There is also a small endotherm at 197°C which could be due to a small fraction of form III melting; form III could have crystallized from the amorphous form but its crystallization exotherm was either too small to be detected or could have overlapped with the crystallization exotherm of form I.

The transformation patterns of sulfameter solvates falls in one of three patterns (Figure 129):

1. Pattern A – follows the behavior of the parent drug (non-solvated) where in the first heating cycle (black thermogram) the solvate desolvates to form I which melts at ~209°C then, upon cooling, an amorphous form is produced (Figure 128a) which crystallizes upon heating (gray thermogram) at 120-124°C to give: form I (major) and form III (minor). These forms subsequently melt at ~198°C and ~209°C, respectively. Such behavior is seen with the dioxolane and dioxane solvates (Figures 130–131).
2. Pattern B – In the first heating cycle (black thermogram), the solvate desolvates to give form I which melts at ~209°C, then upon cooling, an amorphous form is produced (Figure 128a) which crystallizes upon heating (gray thermogram) at 125°C to form I which subsequently melts at ~209°C. This behavior is seen in the oxane solvate (Figure 132).
3. Pattern C – In the first heating cycle (black thermogram), the solvate desolvates to give form I which melts at ~209°C, then upon cooling, an amorphous form is produced (Figure 128b) which crystallizes upon heating (gray thermogram) at 128–135°C to form III. Form III subsequently melts at ~197°C. This behavior is seen in the tetrahydrofuran, oxepane, chloroform and bromoform solvates (Figures 133–136).

This unusual behavior suggests that the effect of desolvation extends beyond melting, so that although all sulfameter solvates desolvate to give form I of sulfameter, the resultant amorphous phase from the melt is different. There could be some degradation of sulfameter upon melting which would account for difference in color of the amorphous form for some solvates (Figure 128b) compared to that of “yellowish” amorphous form from other solvates or the parent drug (Figure 128a). (i.e., orange versus yellow). The same behavior was also observed isothermally and with different particle sizes of the solvates. This behavior suggests that the melt has some “structure” dependent on what solvate it came from.

Table 40. Sulfameter polymorphic forms.

Form	Melting point (°C)	Comments
I	210 – 212	Also called Form α (Ref. [173]) or Form A (Ref. [174])
II	Not reported *	
III	197 – 199	Also called Form B (Ref. [174])

* Form II is believed to transform to either Form I or III and the transformation is too small to be detected [178].

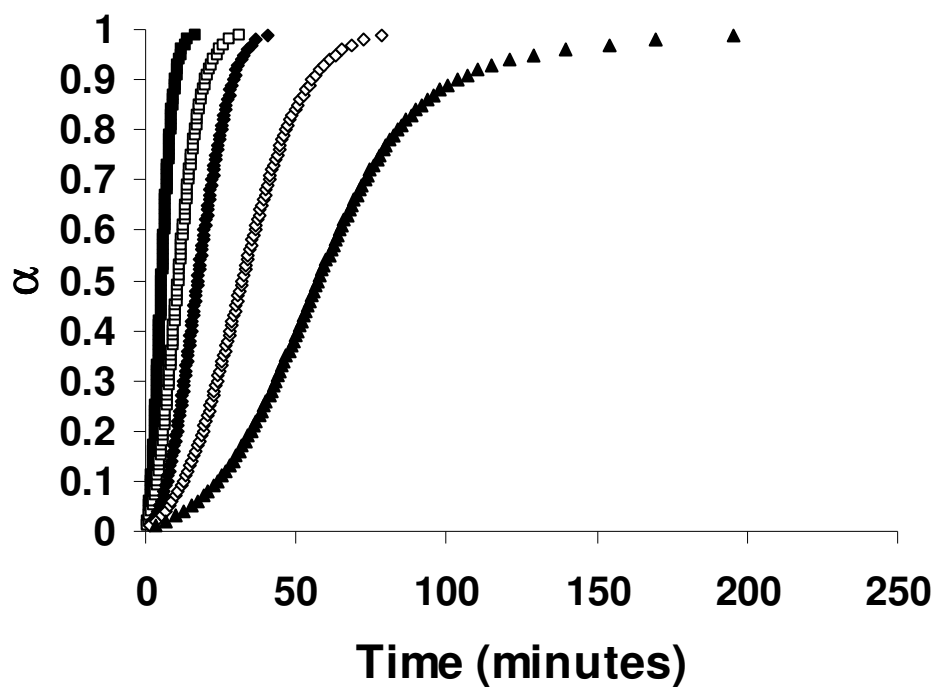


Figure 99. α versus time plots for the isothermal desolvation of sulfameter-tetrahydrofuran solvate at: ■, 341.19 K; □, 336.00 K; ◆, 330.71 K; ◇, 325.41 K and ▲, 320.34 K.

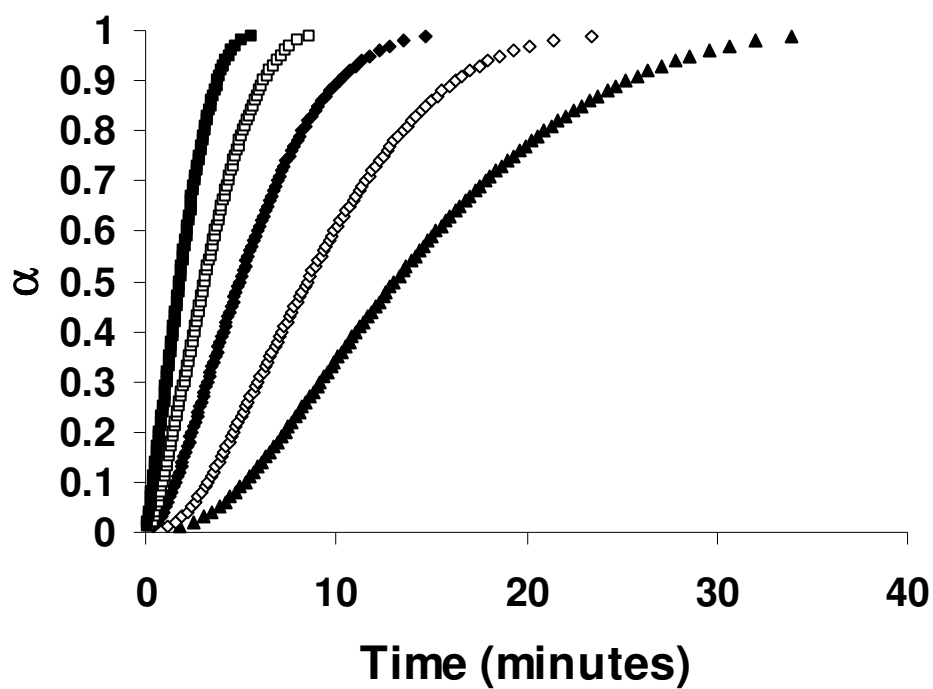


Figure 100. α versus time plots for the isothermal desolvation of sulfameter-dioxolane solvate at: ■, 341.33 K; □, 336.02 K; ◆, 330.83 K; ◇, 325.70 K and ▲, 320.48 K.

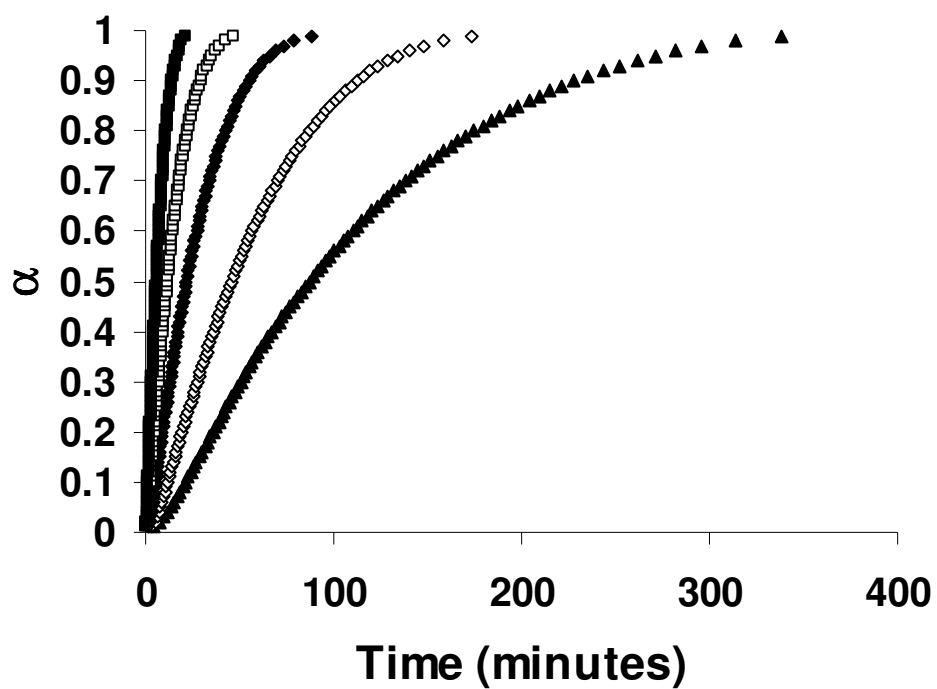


Figure 101. α versus time plots for the isothermal desolvation of sulfameter-oxane solvate at: ■, 341.64 K; □, 336.26 K; ◆, 330.38 K; ◇, 325.68 K and ▲, 320.21 K.

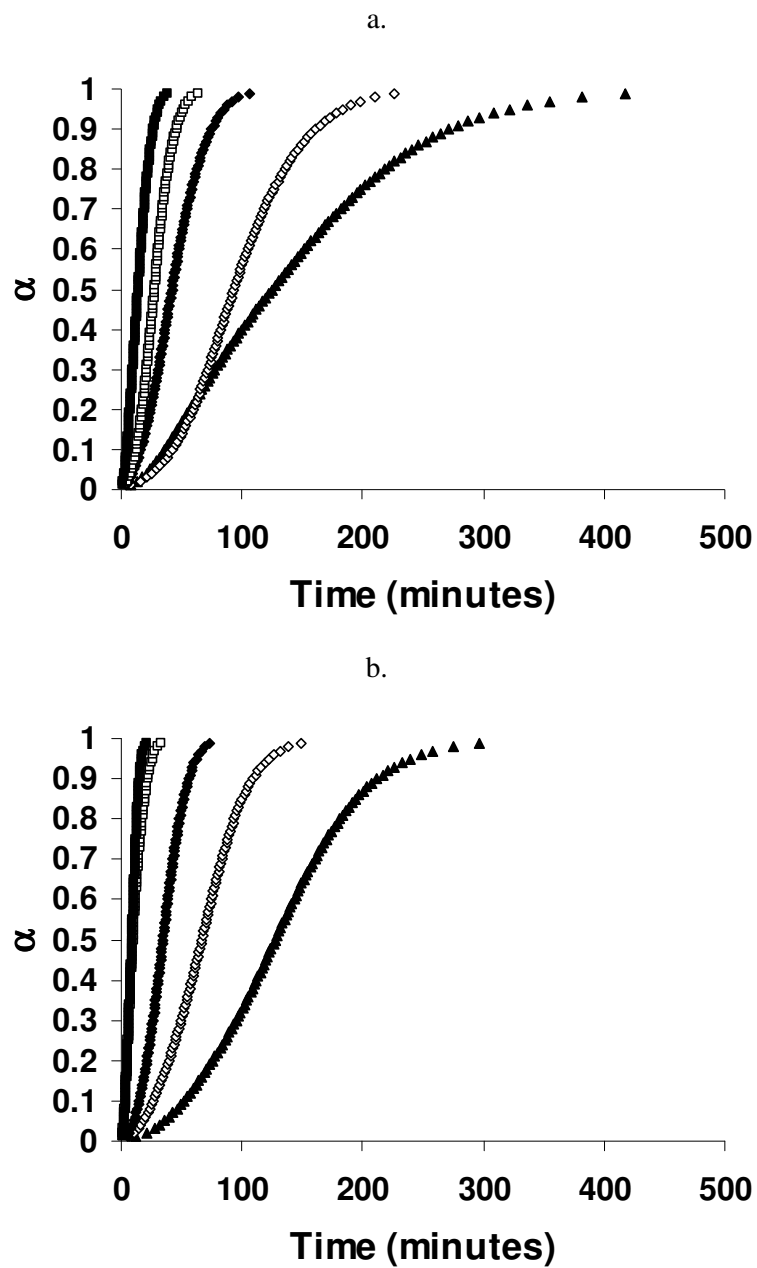


Figure 102. α versus time plots for the isothermal desolvation of sulfameter-dioxane solvate at: a. \blacksquare , 341.38 K; \square , 336.04 K; \blacklozenge , 330.87 K; \diamond , 325.53 K and \blacktriangle , 320.33 K; b. \blacksquare , 346.33 K; \square , 341.07 K; \blacklozenge , 335.90 K; \diamond , 330.64 K and \blacktriangle , 325.45 K.

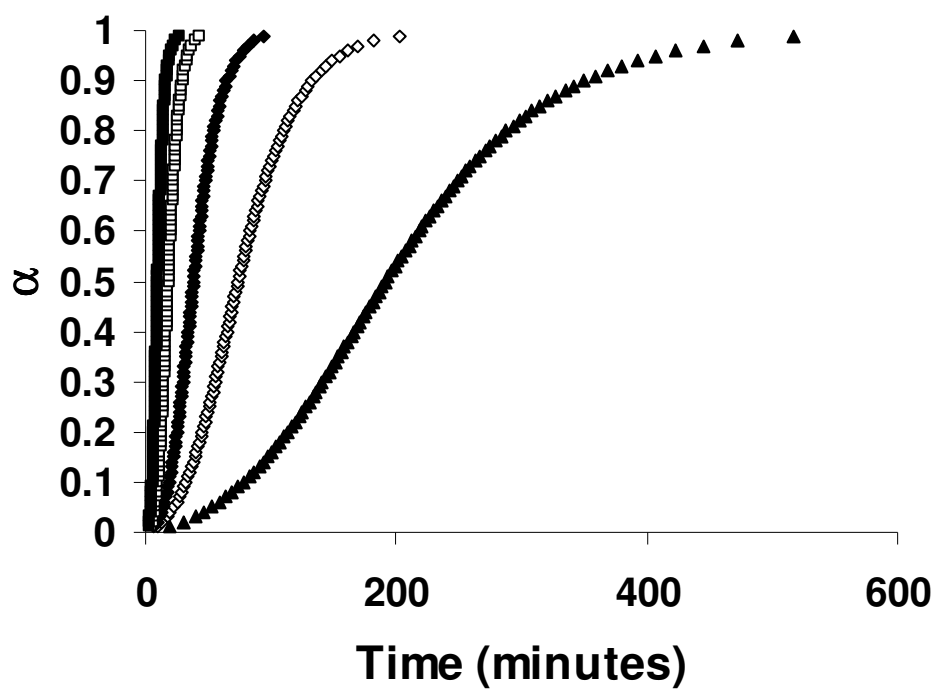


Figure 103. α versus time plots for the isothermal desolvation of sulfameter-oxepane solvate at: ■, 341.64 K; □, 336.26 K; ◆, 330.38 K; ◇, 325.68 K and ▲, 320.21 K.

Table 41. Fitted kinetic parameters for sulfameter-tetrahydrofuran isothermal desolvation kinetics by the conventional model-fitting method.

Model	A (min ⁻¹)	E _a (kJ/mole)	r *
A2**	3.07×10^{14}	100.23	0.9946
A3	2.28×10^{14}	100.40	0.9881
A4	1.82×10^{14}	100.47	0.9801
D1	2.27×10^{14}	100.62	0.9649
D2	1.66×10^{14}	100.18	0.9606
D3	5.92×10^{13}	99.33	0.9258
D4	4.29×10^{13}	99.92	0.9540
F1	4.92×10^{14}	99.61	0.9656
F2	1.94×10^{15}	97.41	0.6679
F3	4.21×10^{16}	96.60	0.4442
P2	1.98×10^{14}	101.00	0.9344
P3	1.58×10^{14}	101.00	0.9149
P4	1.30×10^{14}	100.99	0.9024
R1	2.46×10^{14}	100.93	0.9631
R2	1.71×10^{14}	100.45	0.9846
R3	1.28×10^{14}	100.21	0.9854

* Correlation coefficient for g (α) vs. t plot.

** Best fit model.

Table 42. Fitted kinetic parameters for sulfameter-dioxolane isothermal desolvation kinetics by the conventional model-fitting method.

Model	A (min ⁻¹)	E _a (kJ/mole)	r *
A2**	3.09×10^{11}	78.14	0.9990
A3	2.15×10^{11}	78.14	0.9900
A4	1.67×10^{11}	78.13	0.9802
D1	2.03×10^{11}	78.15	0.9869
D2	1.69×10^{11}	78.08	0.9784
D3	7.86×10^{10}	78.01	0.9294
D4	4.73×10^{10}	78.05	0.9678
F1	6.08×10^{11}	78.09	0.9684
F2	5.28×10^{12}	78.22	0.6306
F3	1.72×10^{14}	78.66	0.3965
P2	1.55×10^{11}	78.22	0.9378
P3	1.22×10^{11}	78.19	0.9133
P4	9.91×10^{10}	78.16	0.8980
R1	2.01×10^{11}	78.24	0.9774
R2	1.61×10^{11}	78.16	0.9979
R3	1.30×10^{11}	78.13	0.9965

* Correlation coefficient for g (α) vs. t plot.

** Best fit model.

Table 43. Fitted kinetic parameters for sulfameter-oxane isothermal desolvation kinetics by the conventional model-fitting method.

Model	A (min ⁻¹)	E _a (kJ/mole)	r *
A2	8.10×10^{16}	117.54	0.9916
A3	5.78×10^{16}	117.63	0.9722
A4	4.55×10^{16}	117.69	0.9569
D1	4.92×10^{16}	117.32	0.9872
D2	4.16×10^{16}	117.25	0.9917
D3	2.02×10^{16}	117.23	0.9609
D4	1.18×10^{16}	117.24	0.9875
F1	1.56×10^{17}	117.36	0.9872
F2	1.46×10^{18}	117.54	0.6769
F3	4.71×10^{19}	117.91	0.4360
P2	4.21×10^{16}	117.81	0.8985
P3	3.43×10^{16}	117.91	0.8686
P4	2.86×10^{16}	117.96	0.8506
R1	5.08×10^{16}	117.59	0.9537
R2	4.07×10^{16}	117.44	0.9929
R3**	3.29×10^{16}	117.41	0.9990

* Correlation coefficient for g (α) vs. t plot.

** Best fit model.

Table 44. Fitted kinetic parameters (averaged from two experiments)^a for sulfameter-dioxane isothermal desolvation kinetics by the conventional model-fitting method.

Model	A (min ⁻¹)	E _a (kJ/mole)	r ^b
A2 ^c	9.59×10^{15}	112.53	0.9978
A3	6.78×10^{15}	112.56	0.9939
A4	5.29×10^{15}	112.57	0.9870
D1	6.46×10^{15}	112.66	0.9751
D2	5.32×10^{15}	112.56	0.9641
D3	2.36×10^{15}	112.36	0.9146
D4	1.47×10^{15}	112.50	0.9530
F1	1.82×10^{16}	112.41	0.9582
F2	1.19×10^{17}	111.77	0.6252
F3	2.87×10^{18}	111.36	0.3966
P2	4.98×10^{15}	112.67	0.9489
P3	3.95×10^{15}	112.66	0.9289
P4	3.25×10^{15}	112.65	0.9159
R1	6.36×10^{15}	112.69	0.9776
R2	5.05×10^{15}	112.60	0.9919
R3	4.03×10^{15}	112.55	0.9887

^a Results averaged from two experiments, by taking the geometric mean of A and arithmetic mean of E_a and r.

^b Correlation coefficient for g (α) vs. t plot.

^c Best fit model.

Table 45. Fitted kinetic parameters for sulfameter-oxepane isothermal desolvation kinetics by the conventional model-fitting method.

Model	A (min ⁻¹)	E _a (kJ/mole)	r *
A2**	2.81×10^{20}	139.79	0.9966
A3	1.84×10^{20}	139.61	0.9875
A4	1.39×10^{20}	139.54	0.9782
D1	1.07×10^{21}	139.81	0.9841
D2	1.57×10^{20}	139.40	0.9694
D3	1.56×10^{20}	139.79	0.9685
D4	1.04×10^{20}	140.67	0.9373
F1	4.89×10^{19}	140.06	0.9634
F2	7.17×10^{20}	140.43	0.9738
F3	2.00×10^{22}	143.59	0.6771
P2	1.41×10^{24}	146.02	0.4486
P3	1.03×10^{20}	139.03	0.9282
P4	8.19×10^{19}	139.03	0.9074
R1	6.77×10^{19}	139.03	0.8943
R2	1.36×10^{20}	139.11	0.9610
R3	1.33×10^{20}	139.56	0.9874

* Correlation coefficient for g (α) vs. t plot.

** Best fit model.

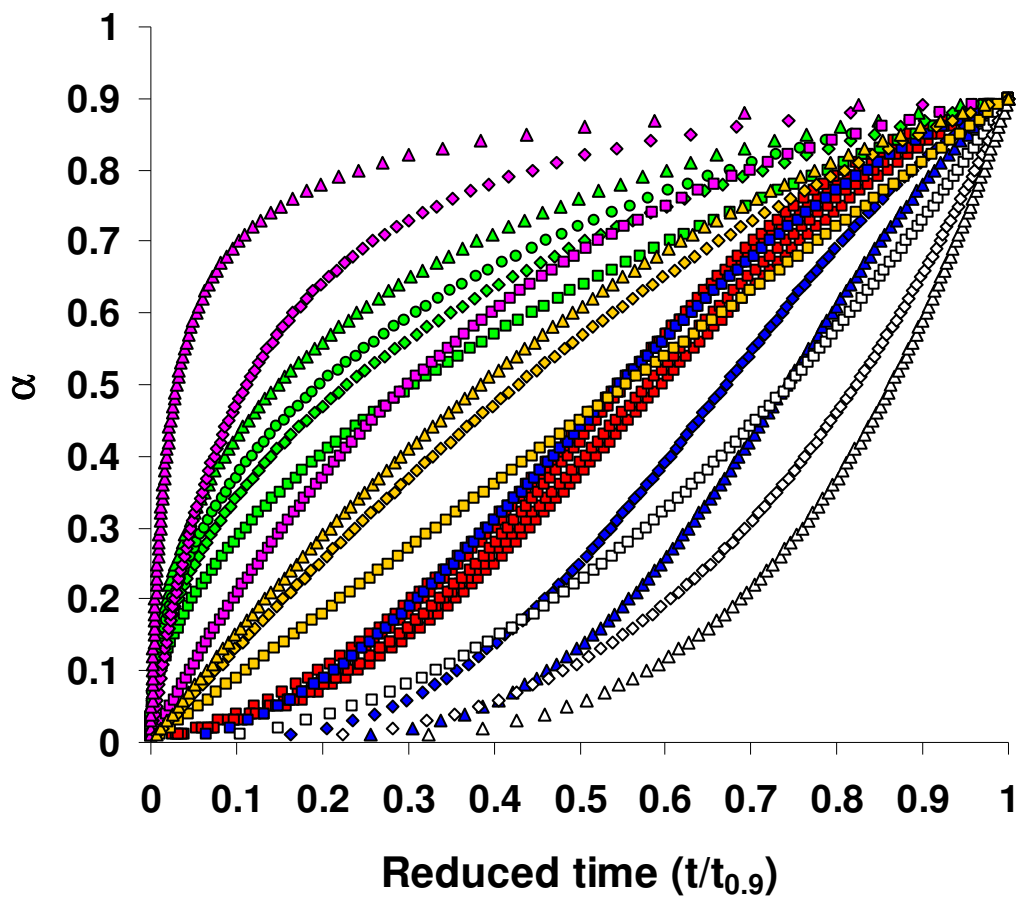


Figure 104. α versus reduced time plots ($t/t_{0.9}$) for the isothermal desolvation of sulfameter-tetrahydrofuran solvate and various reaction models: \blacksquare , desolvation data (Figure 99); \blacksquare , A2; \blacklozenge , A3; \blacktriangle , A4; \blacksquare , D1; \blacklozenge , D2; \blacktriangle , D3; \bullet , D4; \blacksquare , F1; \blacklozenge , F2; \blacktriangle , F3; \square , P2; \diamond , P3; \triangle , P4; \blacksquare , R1; \blacklozenge , R2 and \blacktriangle , R3.

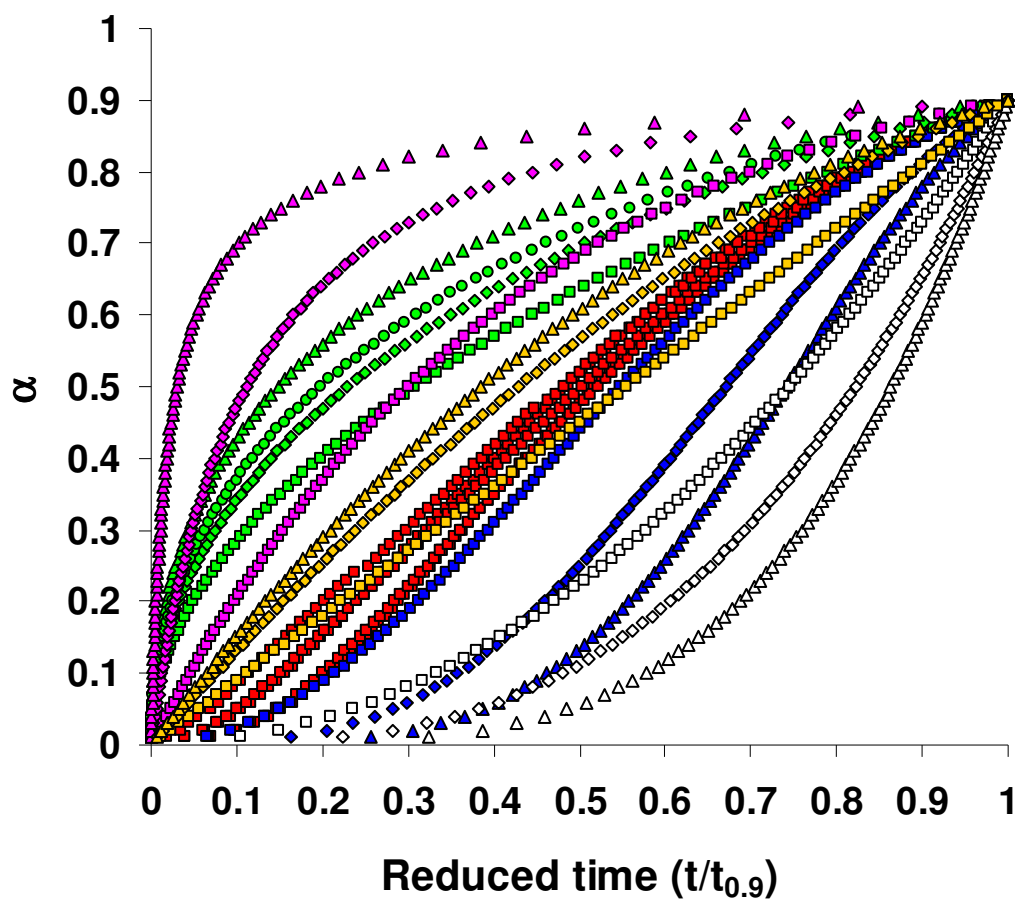


Figure 105. α versus reduced time plots ($t/t_{0.9}$) for the isothermal desolvation of sulfameter-dioxolane solvate and various reaction models: \blacksquare , desolvation data (Figure 100); \blacksquare , A2; \blacklozenge , A3; \blacktriangle , A4; \blacksquare , D1; \blacklozenge , D2; \blacktriangle , D3; \bullet , D4; \blacksquare , F1; \blacklozenge , F2; \blacktriangle , F3; \square , P2; \diamond , P3; \triangle , P4; \blacksquare , R1; \blacklozenge , R2 and \blacktriangle , R3.

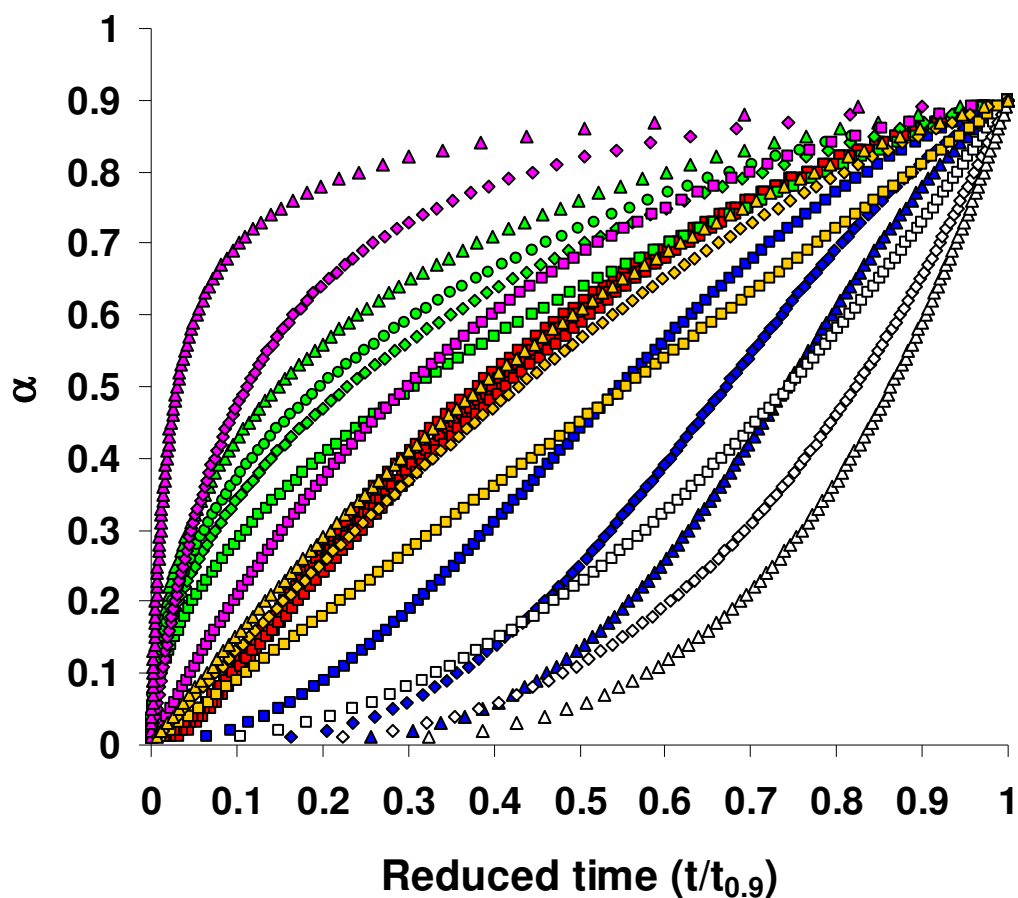


Figure 106. α versus reduced time plots ($t/t_{0.9}$) for the isothermal desolvation of sulfameter-oxane solvate and various reaction models: \blacksquare , desolvation data (Figure 101); \blacksquare , A2; \blacklozenge , A3; \blacktriangle , A4; \blacksquare , D1; \blacklozenge , D2; \blacktriangle , D3; \bullet , D4; \blacksquare , F1; \blacklozenge , F2; \blacktriangle , F3; \square , P2; \diamond , P3; \triangle , P4; \blacksquare , R1; \blacklozenge , R2 and \blacktriangle , R3.

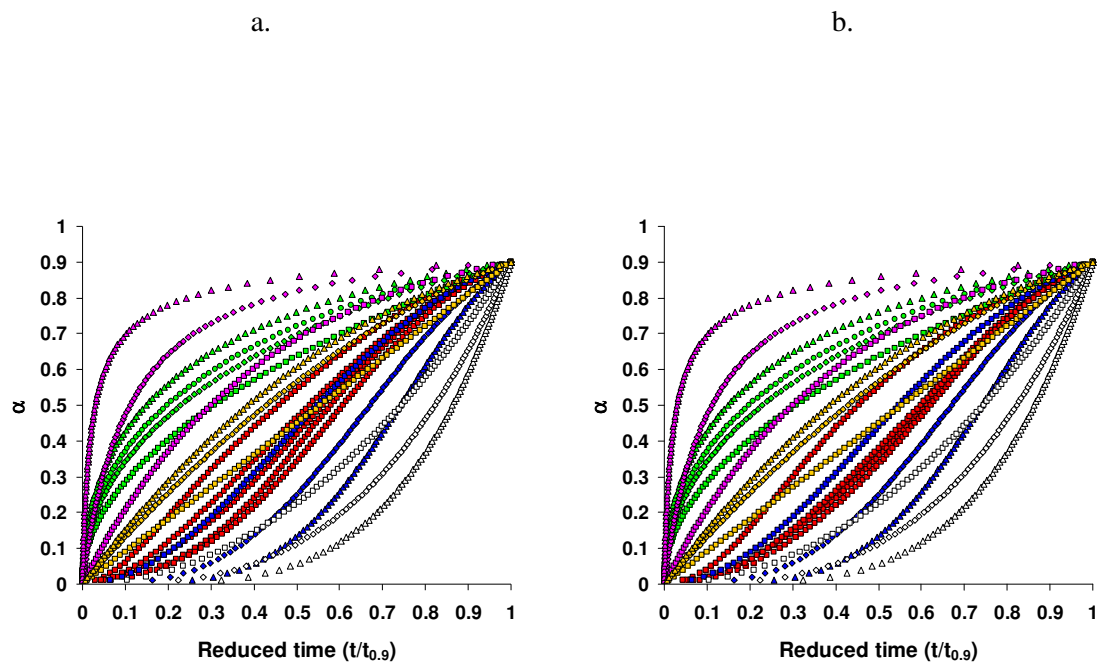


Figure 107. α versus reduced time plots ($t/t_{0.9}$) for the isothermal desolvation of sulfameter-dioxane solvate and various reaction models: ■, desolvation data (Figure 102 a and b); ■, A2; ◆, A3; ▲, A4; ■, D1; ◆, D2; ▲, D3; ●, D4; ■, F1; ◆, F2; ▲, F3; □, P2; ◇, P3; △, P4; ■, R1; ◆, R2 and ▲, R3.

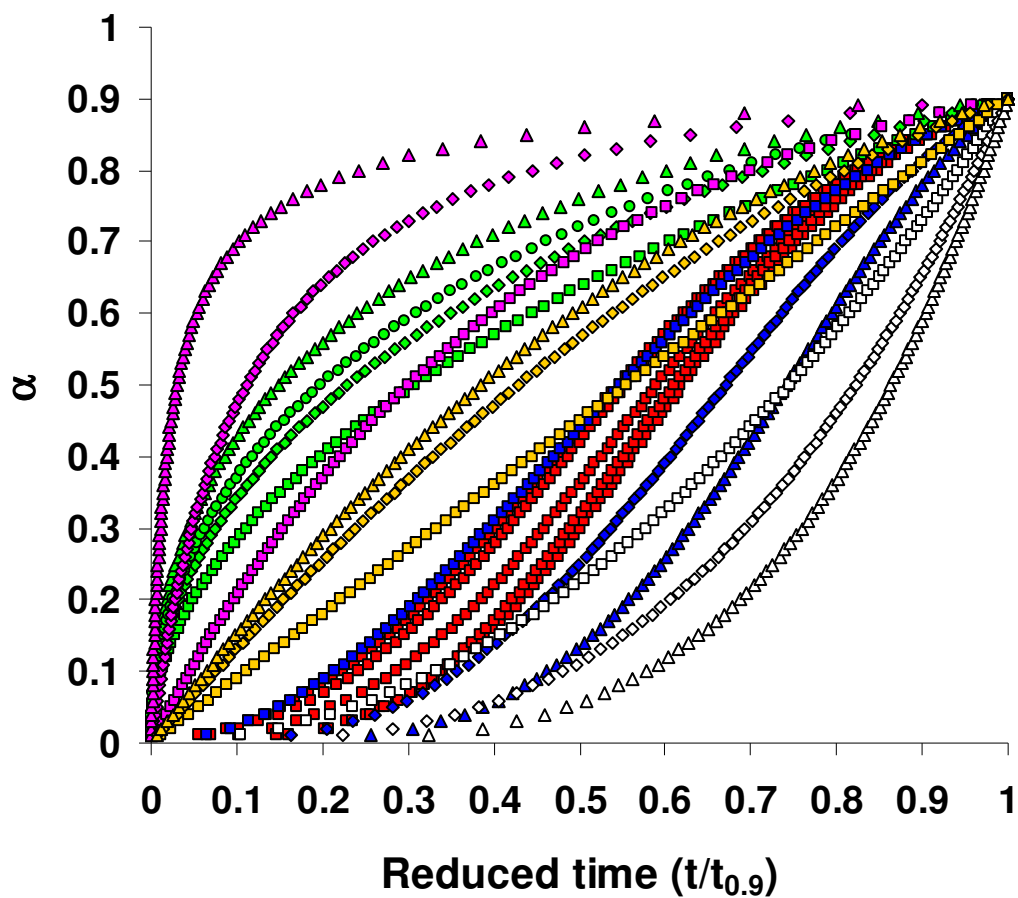


Figure 108. α versus reduced time plots ($t/t_{0.9}$) for the isothermal desolvation of sulfameter-oxepane solvate and various reaction models: ■, desolvation data (Figure 103); ■, A2; ◆, A3; ▲, A4; ■, D1; ◆, D2; ▲, D3; ●, D4; ■, F1; ◆, F2; ▲, F3; □, P2; ◇, P3; △, P4; ■, R1; ◆, R2 and ▲, R3.

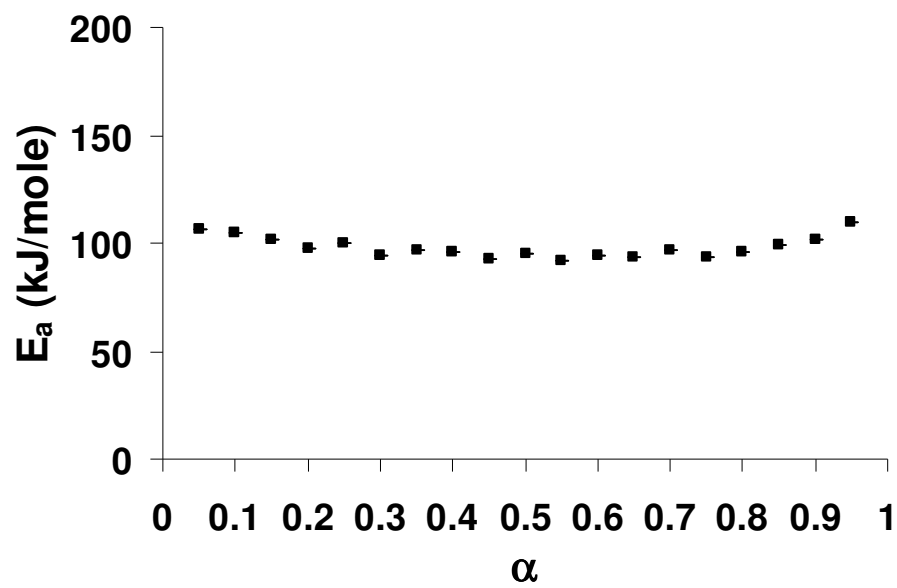


Figure 109. E_a versus α plots for isothermal sulfameter-tetrahydrofuran solvate desolvation evaluated by the AIC method.

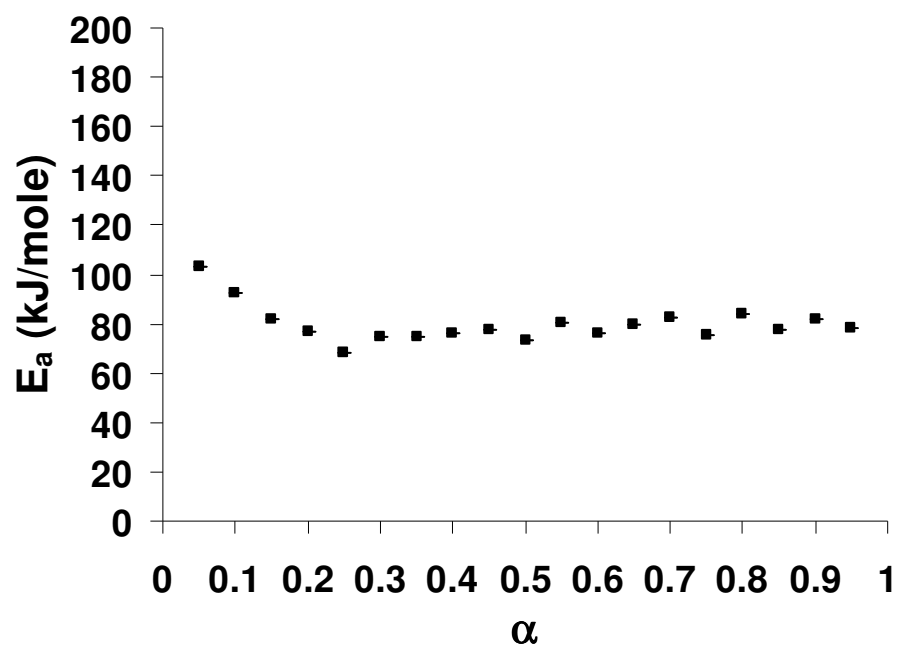


Figure 110. E_a versus α plots for isothermal sulfameter-dioxolane solvate desolvation evaluated by the AIC method.

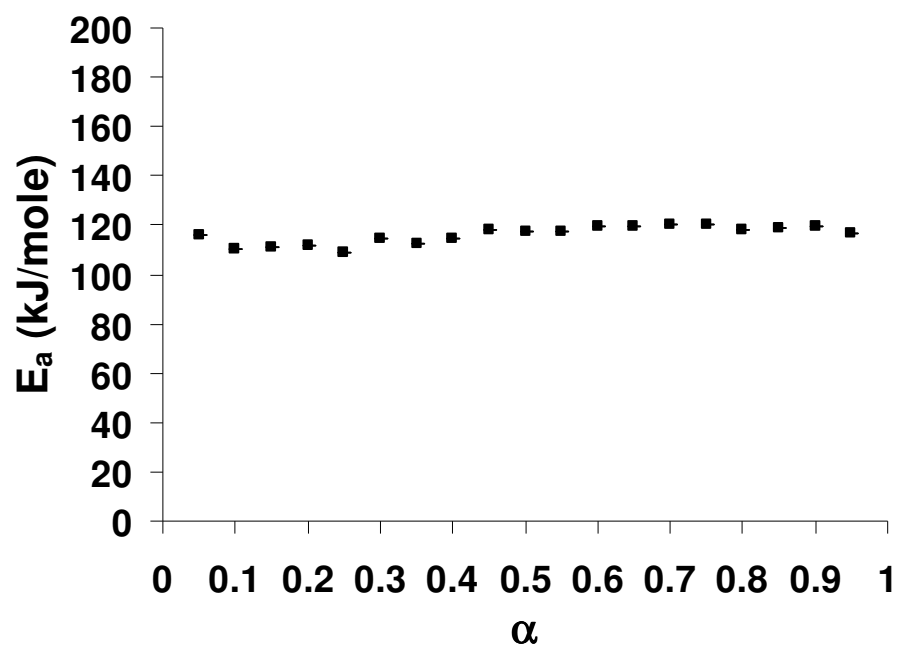


Figure 111. E_a versus α plots for isothermal sulfameter-oxane solvate desolvation evaluated by the AIC method.

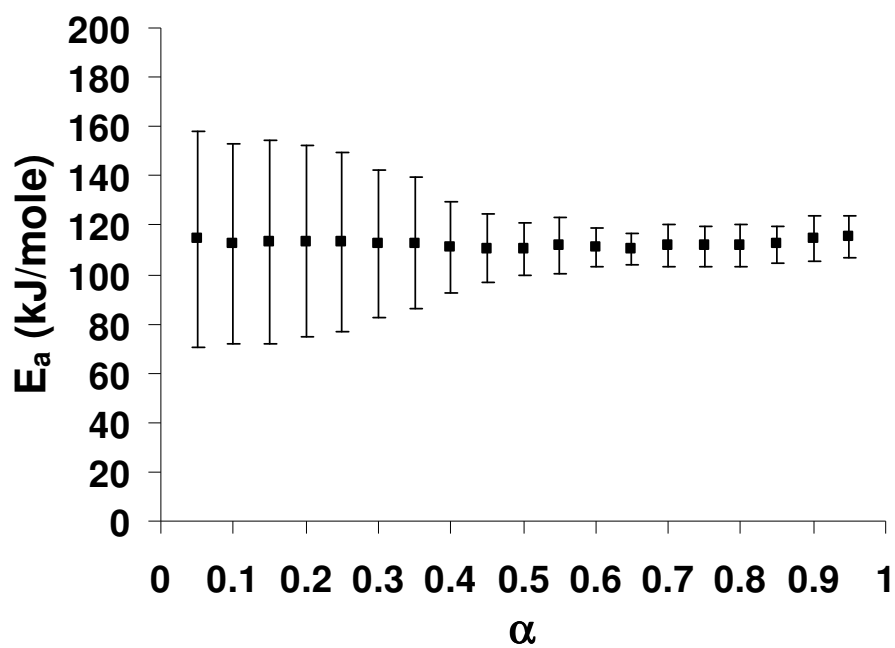


Figure 112. E_a versus α plots for isothermal sulfameter-dioxane solvate desolvation evaluated by the AIC method using two data sets.

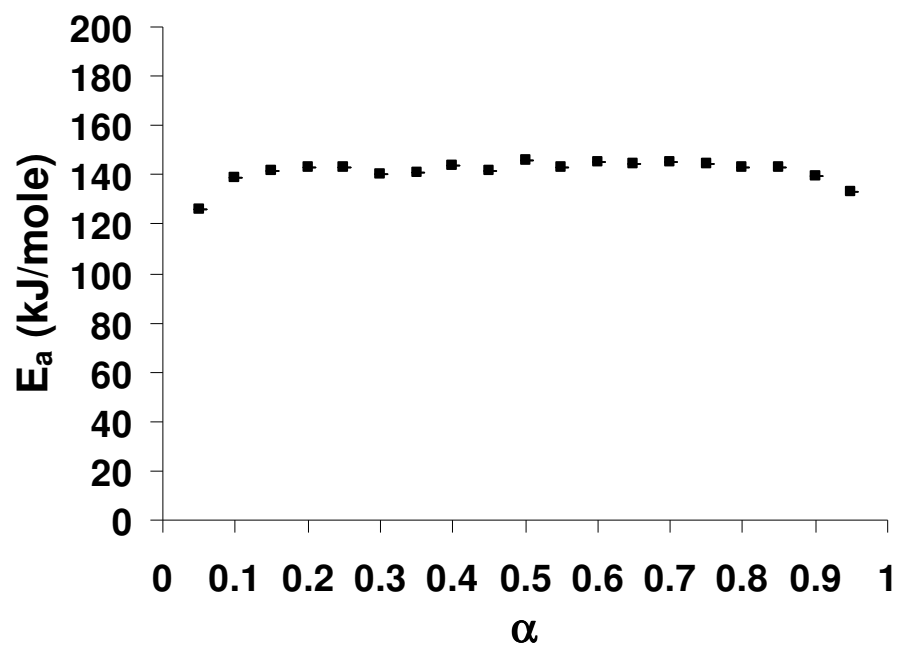


Figure 113. E_a versus α plots for isothermal sulfameter-oxepane solvate desolvation evaluated by the AIC method.

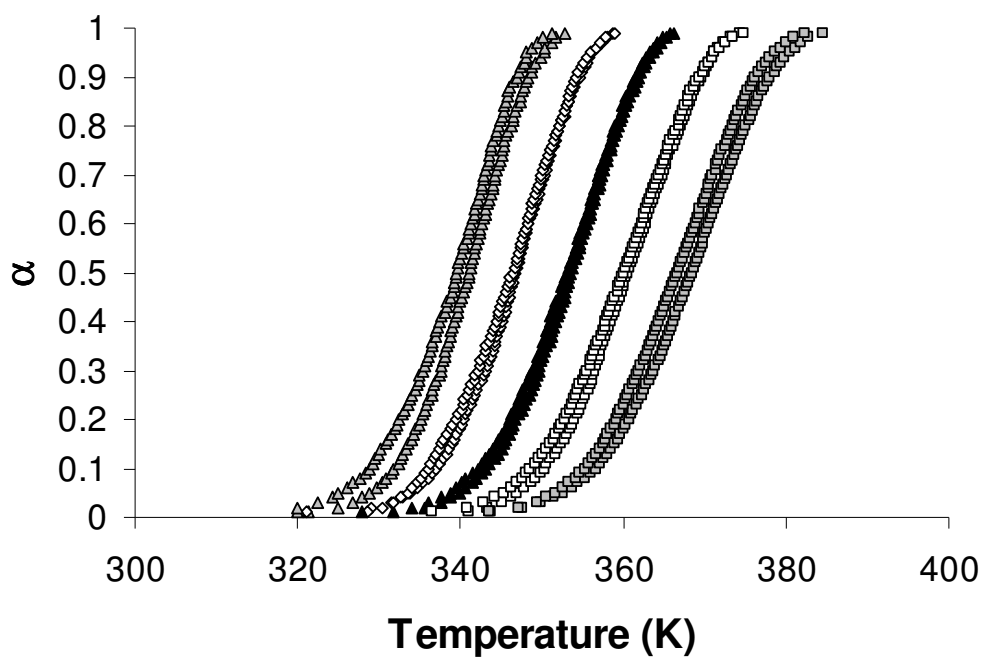


Figure 114. α versus temperature plots for the nonisothermal desolvation of sulfameteroxane solvate at: \blacktriangle , 1; \diamond , 2; \blacktriangle , 4; \square , 8 and \blacksquare , 16 K/min.

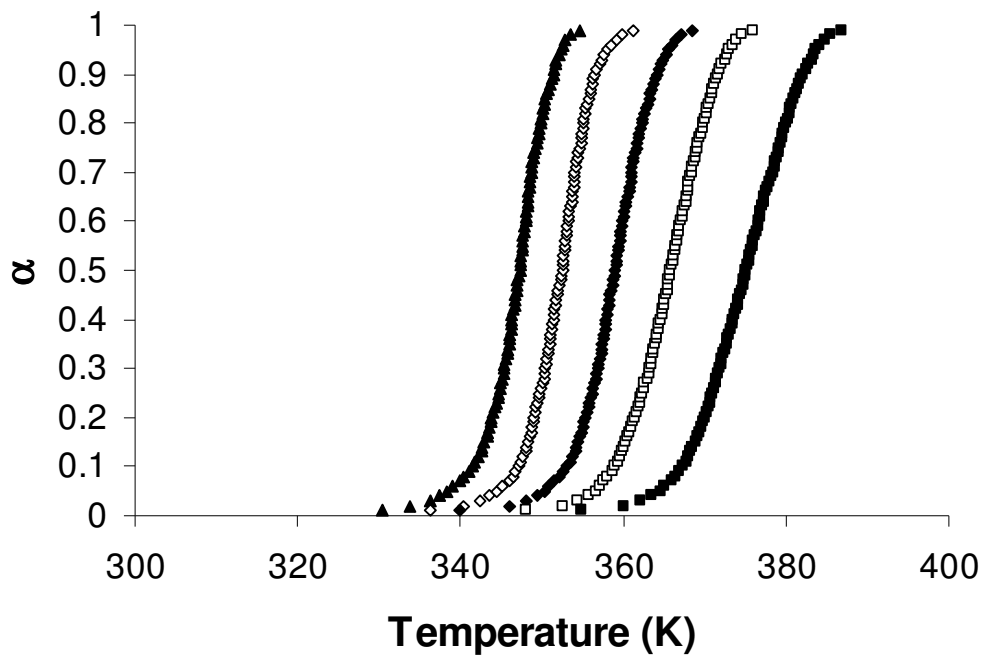


Figure 115. α versus temperature plots for the nonisothermal desolvation of sulfameter-oxepane solvate at: ▲, 1; ◇, 2; ◆, 4; □, 8 and ■, 16 K/min.

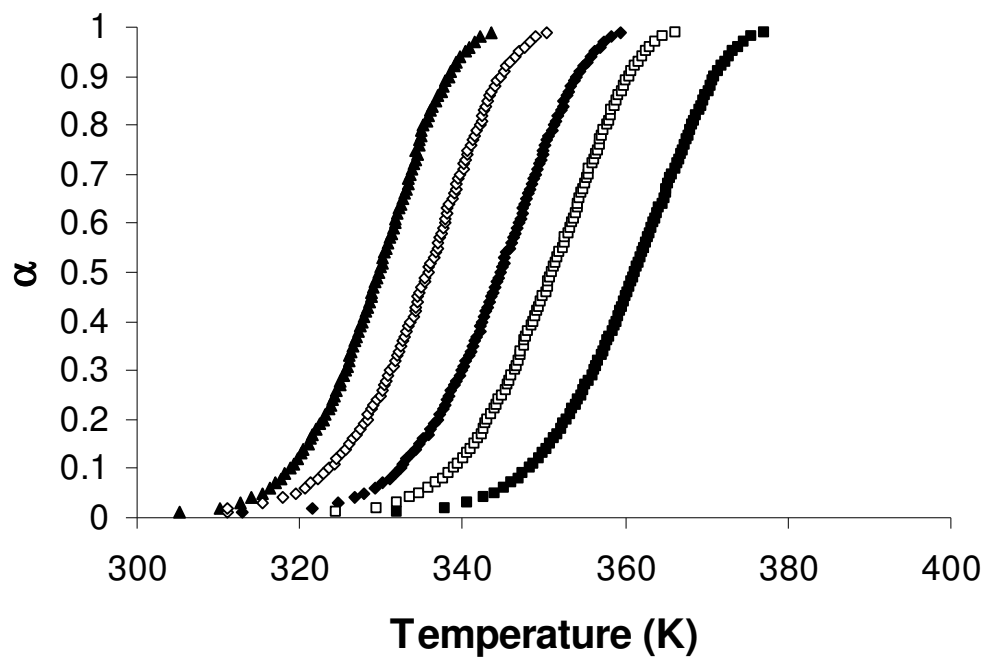


Figure 116. α versus temperature plots for the nonisothermal desolvation of sulfamer-chloroform solvate at: \blacktriangle , 1; \diamond , 2; \blacklozenge , 4; \square , 8 and \blacksquare , 16 K/min.

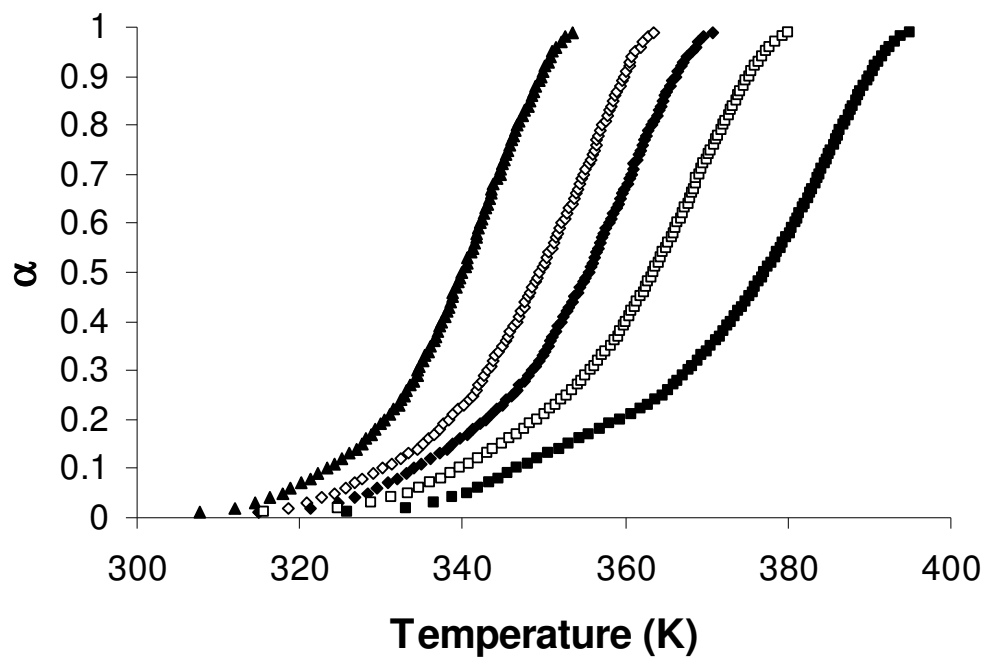


Figure 117. α versus temperature plots for the nonisothermal desolvation of sulfamer-bromoform solvate at: \blacktriangle , 1; \diamond , 2; \blacklozenge , 4; \square , 8 and \blacksquare , 16 K/min.

Table 46. Average fitted kinetic parameters for the nonisothermal desolvation of sulfameter-oxane solvate using the Coats-Redfern method.*

Model	A (min ⁻¹)	E _a (kJ/mole)	r
A2**	1.35×10^{11}	79.10	-0.9953
A3	6.38×10^{06}	50.78	-0.9949
A4	4.07×10^{04}	36.63	-0.9945
D1	4.25×10^{35}	246.22	-0.9640
D2	6.71×10^{38}	268.90	-0.9761
D3	7.71×10^{42}	299.57	-0.9886
D4	5.08×10^{39}	278.86	-0.9809
F1	7.73×10^{23}	164.03	-0.9957
F2	1.93×10^{34}	231.63	-0.9857
F3	1.92×10^{47}	316.54	-0.9527
P2	4.64×10^{07}	57.17	-0.9584
P3	2.86×10^{04}	36.17	-0.9539
P4	6.66×10^{02}	25.67	-0.9487
R1	1.22×10^{17}	120.19	-0.9623
R2	5.74×10^{19}	139.30	-0.9826
R3	5.70×10^{20}	146.87	-0.9881

* Results averaged from ten curves using the geometric mean of A and arithmetic mean of E_a and r.

** Model selected by the complementary approach.

Table 47. Average fitted kinetic parameters for the nonisothermal desolvation of sulfameter-oxepane solvate using the Coats-Redfern method.*

Model	A (min ⁻¹)	E _a (kJ/mole)	r
A2	4.11 × 10 ¹⁸	130.60	-0.9927
A3**	7.10 × 10 ¹¹	85.09	-0.9923
A4	2.72 × 10 ⁰⁸	62.33	-0.9920
D1	9.53 × 10 ⁵⁷	402.58	-0.9695
D2	9.44 × 10 ⁶²	438.02	-0.9785
D3	3.18 × 10 ⁶⁹	486.18	-0.9881
D4	4.50 × 10 ⁶⁴	453.65	-0.9823
F1	4.76 × 10 ³⁸	267.16	-0.9930
F2	4.30 × 10 ⁵⁴	374.13	-0.9791
F3	4.23 × 10 ⁷⁴	508.59	-0.9443
P2	2.45 × 10 ¹³	96.18	-0.9665
P3	2.12 × 10 ⁰⁸	62.14	-0.9644
P4	5.78 × 10 ⁰⁵	45.12	-0.9620
R1	2.25 × 10 ²⁸	198.32	-0.9685
R2	3.53 × 10 ³²	228.24	-0.9838
R3	1.42 × 10 ³⁴	240.12	-0.9878

* Results averaged from five curves using the geometric mean of A and arithmetic mean of E_a and r.

** Model selected by the complementary approach.

Table 48. Average fitted kinetic parameters for the nonisothermal desolvation of sulfameter-chloroform solvate using the Coats-Redfern method.*

Model	A (min ⁻¹)	E _a (kJ/mole)	r
A2**	1.62×10^{09}	64.76	-0.9981
A3	3.23×10^{05}	41.29	-0.9979
A4	4.25×10^{03}	29.55	-0.9977
D1	1.78×10^{30}	204.79	-0.9733
D2	7.91×10^{32}	223.26	-0.9834
D3	1.60×10^{36}	248.18	-0.9934
D4	3.41×10^{33}	231.35	-0.9874
F1	1.25×10^{20}	135.19	-0.9983
F2	6.61×10^{28}	190.00	-0.9816
F3	5.06×10^{39}	258.78	-0.9442
P2	1.94×10^{06}	46.95	-0.9682
P3	3.35×10^{03}	29.41	-0.9639
P4	1.32×10^{02}	20.64	-0.9589
R1	2.35×10^{14}	99.56	-0.9717
R2	3.79×10^{16}	115.11	-0.9888
R3	2.45×10^{17}	121.26	-0.9931

* Results averaged from five curves using the geometric mean of A and arithmetic mean of E_a and r.

** Model selected by the complementary approach.

Table 49. Average fitted kinetic parameters for the nonisothermal desolvation of sulfameter-bromoform solvate using the Coats-Redfern method.*

Model	A (min ⁻¹)	E _a (kJ/mole)	r
A2	4.62 × 10 ⁰⁵	43.71	-0.9934
A3	1.26 × 10 ⁰³	27.21	-0.9925
A4	6.30 × 10 ⁰¹	18.97	-0.9913
D1	2.74 × 10 ²⁰	145.13	-0.9904
D2	1.30 × 10 ²²	157.54	-0.9954
D3	1.15 × 10 ²⁴	173.97	-0.9976
D4	2.03 × 10 ²²	162.89	-0.9967
F1	1.48 × 10 ¹³	93.21	-0.9942
F2	6.15 × 10 ¹⁸	128.58	-0.9525
F3	5.57 × 10 ²⁵	172.71	-0.8996
P2	5.25 × 10 ⁰³	31.94	-0.9872
P3	6.06 × 10 ⁰¹	19.37	-0.9842
P4	6.76	13.08	-0.9801
R1	2.43 × 10 ⁰⁹	69.67	-0.9895
R2	5.74 × 10 ¹⁰	80.04	-0.9970
R3**	1.71 × 10 ¹¹	84.09	-0.9974

* Results averaged from five curves using the geometric mean of A and arithmetic mean of E_a and r.

** Model selected by the complementary approach.

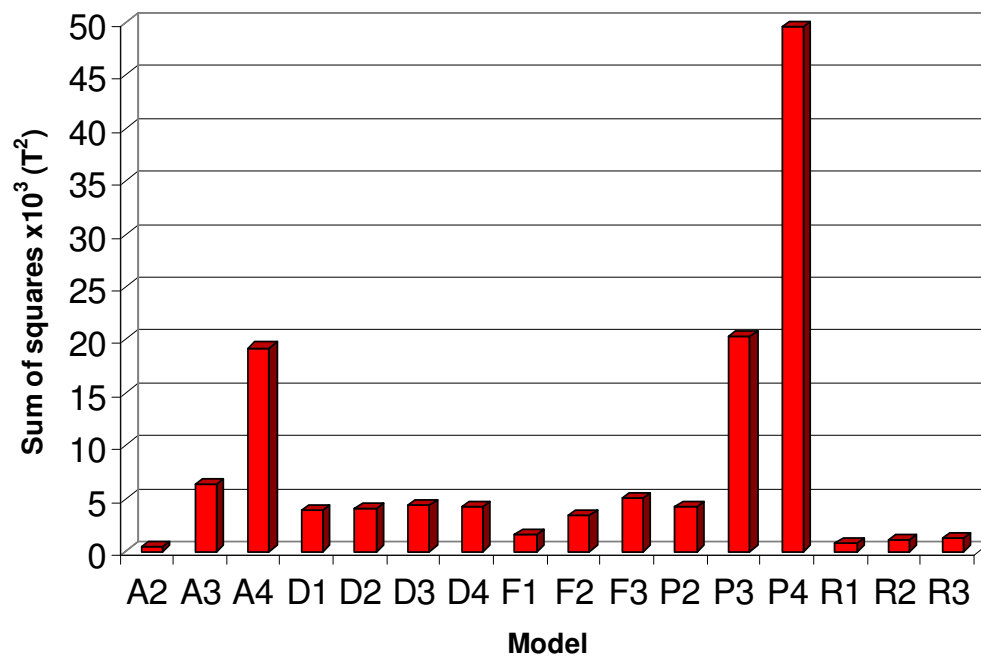


Figure 118. Sum of squared differences between actual and reconstructed nonisothermal desolvation curves ($(T_{\text{actual}} - T_{\text{reconstructed}})^2$) for the sulfameter oxane solvate.

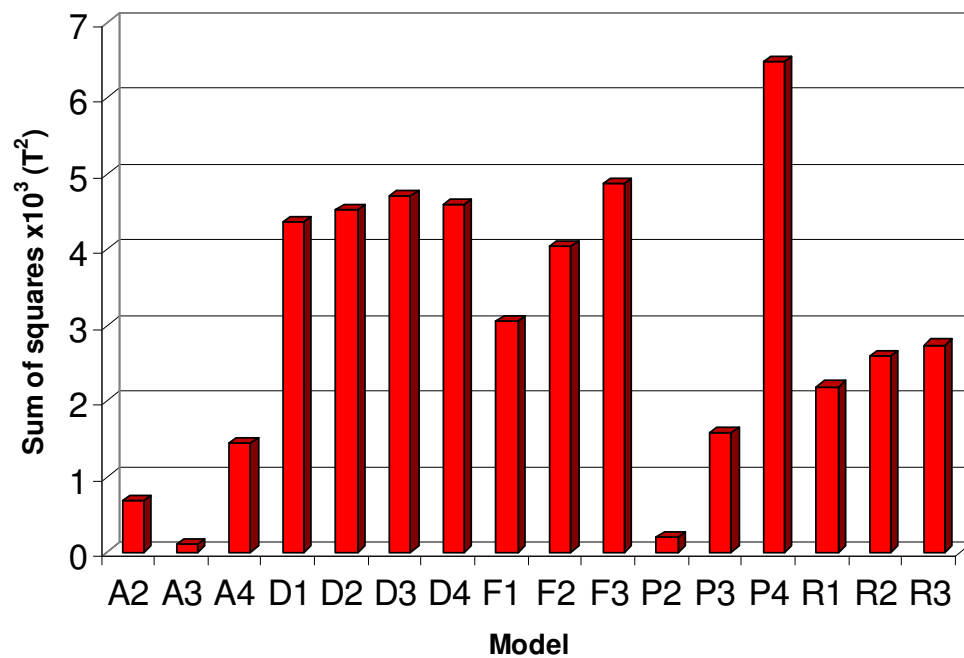


Figure 119. Sum of squared differences between actual and reconstructed nonisothermal desolvation curves ($(T_{\text{actual}} - T_{\text{reconstructed}})^2$) for the sulfameter oxepane solvate.

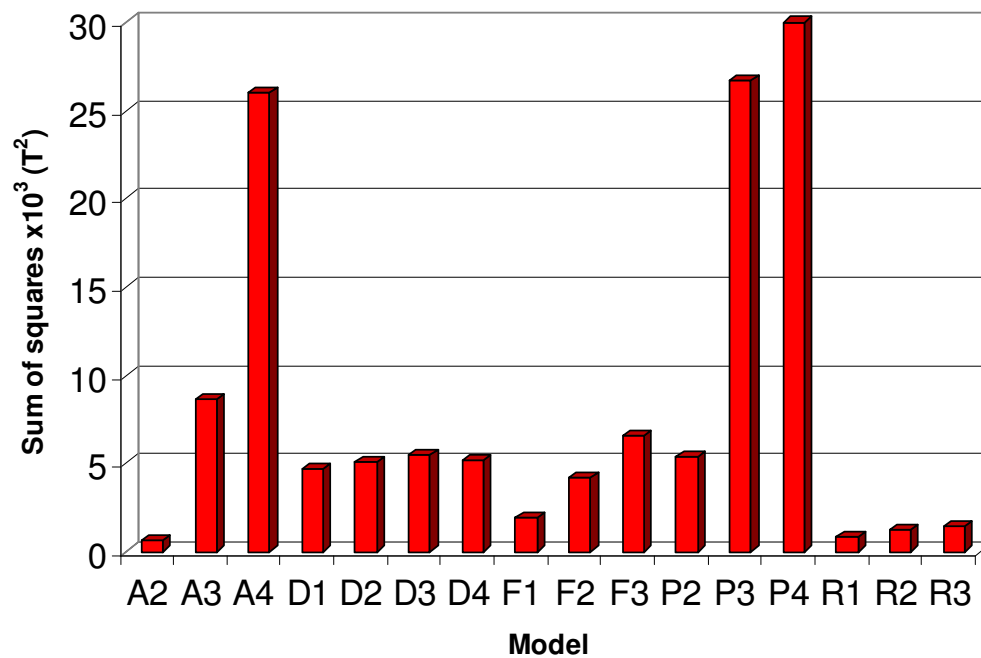


Figure 120. Sum of squared differences between actual and reconstructed nonisothermal desolvation curves ($(T_{\text{actual}} - T_{\text{reconstructed}})^2$) for the sulfameter chloroform solvate.

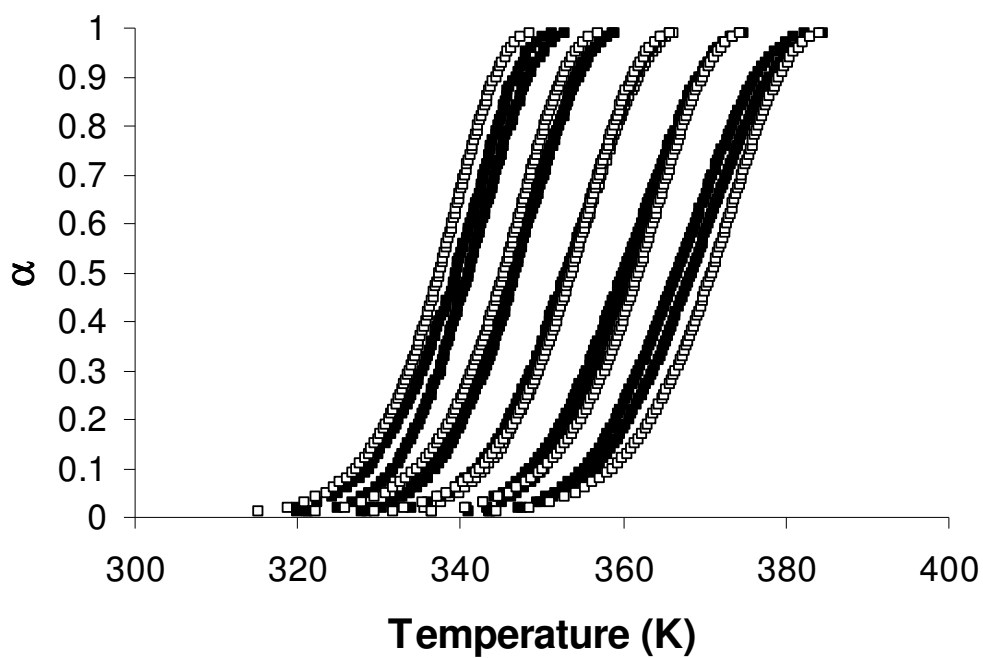


Figure 121. Reconstructed α -T plots for nonisothermal desolvation of sulfameter-oxane solvate for five heating rates (1, 2, 4, 8 and 16 K/min): ■, experimental curves and □, reconstructed curves (A2).

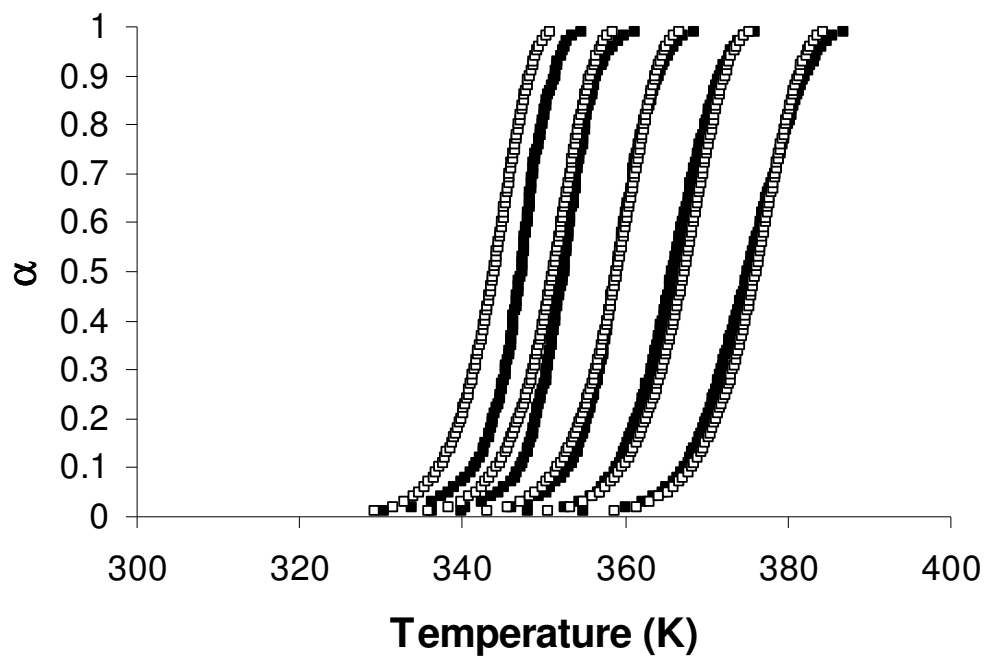


Figure 122. Reconstructed α -T plots for nonisothermal desolvation of sulfameter-oxepane solvate for five heating rates (1, 2, 4, 8 and 16 K/min): ■, experimental curves and □, reconstructed curves (A3).

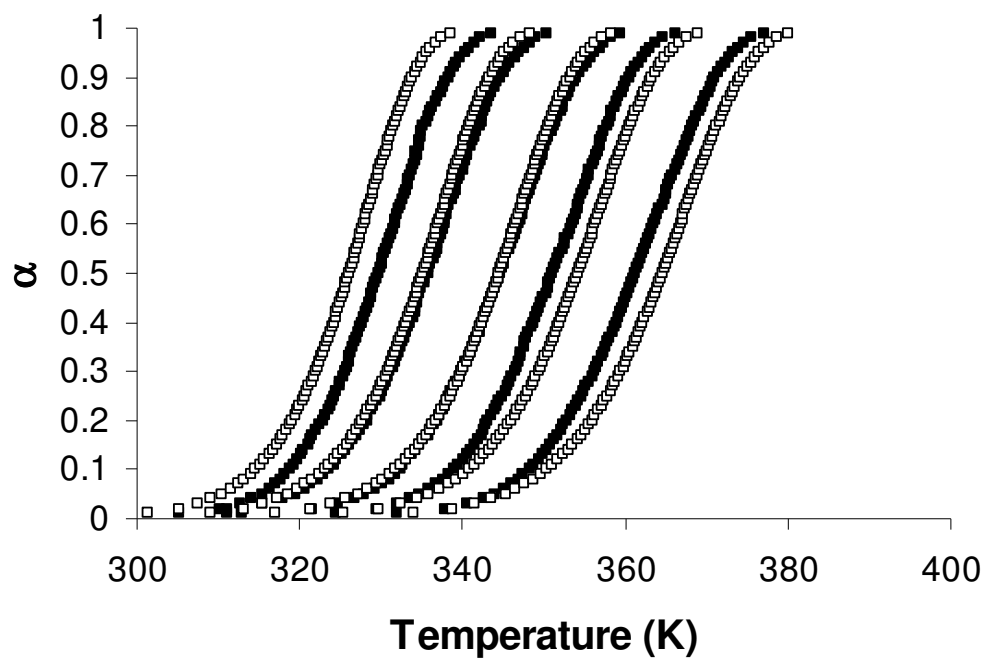


Figure 123. Reconstructed α -T plots for nonisothermal desolvation of sulfamer-chloroform solvate for five heating rates (1, 2, 4, 8 and 16 K/min): ■, experimental curves and □, reconstructed curves (A2).

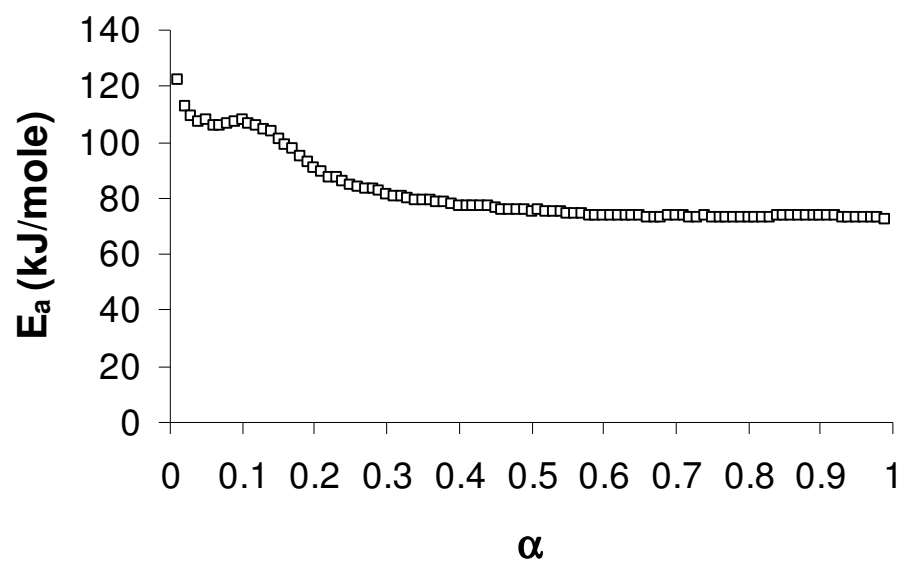


Figure 124. E_a - α plot for nonisothermal sulfameter-bromoform solvate desolvation evaluated by the Vyazovkin (VYZ) isoconversional method.

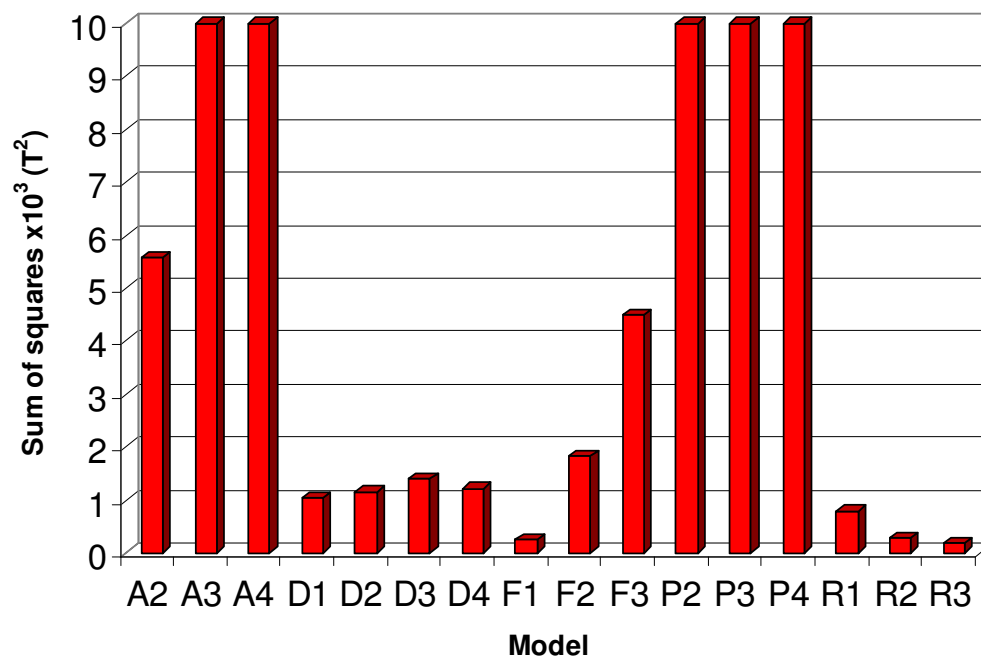


Figure 125. Sum of squared differences between actual and reconstructed nonisothermal desolvation curves ($(T_{\text{actual}} - T_{\text{reconstructed}})^2$) for the sulfameter bromoform solvate.

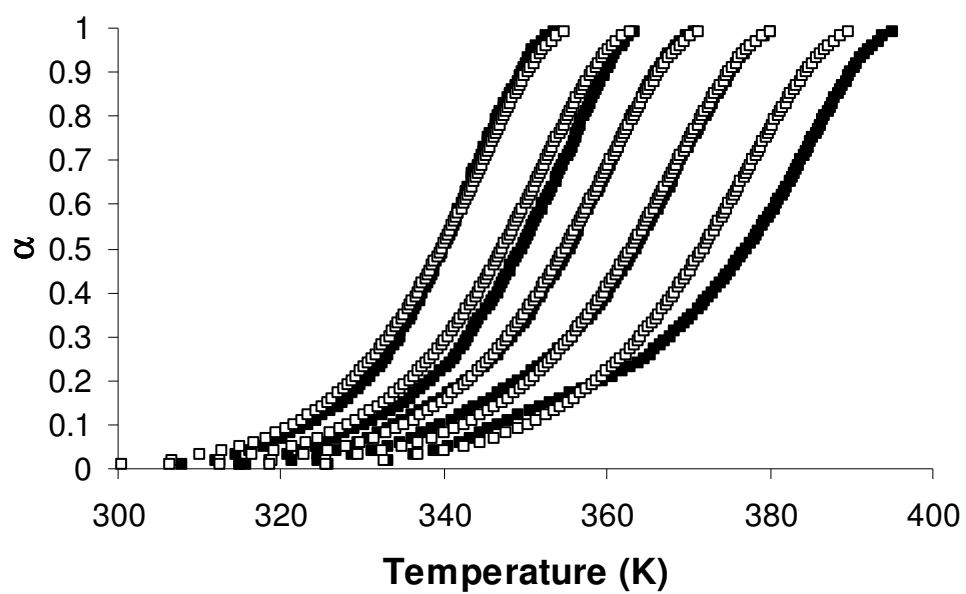


Figure 126. Reconstructed α -T plots for nonisothermal desolvation of sulfameter-bromoform solvate for five heating rates (1, 2, 4, 8 and 16 K/min): \blacksquare , experimental curves and \square , reconstructed curves (R3).

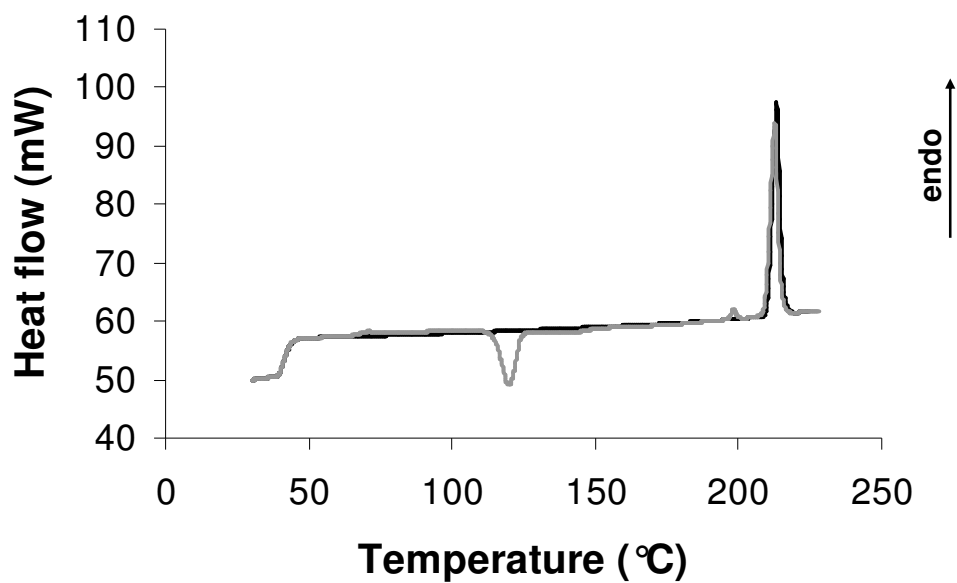


Figure 127. DSC analysis of sulfameter at a heating rate of 16 K/min: (—); first heating cycle, (---) and second heating cycle (after cooling sample at room temperature).

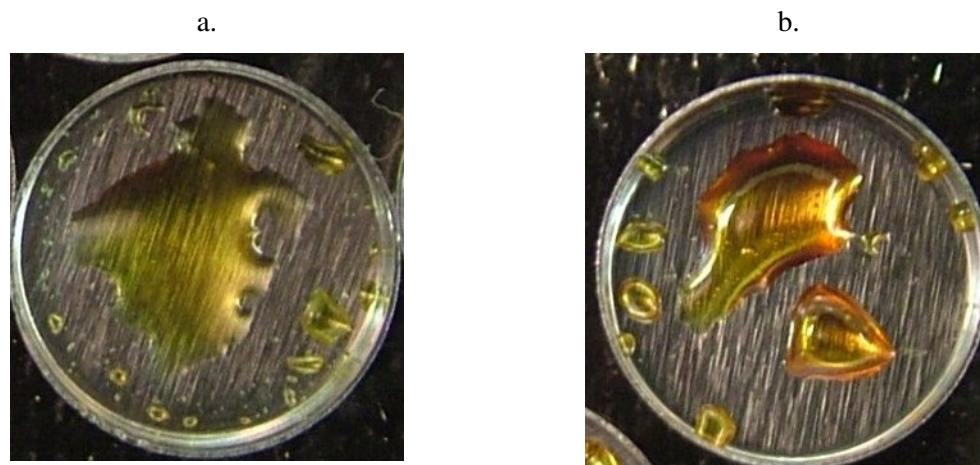


Figure 128. Amorphous forms of sulfameter prepared by melting any crystalline form and slowly cooling: a, amorphous form produced from original bulk drug; dioxolane; oxane and dioxane solvates; b, amorphous form produced from tetrahydrofuran; oxepane; chloroform and bromoform solvates.

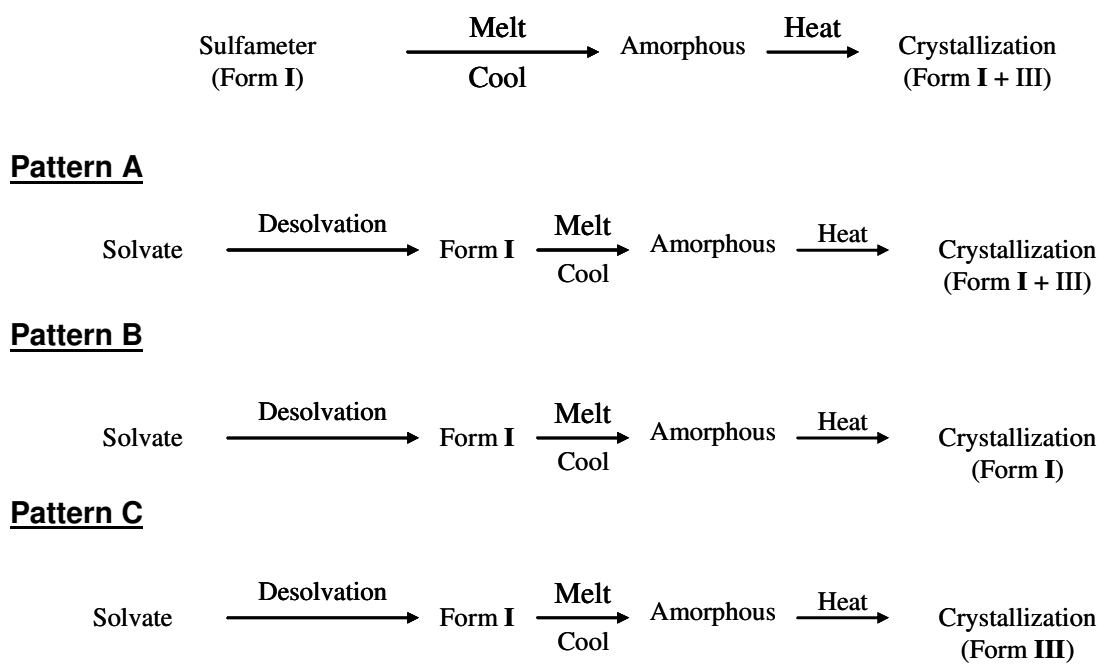


Figure 129. Polymorphic transformations of sulfameter and its solvates upon heating; bolded forms are the major component.

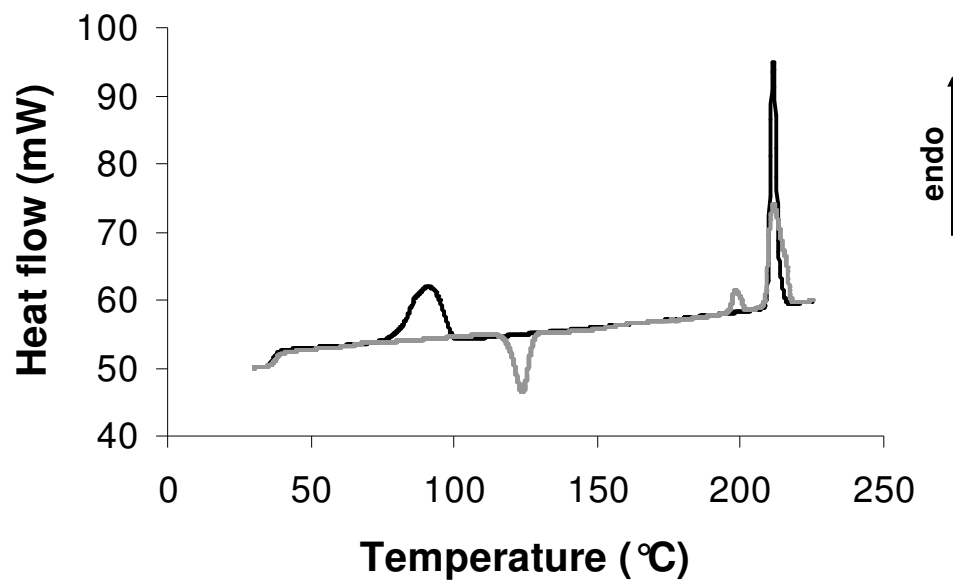


Figure 130. DSC analysis of sulfameter-dioxolane solvate at a heating rate of 16 K/min: (—) first heating cycle and (---) second heating cycle (after cooling sample to room temperature).

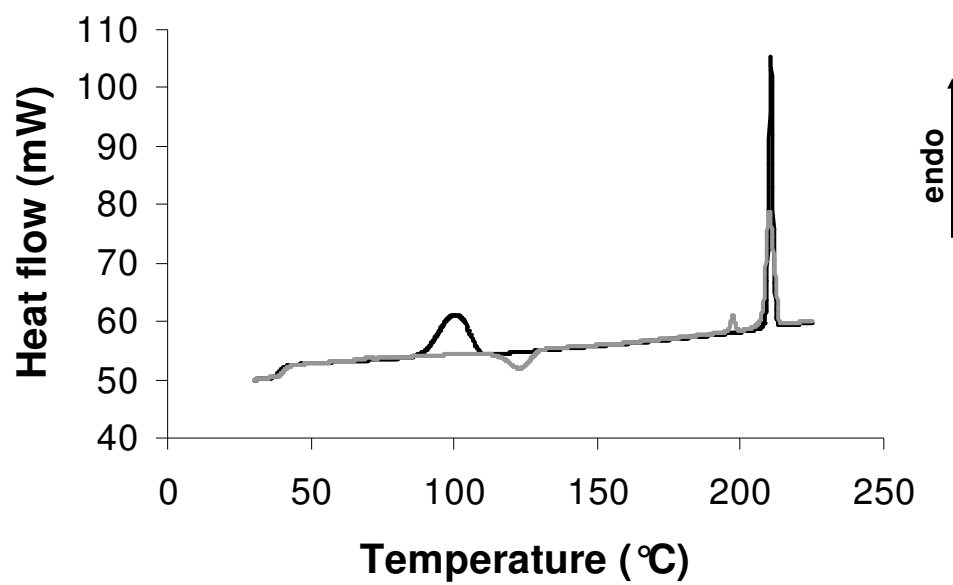


Figure 131. DSC analysis of sulfameter-dioxane solvate at a heating rate of 16 K/min: (—) first heating cycle and (---) second heating cycle (after cooling sample to room temperature).

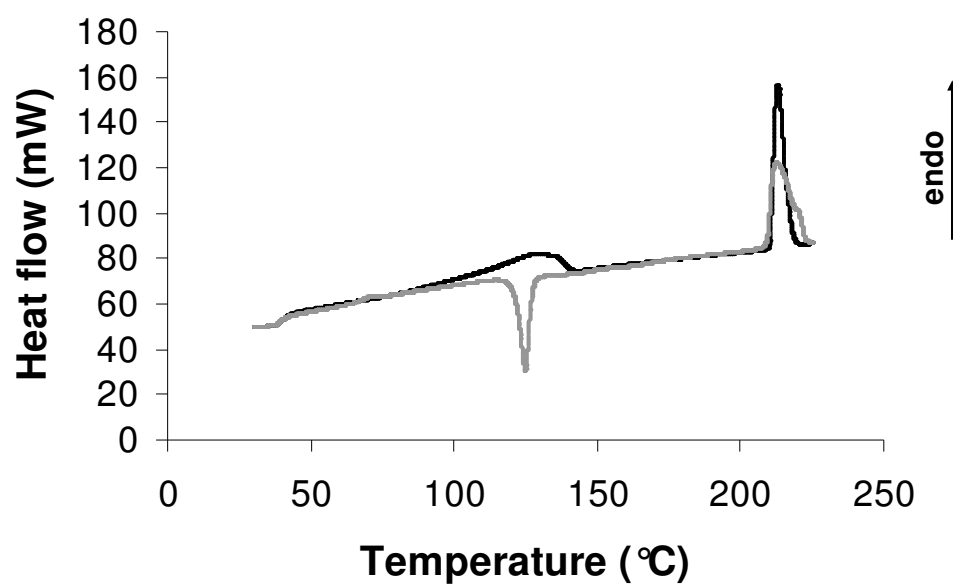


Figure 132. DSC analysis of sulfamer-oxane solvate at a heating rate of 16 K/min: (—) first heating cycle and (---) second heating cycle (after cooling sample to room temperature).

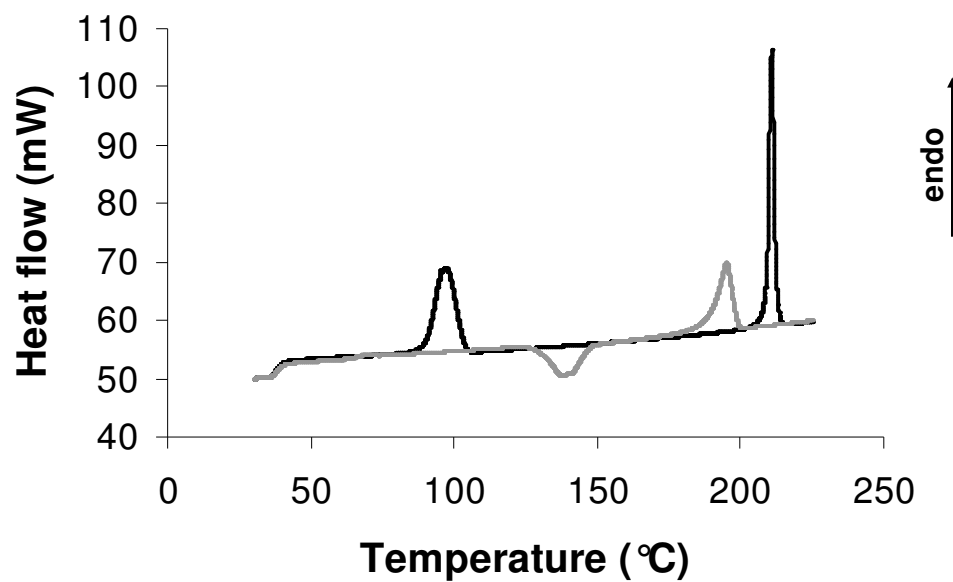


Figure 133. DSC analysis of sulfameter–tetrahydrofuran solvate at a heating rate of 16 K/min: (—) first heating cycle and (---) second heating cycle (after cooling sample to room temperature).

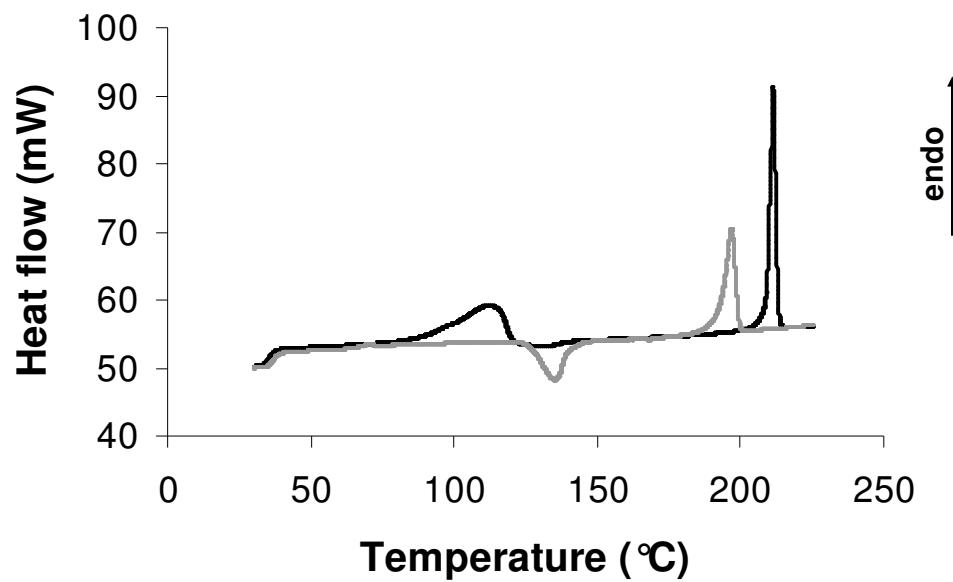


Figure 134. DSC analysis of sulfameter – oxepane solvate at a heating rate of 16 K/min: (—) first heating cycle and (---) second heating cycle (after cooling sample to room temperature).

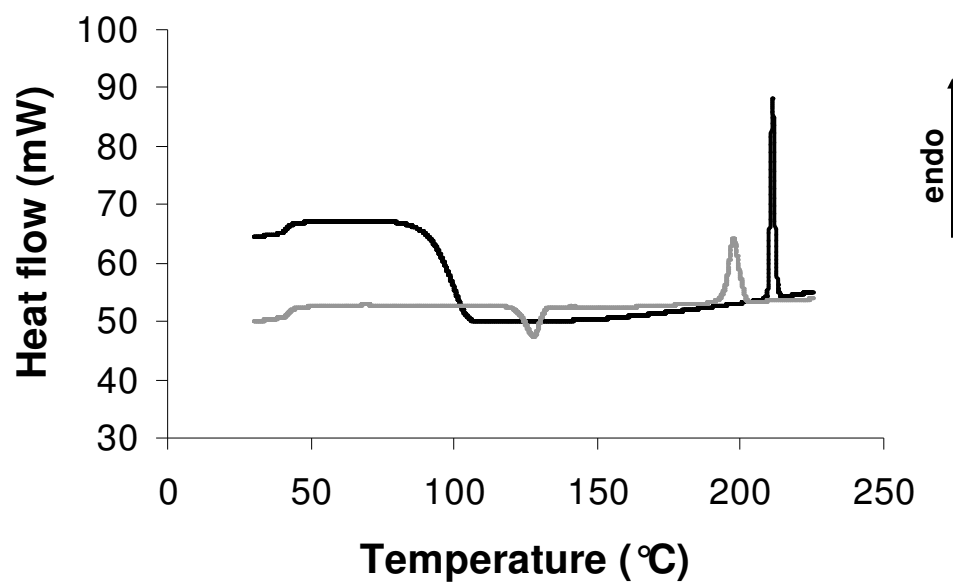


Figure 135. DSC analysis of sulfameter–chloroform solvate at a heating rate of 16 K/min: (—) first heating cycle and (---) second heating cycle (after cooling sample to room temperature).

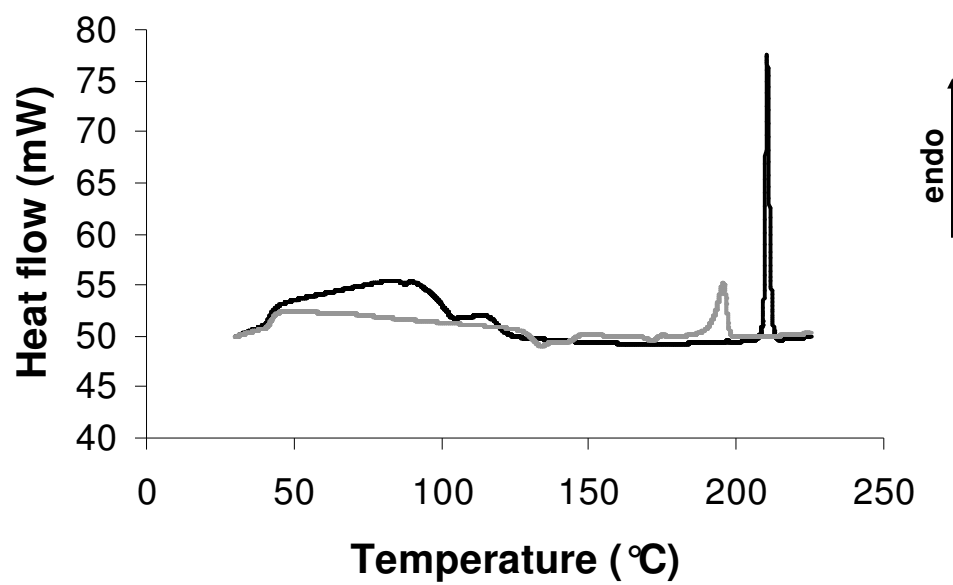


Figure 136. DSC analysis of sulfameter-bromoform solvate at a heating rate of 16 K/min: (—) first heating cycle and (---) second heating cycle (after cooling sample to room temperature).

CHAPTER 8

SUMMARY AND CONCLUSIONS

Isothermal and nonisothermal experiments

I have covered desolvation of different sulfamer solvates both isothermally and nonisothermally. Isothermally, five sulfamer solvates were kinetically analyzed (tetrahydrofuran, dioxolane, oxane, dioxane and oxepane; Chapter 7). Nonisothermally, seven sulfamer solvates were analyzed: (tetrahydrofuran, dioxolane, dioxane (Chapter 5) and oxane, oxepane, chloroform, bromoform (Chapter 7). Desolvation results are summarized in Tables 50 (isothermal) and 51 (nonisothermal). Results show that desolvation kinetic parameters were different for isothermal and nonisothermal experiments. The reaction models were also different for the tetrahydrofuran, oxane, dioxane and oxepane solvates while the same reaction model (A2 model) was selected for the dioxolane solvate isothermally and nonisothermally. Isothermal desolvation curves were reconstructed for each solvate from the kinetic parameters obtained nonisothermally (Table 51) and were compared to experimental desolvation curves obtained isothermally (Figure 137). Figure 137 shows that none of the isothermal desolvation curves (except for the dioxolane solvate) was correctly predicted from nonisothermal parameters; the shape of dioxolane desolvation curves were fairly predicted, however their position was not because the activation energy obtained nonisothermally (Table 51) is higher than that calculated isothermally (Table 50) for the dioxolane solvate.

The order of activation energies was also different from both isothermal and nonisothermal experiments. Isothermally, the order of activation energies was: oxepane > oxane > dioxane > tetrahydrofuran > dioxolane and all followed the A2 model except oxane (R3 model). Nonisothermally, the order was: tetrahydrofuran > dioxolane > oxepane > oxane > dioxane and all followed the A3 model except for dioxolane and

oxane solvates (A2 model). The results show that neither isothermal nor nonisothermal kinetics can be predicted from one another which raises the question – which method should be used to analyze solid-state kinetics?

This question and many others have been raised about analysis and calculation methods used in solid-state kinetics [1]. The use of nonisothermal experiments has been criticized in favor of isothermal experiments for two reasons – firstly, temperature is an experimental variable in nonisothermal analyses while it is fixed in isothermal analyses, which reduces the total number of variables; secondly, nonisothermal experiments involve a temperature integral that has no analytical solution, therefore approximations of this integral are necessary. On the other hand, nonisothermal studies are considered more convenient than isothermal studies because a sample is not subjected to a rapid temperature rise to a fixed reaction temperature (i.e., heat-up time) [53] in which reaction could occur but is not measured which introduces errors in the analysis. This is especially true if the isothermal temperature is high because decomposition likely occurs before the fixed temperature study is initiated.

Another complicating factor is the wide belief that kinetic parameters obtained by both isothermal and nonisothermal experiments should be the same. It was noted [37, 40, 53] that the disagreement in results from isothermal and nonisothermal experiments should be expected because each covers a different temperature range (Table 52) which could affect the complex nature of some solid-state reactions. Our results have demonstrated the differences for the desolvation of different sulfameter solvates. However, the disagreement can not be totally attributed to temperature range difference between isothermal and nonisothermal experiments because if the temperature range was the only variable, it would be expected that nonisothermal runs having low heating rates (i.e. 1 K/min) would be kinetically described by the same isothermal parameters since the temperature range covered in these runs is comparable to those done isothermally.

Variation of results between isothermal and nonisothermal kinetics could be due to the variation of heat dissipation within the crystal in both modes. For example, tetrahydrofuran, dioxane and oxepane show an A2 reaction model for isothermal desolvation while these same solvates show an A3 model nonisothermally. Both models (A2 and A3) are nucleation and growth models that are similar in all aspects except the dimension of crystal growth (Chapter 2). A3 models indicate that crystals are growing in two dimensions while A2 are one-dimensional growing crystals. The rising (dynamic) heat input nonisothermally could generate a two-dimensional nuclei growth while the constant temperature in isothermal experiments could limit growth to one-dimension. The oxane solvate followed the R3 model, which assumes that nuclei growth follows a geometrical shape (contracting cube, Chapter 2); light microscopy of the oxane solvate (Figure 26d) agrees with this finding. Nonisothermal heating of the oxane solvate changes the desolvation kinetic behavior from the R3 to A2 model.

The choice of isothermal or nonisothermal experiments is governed by needs of the study, whether it is desired to study reaction kinetics over a wide temperature range (i.e. up to melting) or if a narrow range is sufficient. However, results show that we can not predict stability isothermally from experiments done nonisothermally or vice versa, unless we ascertain that the kinetics do not change.

Sulfameter system

The sulfameter solvate system has proven to be a good model for studying solid-state kinetics because sulfameter forms many solvates, several of which are structurally related and easy to prepare. One of the most important properties of the sulfameter solvate system is that desolvation is a simple process that can be described by a single kinetic triplet. This was evident from the reconstruction results of desolvation curves where they were described by a single value of the activation energy and preexponential factor for a specific model. Simplicity of the desolvation reaction is also demonstrated by

nearly flat isoconversional plots for desolvation reactions. No other solid-state system has shown these kinetic properties. Calcium oxalate monohydrate is usually used as a reference material to study solid-state kinetic – either the dehydration reaction or the subsequent degradation to calcium oxide and carbon dioxide. There is some disagreement in the reported results [92] and these reactions (dehydration or degradation) can not be described by a flat isoconversional plot as seen in the sulfamer solvate system.

The relationship between kinetic parameters for the desolvation of sulfamer-like compounds (i.e., other sulfonamides) can not be established because results showed that although there were minimal differences in structure, the ability to form solvates changed dramatically. This behavior could be due to changes in drug solubility or change in preferred orientation of a host molecule needed to form a solvate. Therefore, each host structure should be considered separately.

On the other hand, changing guest molecules (i.e., different solvents) for sulfamer produced several structurally-similar solvates with different desolvation kinetic parameters (Tables 50 and 51). Isothermally, there seems to be a relation between solvent size and activation energy (Table 50). Five membered ring solvents (tetrahydrofuran and dioxolane) have a lower activation energy than six membered ring solvents (dioxane and oxane), which was also lower than the seven membered ring solvent (oxepane). This could be due to the bulkiness of the solvent molecule – the more bulky the solvent, the higher the energy barrier for it to desolvate. This is also seen within the same ring sizes. For example, tetrahydrofuran and dioxolane are both five membered rings, however, because dioxolane has a $-\text{CH}_2$ group replaced with oxygen, it is a little less bulky than tetrahydrofuran (i.e., CH_2 is bigger than O) correlating with a lower desolvation activation energy for the dioxolane solvate. This also accounts for why dioxane has a lower E_a than oxane. The relation between the solvent molar volume and desolvation activation energy is shown in Figure 138a which agrees with our conclusion.

Results can be further explained by examining the single crystal structure of sulfameter solvates. The single crystal X-ray structure of three sulfameter solvates (tetrahydrofuran, dioxane and chloroform) was previously reported by Caira and Mohamed [157]. They found a common isostructural host framework where sulfameter forms centrosymmetric dimers via pairs of N–H···N hydrogen bonds giving rise to a cage-like structure in which guest molecules (i.e., solvents) are entrapped. Solvent can escape from the cavities which are 2Å in width at the narrowest point. They concluded that, “the entrapment of relatively bulky solvent molecules in such cavities provide an explanation for the high threshold temperature for desolvation” [157]. These cavities may account for the observed pattern of desolvation E_a increasing with solvent size. Caira and Mohamed [157] further investigated the cavity topology and concluded that there are no guest molecules escaping along the x- or y- directions in the crystal and that the cavities only occur in the z-direction. This finding supports the one dimensional isothermal desolvation mechanism suggested by the A2 model.

Nonisothermally, a relation between solvent size and desolvation energy is not apparent (Figure 138b). This may be due to the difference between isothermal and nonisothermal kinetic behavior discussed above.

A type-1 kinetic compensation effect exists for the different sulfameter solvates both isothermally and nonisothermally (Figure 139). This could indicate a systematic relationship between different sulfameter solvates which was established for isothermal kinetics but it is less evident nonisothermally.

There still exists many aspects of the sulfameter solvate system that can be explored kinetically. Although kinetic results obtained isothermally and nonisothermally are reliable, kinetic information is a piece of the larger picture. Single crystal X-ray studies are needed for each solvate to further explore other physical properties of the solvates and how these properties interact with desolvation kinetic results.

Hopefully, this work has helped narrow the gap between thermochemical kinetics and pharmaceutical science worlds. It has been demonstrated how collected kinetic data of different drug solvates can be transformed or analyzed to obtain modelistic or model-free results. Pharmaceutical investigators should have a better understanding of the models, mathematical tools and software they apply to solid-state kinetic reactions. In addition, principles from solid-state kinetics should be further investigated and applied to nonisothermal solution state kinetic studies, in hopes of improving drug stability testing protocols.

Solid-state kinetics future

Solid-state kinetics like any research field is affected by experimental variables and data reproducibility that could be enhanced by tighter control of experimental variables. Calculated results by any method should be verified by reconstruction of data to determine their correspondence to the original data.

Calculation methods used in the analysis of solid-state kinetics have raised many controversies because there are many methods and their range of application and validity is unclear. Results obtained by various calculation methods have often been different, even when applied to the same data set. Results from model-fitting methods, such as the Coats and Redfern method, have been in disagreement with those from model-free methods. Different calculation methods have been viewed as competing and conflicting, but, hopefully our complementary approach has helped bridge the gap between these two methods. Both modelistic and model-free methods can be used in a complementary fashion to reach reliable kinetic conclusions.

Confusion and conflict in results from different methods continues to appear in the literature and there seems to be no near end to this issue which is partly due to new analysis methods that continue to appear in the literature and add to the many analysis methods already present. Currently, many methods and temperature integral

approximations are being introduced that are claimed to be “more accurate” than those already in place. However, there is little benefit in introducing analysis methods that are claimed to be accurate up to the fourth significant figure while experimental error may be as high as 20% or higher. The current overwhelming number of analysis methods in the literature needs to be appraised and evaluated. A critical evaluation of these methods was initiated in the ICTAC “kinetic project” [39-43] (Chapter 1). This project was vital for evaluating and standardizing the field of solid-state kinetics. However, views of this project were somehow “biased” towards the use of isoconversional methods, which did not reduce the controversy present in this field. Isoconversional analysis methods are useful tools for the analysis of solid-state kinetics. Theoretically, they possess many advantages and applications. However, practically, they have some disadvantages, especially regarding reproducibility (Chapter 4). They, therefore, can not be used solely for kinetic analysis but can be used in conjunction with modelistic methods and should not “replace” them as the kinetic project suggested. Claims that these methods can be universally used to predict isothermal and nonisothermal experiments for any experimental conditions [164] are practically impossible. I believe that the overwhelming focus on isoconversional methods is a step in the wrong direction. Sole use of isoconversional methods will continue to generate more literature in which the results have no useful application. Such papers will report numbers obtained by isoconversional methods and will have no mechanistic interpretation of the results except that “solid-state kinetics is complex.”

Finally, researchers are challenged to develop more models and more work needs to be done to standardize the field of solid-state kinetics experimentally, computationally and conceptually. I hope my contribution has helped move us in that direction.

Table 50. Kinetic results for the isothermal desolvation reaction of several sulfameter solvates evaluated by the conventional model-fitting approach.^a

Solvate	Model	A (min ⁻¹)	E _a (kJ/mole)
Tetrahydrofuran	A2	3.07×10^{14}	100.23
Dioxolane	A2	3.09×10^{11}	78.14
Oxane	R3	3.29×10^{16}	117.41
Dioxane ^b	A2	9.59×10^{15}	112.53
Oxepane	A2	2.81×10^{20}	139.79

^a Results extracted from Tables 41–45.

^b Results averaged by taking the geometric mean of A and arithmetic mean of E_a and r.

Table 51. Averaged kinetic results for the nonisothermal desolvation reaction of several sulfameter solvates evaluated by the complementary approach.^a

Solvate	Model	A (min ⁻¹)	E _a (kJ/mole)
Tetrahydrofuran ^b	A3	5.99×10^{14}	102.48
Dioxolane ^b	A2	9.72×10^{12}	87.67
Oxane ^c	A2	1.35×10^{11}	79.10
Dioxane ^b	A3	2.72×10^{10}	75.98
Oxepane ^d	A3	7.10×10^{11}	85.09
Chloroform ^d	A2	1.62×10^{09}	64.76
Bromoform ^d	R3	1.71×10^{11}	84.09

^a Results averaged from several curves using the geometric mean of A and arithmetic mean of E_a.

^b Results averaged from seven curves.

^c Results averaged from ten curves.

^d Results averaged from five curves.

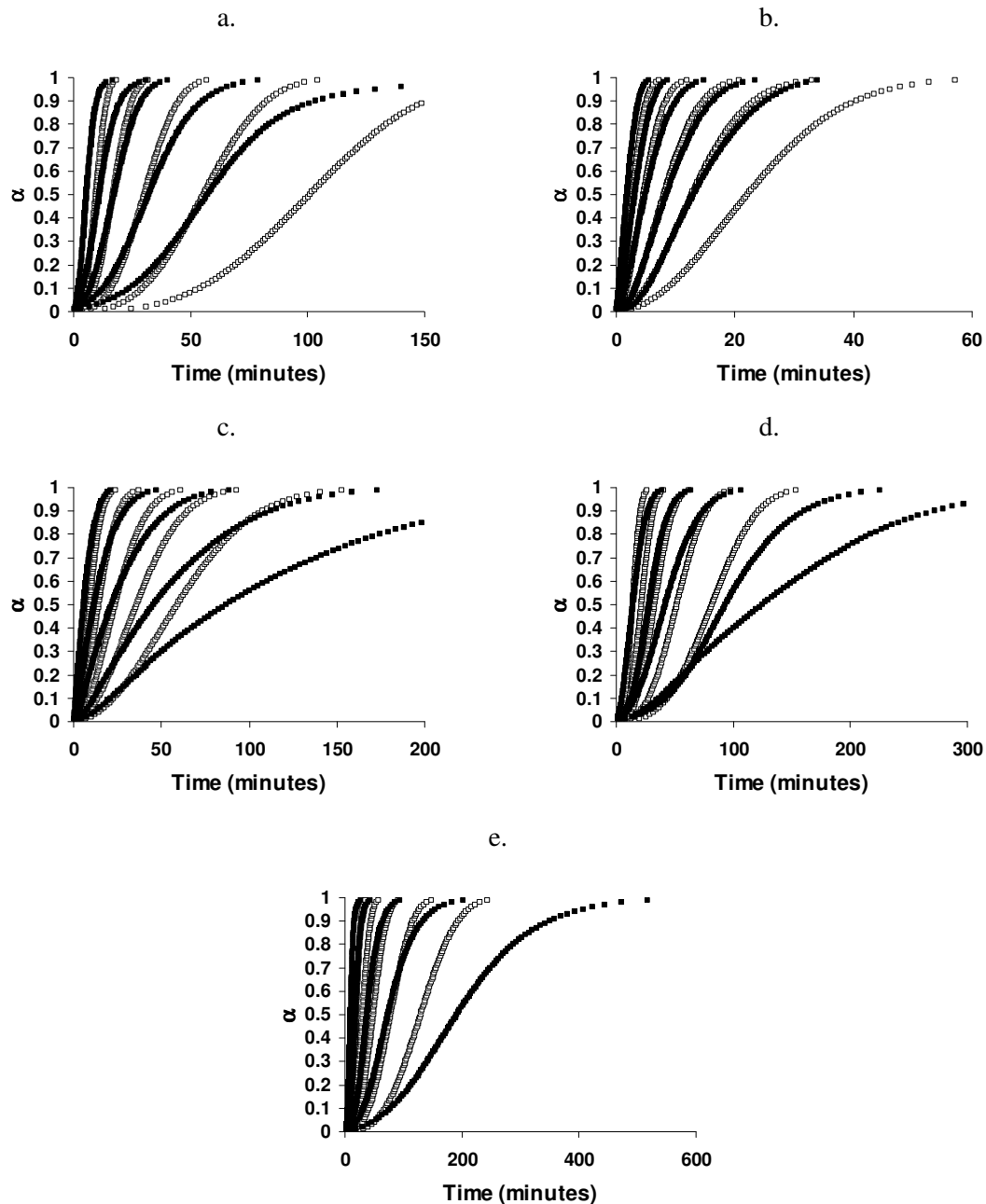


Figure 137. Reconstructed α -time plots for isothermal desolvation of sulfameter solvates (■, experimental and □, reconstructed) at five temperatures (323, 328, 333, 338 and 343 K): a, tetrahydrofuran; b, dioxolane; c, oxane; d, dioxane and e, oxepane. Plots reconstructed from parameters calculated nonisothermally (Table 51).

Table 52. Temperature ranges covered in isothermal and nonisothermal desolvation experiments for several sulfameter solvates.

Solvate	Isothermal		Nonisothermal	
	Range (K)	Difference (K)	Range (K)	Difference (K)
Tetrahydrofuran	320.34 – 341.19	20.85	327.75 – 369.48	41.73
Dioxolane	320.48 – 341.33	20.85	310.13 – 373.75	63.62
Oxane	320.21 – 341.64	21.43	321.21 – 384.50	63.29
Dioxane	320.33 – 341.38	21.05	332.51 – 380.45	47.95
Oxepane	320.43 – 341.01	20.58	330.34 – 376.08	45.74

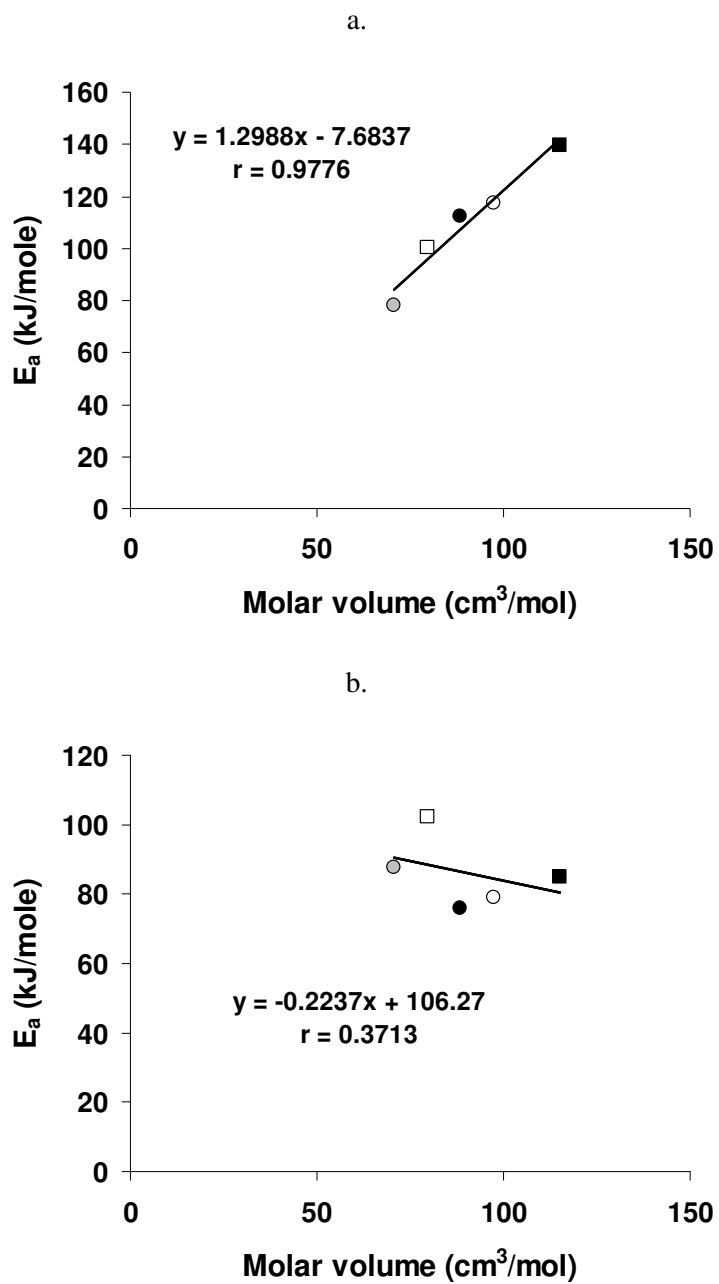


Figure 138. Desolvation activation energy versus solvent molar volume for different sulfameter solvates (\square , tetrahydrofuran; \bullet , dioxolane; \circ , oxane; \bullet , dioxane and \blacksquare , oxepane): a. isothermal and b. nonisothermal.

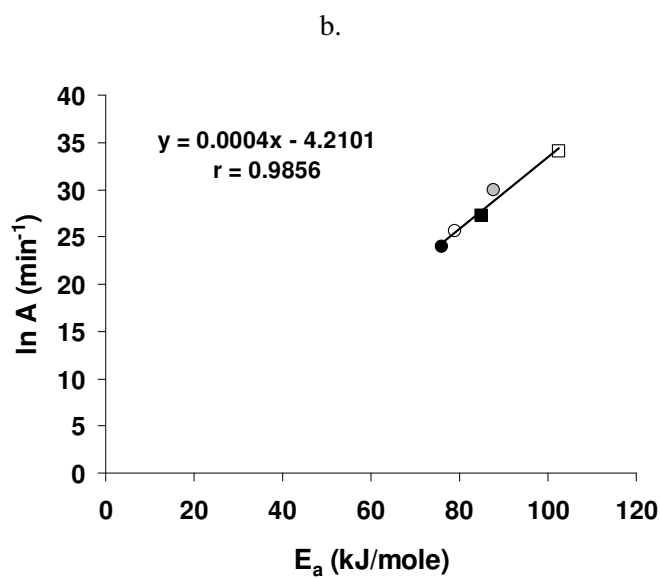
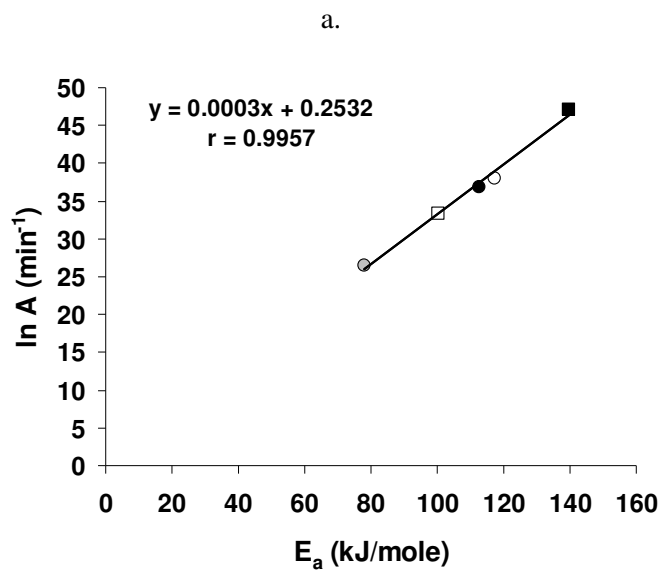


Figure 139. Kinetic compensation effect for different sulfameter solvates (\square , tetrahydrofuran; \bullet , dioxolane; \circ , oxane; \bullet , dioxane and \blacksquare , oxepane): a. isothermal and b. nonisothermal.

REFERENCES

- [1] Brown ME. *Introduction to thermal analysis: Techniques and applications*, Chapman and Hall, London, 1988, pp. 127-151.
- [2] Morris KR. Structural aspects of hydrates and solvates. In H. G. Brittain (ed), *Polymorphism in pharmaceutical solids*, Marcel Dekker, New York, 1999, pp. 125-181.
- [3] Bauer J; Spanton S; Henry R; Quick J; Dziki W; Porter W and Morris J, *Pharm. Res.* **18**: 859-866 (2001).
- [4] Chemburkar SR; Bauer J; Deming K; Spiwek H; Patel K; Morris J; Henry R; Spanton S; Dziki W; Porter W; Quick J; Bauer P; Donaubauber J; Narayanan BA; Soldani M; Riley D and McFarland K, *Org. Process Res. Dev.* **4**: 413-417 (2000).
- [5] Paul IC and Curtin DY, *Acc. Chem. Res.* **6**: 217-225 (1973).
- [6] Galwey AK and Brown ME, *Thermochim. Acta* **386**: 91-98 (2002).
- [7] Byrn SR; Pfeiffer RR and Stowell JG. *Solid-state chemistry of drugs*, SSCI Inc., West Lafayette, 1999, pp. 279-304.
- [8] Galwey AK, *Thermochim. Acta* **355**: 181-238 (2000).
- [9] Steinfeld JI; Francisco JS and Hase WL. *Chemical Kinetics and Dynamics*, second ed., Prentice Hall, Upper Saddle River, N.J., 1999.
- [10] Mullin JW. *Crystallization*, Butterworth-Heinemann, Oxford, 2001, pp. 1 - 31.
- [11] Brown ME. *Introduction to thermal analysis: Techniques and applications*, 2nd ed, Kluwer, Amsterdam, 2001, Chapter 10.
- [12] Shah HV; Babb DA and Smith DW, Jr., *Polymer* **41**: 4415-4422 (2000).
- [13] Kirsch BL; Richman EK; Riley AE and Tolbert SH, *J. Phys. Chem. B* **108**: 12698-12706 (2004).
- [14] Jones AR; Winter R; Florian P and Massiot D, *J. Phys. Chem. B* **109**: 4324-4332 (2005).
- [15] Bertmer M; Nieuwendaal RC; Barnes AB and Hayes SE, *J. Phys. Chem. B* **110**: 6270-6273 (2006).

- [16] Jacobs PWM and Tompkins FC. Classification and theory of solid reactions. In W. E. Garner (ed), *Chemistry of the solid state*, Academic Press, New York, 1955, pp. 184-212.
- [17] Brown ME; Dollimore D and Galwey AK. Theory of solid state reaction kinetics. In C. F. H. Tipper (ed), *Chemical kinetics*, Elsevier, Amsterdam, 1980, pp. 41-72.
- [18] Galwey AK and Brown ME. *Thermal decomposition of ionic solids: Chemical properties and reactivities of ionic crystalline phases*, Elsevier, Amsterdam, 1999, pp. 75-115.
- [19] Laidler KJ, *J. Chem. Educ.* **61**: 494-498 (1984).
- [20] Brown ME, *J. Therm. Anal. Cal.* **82**: 665-669 (2005).
- [21] Khawam A and Flanagan DR, *J. Phys. Chem. B* **109**: 10073-10080 (2005).
- [22] Zoglio MA; Windheuser JJ; Vatti R; Maulding HV, Jr.; Kornblum SS; Jacobs AL and Hamot H, *J. Pharm. Sci.* **57**: 2080-2085 (1968).
- [23] Maulding HV, Jr. and Zoglio MA, *J. Pharm. Sci.* **59**: 333-337 (1970).
- [24] Galwey AK and Brown ME. *Thermal decomposition of ionic solids: Chemical properties and reactivities of ionic crystalline phases*, Elsevier, Amsterdam, 1999, pp. 139-171.
- [25] Vyazovkin S, *J. Comput. Chem.* **18**: 393-402 (1997).
- [26] Flynn JH, *Thermochim. Acta* **300**: 83-92 (1997).
- [27] Gautschi W and Cahill WF. Exponential integral and related functions. In M. Abramowitz and I. Stegun (eds), *Handbook of mathematical functions with formulas, graphs, and mathematical tables*, National Bureau of Standards, Washington, DC, 1964, pp. 227-237.
- [28] Doyle CD, *J. Appl. Polym. Sci.* **5**: 285-292 (1961).
- [29] Doyle CD, *J. Appl. Polym. Sci.* **6**: 639-642 (1962).
- [30] Doyle CD, *Nature* **207**: 290-291 (1965).
- [31] Senum GI and R.T. Yang, *J. Therm. Anal.* **11**: 445-447 (1977).
- [32] Weisstein EW, "Exponential Integral." From MathWorld--A Wolfram Web Resource. <http://mathworld.wolfram.com/ExponentialIntegral.html>

- [33] Weisstein EW, "ExpIntegralE." From MathWorld--A Wolfram Web Resource. <http://functions.wolfram.com/GammaBetaErf/ExpIntegralE/10/0001/>
- [34] Perez-Maqueda LA and Criado JM, *J. Therm. Anal. Cal.* **60**: 909-915 (2000).
- [35] Urbanovici E; Popescu C and Segal E, *J. Therm. Anal. Cal.* **55**: 325-327 (1999).
- [36] Zhou DL; Schmitt EA; Zhang GG; Law D; Vyazovkin S; Wight CA and Grant DJW, *J. Pharm. Sci.* **92**: 1779-1792 (2003).
- [37] Vyazovkin S and Wight CA, *J. Phys. Chem. A* **101**: 8279-8284 (1997).
- [38] Zhou DL and Grant DJW, *J. Phys. Chem. A* **108**: 4239-4246 (2004).
- [39] Brown ME; Maciejewski M; Vyazovkin S; Nomen R; Sempere J; Burnham A; Opfermann J; Strey R; Anderson HL; Kemmler A; Keuleers R; Janssens J; Desseyn HO; Li CR; Tang TB; Roduit B; Malek J and Mitsuhashi T, *Thermochim. Acta* **355**: 125-143 (2000).
- [40] Maciejewski M, *Thermochim. Acta* **355**: 145-154 (2000).
- [41] Vyazovkin S, *Thermochim. Acta* **355**: 155-163 (2000).
- [42] Burnham AK, *Thermochim. Acta* **355**: 165-170 (2000).
- [43] Roduit B, *Thermochim. Acta* **355**: 171-180 (2000).
- [44] Sharp JH and Wentworth SA, *Anal. Chem.* **41**: 2060-2062 (1969).
- [45] Achar BNN; Brindley GW and Sharp. JH. Int. Clay Conf., Jerusalem, 1966, p 67.
- [46] Freeman ES and Carroll B, *J. Phys. Chem.* **62**: 394-397 (1958).
- [47] Freeman ES and Carroll B, *J. Phys. Chem.* **73**: 751-752 (1969).
- [48] Coats AW and Redfern JP, *Nature* **201**: 68-69 (1964).
- [49] Coats AW and Redfern JP, *J. Polym. Sci., Part B: Polym. Lett.* **3**: 917-920 (1965).
- [50] Kissinger HE, *J. Res. Nat. Bur. Stand.* **57**: 217-221 (1956).
- [51] Kissinger HE, *Anal. Chem.* **29**: 1702-1706 (1957).
- [52] Elder JP, *J. Therm. Anal.* **30**: 657-669 (1985).

- [53] Vyazovkin S and Wight CA, *Thermochim. Acta* **341**: 53-68 (1999).
- [54] Simon P, *J. Therm. Anal. Cal.* **76**: 123-132 (2004).
- [55] Zsako J, *J. Therm. Anal.* **5**: 239-251 (1973).
- [56] Zsako J, *J. Therm. Anal.* **46**: 1845-1864 (1996).
- [57] Khawam A and Flanagan DR, *Thermochim. Acta* **429**: 93-102 (2005).
- [58] Friedman HL, *J. Polym. Sci., Part C: Polym. Lett.* **6**: 183-195 (1964).
- [59] Ozawa T, *Bull. Chem. Soc. Jpn.* **38**: 1881-1886 (1965).
- [60] Flynn JH and Wall LA, *J. Polym. Sci., Part B: Polym. Lett.* **4**: 323-328 (1966).
- [61] Burnham AK and Braun RL, *Energy Fuels* **13**: 1-22 (1999).
- [62] Vyazovkin S and Dollimore D, *J. Chem. Inf. Comput. Sci.* **36**: 42-45 (1996).
- [63] Vyazovkin S, *J. Comput. Chem.* **22**: 178-183 (2001).
- [64] Budrugaec P and Segal E, *Int. J. Chem. Kinet.* **33**: 564-573 (2001).
- [65] Vyazovkin S, *Int. J. Chem. Kinet.* **34**: 418-420 (2002).
- [66] Brown ME, *J. Therm. Anal.* **49**: 17-32 (1997).
- [67] Galwey AK, *Thermochim. Acta* **413**: 139-183 (2004).
- [68] Galwey AK and Brown ME, *J. Therm. Anal. Cal.* **60**: 863-877 (2000).
- [69] Galwey AK, *J. Pharm. Pharmacol.* **51**: 879-886 (1999).
- [70] Galwey AK, *Thermochim. Acta* **399**: 1-29 (2003).
- [71] Galwey AK, *Thermochim. Acta* **407**: 93-103 (2003).
- [72] Vyazovkin S and Wight CA, *Annu. Rev. Phys. Chem.* **48**: 125-149 (1997).
- [73] Vyazovkin S, *New J. Chem.* **24**: 913-917 (2000).
- [74] Vyazovkin S, *Int. Rev. Phys. Chem.* **19**: 45-60 (2000).

- [75] Khawam A and Flanagan DR, *Thermochim. Acta* **436**: 101-112 (2005).
- [76] Galwey AK, *Thermochim. Acta* **397**: 249-268 (2003).
- [77] Brown ME and Brown RE, *Thermochim. Acta* **357-358**: 133-140 (2000).
- [78] Wendlandt WW. *Thermal analysis*, Wiley, New York, 1986, pp. 33.
- [79] Garn PD, *J. Therm. Anal.* **7**: 475-478 (1975).
- [80] Garn PD, *J. Therm. Anal.* **10**: 99-102 (1976).
- [81] Garn PD, *J. Therm. Anal.* **13**: 581-593 (1978).
- [82] Garn PD, *Thermochim. Acta* **135**: 71-77 (1988).
- [83] Garn PD, *Thermochim. Acta* **160**: 135-145 (1990).
- [84] Arnold M; Veress GE; Paulik J and Paulik F, *Anal. Chim. Acta* **124**: 341-350 (1981).
- [85] Galwey AK, *Adv. Catal.* **26**: 247-322 (1977).
- [86] Galwey AK and Brown ME, *Thermochim. Acta* **300**: 107-115 (1997).
- [87] Koga N, *Thermochim. Acta* **244**: 1-20 (1994).
- [88] Brown ME and Galwey AK, *Thermochim. Acta* **387**: 173-183 (2002).
- [89] Vyazovkin SV and Lesnikovich AI, *Thermochim. Acta* **128**: 297-300 (1988).
- [90] Brown ME; Maciejewski M and Vyazovkin S, *Thermochim. Acta* **307**: 201-203 (1997).
- [91] Brown ME; Maciejewski M and Vyazovkin S, *J. Therm. Anal. Cal.* **51**: 327-332 (1998).
- [92] Maciejewski M and Reller A, *Thermochim. Acta* **110**: 145-152 (1987).
- [93] Garner WE. *Chemistry of the solid state*, Academic Press, New York (1955).
- [94] Brown ME; Dollimore D and Galwey AK. Reactions in the solid state. In C. H. Bamford and C. F. H. Tipper (eds), *Comprehensive chemical kinetics*, Elsevier, Amsterdam, 1980, Chapter 3.

- [95] Galwey AK and Brown ME. *Thermal decomposition of ionic solids: Chemical properties and reactivities of ionic crystalline phases*, Elsevier, Amsterdam, 1999, Chapter 3.
- [96] Perez-Maqueda LA; Criado JM; Gotor FJ and Malek J, *J. Phys. Chem. A* **106**: 2862-2868 (2002).
- [97] Gotor FJ; Criado JM; Malek J and Koga N, *J. Phys. Chem. A* **104**: 10777-10782 (2000).
- [98] MacNeil DD and Dahn JR, *J. Phys. Chem. A* **105**: 4430-4439 (2001).
- [99] Alkhamis KA; Salem MS and Obaidat RM, *J. Pharm. Sci.* **95**: 859-870 (2006).
- [100] Capart R; Khezami L and Burnham AK, *Thermochim. Acta* **417**: 79-89 (2004).
- [101] Sestak J and Berggren G, *Thermochim. Acta* **3**: 1-12 (1971).
- [102] Yang J; McCoy BJ and Madras G, *J. Phys. Chem. B* **109**: 18550-18557 (2005).
- [103] Yang J; McCoy BJ and Madras G, *J. Chem. Phys.* **122**: - (2005).
- [104] Liu J; Wang JJ; Li HH; Shen DY; Zhang JM; Ozaki Y and Yan SK, *J. Phys. Chem. B* **110**: 738-742 (2006).
- [105] Burnham AK; Weese RK and Weeks BL, *J. Phys. Chem. B* **108**: 19432-19441 (2004).
- [106] Graetz J and Reilly JJ, *J. Phys. Chem. B* **109**: 22181-22185 (2005).
- [107] Wang S; Gao QY and Wang JC, *J. Phys. Chem. B* **109**: 17281-17289 (2005).
- [108] Hromadova M; Sokolova R; Pospisil L and Fanelli N, *J. Phys. Chem. B* **110**: 4869-4874 (2006).
- [109] Wu CZ; Wang P; Yao XD; Liu C; Chen DM; Lu GQ and Cheng HM, *J. Phys. Chem. B* **109**: 22217-22221 (2005).
- [110] Peterson VK; Neumann DA and Livingston RA, *J. Phys. Chem. B* **109**: 14449-14453 (2005).
- [111] Skrdla PJ and Robertson RT, *J. Phys. Chem. B* **109**: 10611-10619 (2005).
- [112] Boldyrev VV, *Thermochim. Acta* **100**: 315-338 (1986).

- [113] Bagdassarian C, *Acta Physicochim. U.S.S.R.* **20**: 441 (1945).
- [114] Allnatt AR and Jacobs PWM, *Can. J. Chem.* **46**: 111-116 (1968).
- [115] Guo L; Radisic A and Searson PC, *J. Phys. Chem. B* **109**: 24008-24015 (2005).
- [116] Avrami M, *J. Chem. Phys.* **7**: 1103-1112 (1939).
- [117] Avrami M, *J. Chem. Phys.* **8**: 212-224 (1940).
- [118] Erofeyev BV, *Doklady Akademii Nauk SSSR, Seriya A* **52**: 511-514 (1946).
- [119] Jacobs PWM, *J. Phys. Chem. B* **101**: 10086-10093 (1997).
- [120] Prout EG and Tompkins FC, *Trans. Faraday Soc.* **40**: 488-498 (1944).
- [121] Carstensen JT. *Drug Stability: Principles and Practices*, 2nd revised, Marcel Dekker, New York, 1995, p. 237.
- [122] Brown ME and Glass BD, *Int. J. Pharm.* **190**: 129-137 (1999).
- [123] Brown ME, *Thermochim. Acta* **300**: 93-106 (1997).
- [124] Prout EG and Tompkins FC, *Trans. Faraday Soc.* **42**: 468-472 (1946).
- [125] Skrdla PJ, *J. Phys. Chem. A* **108**: 6709-6712 (2004).
- [126] Guinesi LS; Ribeiro CA; Crespi. MS; Santos AF and Capela. MV, *J. Therm. Anal. Cal.* **in press**: (2006).
- [127] Carstensen JT, *J. Pharm. Sci.* **63**: 1-14 (1974).
- [128] Chunxiu G; Yufang S and Donghua C, *J. Therm. Anal. Cal.* **76**: 203-216 (2004).
- [129] Liqing L and Donghua C, *J. Therm. Anal. Cal.* **78**: 283-293 (2004).
- [130] Gao ZM; Amasaki I and Nakada M, *Thermochim. Acta* **385**: 95-103 (2002).
- [131] Welch AJE. Solid-solid reactions. In W. E. Garner (ed), *Chemistry of the solid state*, Academic Press, New York, 1955, Chapter 12.
- [132] Wyandt CM and Flanagan DR, *Thermochim. Acta* **196**: 379-389 (1992).
- [133] Booth F, *Trans. Faraday Soc.* **44**: 796-801 (1948).

- [134] Jander W, *Z. Anorg. Allg. Chem.* **163**: 1-30 (1927).
- [135] Ginstling AM and Brounshtein BI, *J. Appl. Chem. USSR* **23**: 1327-1338 (1950).
- [136] Crank J. *The mathematics of diffusion*, 2nd, Clarendon Press, Oxford, England, 1975, p.89.
- [137] Buscaglia V and Milanese C, *J. Phys. Chem. B* **109**: 18475-18482 (2005).
- [138] Eames DJ and Empie HJ, *International Chemical Recovery Conference: Changing Recovery Technology to Meet the Challenges of the Pulp and Paper Industry, Whistler, BC, Canada, June 11-14, (2001)*.
- [139] Crank J. *The mathematics of diffusion*, 2nd, Clarendon Press, Oxford, England, 1975, p. 69.
- [140] Mampel KL, *Z. Phys. Chem.* **A187**: 235-249 (1940).
- [141] Mampel KL, *Z. Phys. Chem.* **A187**: 43-57 (1940).
- [142] Lopes WS; Morais CRD; de Souza AG and Leite VD, *J. Therm. Anal. Cal.* **79**: 343-347 (2005).
- [143] Pap AE; Kordas K; George TF and Leppavuori S, *J. Phys. Chem. B* **108**: 12744-12747 (2004).
- [144] Carniti P; Gervasini A and Bennici S, *J. Phys. Chem. B* **109**: 1528-1536 (2005).
- [145] Kuhnert-Brandstetter M. *Thermomicroscopy in the analysis of pharmaceuticals*, [1st], Pergamon Press, Oxford, New York,, 1971.
- [146] Gorbitz CH and Hersleth HP, *Acta Crystallogr B* **56**: 526-534 (2000).
- [147] Guillory JK. Generation of Polymorphs, Hydrates, Solvates, and Amorphous solids. In H. G. Brittain (ed), *Polymorphism in Pharmaceutical Solids*, Marcel Dekker, Inc., Milford, New Jersey, 1999, chapter 5.
- [148] Dahl O; Ziedrich KH; Marek GJ and Paradies HH, *J. Pharm. Sci.* **78**: 598-606 (1989).
- [149] Trivedi J; Shell JW and Biles JA, *J. Am. Pharm. Assoc. (Wash). Scientific Edition* **48**: 583-587 (1959).
- [150] Michel A; Drouin M and Glaser R, *J. Pharm. Sci.* **83**: 508-513 (1994).

- [151] Jozwiakowski MJ; Williams SO and Hathaway RD, *Int. J. Pharm.* **91**: 195-207 (1993).
- [152] Pienaar EW; Caira MR and Lotter AP, *J. Crystallogr. Spectrosc. Res.* **23**: 739-744 (1993).
- [153] Han J and Suryanarayanan R, *Pharm. Dev. Technol.* **3**: 587-596 (1998).
- [154] Fukumori Y; Fukuda T; Yamamoto Y; Shigitani Y; Hanyu Y; Takeuchi Y and Sato N, *Chem. Pharm. Bull.* **31**: 4029-4039 (1983).
- [155] Beckstead HD; Neville GA and Shurvell HF, *Fresen. J. Anal. Chem.* **345**: 727-732 (1993).
- [156] Neville GA; Beckstead HD and Cooney JD, *Fresen. J. Anal. Chem.* **349**: 746-750 (1994).
- [157] Caira MR and Mohamed R, *Supramol. Chem.* **2**: 201-207 (1993).
- [158] Vyazovkin S, *Thermochim. Acta* **397**: 269-271 (2003).
- [159] Vyazovkin S and Wight CA, *Int. Rev. Phys. Chem.* **17**: 407-433 (1998).
- [160] Sewry JD and Brown ME, *Thermochim. Acta* **390**: 217-225 (2002).
- [161] Bolton S. *Pharmaceutical statistics: practical and clinical applications*, 1st, Dekker, New York, 1984, p 188.
- [162] Tang TB and Chaudhri MM, *J. Therm. Anal.* **18**: 247-261 (1980).
- [163] Gao X; Chen D and Dollimore D, *Thermochim. Acta* **223**: 75-82 (1993).
- [164] Vyazovkin S, *Int. J. Chem. Kinet.* **28**: 95-101 (1996).
- [165] Dong ZD; Salsbury JS; Zhou DL; Munson EJ; Schroeder SA; Prakash I; Vyazovkin S; Wight CA and Grant DJW, *J. Pharm. Sci.* **91**: 1423-1431 (2002).
- [166] Zhou DL; Schmitt EA; Zhang GGZ; Law D; Wight CA; Vyazovkin S and Grant DJW, *J. Pharm. Sci.* **92**: 1367-1376 (2003).
- [167] Weisstein EW, "Arithmetic Mean" From MathWorld-A Wolfram Web Resource. <http://mathworld.wolfram.com/ArithmeticMean.html>
- [168] Weisstein EW, "Geometric Mean" From MathWorld-A Wolfram Web Resource. <http://mathworld.wolfram.com/GeometricMean.html>

- [169] Weisstein EW, "Harmonic Mean" From MathWorld-A Wolfram Web Resource. <http://mathworld.wolfram.com/HarmonicMean.html>
- [170] Cantrell DW, "Pythagorean Means" From MathWorld-A Wolfram Web Resource. <http://mathworld.wolfram.com/PythagoreanMeans.html>
- [171] Cantrell DW and Weisstein EW, "Power Mean" From MathWorld-A Wolfram Web Resource. <http://mathworld.wolfram.com/PowerMean.html>
- [172] Li HQ; Shao TM; Li DS and Chen DR, *Thermochim. Acta* **427**: 9-12 (2005).
- [173] Svatek E; Knobloch E and Budesinsky Z, *Cesk. Farm.* **15**: 470-473 (1966).
- [174] Mesley RJ and Houghton EE, *J. Pharm. Pharmacol.* **19**: 295-304. (1967).
- [175] Kuhnert-Brandstaetter M; Kofler A and Vlachopoulos A, *Sci. Pharm.* **36**: 164-179 (1968).
- [176] Kuhnert-Brandstaetter M and Wunsch S, *Mikrochim. Acta* 1297-1307 (1969).
- [177] Moustafa MA; Ebian AR; Khalil SA and Motawi MM, *J. Pharm. Pharmacol.* **23**: 868-874 (1971).
- [178] Bettinetti GP; Giordano F; La Manna A and Giuseppetti G, *Farm. Ed. Prat.* **29**: 493-507 (1974).

APPENDIX

DERIVATION OF THE SENUM-YANG APPROXIMATION TERMS

According to Eq. (27), the four terms of the Senum-Yang approximation can be derived as follows:

1-term

$$\left(\frac{e^{-x}}{x}\right) \frac{1}{x+2}$$

2-terms

$$\left(\frac{e^{-x}}{x}\right) \frac{1}{x + \frac{2}{1 + \frac{1}{x+3}}} \longrightarrow \frac{1}{x + \frac{2}{\frac{x+4}{x+3}}} \longrightarrow \frac{1}{x + \frac{2x+6}{x+4}} \longrightarrow \frac{1}{\frac{x^2+4x+2x+6}{x+4}} \longrightarrow$$

$$\left(\frac{e^{-x}}{x}\right) \frac{x+4}{x^2+6x+6}$$

3-terms

$$\left(\frac{e^{-x}}{x}\right) \frac{1}{x + \frac{2}{1 + \frac{1}{x + \frac{3}{1 + \frac{2}{x+4}}}}} \longrightarrow \frac{1}{x + \frac{2}{1 + \frac{1}{x + \frac{3}{x+6}}}}} \longrightarrow \frac{1}{x + \frac{2}{1 + \frac{1}{x + \frac{3x+12}{x+6}}}}} \longrightarrow$$

$$\frac{1}{x + \frac{2}{1 + \frac{1}{x^2+9x+12}}} \longrightarrow \frac{1}{x + \frac{2}{1 + \frac{x+6}{x^2+9x+12}}} \longrightarrow \frac{1}{x + \frac{2}{\frac{x^2+10x+18}{x^2+9x+12}}} \longrightarrow$$

$$\frac{1}{x + \frac{2x^2+18x+24}{x^2+10x+18}} \longrightarrow \frac{1}{\frac{x^3+12x^2+36x+24}{x^2+10x+18}} \longrightarrow \left(\frac{e^{-x}}{x}\right) \frac{x^2+10x+18}{x^3+12x^2+36x+24}$$

4-terms

$$\left(\frac{e^{-x}}{x}\right) \frac{1}{x + \frac{1}{1 + \frac{1}{x + \frac{1}{1 + \frac{2}{x + \frac{3}{1 + \frac{3}{x+5}}}}}}} \longrightarrow \frac{1}{x + \frac{1}{1 + \frac{1}{x + \frac{1}{1 + \frac{2}{x + \frac{x+8}{x+5}}}}} \longrightarrow$$

$$\frac{1}{x + \frac{1}{1 + \frac{1}{x + \frac{2}{1 + \frac{4x+20}{x+8}}}}} \longrightarrow \frac{1}{x + \frac{1}{1 + \frac{1}{x + \frac{2}{1 + \frac{x^2+12x+20}{x+8}}}}} \longrightarrow$$

$$\frac{1}{x + \frac{1}{1 + \frac{1}{x + \frac{2x+16}{1 + \frac{2x+16}{x^2+12x+20}}}}} \longrightarrow \frac{1}{x + \frac{1}{1 + \frac{1}{x + \frac{3}{1 + \frac{x^2+14x+36}{x^2+12x+20}}}}} \longrightarrow$$

$$\frac{1}{x + \frac{1}{1 + \frac{1}{x + \frac{3x^2+36x+60}{x^2+14x+36}}}}} \longrightarrow \frac{1}{x + \frac{1}{1 + \frac{1}{x + \frac{x^3+17x^2+72x+60}{x^2+14x+36}}}}} \longrightarrow$$

$$\frac{1}{x + \frac{1}{1 + \frac{1}{x + \frac{x^2+14x+36}{x^3+17x^2+72x+60}}}}} \longrightarrow \frac{1}{x + \frac{2}{x + \frac{x^3+18x^2+86x+96}{x^3+17x^2+72x+60}}} \longrightarrow$$

$$\frac{1}{x + \frac{2x^3+34x^2+144x+120}{x^3+18x^2+86x+96}} \longrightarrow \frac{1}{x + \frac{20x^3+120x^2+240x+120}{x^3+18x^2+86x+96}} \longrightarrow$$

$$\left(\frac{e^{-x}}{x}\right) \frac{x^3+18x^2+86x+96}{x^4+20x^3+120x^2+240x+120}$$